Universidad de Oviedo
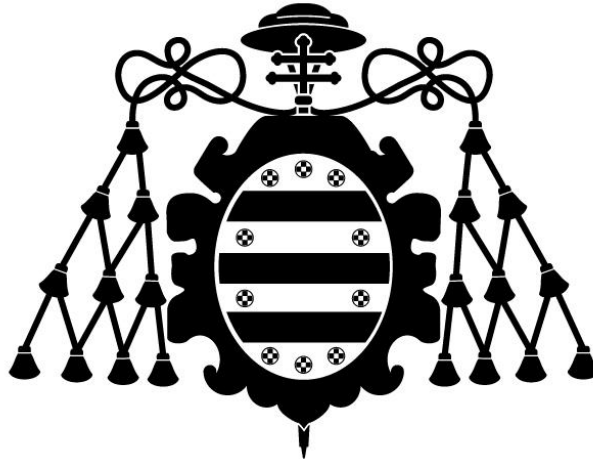## *Universidá d'Uviéu*
University of Oviedo

Programa de Doctorado en Materiales

MODELIZACIÓN NUMÉRICA DE FRACTURA FRÁGIL EN
MATERIALES METÁLICOS

TESIS DOCTORAL

Sandra Fuentes Alonso

Agosto, 2020

Universidad de Oviedo
Universidá d'Uviéu
University of Oviedo

Programa de Doctorado en Materiales

MODELIZACIÓN NUMÉRICA DE FRACTURA FRÁGIL EN MATERIALES METÁLICOS

TESIS DOCTORAL

Directores

Covadonga Betegón Biempica

Emilio Martínez Pañeda

RESUMEN DEL CONTENIDO DE TESIS DOCTORAL

1.- Título de la Tesis	
Español: Modelización numérica de fractura frágil en materiales metálicos	Inglés: Numerical modelling of brittle fracture in metallic materials.

2.- Autora	
Nombre: Sandra Fuentes Alonso	DNI.
Programa de Doctorado: Materiales	
Órgano responsable: Comisión Académica Programa Doctorado en Materiales	

RESUMEN (en español)

La necesidad de desarrollar un nuevo modelo energético y los avances en el campo de la electrónica demandan desarrollos industriales significativos. Un reto importante es comprender, predecir y optimizar el comportamiento de los materiales empleados, frecuentemente sometidos a condiciones extremas. Existe una fuerte necesidad de estimar, de manera precisa, si los materiales elegidos en la fase de diseño pueden garantizar un funcionamiento fiable y seguro durante su vida útil.

Los metales se consideran materiales dúctiles, lo que implica que el material "avisa" antes de la fractura, disminuyendo la sección del área traccionada. Sin embargo, los materiales metálicos pueden también mostrar un comportamiento frágil bajo ciertas circunstancias (factores fragilizantes). Esta tesis doctoral estudia tres fenómenos de especial interés, que constituyen los principales escenarios de fragilización: presencia de hidrógeno, bajas temperaturas y decohesión en la interfaz de un metal con otro material (compuesto bi-material). Los resultados se han divulgado a través de tres artículos científicos, centrándose cada uno de ellos en uno de los tres fenómenos mencionados.

En el primer trabajo se analiza la fragilización generada por la presencia de hidrógeno, modelizando la difusión de hidrógeno y empleando una nueva formulación de campo de fase para capturar la fragilización. El comportamiento mecánico se caracteriza mediante la teoría de plasticidad J2 para deformaciones finitas y el análisis se centra en ensayos de tensión a bajas velocidades de deformación (SSRT, del inglés Slow Strain-Rate Testing). La comparación de los resultados numéricos y los ensayos revela la aparición de grietas mucho antes de la ruptura final. Las implicaciones son importantes, ya que la existencia de grietas previas a la rotura compromete la aplicabilidad del ensayo SSRT, el más popular en la caracterización de la influencia del hidrógeno en el comportamiento de materiales.

En el segundo artículo se desarrolla un modelo para predecir clivaje en aceros ferríticos a bajas temperaturas. El modelo se basa en la estadística de Weibull, el principio del eslabón más débil y el modelo constitutivo de la teoría mecanística de gradientes de deformación plástica (MSG). Los modelos de gradientes de deformación plástica pueden capturar la elevación tensional cerca de la grieta al considerar la influencia de dislocaciones

geométricamente necesarias. Los resultados de elementos finitos son comparados con ensayos de fractura para calibrar los parámetros estadísticos, empleando tanto MSG y como plasticidad J2. Se observan diferencias significativas, subrayando la necesidad de incorporar la influencia de los gradientes de deformación plástica en el frente de grieta.

En el tercer artículo se investiga la fractura frágil en la interfaz de un bi-material metal-cerámico. Este fenómeno no puede ser explicado con plasticidad convencional, ya que las tensiones cerca de la grieta son mucho menores que las necesarias para lograr la decohesión. Se plantea la hipótesis de que el bloqueo de dislocaciones en la interfaz y el endurecimiento en local debido a los gradientes de deformación pueden dar lugar a tensiones suficientemente altas. El caso paradigmático de una interfaz niobio-zafiro es analizado empleando la teoría de gradientes de distorsión plástica (DGP) de orden superior. Los resultados muestran que el modelo puede racionalizar mecanísticamente este fenómeno

Existe una gran necesidad de disponer de modelos de fractura capaces de predecir fracturas frágiles, previniendo así fallos catastróficos. Estos modelos deben capturar los micro-mecanismos físicos que gobiernan la fractura, pero también proporcionar predicciones a escalas relevantes para la práctica ingenieril. Este trabajo tiene el objetivo de desarrollar un marco teórico-numérico en el medio continuo que capture los fenómenos físicos relevantes a una escala apropiada y permita a su vez predecir la fractura a grandes escalas.

RESUMEN (en Inglés)

The need of developing a new energetic model and recent progress in the area of electronics demand significant industrial developments. One of the most important challenges is to understand, predict and optimise the behaviour of the materials employed, often under extreme conditions. There is a strong need to accurately estimate if the materials chosen at the design stage will guarantee a safe and reliable performance during the service lifetime.

Metals are typically considered ductile materials, meaning that if high stresses develop, the material will "warn" before fracture by diminishing the section in the area under tension. However, metallic materials can also exhibit brittle behaviour under certain circumstances (embrittlement factors). This PhD Thesis studies three phenomena of particular interest, that constitute the main scenarios where metals become brittle: presence of hydrogen, low temperatures and interface decohesion in a bi-material. The results are disseminated via three scientific publications in international journals, each of them focusing in one of the above described phenomena.

The first work analyses embrittlement due to the presence of hydrogen, modelling hydrogen transport and using a new phase field formulation for capturing the embrittlement process. The mechanical behaviour is characterized through finite strain J2 plasticity and focus is on modelling Slow Strain-Rate Testing (SSRT). Model predictions are compared with experimental data and it is concluded that early cracking exists, much before final rupture. The implications are profound, as early cracking compromises the applicability of SSRT, the experimental setup most widely used to characterize the influence of environment in the

material behaviour.

In the second paper, a predictive model for cleavage in ferritic steels at low temperatures is developed. The model is grounded on Weibull's statistics, a weakest-link approach and a material description given by the mechanism-based strain gradient (MSG) plasticity theory. Strain gradient plasticity models can capture the influence of Geometrically Necessary Dislocation in elevating crack tip stresses. Finite element results are compared with fracture experiments to calibrate the statistical parameters using both MSG and J2 plasticity. Notable differences are observed, highlighting the need to resolve the influence of plastic strain gradients close to the crack tip.

In the third and last paper, brittle fracture at the interface of a bimaterial (metal-ceramic) is investigated. This phenomenon cannot be rationalised with conventional plasticity, as crack tip stresses are much lower than those needed to achieve decohesion. This work hypothesises that high crack tip stresses can be attained if the model can capture dislocation blockage at the interface and crack tip hardening due to plastic strain gradients. Thus, the paradigmatic case of fracture at a Niobium-Sapphire interface is modelled using the higher order theory of Distortion Gradient Plasticity (DGP). The results reveal that this framework is appropriate for providing a mechanistic understanding of this phenomenon.

There is a strong need in engineering applications for developing fracture models that are capable of predicting brittle fractures, preventing the associated catastrophic failures. These models must account for the underlying physical micro-mechanisms but at the same time deliver predictions at scales relevant to engineering practice. This work aims at developing a theoretical-numerical continuum framework that can capture the relevant physical phenomena at the appropriate scale while addressing the need of reliably predicting fracture at large scales.

SR. PRESIDENTE DE LA COMISIÓN ACADÉMICA DEL PROGRAMA DE DOCTORADO EN MATERIALES

"La ciencia matemática muestra lo que es. Es el lenguaje de las relaciones invisibles entre las cosas. Pero para usar y aplicar ese lenguaje debemos de ser capaces de apreciar plenamente, de sentir, de calibrar lo invisible, lo inconsciente"

Ada Lovelace (1815-1852)

"Para adquirir conocimiento, uno debe estudiar; pero para adquirir sabiduría, uno debe observar"

Marilyn Vos Savant (1946)

Esta Tesis se presenta como un compendio de tres publicaciones para la obtención del título de Doctor por la Universidad de Oviedo, siguiendo el acuerdo de 21 de Julio de 2011, del consejo de Gobierno de la Universidad de Oviedo, por el que se aprueba el Reglamento de los Estudios de Doctorado.

Los artículos que forman parte de esta tesis doctoral y han sido publicados en revistas indexadas en Journal Citation Report (JCR) son:

- E. Martínez-Pañeda, Z. Harris, S. Fuentes-Alonso, J.R. Scully, J.T. Burns, ***"On the suitability of slow strain rate tensile testing for assessing hydrogen embrittlement susceptibility"***, Corrosion Science. Volume 163: 108291 (2020)

   Índice de Impacto: 6.479

- E. Martínez-Pañeda, S. Fuentes-Alonso, C. Betegón. ***"Gradient-enhanced statistical analysis of cleavage fracture"***, European Journal of Mechanics a / solids. Volume 77: 103785 (2019)

   Índice de Impacto: 3.786

- S. Fuentes-Alonso, E. Martínez-Pañeda. ***"Fracture in distortion gradient plasticity"***, International Journal of Engineering Science, 156: 103369 (2020)

   Índice de Impacto: 9.219

RESUMEN

La necesidad de desarrollar un nuevo modelo energético y los avances en el campo de la electrónica demandan desarrollos industriales significativos. Un reto importante es comprender, predecir y optimizar el comportamiento de los materiales empleados, frecuentemente sometidos a condiciones extremas. Existe una fuerte necesidad de estimar, de manera precisa, si los materiales elegidos en la fase de diseño pueden garantizar un funcionamiento fiable y seguro durante su vida útil.

Los metales se consideran materiales dúctiles, lo que implica que el material "avisa" antes de la fractura, disminuyendo la sección del área traccionada. Sin embargo, los materiales metálicos pueden también mostrar un comportamiento frágil bajo ciertas circunstancias (factores fragilizantes). Esta tesis doctoral estudia tres fenómenos de especial interés, que constituyen los principales escenarios de fragilización: presencia de hidrógeno, bajas temperaturas y decohesión en la interfaz de un metal con otro material (compuesto bi-material). Los resultados se han divulgado a través de tres artículos científicos, centrándose cada uno de ellos en uno de los tres fenómenos mencionados.

En el primer trabajo se analiza la fragilización generada por la presencia de hidrógeno, modelizando la difusión de hidrógeno y empleando una nueva formulación de campo de fase para capturar la fragilización. El comportamiento mecánico se caracteriza mediante la teoría de plasticidad J2 para deformaciones finitas y el análisis se centra en ensayos de tensión a bajas velocidades de deformación (SSRT, del inglés Slow Strain-Rate Testing). La comparación de los resultados numéricos y los ensayos revela la aparición de grietas mucho antes de la ruptura final. Las implicaciones son importantes, ya que la existencia de grietas previas a la rotura compromete la aplicabilidad del ensayo SSRT, el más popular en la caracterización de la influencia del hidrógeno en el comportamiento de materiales.

En el segundo artículo se desarrolla un modelo para predecir clivaje en aceros ferríticos a bajas temperaturas. El modelo se basa en la estadística de Weibull, el principio del eslabón más débil y el modelo constitutivo de la teoría mecanística de gradientes de deformación plástica (MSG). Los modelos de gradientes de deformación plástica pueden capturar la elevación tensional cerca de la grieta al considerar la influencia de dislocaciones geométricamente necesarias. Los resultados de elementos finitos son comparados con ensayos de fractura para calibrar los parámetros estadísticos,

empleando tanto MSG y como plasticidad J2. Se observan diferencias significativas, subrayando la necesidad de incorporar la influencia de los gradientes de deformación plástica en el frente de grieta.

En el tercer artículo se investiga la fractura frágil en la interfaz de un bi-material metal-cerámico. Este fenómeno no puede ser explicado con plasticidad convencional, ya que las tensiones cerca de la grieta son mucho menores que las necesarias para lograr la decohesión. Se plantea la hipótesis de que el bloqueo de dislocaciones en la interfaz y el endurecimiento en local debido a los gradientes de deformación pueden dar lugar a tensiones suficientemente altas. El caso paradigmático de una interfaz niobio-zafiro es analizado empleando la teoría de gradientes de distorsión plástica (DGP) de orden superior. Los resultados muestran que el modelo puede racionalizar mecanísticamente este fenómeno

Existe una gran necesidad de disponer de modelos de fractura capaces de predecir fracturas frágiles, previniendo así fallos catastróficos. Estos modelos deben capturar los micro-mecanismos físicos que gobiernan la fractura, pero también proporcionar predicciones a escalas relevantes para la práctica ingenieril. Este trabajo tiene el objetivo de desarrollar un marco teórico-numérico en el medio continuo que capture los fenómenos físicos relevantes a una escala apropiada y permita a su vez predecir la fractura a grandes escalas.

ABSTRACT

The need of developing a new energetic model and recent progress in the area of electronics demand significant industrial developments. One of the most important challenges is to understand, predict and optimise the behaviour of the materials employed, often under extreme conditions. There is a strong need to accurately estimate if the materials chosen at the design stage will guarantee a safe and reliable performance during the service lifetime.

Metals are typically considered ductile materials, meaning that if high stresses develop, the material will "warn" before fracture by diminishing the section in the area under tension. However, metallic materials can also exhibit brittle behaviour under certain circumstances (embrittlement factors). This PhD Thesis studies three phenomena of particular interest, that constitute the main scenarios where metals become brittle: presence of hydrogen, low temperatures and interface decohesion in a bi-material. The results are disseminated via three scientific publications in international journals, each of them focusing in one of the above described phenomena.

The first work analyses embrittlement due to the presence of hydrogen, modelling hydrogen transport and using a new phase field formulation for capturing the embrittlement process. The mechanical behaviour is characterized through finite strain J2 plasticity and focus is on modelling Slow Strain-Rate Testing (SSRT). Model predictions are compared with experimental data and it is concluded that early cracking exists, much before final rupture. The implications are profound, as early cracking compromises the applicability of SSRT, the experimental setup most widely used to characterize the influence of environment in the material behaviour.

In the second paper, a predictive model for cleavage in ferritic steels at low temperatures is developed. The model is grounded on Weibull's statistics, a weakest-link approach and a material description given by the mechanism-based strain gradient (MSG) plasticity theory. Strain gradient plasticity models can capture the influence of Geometrically Necessary Dislocation in elevating crack tip stresses. Finite element results are compared with fracture experiments to calibrate the statistical parameters using both MSG and J2 plasticity. Notable differences are observed, highlighting the need to resolve the influence of plastic strain gradients close to the crack tip.

In the third and last paper, brittle fracture at the interface of a bimaterial (metal-ceramic) is investigated. This phenomenon cannot be rationalised with conventional plasticity, as crack tip stresses are much lower than those needed to achieve decohesion. This work hypothesises that high crack tip stresses can be attained if the model can capture dislocation blockage at the interface and crack tip hardening due to plastic strain gradients. Thus, the paradigmatic case of fracture at a Niobium-Sapphire interface is modelled using the higher order theory of Distortion Gradient Plasticity (DGP). The results reveal that this framework is appropriate for providing a mechanistic understanding of this phenomenon.

There is a strong need in engineering applications for developing fracture models that are capable of predicting brittle fractures, preventing the associated catastrophic failures. These models must account for the underlying physical micro-mechanisms but at the same time deliver predictions at scales relevant to engineering practice. This work aims at developing a theoretical-numerical continuum framework that can capture the relevant physical phenomena at the appropriate scale while addressing the need of reliably predicting fracture at large scales.

AGRADECIMIENTOS

Me gustaría expresar mi especial gratitud hacia mis directores de tesis, Covadonga Betegón Biempica y Emilio Martínez Pañeda. Por su infinita paciencia en mis inicios hacia la mecánica de la fractura y por su disponibilidad para resolver dudas en cualquier momento. Especial mención a la persistencia de Emilio, intentando abrirme los ojos hacia las bondades del mundo investigador en los momentos en los que veía la tesis como un imposible fuera de mi alcance.

Agradecer a todos los Doctores que han colaborado en la consecución de la tesis y han aportado su conocimiento. A Miguel Muñiz Calvente por orientarnos en el mundo de la probabilidad de fallo. A los compañeros de la Universidad de Virginia, por recurrir a nosotros tratando de encontrar una solución numérica a su problema. A Christian Niordson y Viggo Tvergaard, por hacerme participe de la ilusión con la que viven la vida investigadora y contagiarme ese sentimiento.

Agradecer a mis padres, que me enseñaron el camino de la constancia y la organización para ser capaz de llegar a donde me proponga en la vida. A mi hermano, que con su capacidad de resolución procrastinadora siempre me enseñó a apreciar más el día a día y relativizar los problemas. A mis abuelas, que aunque no tuvieron opción a una educación, siempre aportan una sabiduría incalculable.

CONTENIDO

LISTA DE FIGURAS

ACRÓNIMOS

MFEL - Mecánica de Fractura Elástico Lineal

CTOD – Crack tip opening displacement

EAC - Environment Assisted Cracking.

HAC - Hydrogen Asssisted Cracking

HE - Hydrogen Embrittlement

IHAC - Internal Hydrogen Assisted Cracking

HEAC - Hydrogen Environment Assisted Cracking.

HEDE - Hydrogen Enhanced Decohesion

HELP - Hydrogen Enhanced Localized Plasticity

IG – Intergranular

FCC – Faced Centred Cubic

BCC – Body Centred Cubic

GND – Geometrically Necessary Dislocation

SSD – Statistical Stored Dislocation

SGP – Strain Gradient Plasticity

MSG – Mechanism-based Strain Gradient

CMSG – Conventional Mechanism-based Strain Gradient

DGP – Distorsion Gradient Plasticity

SSRT - Slow Strain-Rate Technique

FGM – Functionally Graded Materials

1. INTRODUCCIÓN

1.1. ANTECEDENTES

Tradicionalmente, los metales se conocen por ser materiales que desarrollan un comportamiento dúctil y el desarrollo de fracturas en los mismos se asocia con la nucleación de microhuecos internos que acaban por unirse y generar fractura dúctil. La formación de la fractura dúctil consta de varias fases y se desarrolla de una manera lenta, produciendo cambios visibles en la geometría del elemento.

La fractura frágil, por otro lado, se desencadena de una manera mucho más rápida, sin que se produzcan señales en la geometría de la pieza previas a la rotura. Mientras que para llegar a producirse fractura dúctil se requiere una carga externa elevada, las cargas necesarias para desarrollar fractura frágil son bajas.

El diseño de estructuras o componentes metálicos se realiza convencionalmente considerando su comportamiento dúctil y por lo tanto, se asume una capacidad del metal para soportar tensiones aplicadas altas, es decir, se asume que el metal tiene una tenacidad a fractura alta.

Al estudiar el comportamiento de materiales metálicos se ha observado que, ante ciertos fenómenos físicos, estos modifican su comportamiento, presentando fractura frágil. Esta fragilización de los metales, reduce sustancialmente su tenacidad a fractura, pudiendo desencadenar el fallo estructural y colapso para tensiones aplicadas mucho menores a las máximas consideradas en su diseño.

1.1.1. FRACTURA FRÁGIL EN METALES

La mecánica de la fractura comenzó a estudiarse en 1920, cuando Griffith advierte que la resistencia a tracción de un sólido cristalino obtenida experimentalmente, es mucho menor que su resistencia teórica. Para explicar estas observaciones

experimentales, Griffith formuló la hipótesis de que el sólido está debilitado por la presencia de grietas o fisuras microscópicas en su superficie o en su interior. La consideración de estas microgrietas altera el valor de la resistencia teórica, ya que actúan como concentradores de tensiones. Griffith aplica el primer principio de la termodinámica para determinar el crecimiento de una grieta en un sólido, sugiriendo que una grieta crecerá espontáneamente solo si durante esa acción disminuye la energía total del sistema [1].

Posteriormente, la formulación de Griffith fue modificada por G.R. Irwin [2] y E. Orowan [3] , para extenderla a metales. Se basa también en un balance energético, pero considera que la energía necesaria para que se produzca la fractura ha de ser la suficiente no sólo para romper los enlaces interatómicos, como sugería Griffith, sino que además es necesario producir la plastificación del material.

Este modelo energético establece la condición para que se produzca la fractura como la comparación entre el valor que toman dos factores: la denominada **energía disponible para la propagación de la grieta, $\mathcal{G}$**, y la **resistencia a fractura del material, R**. Para el caso de una placa infinita con una grieta de longitud $2a$ sometida a una tensión remota σ, el valor de la energía disponible para la propagación de la grieta, viene dado por:

$$\mathcal{G} = \frac{\pi\sigma^2 a}{E},$$ (1)

Siendo $\mathcal{G}$ función de la carga aplicada σ, de la longitud de grieta a y del módulo elástico del material E. Por el contrario, la resistencia a fractura R es una propiedad del material, que tras la modificación de Irwin y Orowan, puede considerarse como la suma de la energía necesaria para la creación de la nuevas superficies que suponen el crecimiento de la grieta, γ_s, más la energía necesaria para producir la plastificación inherente a los metales, W_P

$$R = 2\gamma_S + W_p$$ (2)

De esta forma, la fractura se producirá cuando ambas cantidades se igualen:

$$\mathcal{G} = \frac{\pi\sigma^2 a}{E} = 2\gamma_s + W_P = R$$ (3)

A pesar de que existe plastificación, ésta puede considerarse como local, de forma que el comportamiento del material puede continuar describiéndose mediante modelos elásticos.

En 1968, Rice [4] amplía el **criterio energético** para caracterizar materiales no lineales. Justifica que el cálculo de la energía disponible para la propagación de la grieta puede hacerse mediante una integral lineal, a la cual denomina **integral J**, que evalúa la energía a lo largo de un contorno arbitrario alrededor de la grieta.

Por otro lado, G.R. Irwin se apoya en un artículo publicado por Westergaard [5] para mostrar que las tensiones y desplazamientos en cualquier punto de un sólido agrietado pueden ser descritos mediante una única constante, que caracteriza la energía disponible para la propagación de la grieta [6,7]. Este parámetro se conoce como el **factor de intensidad de tensiones (K_I),** una variable que caracteriza las tensiones y que depende de la longitud de la grieta y la tensión aplicada. En el caso de estudio en condiciones de tensión plana para una placa infinita con una grieta de longitud $2a$, K_I viene dado por:

$$K_I = \sigma\sqrt{\pi a}$$

(4)

De esta forma, el criterio de fractura puede reformularse en función del factor de intensidad de tensiones, de tal forma que la propagación de la grieta se producirá si:

$$K_I = K_{IC}$$

(5)

Siendo K_{IC} una propiedad del material que se denomina tenacidad a fractura.

Para evaluar la distribución de tensiones, se definen tres modos de carga: el modo I separa las caras de la grieta en el mismo plano de estudio, el modo II desliza las dos caras de la grieta en el mismo plano y el modo III desliza las dos caras de la grieta en el plano perpendicular a la misma. Los casos en los que la grieta no se encuentra en el plano ortogonal se denominan modos mixtos.

| Modo I: Apertura | Modo II: Deslizamiento | Modo III: Desgarro |
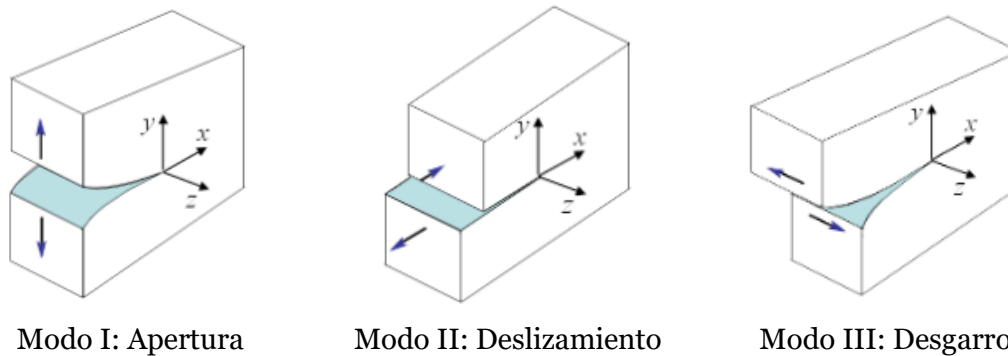
Figura 1. Modos de fractura

Tanto el criterio energético como el factor de intensidad de tensiones son métodos que analizan la fractura considerando un **enfoque global** del componente o estructura. Se determina una tenacidad a fractura general, la cual se compara con un valor crítico, K_I o J, que depende principalmente del tamaño de la grieta y de la tensión global aplicada.

En el estudio de fractura frágil en metales, cobra una especial importancia comprender y considerar aspectos de la microestructura ya que, al tratarse de materiales con una red policristalina muy heterogénea, las particularidades de la pequeña escala tienen una gran influencia en el comportamiento general macroscópico. El **enfoque local** se basa en el estudio de las tensiones y deformaciones en el frente de la grieta empleando modelos basados en micro-mecanismos. Los modelos que consideran un enfoque local, asumen que la fractura ocurre cuando se alcanza una tensión o deformación crítica en un área delimitado, en las cercanías de la grieta.

Existen dos micro-mecanismos característicos de la fractura frágil en metales: transgranular e intergranular. La **fractura transgranular** se produce cuando el camino de la grieta atraviesa los granos buscando el plano orientado de manera favorable, perpendicular a las tensiones principales máximas. Esto produce cambios de dirección al cruzar un límite de grano. Este tipo de fractura también se conoce como **clivaje**. Por otro lado, la **fractura intergranular** se caracteriza por presentar un avance de la grieta a través de las fronteras de los granos. En general, la rotura de los enlaces entre granos se genera al debilitarse las uniones en las fronteras de granos por acumulación de solutos o presencia de defectos.
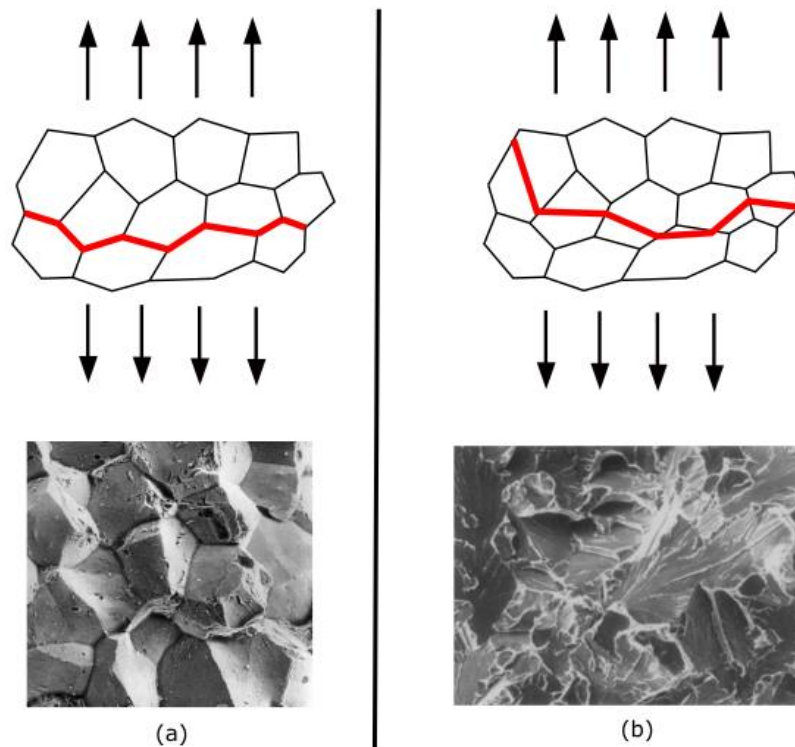
Figura 2. Representación de los dos micro-mecanismos de fractura frágil en metales (a) fractura intergranular y (b) fractura transgranular

Existen numerosos factores fragilizantes que modifican el comportamiento de los materiales metálicos. Los más representativos para la caracterización de la fractura frágil y que agrupan un mayor espectro son: la exposición a bajas temperaturas, la presencia de hidrógeno y la interfaz de materiales compuestos. El presente trabajo se centra en la comprensión, análisis y estudio del comportamiento de materiales metálicos ante la acción de estos agentes fragilizantes.

1.1.1.1. <u>FRAGILIZACIÓN POR HIDRÓGENO</u>

En los años 80, el empleo del hidrógeno en procesos petroquímicos impulsó la investigación del comportamiento de materiales metálicos, necesarios para su almacenamiento y transporte. En la actualidad, el creciente interés para emplear el hidrógeno como vector energético ha propulsado de nuevo este interés.

Los átomos de hidrógeno tienen un tamaño muy inferior a los átomos de materiales metálicos, hecho que facilita su entrada en la red cristalina de los metales, tanto intersticialmente como en los contornos de grano. Cuando el hidrógeno entra a formar parte de la estructura atómica de un material metálico, modifica su red atómica y se

produce una reducción drástica en la tenacidad y la ductilidad, favoreciendo el crecimiento de grietas.
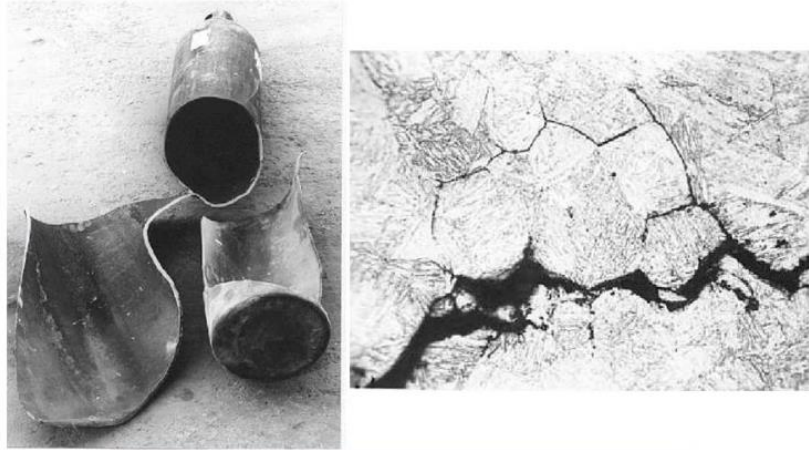
Figura 3 .Cilindros empleados para almacenar hidrógeno tras sufrir fractura intergranular.
Fuente: Air Liquide

El **agrietamiento asistido por hidrógeno** (HAC, hydrogen assisted cracking) afecta a todo tipo de metales, observándose que la rotura producida es mayoritariamente intergranular (IG), aunque dependiendo de la fuerza de unión entre los átomos también se observan casos con rotura transgranular [8].

Para estudiar el proceso de **fragilización por hidrógeno** (HE, hydrogen embrittlement), se deben analizar tres factores principales: (1) el origen del hidrógeno, (2) el mecanismo de fragilización y (3) el modelo de difusión y transporte del hidrógeno desde la fuente hasta la posición en la que interactúa con el metal y se genera la fragilización.

El **origen del hidrógeno** que produce la fragilización puede dividirse en: presencia de hidrógeno en el interior del metal (IHAC, internal hydrogen assisted cracking) y exposición a un ambiente con hidrógeno (HEAC, hydrogen environment assisted cracking).

El **mecanismo a nivel atomístico** que gobierna la fragilización por hidrógeno sigue siendo un tema de discusión, con dos corrientes basadas en las observaciones experimentales: la decohesión atomística potenciada por el hidrógeno (HEDE, hydrogen enhanced decohesion) [9,10] y la plastificación local producida por el hidrógeno (HELP, hydrogen enhanced localized plasticity) [11,12]. Aunque todavía no existe consenso, algunos autores (por ejemplo, [13]) han aportado evidencias en los últimos años que

sugieren que la modelización del mecanismo de fragilización debe ser una combinación de ambos mecanismos.

El modelo de **difusión del hidrógeno** a través de la red cristalina del metal considerado inicialmente se basaba únicamente en la ley de Fick. Esta ley determina que el flujo difusivo que atraviesa una superficie es directamente proporcional al gradiente de concentración del mismo. Troiano [14] y numerosos estudios posteriores [15,16] sugieren que el proceso se encuentra muy influenciado por los gradientes de tensión hidrostática, concluyendo que las consideraciones de la ley de Fick no son suficientes en la descripción de la difusión del flujo.

Sofronis y McMeeking [17] proponen un modelo de transporte de hidrógeno en grandes deformaciones basado en la hipótesis de plasticidad de corto alcance. Este modelo establece que el flujo de hidrógeno J está determinado por el potencial químico $\nabla \mu$:

$$J = -\frac{DC}{RT}\nabla \mu \qquad (6)$$

Siendo D el coeficiente de difusión, C la concentración de hidrógeno, R la constante universal de los gases y T la temperatura. El potencial químico del hidrógeno en la red μ se puede expresar como:

$$\mu = \mu^0 + RT \ln C + \mu_\sigma \qquad (7)$$

Donde μ^0 es el potencial químico para el caso base y μ_σ es la parte de μ dependiente principalmente de la tensión hidrostática. De esta manera, el flujo se puede expresar tal que:

$$J = -D\nabla C - \frac{DC}{RT}\nabla \mu_\sigma \qquad (8)$$

Con este modelo se establece la relación entre la concentración y la tensión hidrostática, σ_H, determinando que el valor de la concentración alcanza su valor máximo en el punto donde se alcanza una mayor tensión hidrostática. (Figura 4).
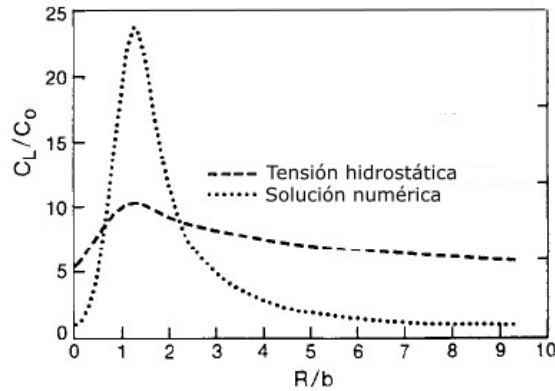
Figura 4. Concentración de hidrógeno en función de la distancia a la punta de la grieta. Alcanza su máximo valor en el punto de mayor tensión hidrostática. Adaptada de [17].

Aunque el modelo propuesto por Sofronis et al. [17] se ha ido modificando para incluir el efecto de distintos factores [18–23], se ha constituido como la base para la evaluación de la difusión y transporte de hidrógeno. En la actualidad, se consideran modelos de difusión en los que domina el efecto de la **tensión hidrostática**, siendo importante determinar su valor para predecir la concentración de hidrógeno.

De esta forma, la evaluación de la concentración de hidrógeno se realiza considerando que el potencial químico del hidrógeno en la red del metal se puede expresar como:

$$\mu = \mu^0 + RT \ln \frac{\theta_L}{1 - \theta_L} - \bar{V}_H \sigma_H \tag{9}$$

Donde θ_L es la ocupación por parte del hidrógeno de huecos en la malla, y $\bar{V}_H$ es el volumen molar parcial de hidrógeno disuelto en un sólido. Considerando la relación entre la ocupación y el número de huecos N, $\theta_L = C/N$, asumiendo baja ocupación ($\theta_L \ll 1$) y concentración intersticial de huecos constante ($\nabla N = 0$) se puede expresar el flujo de hidrógeno como:

$$J = -D\nabla C + \frac{DC}{RT} \bar{V}_H \nabla \sigma_H \tag{10}$$

1.1.1.2. CLIVAJE A BAJAS TEMPERATURAS

La primera vez que se reportó un problema de clivaje en metales por el efecto de bajas temperaturas fue durante la II Guerra Mundial. EEUU requería disponer de una numerosa cantidad de barcos para lo cual se implementó un proceso de fabricación más rápido y barato que el habitual con uniones abulonadas, dando lugar a los barcos Liberty fabricados con uniones soldadas. El diseño de los barcos se realizó considerando el comportamiento dúctil del acero que parecía funcionar adecuadamente en los ensayos realizados en el puerto cercano al astillero. Sin embargo, al adentrarse en aguas a temperaturas menores se produjeron importantes fracturas que hicieron colapsar los barcos.

Con el conocimiento ganado a día de hoy es fácil saber lo que sucedió: las uniones soldadas hacen trabajar a ambas partes del acero como una única pieza, generando tensiones elevadas en la unión. En un ambiente con temperaturas medias, la tenacidad a fractura es elevada pero al disminuir la temperatura, el comportamiento de la red cristalina se modifica, cambiando el mecanismo de fallo al disminuir la energía de fractura y la tensión crítica. Además, la soldadura era un procedimiento poco extendido por lo que el personal no disponía del conocimiento para ejecutar unas uniones soldadas con el suficiente grado de calidad, aumentando el número de impurezas o defectos, susceptibles de iniciar la fractura.
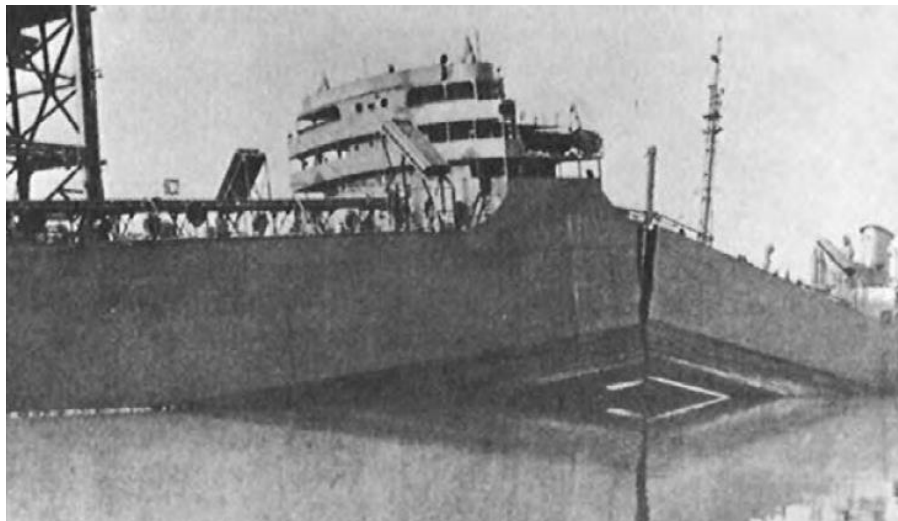
Figura 5. Barco Liberty colapsado debido a fractura frágil.

El comportamiento de los metales a bajas temperaturas cambia sustancialmente dependiendo de su red cristalina [24]. El comportamiento plástico de los metales, viene

determinado por los deslizamientos entre átomos. De esta manera, si existe un alto número de sistemas de deslizamientos, se favorece el comportamiento dúctil y al reducirse este número, el comportamiento es más frágil. Los planos preferentes de generar clivaje son aquellos que tienen una menor densidad de empaquetamiento, de esta manera el número de enlaces a separar es menor y la distancia interplanar es mayor.

Como se puede apreciar en la Figura 6, los átomos de metales con **estructura cúbica centrada en las caras (FCC)** disponen de un empaquetamiento de la red denso, favoreciendo un comportamiento plástico [25]. Sin embargo, los metales con **estructura cúbica centrada en el cuerpo (BCC)** disponen de una menor densidad de empaquetamiento, lo que no favorece su comportamiento plástico.
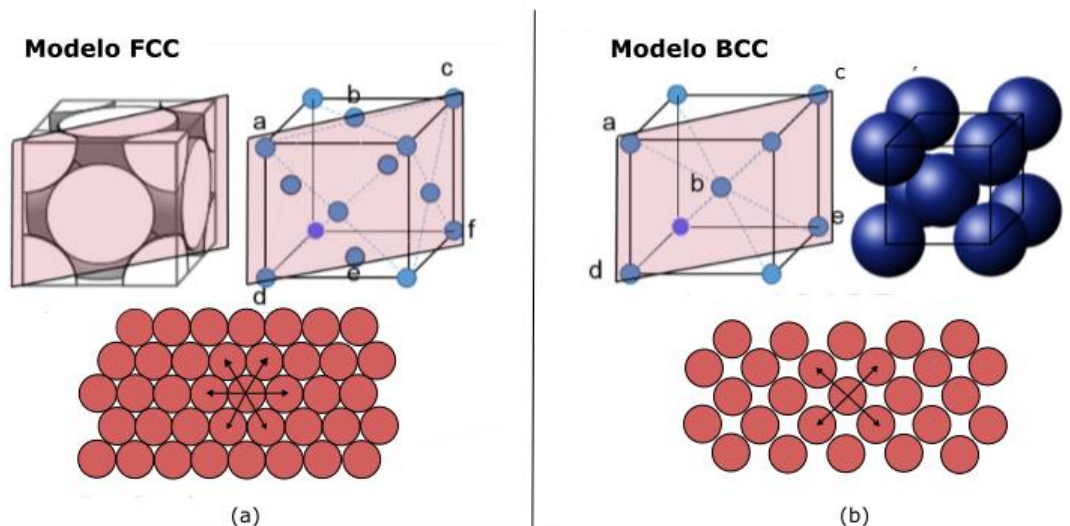
Figura 6. Representación de un cristal y sus modos de deslizamiento para (a) FCC y (b) BCC.

A bajas temperaturas, se disminuye la energía de los átomos en la estructura cristalina BCC, reduciendo la propagación de las dislocaciones y aumentando las tensiones locales, hecho que favorece un comportamiento local frágil. El micro-mecanismo de fractura frágil que se aprecia en estos metales a bajas temperaturas es transgranular, caracterizado por la rotura de los granos y cambio de dirección de la grieta en la frontera entre granos.

Los metales, por su estructura policristalina no uniforme, contienen una amplia variedad de elementos microestructurales singulares propiciando un comportamiento diferente según la distribución y presencia de impurezas o defectos. Estos defectos producen una variación en las propiedades mecánicas y físicas de los materiales.

Al existir una discontinuidad en el frente de la grieta, puede generarse una inestabilidad que sea suficiente para exceder la fuerza de adhesión. La distribución de estas discontinuidades y por lo tanto, la predisposición al inicio de la fractura frágil, solo se puede estudiar de manera estadística, analizando la probabilidad de existencia de defectos en el frente de la grieta y considerando un criterio de fallo local.

1.1.1.3. DECOHESIÓN EN LA INTERFAZ DE DOS MATERIALES

La investigación del comportamiento de materiales compuestos con núcleo metálico se ha desarrollado durante los últimos 50 años debido a su importante papel en tecnologías avanzadas, tanto estructurales como biomédicas y electrónicas. Sus buenas propiedades mecánicas y térmicas los hacen especialmente interesantes en aplicaciones industriales [26].

La resistencia a fractura de los materiales compuestos se ve muy influenciada por la región de la interfaz y se ha observado fractura frágil en numerosos sistemas formados por bimateriales, detectando presencia de plasticidad [27–29].

Durante los años noventa se realizaron numerosas investigaciones sobre el comportamiento a fractura de materiales compuestos, observando que se produce fractura por clivaje en la zona de contacto con el metal. Este comportamiento ha sido observado en la interfaz entre oro-zafiro [30], cobre-cristal [27], cobre-zafiro [31] y niobio-alúmina [32] entre otros.
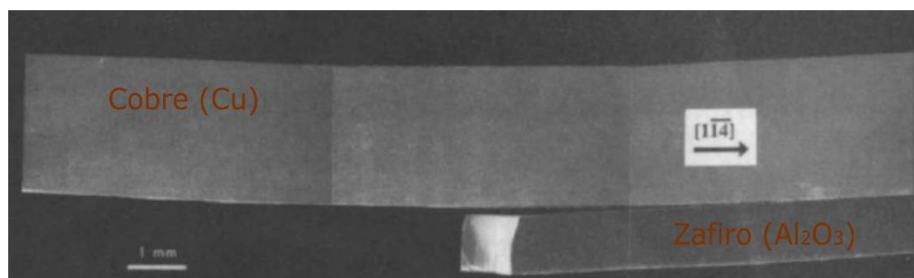
Figura 7. Decohesión entre cobre y zafiro según ensayos realizados por Beltz et al. [31]. Adaptada de [31]

En 1994, Elssnet et al. [33] y Korn et al. [34] comienzan un amplio trabajo investigador en el que se profundiza en el estudio de materiales compuestos con matriz metálica, analizando los mecanismos que producen la fractura tanto a nivel macroscópico como a nivel atomístico. En concreto, Elssnet et al. y Korn et al. centran su

estudio en el comportamiento de la interfaz entre niobio y zafiro, midiendo la resistencia a fractura macroscópica y realizando un análisis a nivel atómico del trabajo necesario para que aparezca la decohesión en la interfaz.

Los ensayos experimentales llevados a cabo en una probeta sometida a flexión en 4 puntos, determinaron que el trabajo de fractura macroscópico era 1000 veces mayor que el trabajo de fractura a nivel atómico necesario para separar los átomos en el contacto. Esta gran diferencia entre la pequeña y gran escala se asocia a la disipación plástica en el niobio. Sin embargo, si se aplica la teoría de plasticidad convencional, las tensiones obtenidas no son lo suficientemente elevadas para producir la decohesión de la interfaz.
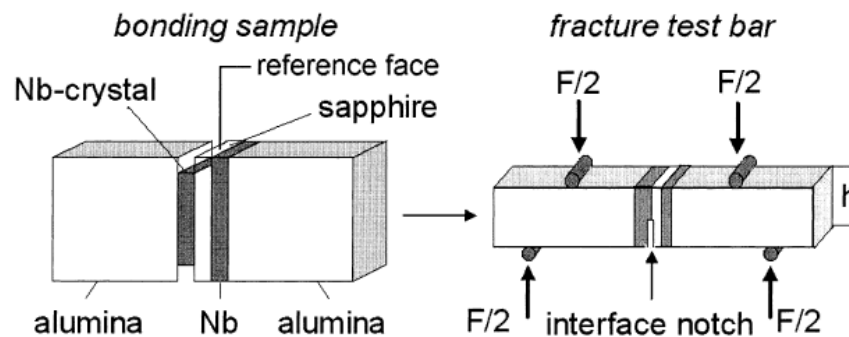
Figura 8. Probeta de flexión en 4 puntos utilizada por Korn et al. [34] *para estudiar la decohesión. Fuente* [34]

Al analizar la superficie de fractura, se encontraron características similares a las de una fractura frágil transgranular. Estas observaciones experimentales se interpretaron como un comportamiento frágil derivado del bloqueo de dislocaciones en la interfaz, al no poder transmitirse del material metálico al material cerámico, lo cual generaría una reducción en la plasticidad general del material metálico.

1.1.2. MODELIZACIÓN DE LA FRACTURA FRÁGIL EN METALES

El análisis de fractura frágil en materiales metálicos se realiza considerando propiedades comunes del material a escala macroscópica. Sin embargo, como hemos visto en los apartados anteriores, el área de mayor importancia a estudiar es la región próxima a la grieta. Según se ha analizado en el apartado 1.1.1, por un lado hay que prestar atención a las singularidades y bloqueos existentes en el frente de la grieta, analizando su probabilidad de existencia dentro de una distancia crítica desde la punta de la grieta, y por otro lado, se debe analizar la distancia alcanzada por el agente fragilizante y el grado de daño del material afectado. Todos estos factores que determinan las condiciones de propagación de la grieta se concentran en un área de pequeño tamaño.

Con la finalidad de ahorrar en costes computacionales, los modelos desarrollados en el presente trabajo de tesis centran su atención en implementar las características de esta área en los modelos macroscópicos. De esta manera, el método de estudio considera la aplicación de una carga remota y analiza las condiciones de fallo de forma local (microestructura en el frente de la grieta).

1.1.2.1. TEORÍAS DE GRADIENTES DE DEFORMACIÓN PLÁSTICA

Las teorías convencionales de plasticidad clásica se basan en parámetros macroscópicos que caracterizan el comportamiento del material para cualquier geometría. Sin embargo, la realización de ensayos experimentales a pequeña escala ha puesto de manifiesto la existencia de un efecto plástico de escala en los materiales metálicos [35–38]. Los resultados obtenidos en los numerosos experimentos llevados a cabo ponen de relieve la necesidad de mejorar las teorías convencionales de plasticidad para capturar estos efectos plásticos de escala.

Las dislocaciones producidas en la zona próxima a la grieta actúan como obstáculos al movimiento de otras dislocaciones, lo que se traduce por tanto en un endurecimiento de la zona, aumentando las tensiones. En este endurecimiento están involucradas las dislocaciones que quedan atrapadas de manera aleatoria (SSDs–Statistically Stored Dislocations) y las dislocaciones que son necesarias para producir una deformación de los cristales (GNDs–Geometrically Necessary Dislocations) [35]. La respuesta de los metales, al acumular gradientes de deformación plástica elevados en un volumen pequeño, se expresa mediante el aumento del límite elástico y del coeficiente de endurecimiento.

La idea principal en la que se trabaja es en implementar el comportamiento en la pequeña escala considerando una o varias longitudes características del material que reproduzcan los efectos de escala en la zona próxima a la grieta. Esta idea ha dado lugar a diversos modelos de Gradientes de Deformaciones Plásticas (SGP), con diferentes grados de complejidad, que tratan de reproducir los efectos de escala mediante la integración en las ecuaciones de uno o varios parámetros de escala.

En la Figura 9, se representa esquemáticamente la zona con comportamiento plástico en el frente de grieta en la que se implementan las teorías de deformación plástica. Los efectos de los gradientes de deformación plástica son mayores cuanto menor es la zona plástica. Si la resistencia a fractura (tenacidad a fractura) de un material es baja, los efectos de gradientes tienen una mayor influencia, haciendo especialmente importante la implementación de estas teorías en el estudio de la fractura frágil [39−41].
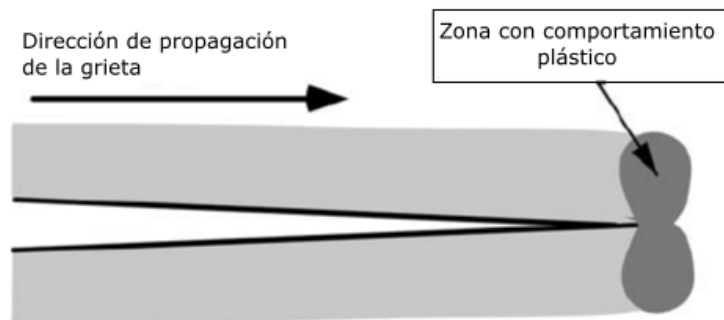
Figura 9. Representación de la zona plástica en el frente de grieta. Adaptado de [42]

Se pueden diferenciar las teorías desarrolladas en dos subgrupos. Por un lado las teorías basadas en mecanismos (MSG) [43] y por otro, las fenomenológicas [44−46].

- Teorías basadas en mecanismos (MSG).

Las teorías basadas en mecanismos están fundamentadas en el modelo de dislocaciones de Taylor, expresándose la tensión cortante en función de la densidad de dislocaciones:

$$\tau = \alpha \mu b \sqrt{\rho} \tag{11}$$

Donde μ es el módulo de cortante, b es la magnitud del vector de Burgers y α es un coeficiente empírico que toma valores entre 0.3 y 0.5. La densidad de dislocaciones se

compone de la densidad ρ_S, asociada a dislocaciones acumuladas estadísticamente y la densidad ρ_G, debida a dislocaciones geométricamente necesarias:

$$\rho = \rho_S + \rho_G \tag{12}$$

Donde ρ_G se relaciona con los gradientes de deformación plástica efectivos mediante:

$$\rho_G = \bar{r}\frac{\eta^p}{b} \tag{13}$$

Siendo $\bar{r}$ el factor de Nye. ρ_S se determina conociendo la relación entre la tensión de plastificación y la curva tensión – deformación del material para tracción uniaxial ($\eta^p = 0$):

$$\rho_S = \left[\frac{\sigma_{ref}f(\varepsilon^p)}{M\ \alpha\mu b}\right]^2 \tag{14}$$

Donde σ_{ref} es una tensión de referencia y f es una función de la deformación plástica determinada a partir de la curva tensión-deformación del material.

Al relacionar la tensión de tracción con la tensión cortante y sustituir (13) y (14) se obtiene:

$$\sigma_{flow} = M\tau = \sigma_{ref}\sqrt{f^2(\varepsilon^p) + l\eta^p} \tag{15}$$

Donde l es la longitud intrínseca del material basada en los parámetros de elasticidad (μ), plasticidad (σ_{ref}) y espacio atómico (b):

$$l = M^2\bar{r}\alpha^2\left(\frac{\mu}{\sigma_{ref}}\right)^2 b \tag{16}$$

Como simplificación de las teorías MSG, Huang et al. [47] desarrollaron una versión de orden inferior denominada **teoría convencional de gradientes de deformación basada en mecanismos (CMSG)**. El desarrollo de esta teoría viene motivado por el amplio espectro de casos en los que los efectos de las condiciones de contorno de orden superior son despreciables y el interés de una teoría con mayor simplicidad de cara a su empleo ingenieril. La implementación de este modelo se basa en considerar una formulación viscoplástica para obtener la velocidad deformación plástica ($\dot{\varepsilon}^p$) como función de la tensión (σ_e).

- **Teorías fenomenológicas**

Las teorías fenomenológicas tienen su origen en la generalización de la teoría de flujo J2, propuesta por Fleck y Hutchinson [46] en 2001 en la cual el endurecimiento producido por los gradientes de deformación se considera mediante la definición de una deformación plástica efectiva generalizada como E_p:

$$E_p = \sqrt{\varepsilon_p^2 + l_1^2 I_1 + l_2^2 I_2 + l_3^2 I_3}$$

(17)

Donde l_1, l_2 y l_3 son parámetros de longitud del material e I_1, I_2 e I_3 son tres invariantes del tensor gradiente de deformación plástica.

Considerando la teoría de gradientes de deformación plástica desarrollada por Aifantis [48] en 1984, la expresión anterior se puede reformular considerando una única longitud característica del material (l^*):

$$E_p = \sqrt{\varepsilon_p^2 + l^{*2}\varepsilon_{p,i}\varepsilon_{p,i}}$$

(18)

- **Teorías de Gradientes de Deformación Avanzadas y teoría de Distorsión de Gradientes de Plasticidad**

En 2004, Gudmunson [49] advirtió que la teoría desarrollada por Fleck y Hutchinson no siempre cumple con los principio de la termodinámica relativos a disipación plástica. Desde entonces, se ha desarrollado una nueva formulación SGP en la cual se incorporan tensiones de alto orden energéticas (recuperables) y disipativas (no recuperables) [49,50].

En los últimos años ha aumentado el interés por extender las teorías SGP avanzadas para considerar la rotación plástica según la teoría de distorsión de gradientes de deformación (DGP) de Gurtin [51], con la finalidad de describir rigurosamente la incompatibilidad de la fluencia plástica y la densidad de dislocaciones asociada a la misma. En varios trabajos ha quedado demostrado que el uso de modelos fenomenológicos de orden superior que consideran las distorsiones permiten capturar con mayor precisión los ensayos experimentales[52–54].

La teoría de gradientes de distorsión plástica (DGP) propuesta por Gurtin [51] considera la rotación plástica mediante el tensor de dislocaciones de Nye (α_{ij}) el cual se define como el tensor rotacional de la distorsión plástica:

$$\boldsymbol{\alpha} = curl\ \boldsymbol{\gamma}^p, \tag{19}$$

Y considerando que el vector de Burgers involucra tanto la parte simétrica como la parte anti-simétrica de la distorsión plástica:

$$curl\ \boldsymbol{\gamma}^p = curl\ \boldsymbol{\varepsilon}^p + curl\ \boldsymbol{\vartheta}^p \tag{20}$$

Para tener en cuenta la influencia de las Dislocaciones Geométricamente Necesarias (GNDs), la contribución energética se establece a partir de la siguiente expresión de la energía libre Ψ, que depende así de la deformación elástica (ε_{ij}^e) y el tensor de Nye (α_{ij}):

$$\psi = \frac{1}{2}C_{ijkl}\varepsilon_{ij}^e\varepsilon_{kl}^e + \Phi(\alpha_{ij}) \tag{21}$$

Siendo $\Phi(\alpha_{ij})$ la energía de defectos, la cual asumimos que toma una forma cuadrática:

$$\Phi(\alpha_{ij}) = \frac{1}{2}\mu L_E^2\alpha_{ij}\alpha_{ij} \tag{22}$$

La tensión de defectos corresponde con la siguiente ecuación:

$$\zeta_{ij} = \frac{\partial\Phi(\alpha_{ij})}{\partial\alpha_{ij}} = \mu L_E^2\alpha_{ij} \tag{23}$$

Donde μ es el módulo de cortante y L_E la longitud de escala energética del material.

Por otro lado, la contribución disipativa se incluye mediante el factor de gradientes de deformación plástica como:

$$\dot{E}_p = \sqrt{\frac{2}{3}\ \dot{\varepsilon}_{ij}^p\dot{\varepsilon}_{ij}^p + \chi\dot{\vartheta}_{ij}^p\dot{\vartheta}_{ij}^p + \frac{2}{3}L_D^2\dot{\varepsilon}_{ij,k}^p\dot{\varepsilon}_{ij,k}^p} \tag{24}$$

Donde L_D es la longitud de escala disipativa y χ el parámetro que controla la disipación por el rotacional plástico.

$$\chi = \left[\frac{3}{2} + \frac{\sigma_Y}{\mu\varepsilon_Y}\left(\frac{L_D}{L_E}\right)^2\right]^{-1} \tag{25}$$

Siendo σ_Y y ε_Y parámetros del material positivos, lo que implica que el valor de χ se encuentra en un rango entre 0 y 2/3.

Las teorías de gradientes de deformación plástica son de vital importancia en la caracterización mecánica del comportamiento de la grieta, ya que independientemente del tamaño de la probeta, la zona plástica en el frente de la grieta es pequeña y contiene elevados gradientes de deformación plástica [55].

1.1.2.2. **MODELOS PROBABILÍSTICOS**

La fractura por clivaje o transgranular se asocia a la presencia de inclusiones que generan inestabilidad, reduciendo la resistencia a fractura del material. La presencia o no de estas inclusiones y su posición respecto de la punta de la grieta caracterizan el comportamiento de la grieta y su desarrollo. A la hora de desarrollar modelos de fractura frágil por clivaje, nos encontramos con que la presencia de estas inclusiones es aleatoria, haciendo necesario el empleo de modelos estadísticos para determinar el valor de la resistencia a fractura, que se ve condicionada por la probabilidad de existencia de defectos en el material.

Ritchie et al. [56] determinaron que el fallo por clivaje ocurre cuando la tensión en el frente de la grieta excede una tensión crítica a una distancia característica de la punta de grieta, la cual es igual a dos veces el tamaño de grano. Aunque en trabajos posteriores se concluyó que no existía relación entre el tamaño de grano y esta distancia, quedó establecido el concepto de **distancia crítica** (ver Figura 10).
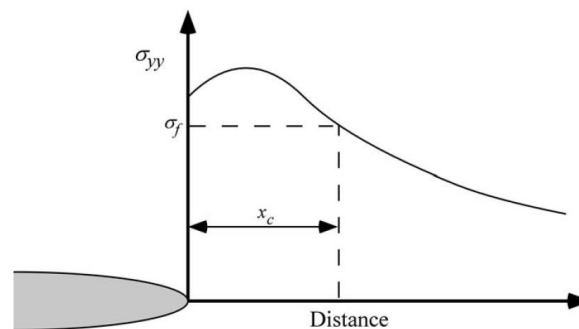
Figura 10. Valor de las tensiones en función de la distancia a la punta de la grieta. El fallo se produce cuando la tensión de fractura excede una distancia característica (x_c), asociada a una tensión de fallo (σ_f). Fuente [42], adaptado de [56]

Apoyándose en el trabajo desarrollado por Ritchie et al., Curry et al. [57] introdujeron una interpretación estadística para el concepto de distancia crítica,

determinando que se debe analizar un volumen en el frente de la grieta con la finalidad de determinar la probabilidad de encontrar una partícula lo suficientemente grande para desencadenar clivaje.

Numerosos trabajos [58–60] han continuado desarrollando el trabajo comenzado por Curry et al. para la consecución de un modelo estadístico de clivaje. Estos modelos analizan el clivaje bajo la consideración del **principio del eslabón más débil**, en el cual se establece que la probabilidad de fallo es igual a la probabilidad de encontrar al menos una partícula desencadenante de la fractura.

La **probabilidad de fallo** en un volumen de material V, con una densidad de partículas críticas por unidad de volumen ρ se puede deducir mediante la distribución de Poisson:

$$Pf = 1 - \exp(-\rho V) \tag{26}$$

Considerando que la densidad de partículas no es constante en los distintos puntos de un mismo material, la probabilidad se presenta como una integral que evalúa la densidad en los diferentes volúmenes:

$$Pf = 1 - exp\left[-\int_V \rho dV\right] \tag{27}$$

Mediante la adaptación de la **ecuación de Weibull biparamétrica** [61] llevada a cabo por Beremin [62] se expresa la probabilidad de fallo en función de la tensión de fractura de Weibull:

$$Pf = 1 - exp\left[-\left(\frac{\sigma_w}{\sigma_u}\right)^m\right], \tag{28}$$

la cual representa la tensión de fractura para una carga uniforme en una muestra de volumen V_o y donde m y σ_u son los dos parámetros del modelo, que se denominan respectivamente: módulo y parámetro de escala.

Despejando el valor de la densidad ρ, igualando (27) y (28) y despejando la tensión de Weibull:

$$\sigma_w = \left[\frac{1}{V_o}\int_{Vf} \sigma_1^m dV\right]^{1/m} \tag{29}$$

Donde V_o es un volumen de referencia y V_f volumen de la zona de fractura. Se denomina zona de fractura a la región en la cual las tensiones son lo suficientemente altas para que exista la probabilidad de clivaje.

Este modelo determina la probabilidad de fallo considerando la distribución de tensiones y obteniendo una tensión constante equivalente que actúa sobre todo el elemento de tal modo que la probabilidad de fractura sea la misma que considerando la distribución real. Partiendo de este modelo de Beremin, Muñiz-Calvente et al. [63] han desarrollado un modelo triparamétrico, basado en un enfoque de tamaño equivalente y en el que los tres parámetros del modelo tienen una base fenomenológica. Se ha demostrado que este modelo tiene la capacidad de predecir fractura frágil y dúctil sin asunciones experimentales previas, solventando así uno de los problemas del modelo biparamétrico.

En el modelo triparamétrico se incluye de forma explícita el parámetro umbral, σ_{th}, que representa el valor de la tensión por debajo del cual las fracturas no se pueden propagar:

$$\sigma_w = \sigma_{th} + \left[\sum_{i=1}^{n_e}\left(\sigma_1^i - \sigma_{th}\right)^m (V_i/V_0)\right]^{1/m} \tag{30}$$

El proceso iterativo consiste en asumir un valor de σ_{th} y determinar el valor de m y σ_u empleando un ajuste de los valores experimentales mediante el método de mínimos cuadrados [64,65].

1.1.2.3. MODELOS PHASE FIELD (O MODELOS DE CAMPO DE FASE)

La aplicación del **modelo de campo de fase (phase field),** inicialmente formulado por Francfort et al. [66], a la mecánica de la fractura se basa en el criterio de energía de Griffith. Se trata de un modelo que considera la degradación del material introduciendo el concepto de daño que evalúa la pérdida de rigidez.

El modelo de campo de fase aplicado a problemas de fractura se ha desarrollado enormemente en los últimos años ya que da solución a las limitaciones de los modelos basados en discontinuidades [67–69]. Su primera aplicación fue el estudio de la fractura frágil [66] pero desde entonces se han abordado modificaciones para resolver daño dúctil [68,70], fractura hidráulica [71], materiales funcionalmente graduados (FGM) [72,73] y agrietamiento por corrosión [74], entre otros.

La capacidad del modelo de campo de fase para capturar la dependencia de la energía de fractura con la concentración de hidrógeno le hace especialmente interesante para evaluar la fragilización por hidrógeno [75–77]. Otras características que le hacen útil es su capacidad para considerar condiciones complejas de grieta intrínsecas a fragilización por hidrogeno y su fácil acoplamiento con el problema de difusión.

Considerando un sólido agrietado en ausencia de fuerzas externas, la variación de la energía total Π debida a un incremento en el área de la grieta dA, empleando el criterio energético de Griffith [1] puede expresarse como sigue:

$$\frac{d\Pi}{dA} = \frac{d\psi(\boldsymbol{\varepsilon})}{dA} + \frac{dW_c}{dA} = 0 \tag{31}$$

Siendo $\psi(\boldsymbol{\varepsilon})$ la densidad de energía de deformación, expresada como función del tensor de deformaciones $\boldsymbol{\varepsilon}$. W_c es el trabajo requerido para crear una nueva superficie. El último término es el valor crítico de la energía disponible para la propagación de la grieta ($G_c = dW_c/dA$), una propiedad del material que caracteriza su tenacidad a fractura. Expresando el balance de energía de Griffith de forma variacional:

$$\Pi = \int_{\Omega} \psi(\boldsymbol{\varepsilon})dV + \int_{\Gamma} G_c d\Gamma \tag{32}$$

Donde V es el volumen del sólido y Γ la superficie de fractura. Este último valor es desconocido, dificultando la resolución de la ecuación (32). Sin embargo, es posible utilizar el parámetro de campo de fase ϕ para localizar la interfaz de la grieta, según se muestra en la Figura 11.
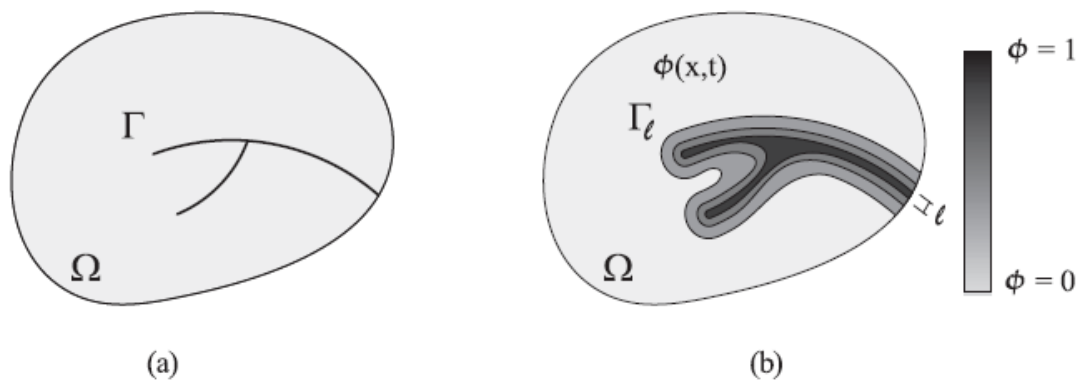
Figura 11. Representación esquemática del cuerpo sólido con (a) discontinuidad interna y (b) aproximación de campo de fase de las discontinuidades discretas. Fuente [75]

La evaluación del daño se cuantifica con una variable de campo conocida como parámetro de fractura $\phi(x)$ y se determina mediante una función exponencial:

$$\phi(x) = e^{-\frac{|x|}{\ell}}$$

(33)

Este parámetro ϕ es una variable de daño que toma el valor cero si un determinado elemento del material está intacto y el valor uno cuando un elemento del material está completamente agrietado.

Considerando la función de degradación de manera continua como $g(\phi) = (1 - \phi)^2$, la energía potencial total puede ser formulada como:

$$\Pi = \int_{\Omega} \left\{ (1 - \phi)^2 \psi_0(\varepsilon) + G_c \left(\frac{1}{2\ell} + \frac{\ell}{2} |\nabla \phi|^2 \right) \right\} dV$$

(34)

Donde ℓ en el parámetro de longitud de escala que gobierna el tamaño del área de fractura y ψ_0 representa la energía de deformación elástica de un sólido sin daño. El trabajo necesario para crear una superficie agrietada Γ, se expresa ahora como una integral de volumen, consiguiendo que el problema sea computacionalmente abordable.

Martínez-Pañeda et al. [75] han extendido la teoría de campo de fase para evaluar el agrietamiento por hidrógeno. En este trabajo se define la energía de fractura como una función de la cobertura de hidrógeno:

$$G_c(\theta) = (1 - \chi_{\theta})\, G_c(0)$$

(35)

Donde $G_c(0)$ es la energía de fractura en ausencia de hidrógeno, θ es un factor que determina la ocupación de las fronteras de granos y χ es el coeficiente de daño.

El coeficiente de daño χ, simboliza la reducción de energía de fractura debida a la presencia de hidrógeno y su valor se obtiene mediante ensayos o estudios atomísticos. El valor de θ depende de la concentración de hidrógeno en la red cristalina. Para su cálculo se emplea la isoterma de Langmuir-McLean que determina la cobertura en la superficie conociendo la concentración de hidrógeno (C):

$$\theta = \frac{C}{C + \exp\left(\frac{-\Delta g_b^0}{RT} \right)}$$

(36)

Siendo R la constante universal de los gases, T la temperatura y Δg_b^0 la diferencia de energía libre de Gibbs entre el interfaz decohesionado y el material alrededor.

- **Evaluación de la fractura**

El efecto del hidrógeno en la resistencia a fractura se puede evaluar expresando la ecuación de campo de fase mediante la tensión de Cauchy para un problema cuasi-estático unidimensional, $\sigma = g(\phi)E\epsilon$, siendo E el módulo de Young y ϵ la deformación y teniendo en cuenta la densidad de energía de deformación $\psi_0 = E\epsilon^2/2$:

$$\phi = \frac{E\epsilon^2\ell}{G_c(\theta) + E\epsilon^2\ell} \tag{37}$$

De esta forma, se obtiene la relación característica entre la deformación homogénea y la tensión homogénea:

$$\sigma = \left(\frac{G_c(\theta)}{G_c(\theta) + E\epsilon^2\ell}\right)^2 E\epsilon \tag{38}$$

Adoptando un valor máximo que se corresponde con la tensión crítica

$$\sigma_c = \left(\frac{27EG_c(\theta)}{256\ell}\right)^{1/2} \tag{39}$$

Como se puede ver en la ecuación anterior, el valor de ℓ gobierna la magnitud de la tensión crítica a la cual se inicia el daño y el tamaño de la zona de fractura.

1.2. MOTIVACIÓN

El acuerdo de París de 2015 marcó un hito histórico al establecer las bases para una transición ecológica con una serie de objetivos, cuya consecución está ligada a una transformación en el sistema energético. El mercado y sistema actual se encuentra en un punto de máximo desarrollo y se está produciendo un cambio que deriva en la necesidad de optar por nuevas tecnologías. Por otro lado, los avances electrónicos en un mundo global y conectado requieren conocer con mayor precisión el comportamiento de los microcomponentes para asegurar su correcto funcionamiento.

El desarrollo de estas tecnologías está reclamando un mejor conocimiento del comportamiento de materiales metálicos que, bajo el efecto de agentes fragilizantes, sufren una mayor degradación y hacen colapsar estructuras durante la vida útil para la cual fueron diseñadas. Como bien es sabido, la propagación de una fractura frágil requiere mucha menos energía que la de una fractura dúctil, pudiendo ocurrir que para un elemento diseñado considerando que el comportamiento del material es dúctil, como es el caso de los metales, se produzca fallo estructural aplicando una tensión mucho menor que la máxima justificada en el diseño [78]. Este hecho justifica la importancia de analizar y comprender el comportamiento de los metales susceptibles de fragilización.

Tradicionalmente se ha asociado fractura frágil en metales únicamente a los aceros ferríticos, que por su estructura BCC son más vulnerables de sufrir clivaje a bajas temperaturas. Sin embargo, existen otros factores fragilizantes, en los cuales se aprecian fenómenos físicos diferentes que afectan a un mayor rango de metales.

La fractura frágil cuenta con una característica común en todos los casos, siempre va asociada a una concentración de tensiones en un pequeño área en el frente de la grieta. Esta particularidad depende de la existencia de impurezas, huecos o una debilitación de la red cristalina haciendo necesario un conocimiento preciso de esta área a nivel microscópico. Con este fin, para una correcta identificación numérica del problema se hace indispensable el empleo de las teorías de gradientes de deformación plástica junto con el aporte de un conocimiento predictivo para determinar la probabilidad de existencia de un fallo. Una buena manera de visualizar el problema y hacer más intuitiva la determinación del grado de afección en una sección de estudio, es introduciendo el concepto de coeficiente de daño. Con este parámetro se pueden obtener gráficos que determinan el grado de daño en cada elemento, haciendo más sencilla la interpretación ingenieril.

1.3. ESTRUCTURA DE LA TESIS

La tesis comienza con una *Introducción* donde se presentan los principales fenómenos físicos en los cuales se ha detectado fractura frágil en metales:

- Fragilización por hidrógeno
- Clivaje a bajas temperaturas
- Decohesión en la interfaz de dos materiales.

Una vez expuesto el amplio espectro en el que nos encontramos con fractura frágil en metales, se continúa la revisión bibliográfica de los modelos numéricos involucrados en el análisis de fractura frágil, subdividiendo el estudio en:

- Teorías de gradientes de deformación plástica
- Modelos probabilísticos
- Modelos phase field (o modelos de campo de fase)

Con el conocimiento del estado del arte y las necesidades actuales para caracterizar correctamente y unificar los criterios para el análisis numérico de fractura frágil, se fijan los *Objetivos* del presente trabajo.

En el capítulo *Discusión de Resultados* se aclaran y complementan los trabajos desarrollados en los tres artículos presentados como compendio, ofreciendo una mayor explicación de los puntos clave de estudio en esta tesis doctoral.

En el capítulo *Conclusiones* se ofrece una visión global de los resultados obtenidos con el desarrollo del trabajo así como un análisis de los retos futuros.

Al tratarse de una Tesis Doctoral presentada bajo la modalidad de compendio de publicaciones, en el capítulo *Publicaciones* se recogen los artículos publicados en revistas de alto impacto que componen el conjunto del trabajo de investigación desarrollado.

2. OBJETIVOS

El objetivo principal que ha motivado el desarrollo de esta tesis doctoral es:

"Contribuir al desarrollo de un modelo numérico que caracterice la fractura frágil en materiales metálicos consiguiendo unificar y racionalizar las diferentes teorías para su implementación ingenieril"

La consecución del objetivo principal se puede dividir en los siguientes objetivos intermedios:

- Identificar los mecanismos físicos que caracterizan los diferentes modos de fractura frágil en metales con el fin de seleccionar los métodos numéricos más adecuados para reproducir el fenómeno físico.

- Adaptar las teorías de gradientes de deformación plástica para su implementación en problemas específicos de fractura frágil en metales.

- Implementar un modelo estadístico que ayude a determinar la probabilidad de fallo sin considerar suposiciones previas que pueden distorsionar los resultados.

- Interpretación de las ecuaciones constitutivas de un modelo DGP para su empleo en el estudio de la fractura frágil y el análisis de los micro-mecanismos que suceden en la punta de la grieta.

3. DISCUSIÓN DE RESULTADOS

3.1. ON THE SUITABILITY OF SLOW STRAIN RATE TENSILE TESTING FOR ASSESSING HYDROGEN EMBRITTLEMENT SUSCEPTIBILITY

- Sobre la idoneidad del ensayo SSRT para evaluar la susceptibilidad de la fragilización por hidrógeno .- Ref.[77]

El hidrógeno es un elemento que por su abundancia y características, es especialmente interesante para el desarrollo de un nuevo modelo energético y procesos industriales. Uno de los principales problemas con los que se encuentra la industria energética es la vulnerabilidad de los materiales metálicos en presencia de hidrógeno. El hidrógeno entra a formar parte de la malla cristalina del metal, modificándola y debilitando sus enlaces. Esto tiene como consecuencia un comportamiento frágil de los metales favoreciendo el desarrollo de fractura intergranular [79–81].

Uno de los ensayos experimentales más extendidos para la evaluación del agrietamiento asistido por el ambiente (EAC, Environment Assisted Cracking) es el ensayo de tracción a bajas velocidades de deformación (SSRT, Slow Strain-Rate Testing). Se trata de un ensayo a tracción realizado mediante la aplicación de una deformación a baja velocidad mientras se expone a la probeta al ambiente de interés, obteniendo el tiempo de fallo asociado al grado de contaminación del ambiente. Su uso está muy extendido y es la base de numerosas normativas internacionales por su sencillez y flexibilidad para adaptarlo a los requerimientos técnicos [82,83].

En el presente estudio, se analiza el comportamiento de las probetas a las que se ha realizado una entalla en la zona central. Las probetas fueron cargadas durante 10 días a distintos potenciales químicos. El material de las mismas es una superaleación de níquel, Monel K-500, sometida a distintos tratamientos térmicos. Se llevaron a cabo ensayos sobre 4 materiales distintos (cuatro tratamientos térmicos distintos) y 3 concentraciones iniciales de hidrógeno (tres cargar electroquímicas distintas) además de los ensayos en aire.
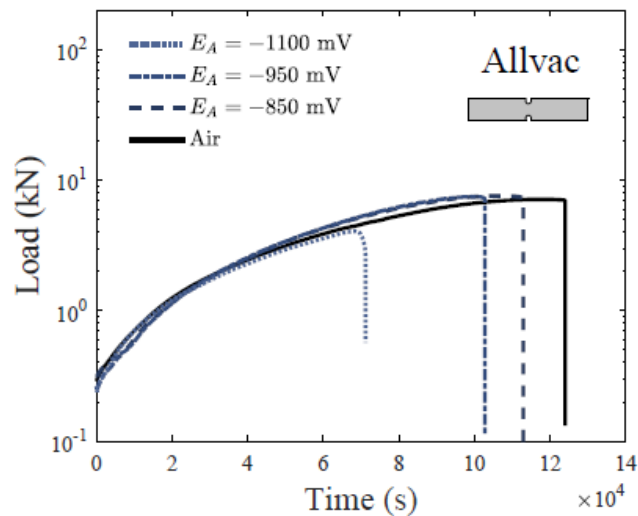
Figura 12. Influencia de diferentes concentraciones de hidrógeno en la resistencia de un material
(hidrógeno aplicado como potencial)

En la Figura 12 se muestran las curvas carga-desplazamiento obtenidas para uno de los tratamientos térmicos bajo cuatro condiciones de carga de hidrógeno, pudiendo apreciarse el efecto fragilizante del mismo. Tras observaciones fractográficas se ha detectado la presencia de crecimiento de grietas sub-críticas, que anularían la validez de los resultados. Este hecho está en consonancia con recientes investigaciones llevadas a cabo mediante análisis de morfología y topografía de grietas con rayos X [84,85]. Bajo este supuesto, no se podría tomar la tensión aplicada máxima como la fuerza impulsora característica de ese material, poniendo en entredicho la validez de los ensayos SSRT para analizar metales ante ambientes agresivos.

El trabajo llevado a cabo en esta tesis tiene como objetivo demostrar numéricamente la existencia de grietas sub-críticas. Para ello, se analizan los mecanismos implicados y se opta por la implementación numérica mediante un modelo de campo de fase. Según explicado en el apartado 1.1.2.3., este modelo ha sido recientemente implementado para la evaluación de agrietamiento asistido por hidrógeno [75,76]. En el presente trabajo se

complementa considerando plasticidad en deformaciones finitas con la teoría de Von Misses (J2) para modelizar las deformaciones elásticas y plásticas.

La formulación del modelo de campo de fase proporciona la base para el estudio de fractura de manera difusa, a través de la variable de fase ϕ que caracteriza el daño en cada punto del material y la función de degradación $(1-\phi)^2$. La variable de fase caracteriza el grado de degradación del material en un punto asignando un valor entre 0 y 1, siendo 0 cuando no existe daño y 1 cuando está completamente dañado.

La energía potencial de un cuerpo agrietado se obtiene mediante la suma de la energía de superficie asociada con la formación de la grieta Π^s (ϕ, C) y la energía del sólido Π^b (ε, ϕ):

$$\Pi = \Pi^b(\varepsilon, \phi) + \Pi^s(\phi, C) = \int_\Omega \{(1-\phi)^2 \psi(\varepsilon) + G_0(C)\Gamma_\ell(\ell, \phi)\} \, dV \qquad (40)$$

La energía del sólido viene definida por la densidad de energía de deformación $\psi(\varepsilon)$ del sólido elastoplástico y la función de degradación $(1-\phi)^2$ Donde la densidad de energía de deformación se descompone a su vez en un término elástico ψ^e y otro plástico ψ^p, tal que $\psi = \psi^e + \psi^p$. La energía disponible para la fractura se determina a partir de la densidad de energía de deformación total ψ, considerando la parte plástica en cada punto de integración como:

$$\psi^p = \int_0^t \dot{\psi}^p \, dt = \int_0^t \sigma : \dot{\varepsilon}^p \, dt \qquad (41)$$

El modelo completo de cálculo se incluye en una subrutina en la que se integra plasticidad de Von Misses (J2), transporte de hidrógeno y la teoría de campo de fase. Para la resolución se emplea el software de elementos finitos Abaqus, donde se modelan las probetas SSRT, con las cuatro mismas variantes de Monel K-500 que en los ensayos experimentales y se simulan las condiciones de concentración de hidrógeno correspondientes a los tres potenciales así como su exposición el aire. La carga se aplica mediante un desplazamiento en el extremo superior de las probetas, reproduciendo el método experimental. Además, para evaluar el transporte de hidrógeno, se consideran los coeficientes de difusión efectiva D_{eff}, medidos en estudios anteriores.

En primer lugar, se realiza un análisis de difusión del hidrógeno para determinar la profundidad hasta la cual se detecta la presencia de hidrógeno en el frente de la entalla considerando la misma duración de exposición que el ensayo experimental. El objetivo de este estudio es revisar si el hidrógeno puede alcanzar mediante difusión la misma

profundidad en el frente de la entalla que las zonas afectadas por fractura frágil observadas experimentalmente en la fractografía de las probetas.

En la Figura 13 se representan los valores de concentraciones normalizadas en el contorno de la grieta (siendo Cb la concentración de hidrógeno difusible). Se ha representado la profundidad experimental hasta la cual se observa fractura intergranular mediante una línea vertical discontinua. La línea continua representa la concentración de hidrógeno normalizada en el frente de entalla. Como se puede observar, considerando la difusión teórica durante el tiempo del experimento, el hidrógeno solo alcanza una profundidad de aproximadamente 0.2mm desde la entalla, mientras que la fractura intergranular tiene lugar hasta una profundidad cercana a los 0.6mm. Considerando que la rotura intergranular en este tipo de materiales está asociada a una fragilización por la presencia de hidrógeno, se aboga la hipótesis de la existencia de grietas sub-críticas que favorezcan la difusión del hidrógeno y justifiquen la profundidad de fractura IG observada experimentalmente.
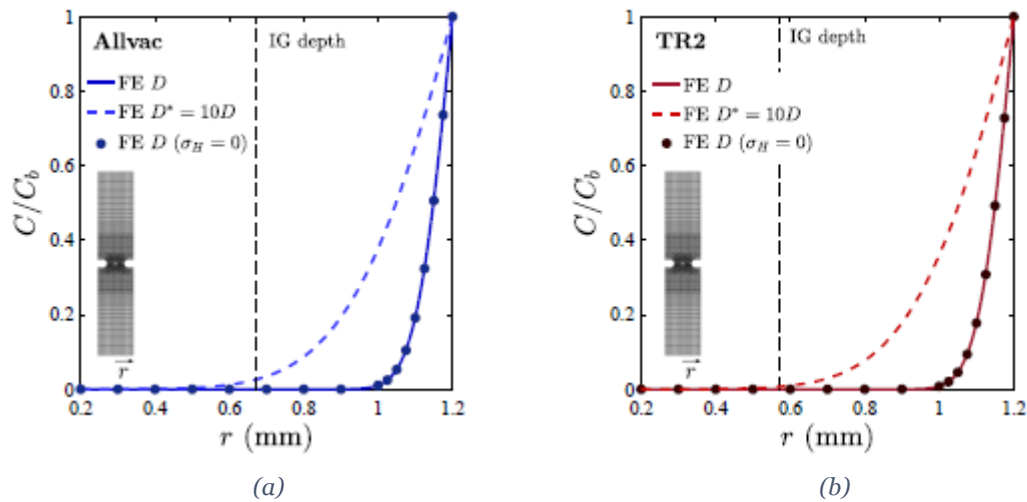
Figura 13. Perfiles de concentración de hidrógeno normalizados (a) Allvac y (b) TR2 en ausencia de tensiones hidrostáticas (círculos) y considerando tensiones hidrostáticas (línea solida). La línea vertical a trazos indica la profundidad de fractura intergranular observada en los ensayos de -1100mV en 0.6M NaCl. La línea a trazos de color representa el perfil de concentración si la difusividad del hidrógeno se eleva un orden de magnitud.

- *Efecto del valor del coeficiente de difusión empleado.*

El coeficiente de difusión es un parámetro clave para validar las conclusiones presentadas por su influencia en la longitud afectada por la entrada de hidrógeno en el frente de la entalla. Se ha tomado un valor de $D_{eff} = 1.3x10^{-10}$ cm²/s, el cual se encuentra en línea con la información recogida en la bibliografía experimental. Según indicado por Ai et al. [86], el rango de valores de este coeficiente en las aleaciones Monel K-500 se encuentra entre 8x10⁻¹¹ y 4x10⁻¹⁰ cm²/s.

Algunos autores han especulado que la difusión de hidrógeno puede acelerarse si se produce por las fronteras de granos, encontrando diversos estudios que relacionan este aumento en el coeficiente de difusión con: el tamaño de grano [87–89]; las características del contorno de grano [90,91]; las conexiones entre los borde de grano [92]; la presencia de solutos en los borde de grano [93] y las concentraciones de hidrógeno [93]. Los estudios llevados a cabo con níquel puro con un tamaño de grano similar al evaluado han observado que, debido a estos factores, la difusión efectiva podría verse aumentada como máximo entre 2 y 8 veces [87,89,94].

Conociendo que el coeficiente de difusión en níquel no puede llegar a alcanzar un valor mayor de 8 veces su valor característico se realiza un análisis considerando un coeficiente de difusión 10 veces superior al inicialmente considerado para estudiar la longitud afectada. Lo que se observa en los resultados obtenidos y mostrados en la Figura 13, es que la longitud afectada por hidrógeno sigue siendo menor que las longitudes de grieta con rotura IG, manteniendo válida la hipótesis de la existencia de grietas sub-críticas que aceleren la difusión de hidrógeno.

- *Implicaciones de la interpretación de los experimentos SSRT.*

El modelo se calibra con los datos experimentales en ambiente normal (aire, sin potencial de hidrógeno). En la Figura 14 (a) se pueden observar que los resultados obtenidos determinan rotura dúctil, con estrechamiento e iniciación de grieta en el centro de la probeta. Este resultado encaja con el comportamiento esperado para este tipo de material sin presencia de hidrógeno.

Por el contrario, al realizar los análisis para ambientes con hidrógeno la rotura se produce por fractura frágil en el exterior de la hendidura, en la zona de entalla, validando

el modelo empleado también para ambiente hidrógeno, como se puede observar en la Figura 14 (b).

(a)   *(b)*
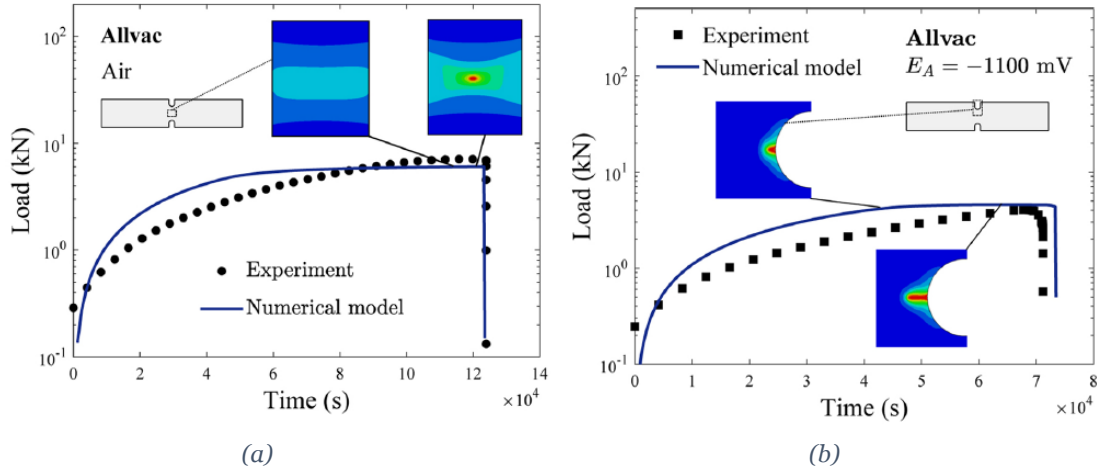
Figura 14. Comparación entre la carga experimental y simulada en función del tiempo de respuesta para el material Allvac (a) sin hidrógeno y (b) con potencial hidrógeno 1100mV. Las imágenes muestran la distribución del parámetro de daño de phase field. El color azul corresponde a material intacto y el color rojo al completamente dañado.

Según mostrado en la Figura 14, el modelo de campo de fase permite evaluar el tiempo necesario para que se produzca inicio de grieta, siendo una herramienta muy útil para establecer cuantitativamente las implicaciones del crecimiento de grietas sub-críticas e interpretar los ensayos SSRT.

En la Figura 15 (a) se puede observar como el tiempo para el inicio de fractura disminuye según aumenta el potencial en todos los tratamientos de Monel K-500 ensayados. Actualmente, la elección de los materiales para diseños estructurales se suele realizar mediante un ranking que clasifica los diferentes materiales empleados en la industria según su vulnerabilidad a un determinado ambiente corrosivo. Esta calificación se basa en los resultados experimentales obtenidos de ensayos SSRT [95]. Al comparar dicha clasificación con los resultados numéricos obtenidos en el presente trabajo, se observan discrepancias. Se puede observar que, por ejemplo en el material NRL HS, reconocido en la bibliografía por tener un buen comportamiento frente a fragilización asistida por hidrógeno (HEAC), el tiempo hasta el inicio de grieta es similar a tratamientos considerados más susceptibles de HEAC como son NRL LS o TR2. Igualmente, si se analiza el ratio entre el tiempo discurrido hasta el inicio de grieta y el tiempo hasta el fallo, según se presenta en la Figura 15 (b), el material NRL HS tendría

el peor comportamiento ya que el agrietamiento comienza a un tiempo menor del 40% del tiempo de fallo.

(a)   (b)
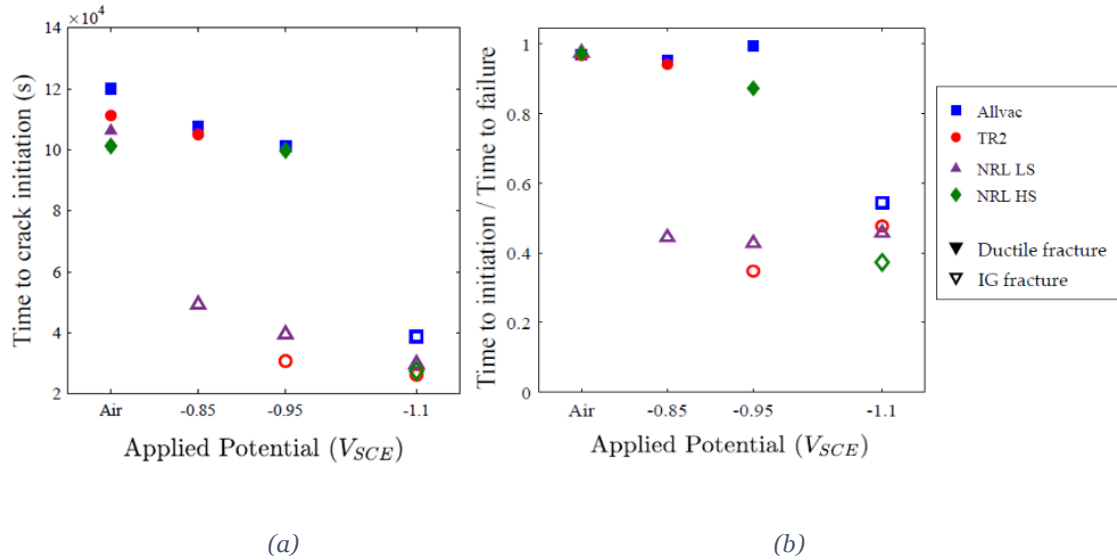
Figura 15. (a) Tiempo hasta el inicio de grieta y (b) ratio entre el tiempo para el inicio de grieta y el tiempo hasta el fallo de la probeta en función del potencial aplicado para los cuatro tratamientos de Monel K-500 ensayados. Los símbolos rellenos indican fractura dúctil y los símbolos vacíos fractura intergranular.

Estos resultados ponen en duda la eficacia de la metodología SSRT empleada en la industria como evaluación de la susceptibilidad a la fragilización por ambientes agresivos, como el hidrógeno, y se sugiere la re-evaluación cautelosa de los ensayos, ya que los resultados obtenidos determinan que pueden ser susceptibles de desarrollar fracturas sub-críticas por la concentración de tensiones.

3.2. GRADIENT-ENHANCED STATISTICAL ANALYSIS OF CLEAVAGE FRACTURE

- Análisis estadístico de fractura por clivaje considerando la influencia de los gradientes de deformación plástica.- Ref. [96]

Una de las causas más frecuentes de fractura por clivaje en metales a bajas temperaturas es la presencia de grietas sub-críticas provenientes de defectos o inclusiones en los materiales [97]. Estos defectos, dependiendo de su ubicación y condiciones ambientales, pueden causar una disminución en la tenacidad a fractura de los metales. La presencia de defectos en la red cristalina de materiales tan heterogéneos microestructuralmente como los metales solo se puede estudiar desde un punto de vista estadístico.

El trabajo desarrollado en esta tesis tiene como objetivo contribuir al desarrollo de un modelo que caracterice la fractura frágil mediante el análisis de la probabilidad de fallo sin suposiciones iniciales, y el estudio de los mecanismos que suceden en la microestructura. Para ello, se presenta un marco numérico en el que se acopla un modelo triparamétrico de Weibull [63,98], aplicando el principio del eslabón más débil, y se realiza la caracterización de tensiones mediante teorías basadas en mecanismos de gradientes de deformación plástica (MSG). El estudio de clivaje se basa en el marco estadístico desarrollado por Beremin, en el cual se relaciona probabilidad de fallo con la tensión de fractura local [62].

El modelo numérico se implementa mediante el programa de elementos finitos Abaqus y el programa de análisis matemático Matlab. La vinculación de los resultados entre los dos programas, necesaria para relacionar el análisis probabilístico de Weibull con la evaluación de las teorías SGP, se ha realizado mediante la herramienta Abaqus2Matlab [99], que permite el intercambio automático de información entre ambos programas. La implementación de las teorías de gradientes plásticos en el programa ABAQUS se realiza mediante la subrutina UMAT.

La teoría de deformación plástica (SGP) empleada se fundamenta en el modelo basado en mecanismos (MSG) desarrollado por Gao et al. [43], que considera la teoría de dislocaciones de Taylor teniendo en cuenta tanto las dislocaciones geométricamente necesarias como las estadísticamente almacenadas. Según lo explicado en el apartado

1.1.2.1, el modelo MSG considera la longitud intrínseca del material, obtenida tras un ajuste experimental, y cuya función es caracterizar la pequeña escala. Así, cuando $\ell = 0$ sería el equivalente a evaluar plasticidad convencional, caso también estudiado en el trabajo desarrollado con el fin de analizar las diferencias entre modelos SGP y plasticidad convencional. La consideración de un modelo SGP es fundamental para caracterizar los micro-mecanismos de plasticidad que tienen lugar en la vecindad de la punta de la grieta, lo que puede dar lugar a un estado tensional muy diferente del considerado con teorías de plasticidad convencional [100].

Como se ha comentado en el apartado 1.1.2.2, los modelos de Weibull cuentan con dos parámetros de ajuste denominados parámetro de escala (σ_u) y módulo (m). El modelo probabilístico empleado en el presente estudio, desarrollado por Muñiz-Calvente et al. [63], incluye un tercer parámetro que analiza la tensión umbral para que se produzca el crecimiento de la grieta (σ_{th}):

$$Pf = 1 - exp\left[-\left(\frac{\sigma_w - \sigma_{th}}{\sigma_u}\right)^m\right] \qquad (42)$$

Para obtener el ajuste de estos tres parámetros, se requiere de un proceso iterativo así como de un ajuste por mínimos cuadrados mediante el cual se determina el valor de σ_u y m para un valor inicial de σ_{th}. Para realizar el ajuste por mínimos cuadrados se presenta la probabilidad de fallo acumulada siguiendo la ecuación de una recta:

$$\log(\sigma_u) + \log\left(-\log\left(1 - P_f\right)\right)\frac{1}{m} = \log(\sigma_w - \sigma_{th}) \qquad (43)$$

El proceso iterativo finaliza cuando la tolerancia entre los valores de inicio de la iteración y los valores al final es menor a 0.0001, garantizando así un buen ajuste. El proceso completo llevado a cabo se presenta en forma de diagrama de flujo en la Figura 16.
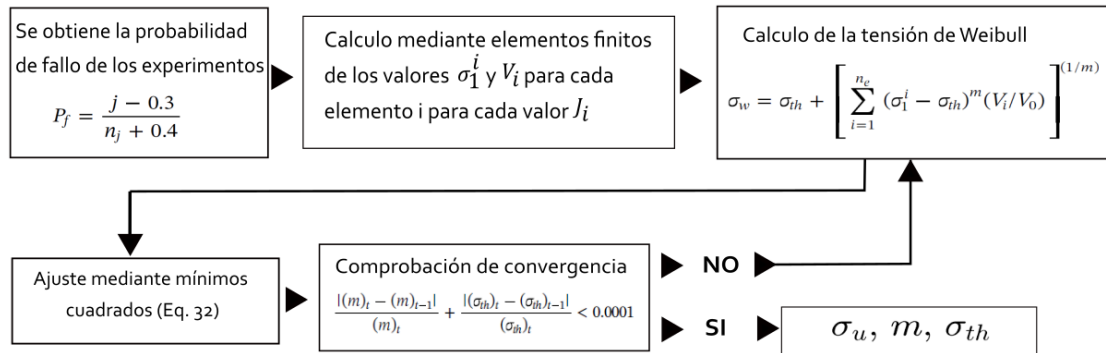
Figura 16. Diagrama de flujo del proceso iterativo para determinar los tres parámetros estadísticos de Weibull

La validación del modelo numérico desarrollado se realiza mediante la comparación de sus predicciones con la serie de experimentos desarrollada en el proyecto Euro Toughness [101]. En este proyecto se llevaron a cabo numerosos experimentos estudiando el acero definido por la normativa DIN como 22NiMOCr37. Este tipo de acero ferrítico se ensaya en un amplio rango de temperaturas (siete temperaturas entre -154 ºC y +20 ºC) y en cuatro tamaños de probetas de fractura compactas.

El primer paso consiste en ajustar el modelo numérico mediante la ley de endurecimiento uniaxial que relaciona tensiones y deformaciones:

$$\sigma = \sigma_Y \left(1 + \frac{\varepsilon^P}{\sigma_Y} \right)^N$$

(44)

Donde N es el coeficiente de endurecimiento por deformación. Para ello, se consideran los siguientes valores característicos del material: coeficiente de Poisson $v = 0.3$ y módulo de Young $E = 200$ GPa y se procede a calibrar los valores de N y σ_Y mediante la ecuación (44) y los ensayos uniaxiales del proyecto Euro Toughness. Los valores obtenidos para las diferentes temperaturas se indican en Tabla 1.

Temperature (°C)	−154	−91	−60	−40	−20	0	20
Yield stress σ_Y (MPa)	570	490	470	450	440	430	425
Strain hardening exponent N	0.14	0.14	0.13	0.13	0.13	0.12	0.12

Tabla 1. Propiedades de los materiales según la temperatura de estudio.

Una vez ajustado el modelo numérico, se obtienen las tensiones en las proximidades de la punta de la grieta, mediante la teoría MSG y plasticidad convencional. Según se observa en la Figura 17, al alejarse de la punta de la grieta ambas teorías presentan tensiones similares pero, en las cercanías de la punta de la grieta la teoría MSG predice unas tensiones mayores. Este aumento de tensiones representa el efecto de considerar dislocaciones geométricamente necesarias (GND) que actúan como obstáculos en el movimiento de las dislocaciones estadísticamente acumuladas (SSD) y consiguen elevar las tensiones en el frente de grieta.
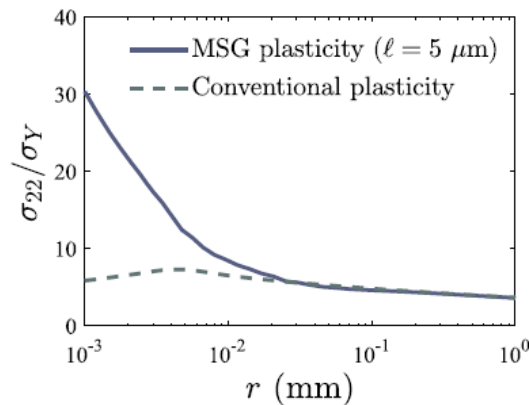
Figura 17. Valor de la tensión a lo largo del plano de fractura para plasticidad MSG y plasticidad convencional. La distancia en el frente de la grieta se indica en escala logarítmica.

Esta elevación de las tensiones afecta al modelo de clivaje ya que se traduce en un aumento de los valores de la tensión de Weibull σ_w. Este hecho se representa gráficamente en la Figura 18, mostrando como al considerar una longitud de escala mayor (mayor efecto de los gradientes de deformación plástica), aumenta el valor de la tensión de Weibull (σ_w). Una mayor tensión de Weibull, implica una mayor probabilidad de fallo considerando unos valores fijos de σ_u, m y σ_{th} (según la ecuación (42)).
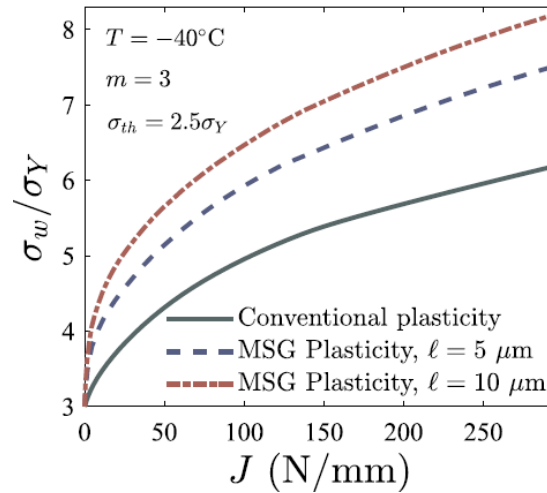
Figura 18. Representación de la dependencia entre σ_w y la carga externa aplicada para plasticidad MSG con $\ell = 5$, $\ell = 10$ y plasticidad convencional ($\ell = 0$).

En la Tabla 2 se presentan los parámetros de Weibull calibrados para cada temperatura y tamaño de probeta, tanto para el estudio de plasticidad convencional como el estudio considerando teorías de gradiente de deformación plástica.

Plasticidad MSG							
Temperatura (°C)	-154	-91	-60	-40	-20	0	20
σ_u (MPa)	23.6	46.9	632.3	611.7	1060.4	183.0	16948.0
σ_{th} (MPa)	5489.3	7295.1	7670.6	8136.7	8295.9	19888.0	13516.0
m	2.0	1.9	2.9	3.1	3.2	1.7	12.7
Plasticidad Convencional							
Temperatura (°C)	-154	-91	-60	-40	-20	0	20
σ_u (MPa)	9.2	14.9	1380.4	911.3	146.0	46.1	1731.7
σ_{th} (MPa)	2251.7	2459.0	1015.7	1477.5	2289.1	2205.0	1474.7
m	1.9	1.8	13.5	12.8	3.2	0.8	19.9

Tabla 2. Calibración de los parámetros de Weibull para plasticidad convencional y MSG en función de la temperatura.

Considerando los valores presentados en la Tabla 2, se representa la probabilidad de fallo en función de la carga remota aplicada (*J*), considerando tanto plasticidad convencional como teorías MSG y se analizan los resultados con las curvas obtenidas de los ensayos experimentales. Según se muestra en la Figura 19, ambas teorías muestran una buena correspondencia con los resultados experimentales:
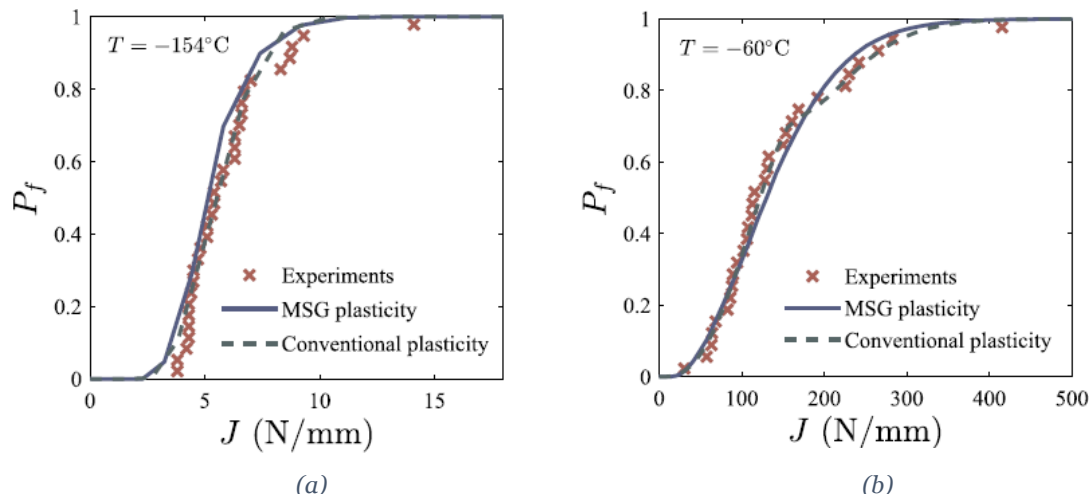
Figura 19. Probabilidad de fallo en función de la carga externa aplicada. Se representan los valores de los datos experimentales [101] y las predicciones estadísticas para los valores de σ_u, m y σ_{th} calibrados para plasticidad convencional y MSG (ver Tabla 2) (a) Temperatura -154ºC y (b) Temperatura -40ºC.

Al analizar los valores presentados en la Tabla 2, se pueden observar las principales diferencias entre considerar plasticidad convencional o gradientes de deformación plástica. El valor de la tensión umbral (σ_{th}), anticipa la necesidad de mayores tensiones para propagar grietas sub-críticas si se tienen en cuenta las dislocaciones. Igual de importante es resaltar la relación entre el parámetro σ_{th} y la temperatura. La teoría MSG muestra que a menor temperatura, menor es el valor de tensión umbral para que se produzca el crecimiento de la grieta, anticipando el comportamiento frágil del metal al reducir la temperatura. Esta relación no es capturada considerando plasticidad convencional.

Una vez analizadas las diferencias numéricas entre teorías MSG y plasticidad convencional, se recurre a los mapas de daño como método para representar de manera gráfica e intuitiva la probabilidad de fallo. Los mapas de daño, desarrollados por Muñiz-Calvente et al. [64], representan el valor de la probabilidad de fallo en cada unidad de material mostrando, de una manera intuitiva, el área en el que están confinados los defectos capaces de desencadenar el fallo.

En la Figura 20 se estudia el daño en las inmediaciones de la grieta considerando plasticidad MSG y plasticidad convencional. Mientras que las teorías de gradientes de deformación plástica determinan que los defectos que pueden ocasionar daño están confinados a una zona más cercana al área de la grieta (10 micras desde el frente de grieta), con plasticidad convencional se considera que los defectos desencadenantes de

fallo pueden estar en un área 100 veces mayor (varios milímetros desde el frente de grieta).
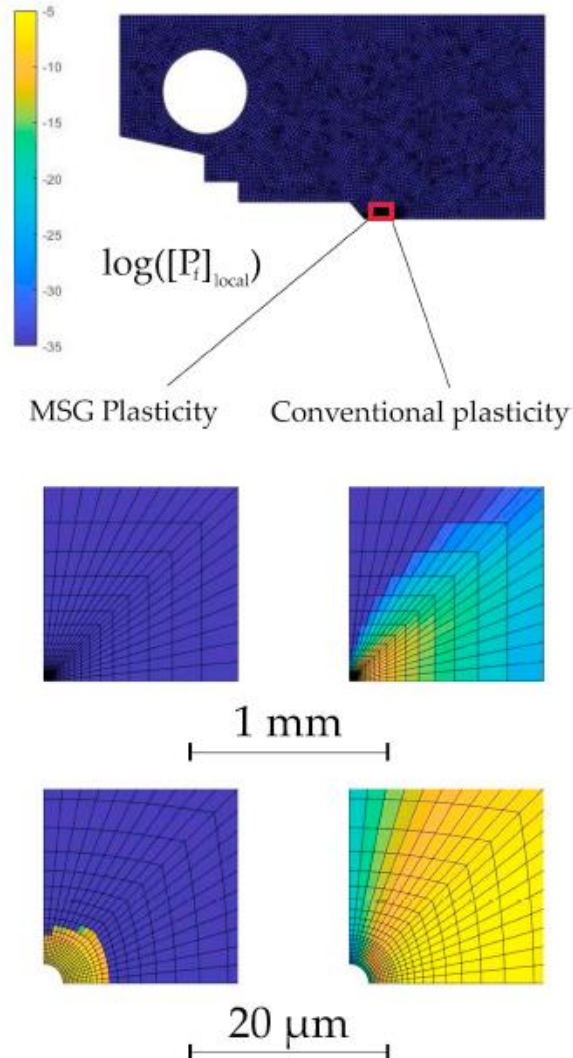
Figura 20. Mapa de daño donde se muestra la probabilidad de fallo considerando plasticidad convencional y plasticidad MSG.

Con el presente trabajo se pone de manifiesto la importancia de considerar gradientes de deformación plástica a la hora de evaluar el comportamiento a fractura de materiales metálicos y su importancia para evaluar la probabilidad de fallo. Se ha demostrado que para unos valores de los parámetros de Weibull fijos, la probabilidad de fallo con teorías MSG es mayor que con plasticidad convencional, hecho importante a la hora de garantizar el buen comportamiento estructural. Además, el análisis particularizado de los parámetros de Weibull pone de relieve que la tendencia del valor

de la tensión umbral varía de diferente manera con la temperatura, cobrando más sentido físico los valores obtenidos mediante teorías MSG.

3.3. FRACTURE IN DISTORTION GRADIENT PLASTICITY

- Fractura considerando gradientes de distorsión plástica.- Ref. [102]

El empleo de materiales compuestos metal-cerámicos es cada vez más común en la insdustria. Comenzaron a desarrollarse en el ámbito aeroespacial y se han popularizado por su utilidad en componentes electrónicos. Además, sus buenas propiedades térmicas, que mejoran las de los metales, los hacen especialmente interesantes para un amplio rango de aplicaciones estructurales e industriales, como en el campo de la biomecánica.

Numerosos estudios de los materiales compuestos se centran en comprender el comportamiento en la interfaz entre los dos materiales. En experimentos llevados a cabo en bimateriales, formados por un elemento metálico y otro cerámico o cristalino, se ha detectado fractura frágil en presencia de plasticidad [27–32]. Como se ha mencionado en el apartado 1.1.1.3., Elssner et al, [33] y Korn et al. [34] desarrollaron una serie de experimentos en los que estudiaban la decohesión entre niobio y zafiro tanto a nivel macroscópico como atomístico, dando lugar al trabajo experimental más completo sobre la decohesión de un bimaterial formado por un metal monocristalino y un material cerámico. La resistencia teórica a nivel macroscópico resulta ser 1000 veces mayor que el trabajo de separación atomística, atribuyendo esta diferencia a las dislocaciones observadas en el niobio.

En el presente trabajo se estudia este fenómeno y la caracterización de los mecanismos en la interfaz, optando por implementar el problema considerando teorías de distorsión plástica (DGP). La idea de implementar el problema considerando DGP, viene motivada por el trabajo desarrollado por Bardella [103–105] y Poh y Peerlings [53], en el cual resaltan la importancia de considerar la parte plástica no simétrica de los gradientes de desplazamiento para capturar características esenciales de plasticidad en cristales. Además, Poh y Peerlings [53] realizan un análisis del problema de referencia investigado por Bittencourt et al. [106], reflejando la importancia de considerar las teorías DGP puesto que, son las únicas que capturan el fenómeno local. Los trabajos anteriormente citados muestran que las teorías de distorsión plástica tienen mayores capacidades de modelización. Además, aportan un enfoque más riguroso debido a que el vector de Burgers se caracteriza macroscópicamente por el rotacional de la distorsión.

El objetivo del trabajo desarrollado es caracterizar correctamente la interfaz entre un sólido plástico y uno elasto-plástico incorporando condiciones de contorno de alto orden para modelar la obstrucción de dislocaciones. Para ello, se consideran por primera vez las teorías de gradientes de distorsión plástica para modelizar el comportamiento de la punta de la grieta y se realiza un análisis sobre la importancia de considerar el tensor de Nye en el estudio de la mecánica de la fractura.

El trabajo desarrollado combina un estudio analítico sobre la naturaleza asintótica de los campos de tensiones en la punta de la grieta con el análisis numérico detallado mediante elementos finitos de estos campos bajo condiciones de modo I y modo mixto. Para el estudio con elementos finitos se emplea el software Abaqus implementando a través de una subrutina de usuario de elemento (UEL) el modelo numérico de las teorías DGP. Aplicando este marco numérico, se investiga la influencia del rotacional plástico y de los parámetros del material en los campos de tensiones en el frente de grieta.

- *Comportamiento asintótico en Modo I y estudio de las longitudes de escala L_E y L_D*

En el estudio asintótico se revela la existencia de un área elástica cercana a la punta de la grieta, sugiriendo que se trata de una zona sin dislocaciones. La existencia de estos campos elásticos se confirma mediante el análisis numérico por elementos finitos, asumiendo condiciones de Modo I ($K_{II} = 0$) y flujo de plasticidad irrotacional ($\chi \to \infty$). Como se puede ver en la Figura 21 (a), para todos los valores $\ell/R_p > 0$ existe una zona cercana a la punta de la grieta en la que el comportamiento es elástico ($\sigma_{yy} \sim r^{-1/2}$).

En la Figura 21 (b) se observa que considerando plasticidad convencional ($\ell = 0$), la relación entre deformaciones a tracción plásticas y elásticas aumenta según nos acercamos a la punta de la grieta. Sin embargo, cuando $\ell > 0$ el ratio $\varepsilon_{yy}^p/\varepsilon_{yy}^e$ alcanza un máximo que después decrece según se acerca a la punta de la grieta debido al dominio de las deformaciones elásticas. De ambas figuras se concluye que existe una zona en la punta de la grieta en la cual las deformaciones plásticas son insignificantes.
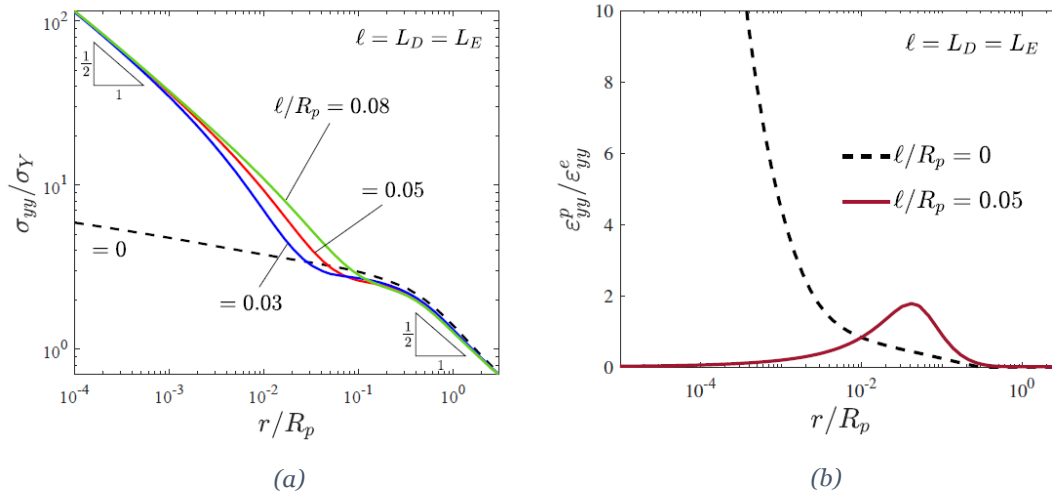
Figura 21. Zona elástica cerca de la punta de la grieta(a) Distribución de tensiones en el frente de grieta para varios valores de ℓ/R_p.y (b) Distribución en el frente de grieta del ratio entre la deformación a tracción plástica y elástica $\varepsilon_{yy}^p/\varepsilon_{yy}^e$.

A continuación, se investiga la contribución individual de la parte energética (L_E) y la parte disipativa (L_D). En las Figura 22 (a) y (b) se muestran respectivamente la distribución de tensiones en la punta de la grieta y la distancia a la punta de la grieta donde los efectos de gradientes elevan las tensiones relativas a plasticidad convencional, viendo que los efectos de alto orden disipativos dominan la respuesta en la punta de la grieta.

En la Figura 22 (a) se observa que la magnitud de L_E/R_p se ha tenido que incrementar 50 veces relativo al valor de L_D/R_p para llegar a una tensión en el frente de la grieta similar. De la misma manera, en la Figura 22 (b) se analiza la zona dominada por gradientes, siendo r_{DGP} la longitud del área en el frente de la grieta donde la distribución de tensiones se desvía de la plasticidad convencional $\sigma_{DGP} > 2\sigma_{HRR}$ [107]. En este caso se observa que para el caso $L_E > 0$ apenas hay desviación respecto de la plasticidad convencional pero en el caso $L_D > 0$ el efecto de los gradientes modifica la distribución de tensiones en el frente de la grieta.
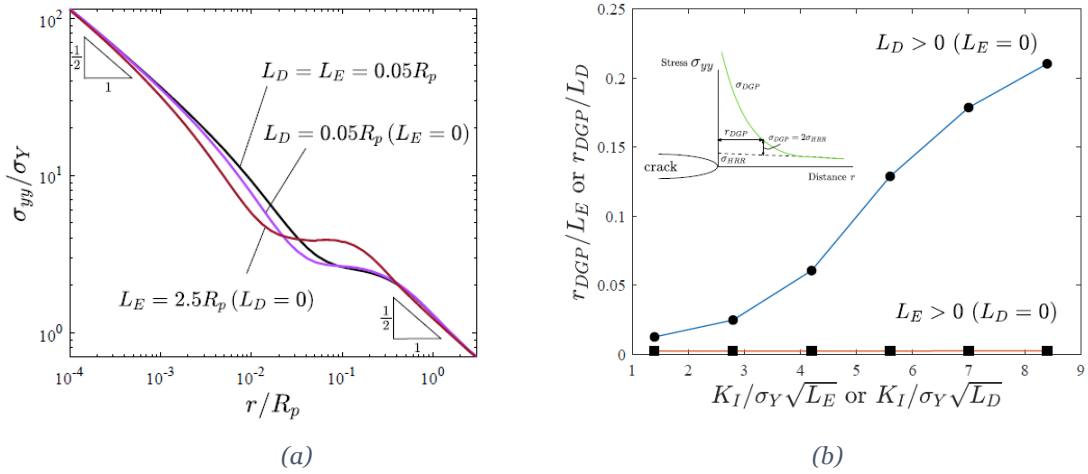
Figura 22. Influencia de las longitudes de escala energética y disipativa: (a) Distribución de la tensión a tracción en el frente de grieta y (b) distancia a la punta de la grieta donde los efectos de gradientes elevan las tensiones relativas a plasticidad convencional

Los resultados muestran que son necesarios mayores valores de L_E/R_p para que la energía asociada a los rotacionales tenga un impacto en las distribución de tensiones similar a las teorías constitutivas basadas en gradientes, haciendo necesario un estudio experimental que analice los valores de L_E que mejor se adaptan a los ensayos en la microescala según las teorías DGP.

- ### *Estudio de la influencia de χ*

El parámetro χ gobierna la disipación generada por el rotacional plástico bajo condiciones de modo mixto (eq. (25)). En el presente trabajo, se estudian las condiciones de modo mixto considerando $K_I > 0$ y $K_{II} > 0$ y siendo el ángulo que caracteriza el grado del modo mixto $\psi = tan^{-1}(K_{II}/K_I)$.

En la Figura 23 (a) se muestran los campos de tensiones en la punta de la grieta para $\psi = 45°$ y diferentes valores representativos de χ, confirmando la tendencia observada por Bardella [105]: al aumentar el valor de χ se produce un endurecimiento del material. En la Figura 23 (b) se representa la elevación de las tensiones relativas a la plasticidad convencional $\sigma_{DGP}/\sigma_{HRR}$ para diferentes ángulos de modo mixto, observando que la influencia del rotacional plástico aumenta según se disminuye ψ.
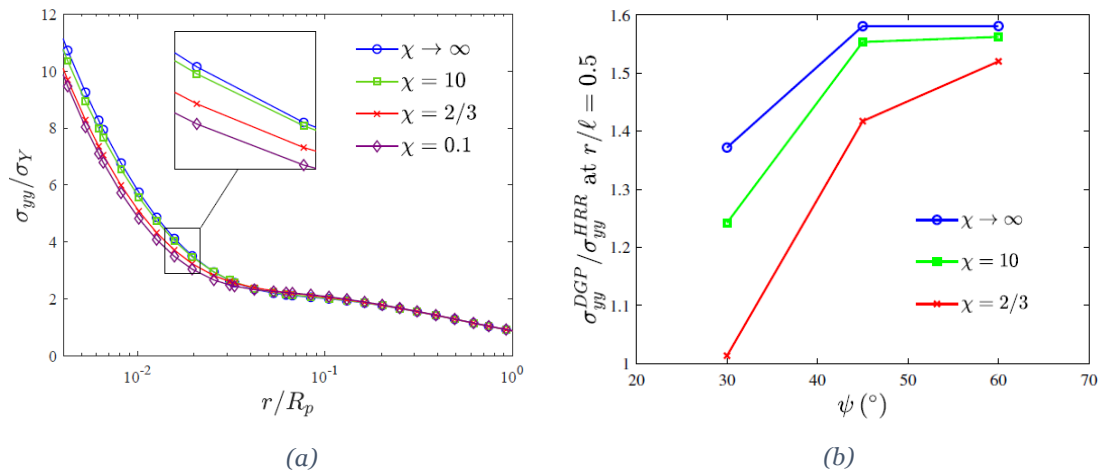
Figura 23. Influencia del valor de χ en condiciones de modo mixto: (a) Distribución de la tensión de tracción en el frente de grieta y (b) Elevación de las tensiones previstas en función de plasticidad convencional.

- ***Estudio de fractura en la interfaz de un material compuesto.***

El estudio de fractura frágil en presencia de importante flujo plástico es un problema no resuelto en fractura de metales. El objetivo del presente trabajo es caracterizar la interfaz entre un sólido elástico y un sólido elasto-plástico empleando, por primera vez en fractura, las condiciones de contorno de orden superior que consideran el bloqueo de dislocaciones. Para ello, se reproducen numéricamente los experimentos llevados a cabo por Elssner et al.[33] y Korn et al. [34] en la interfaz entre niobio y zafiro.

La probeta empleada en los ensayos experimentales y, reproducida en el presente trabajo, es una probeta sometida a flexión en 4 puntos. Las características y las dimensiones, indicadas en milímetros, se pueden observar en la Figura 24. El espesor de la probeta de estudio es de 2mm.
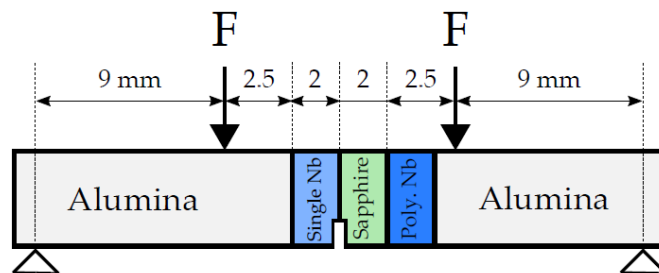
Figura 24. Geometría y dimensiones de la probeta estudiada en los experimentos por Korn et al.
[34].

La lámina de zafiro está dispuesta entre dos láminas, una de niobio (Nb) policristalino y otra de niobio monocristalino, que a su vez están situadas entre dos láminas de alúmina. La probeta cuenta con una grieta de 0.4mm en el contacto entre el niobio de un cristal y el zafiro y la carga aplicada F es de 42.5 N. Las propiedades de los diferentes componentes se han obtenido de referencias en la literatura [33,34,108] y se presentan en la Tabla 3, considerándose tanto la alúmina como el zafiro elástico lineales.

	$E\ (GPa)$	ν	$\sigma_Y\ (MPa)$	N
Niobio policristalino	105	0.39	105	0.24
Niobio de 1 grano	145	0.36	145	0.05
Alúmina	390	0.27	-	-
Zafiro	425	0.16	-	-

Tabla 3. Propiedades de los materiales empleados en los experimentos [34,47].

Los parámetros de longitud de escala se consideran iguales $L_E = L_D = \ell$. Para determinar el valor de la longitud de escala se realiza una revisión bibliográfica mediante la cual, se valida el valor $\ell = 5.29\ \mu m$ empleado por Qu et al. [108] para Nb policristalino. Según el trabajo desarrollado por Nix y Gao [36], los experimentos realizado en muestras monocristalinas se reproducen de manera más precisa considerando una longitud de escala del doble del valor que en las muestras policristalinas. Aplicando esta observación, se determina una longitud de escala para Nb monocristalino igual a $\ell = 10.58\ \mu m$. En ambos casos, para Nb policritalino y monocristalino, se considera el parámetro que gobierna la disipación debido al rotacional plástico como $\chi = 2/3$. Las condiciones de contorno se simulan empleando micro-endurecimiento para emular el bloqueo de las dislocaciones en las intercaras entre dos materiales.

En la Figura 25 se representan los valores de la tensión de tracción obtenidos en la interfaz en el frente de la grieta mediante gradientes de distorsión plástica y plasticidad convencional, normalizando la distribución de tensiones por la tensión de fluencia del Nb monocristalinos.
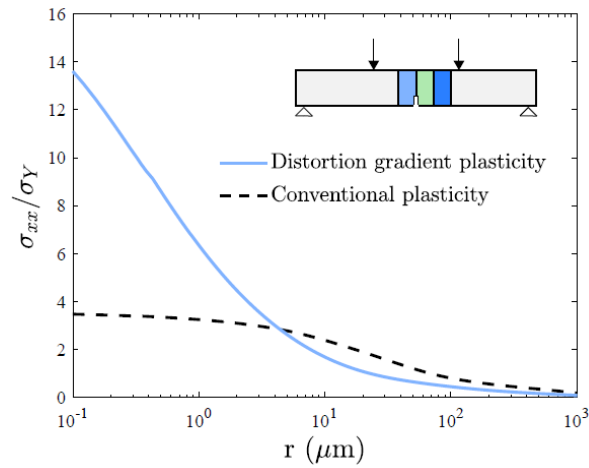
Figura 25. Tensión de tracción en la interfaz entre niobio y zafiro en el frente de la grieta.

Mientras que, con plasticidad convencional la máxima tensión se encuentra cuatro veces por debajo de su tensión de fluencia ($4\sigma_Y$), y no se podría desencadenar la fractura frágil, la tensión que se predice mediante gradientes de distorsión plástica supera la fuerza teórica de cohesión ($10\sigma_Y$). La consideración de gradientes de distorsión plástica y la consideración de bloqueo de dislocaciones genera un método racional para el estudio de la decohesión en la interfaz de bi-materiales en presencia de plasticidad.

4. CONCLUSIONES

El trabajo investigador de la presente tesis doctoral se ha centrado en el estudio de las condiciones que generan fractura frágil en metales, determinando los mecanismos de fallo asociados para desarrollar modelos mecanísticos capaces de capturar la física que gobierna el proceso. En paralelo con estas formulaciones teóricas se han desarrollado modelos numéricos que permiten su implementación y aplicación para interpretar las observaciones experimentales y la predicción de la fractura, tanto a nivel de laboratorio como en casos prácticos ingenieriles.

La tesis se puede dividir en tres etapas, que se corresponden con cada uno de los artículos publicados. En primer lugar, se ha estudiado el comportamiento de un metal en presencia de hidrógeno para lo que se ha empleado plasticidad J2 y un modelo de campo de fase con el objetivo de conocer en detalle la degradación de un metal en presencia de un agente fragilizante. Se continúa el trabajo estudiando el caso de clivaje en metales producido por la exposición a bajas temperaturas. Para este segundo trabajo, se realiza un modelo numérico que considera las teorías de gradientes de deformación plástica (MSG) y un nuevo modelo probabilístico triparamétrico. La influencia de los gradientes de deformación plástica se cuantifica relativa a los resultados obtenidos con la plasticidad convencional. En el último trabajo se utiliza la teoría de gradientes de distorsión plástica (DGP) de orden superior para evaluar por primera vez su influencia en fractura e interpretar problemas de fractura frágil en la interfaz de materiales compuestos metal-cerámicos, donde hay presencia de plasticidad. En particular, del trabajo realizado se pueden extraer las siguientes conclusiones específicas:

- La consideración de la teoría de campo de fase para la evaluación del concepto de daño permite interpretar de manera sencilla e intuitiva el grado de degradación en el que se encuentra cada elemento, siendo una eficaz herramienta ingenieril.

- La relación entre fractura frágil y existencia de defectos a una distancia crítica en el frente de la grieta exige un estudio estadístico capaz de predecir la probabilidad de fallo determinando las tensiones locales y estableciendo un valor umbral asociado a la energía necesaria para que se propague una grieta.

- Las teorías de gradientes de deformación plástica son fundamentales para analizar el comportamiento de fractura frágil. La fractura frágil se produce con energías de fractura menores que la fractura dúctil, generando una zona plástica más pequeña dónde los gradientes de deformación plástica son mayores.

- Es necesario considerar el papel de las condiciones de contorno de orden superior para modelizar el bloqueo en la transmisión de dislocaciones y capturar así la fractura frágil que se observa en el estudio de interfaz de materiales compuestos.

Así, la conclusión general principal es que el desarrollo de un marco teórico/numérico en el medio continuo que de lugar a predicciones fiables de fractura frágil en metales requiere de tres ingredientes fundamentales:

(1) Una caracterización micro-mecánica del fenómeno de plasticidad, capaz de capturar la influencia de las dislocaciones geométricamente necesarias asociadas con los gradientes de deformación y de simular efectos como el bloqueo de las dislocaciones.

(2) Un tratamiento probabilístico riguroso para caracterizar la distribución estadística de defectos como inclusiones o partículas de segunda fase, y su influencia en la nucleación de micro-grietas que favorezcan clivaje.

(3) El desarrollo de un marco computacional multi-físico capaz de capturar, en geometrías y dimensiones arbitrarias, la difusión de especies agresivas y su impacto sobre la tenacidad local del material. Los resultados obtenidos revelan que los modelos de fase constituyen un candidato idóneo para estas simulaciones

4.1. TRABAJOS FUTUROS

El análisis del trabajo realizado pone de manifiesto la necesidad de completar la búsqueda de un modelo común que permita analizar la fractura frágil en metales, incorporando las particularidades de cada agente fragilizante. Con este fin, se establecen los siguientes objetivos intermedios en los que continuar el trabajo investigador:

- Desarrollar un modelo común en el que se implementen las teorías de campo de fase y teorías avanzadas de gradientes de deformación plástica. Como se ha observado, aunque en entallas la influencia es menor, en la evaluación de grietas es fundamental considerar el endurecimiento debido a las dislocaciones.

- Ampliar y mejorar el marco numérico de transporte de hidrógeno para introducir modelos de difusión más avanzados, fundamental en los casos que no se dispone de la difusión efectiva. Estos modelos deben incluir la consideración de existencia de trampas y dislocaciones geométricamente necesarias.

- Completar el estudio de las teorías de gradientes de distorsión plástica reproduciendo un amplio espectro de casos experimentales que proporcionen información fenomenológica que sirva para ajustar los diferentes parámetros, con especial importancia determinar la longitud de escala energética (L_E) asociada a diferentes materiales.

BIBLIOGRAFÍA

[1]   A.A. Griffith, "The phenomena of rupture and flow in solids," Philos. Trans. R. Soc. London. Ser. A. Contain. Pap. a Math. or Phys. Character. 221 (1921) 163–198. http://mbarkey.eng.ua.edu/courses/AEM644/Griffith1921fracture.pdf.

[2]   G.R. Irwin, "Fracture Dynamics. Fracturing of Metals.," Am. Soc. Met. Clevel. OH. (1948) 147–166.

[3]   E. Orowan, "Fracture and strength of solids," Reports Prog. Phys. 12 (1949) 185–232.

[4]   J.R.Rice, "A Path Independent Integral and the Approximate Analysis of Strain Concentration by Notches and Cracks," J. Appl. Mech. 35 (1968) 379–386.

[5]   H.M. Westergaard, "Bearing Pressures and Cracks," J. Appl. Mech. 6 (1939) 53.

[6]   G.R. Irwin, "Onset of Fast Crack Propagation in High Strength Steel and Aluminum Alloys," Sagamore Res. Conf. Proc. 2 (1956) 289–305.

[7]   G.R. Irwin, "Analysis of Stresses and Strains near the End of a Crack Traversing a Plate," J. Appl. Mech. 24 (1957) 361–364.

[8]   N. Eliaz, A. Shachar, B. Tal, D. Eliezer, "Characteristics of hydrogen embrittlement, stress corrosion cracking and tempered martensite embrittlement in high-strength steels," Eng. Fail. Anal. 9 (2002) 167–184.

[9]   R.A. Oriani, "The diffusion and trapping of hydrogen in steel," Acta Metall. 18 (1970) 147–157.

[10]   E. Martínez-Pañeda, C.F. Niordson, R.P. Gangloff, "Strain gradient plasticity-based modeling of hydrogen environment assisted cracking," Acta Mater. 117 (2016) 321–332.

[11]   I.M. Robertson, H.K. Birnbaum, "An HVEM study of hydrogen effects on the deformation and fracture of nickel," Acta Metall. 34 (1986) 353–366.

[12]   Y. Liang, P. Sofronis, R.H. Dodds, "Interaction of hydrogen with crack-tip plasticity: Effects of constraint on void growth," Mater. Sci. Eng. A. 366 (2004) 397–411.

[13]   P. Novak, R. Yuan, B.P. Somerday, P. Sofronis, R.O. Ritchie, "A statistical , physical-based , micro-mechanical model of hydrogen-induced intergranular fracture in steel," J. Mech. Phys. Solids. 58 (2010) 206–226.

[14]   A.R. Troiano, "The Role of Hydrogen and Other Interstitials in the Mechanical Behavior of Metals: (1959 Edward De Mille Campbell Memorial Lecture)," Metallogr. Microstruct. Anal. 5 (2016) 557–569.

[15]   S. Sun, K. Shiozawa, J. Gu, N. Chen, "Investigation of deformation field and hydrogen partition around crack tip in fcc single crystal," Metall. Mater. Trans. A. 26 (1995) 731–739.

[16]   T. Zhang, W.Y. Chu, K.W. Gao, L.J. Qiao, "Study of correlation between hydrogen-induced stress and hydrogen embrittlement," Mater. Sci. Eng. A. 347 (2003) 291–299.

[17]   P. Sofronis, R.M. McMeeking, "Numerical analysis of hydrogen transport near a blunting crack tip," J. Mech. Phys. Solids. 37 (1989) 317–350.

[18]   A.H.M. Krom, R.W.J. Koers, A. Bakker, "Hydrogen transport near a blunting crack tip," J. Mech. Phys. Solids. 47 (1999) 971–992.

[19]   P. Novak, R. Yuan, B.P. Somerday, P. Sofronis, R.O. Ritchie, "A statistical, physical-based, micro-mechanical model of hydrogen-induced intergranular fracture in steel," J. Mech. Phys. Solids. 58 (2010) 206–226.

[20]   A. Turnbull, D.H. Ferriss, H. Anzai, "Modelling of the hydrogen distribution at a crack tip," Mater. Sci. Eng. A. 206 (1996) 1–13.

[21]   C. V. Di Leo, L. Anand, "Hydrogen in metals: A coupled theory for species diffusion and large elastic-plastic deformations," Int. J. Plast. 43 (2013) 42–69.

[22]   E. Martínez-Pañeda, S. Del Busto, C.F. Niordson, C. Betegón, "Strain gradient plasticity modeling of hydrogen diffusion to the crack tip," Int. J. Hydrogen Energy. 41 (2016) 10265–10274.

[23]   E. Martínez-Pañeda, A. Díaz, L. Wright, A. Turnbull, "Generalised boundary conditions for hydrogen transport at crack tips," Corros. Sci. 173 (2020) 108698.

[24]   M. Yaghoobi, G.Z. Voyiadjis, "The effects of temperature and strain rate in fcc and bcc metals during extreme deformation rates," Acta Mater. 151 (2018) 1–10.

[25]   P. Dunne, Introduction to Computational Plasticity, 2006.

[26] S. Suresh, A. Mortensen, A. Needleman, Metal Matrix Composites, 1993.

[27] T.S. Oh, R.M. Cannon, R.O. Ritchie, "Subcritical crack growth along Ceramic-Metal interfaces," J. Am. Ceram. Soc. 70 (1987) 352–355.

[28] J.S. Wang, P.M. Anderson, "Fracture behavior of embrittled F.C.C. metal bicrystals," Acta Metall. Mater. 39 (1991) 779–792.

[29] A. Bagchi, A.G. Evans, "The mechanics and physics of thin film decohesion and its measurement," Interface Sci. 3 (1996) 169–193.

[30] I.E. Reimanis, B.J. Dalgleish, A.G. Evans, "The fracture resistance of a model metal/ceramic interface," Acta Metall. Mater. 39 (1991) 3133–3141.

[31] G.E. Beltz, J.S. Wang, "Crack direction effects along copper/sapphire interfaces," Acta Metall. Mater. 40 (1992) 1675–1683.

[32] N.P. O'Dowd, M.G. Stout, C.F. Shih, "Fracture toughness of alumina- niobium interfaces : Experiments and analyses," Philos. Mag. 66 (1992) 1037–1064.

[33] G. Elssner, D. Korn, M. Rühle, "The influence of interface impurities on fracture energy of UHV diffusion bonded metal-ceramic bicrystals," Scr. Metall. Mater. 31 (1994) 1037–1042.

[34] D. Korn, G. Elssner, R.M. Cannon, M. Rühle, "Fracture properties of interfacially doped Nb-Al2O3 bicrystals: I, fracture characteristics," Acta Mater. 50 (2002) 3881–3901.

[35] N.A. Fleck, G.M. Muller, M.F. Ashby, J.W. Hutchinson, "Strain gradient plasticity: Theory and experiment," Acta Metall. Mater. 42 (1994) 475–487.

[36] W.D. Nix, H. Gao, "Indentation size effects in crystalline materials: A law for strain gradient plasticity," J. Mech. Phys. Solids. 46 (1998) 411–425.

[37] J.S. Stölken, A.G. Evans, "A microbend test method for measuring the plasticity length scale," Acta Mater. 46 (1998) 5109–5115.

[38] T. V. Mathew, S. Natarajan, E. Martínez-Pañeda, "Size effects in elastic-plastic functionally graded materials," Compos. Struct. 204 (2018) 43–51.

[39] Y. Wei, J.W. Hutchinson, "Models of interface separation accompanied by plastic dissipation at multiple scales," Int. J. Fract. 95 (1999) 1–17.

[40] E. Martínez-Pañeda, V.S. Deshpande, C.F. Niordson, N.A. Fleck, "The role of

plastic strain gradients in the crack growth resistance of metals," J. Mech. Phys. Solids. 126 (2019) 136–150.

[41]   E. Martínez-Pañeda, N.A. Fleck, "Mode I crack tip fields: Strain gradient plasticity theory versus J2 flow theory," Eur. J. Mech. A/Solids. 75 (2019) 381–388.

[42]   T.L. Anderson, Fracture Mechanics, 2005.

[43]   H. Gao, Y. Huang, W.D. Nix, J.W. Hutchinson, "Mechanism-based strain gradient plasticity - I. Theory," J. Mech. Phys. Solids. 47 (1999) 1239–1263.

[44]   N.A. Fleck, J.W. Hutchinson, "A phenomenological theory for strain gradient effects in plasticity," J. Mech. Phys. Solids. 41 (1993) 1825–1857.

[45]   N.A. Fleck, J.W. Hutchinson, "Strain Gradient Plasticity," Adv. Appl. Mech. 33 (1997) 295–361.

[46]   N.A. Fleck, J.W. Hutchinson, "A reformulation of strain gradient plasticity," J. Mech. Phys. Solids. 49 (2001) 2245–2271.

[47]   Y. Huang, S. Qu, K.C. Hwang, M. Li, H. Gao, "A conventional theory of mechanism-based strain gradient plasticity," 20 (2004) 753–782.

[48]   E.C. Aifantis, "On the Microstructural Origin of Certain Inelastic Models," J. Eng. Mater. Technol. 106 (1984) 326–330.

[49]   P. Gudmundson, "A unified treatment of strain gradient plasticity," J. Mech. Phys. Solids. 52 (2004) 1379–1406.

[50]   M.E. Gurtin, L. Anand, "A theory of strain-gradient plasticity for isotropic , plastically irrotational materials . Part I : Small deformations," J. Mech. Phys. Solids. 53 (2005) 1624–1649.

[51]   M.E. Gurtin, "A gradient theory of small-deformation isotropic plasticity that accounts for the Burgers vector and for dissipation due to plastic spin," J. Mech. Phys. Solids. 52 (2004) 2545–2568.

[52]   L. Bardella, A. Panteghini, "Modelling the torsion of thin metal wires by distortion gradient plasticity," J. Mech. Phys. Solids. 78 (2015) 467–492.

[53]   L.H. Poh, R.H.J. Peerlings, "The plastic rotation effect in an isotropic gradient plasticity model for applications at the meso scale," Int. J. Solids Struct. 78–79 (2016) 57–69.

[54] E. Martínez-Pañeda, C.F. Niordson, L. Bardella, "A finite element framework for distortion gradient plasticity with applications to bending of thin foils," Int. J. Solids Struct. 96 (2016) 288–299.

[55] E. Martínez-Pañeda, C. Betegón, "Modeling damage and fracture within strain-gradient plasticity," Int. J. Solids Struct. 59 (2015) 208–215.

[56] R.O. Ritchie, J.F. Knott, J.R. Rice, "On the relationship between critical tensile stress and fracture toughness in mild steel," J. Mech. Phys. Solids. 21 (1973) 395–410.

[57] D.A. Curry, J.F. Knott, "Effect of microstructure on cleavage fracture toughness of quenched and tempered steels," Met. Sci. 13 (1979) 341–345.

[58] A.G. Evans, "Statistical Aspects of Cleavage Fracture in Steel," Metall. Trans. 14A (1983) 1349–1355.

[59] T. Lin, A.G. Evans, R.O. Ritchie, "A statistical model of brittle fracture by transgranular cleavage," J. Mech. Phys. Solids. 34 (1986) 477–497.

[60] K. Wallin, T. Saario, K. Törrönen, "Statistical model for carbide induced brittle fracture in steel," Met. Sci. 18 (1984) 13–16.

[61] W. Weibull, "A Statistical Distribution Function of Wide Applicability," J. Od Appl. Mech. 18 (1953) 293–297.

[62] F.M. Beremin, "A Local Criterion for Cleavage Fracture of a Nuclear Pressure Vessel Steel," Metall. Trans. A. 14 (1983) 2277–2287.

[63] M. Muñiz-Calvente, A. Fernández Canteli, V. Shlyannikov, E. Castillo, "Probabilistic Weibull Methodology for Fracture Prediction of Brittle and Ductile Materials," Appl. Mech. Mater. 784 (2015) 443–451.

[64] M. Muñiz-Calvente, A. Ramos, V. Shlyannikov, M.J. Lamela, A. Fernández-Canteli, "Hazard maps and global probability as a way to transfer standard fracture results to reliable design of real components," Eng. Fail. Anal. 69 (2016) 135–146.

[65] M. Muniz-Calvente, A. Ramos, F. Pelayo, M.J. Lamela, A. Fernández-Canteli, "Statistical joint evaluation of fracture results from distinct experimental programs: An application to annealed glass," Theor. Appl. Fract. Mech. 85 (2016) 149–157.

[66] G. Francfort, J.J. Marigo, "Revisiting brittle fracture as an energy minimization problem," J. Mech. Phys. Solids. 46 (1998) 1319–1342.

[67] B. Bourdin, G.A. Francfort, J.J. Marigo, "Numerical experiments in revisited brittle fracture," J. Mech. Phys. Solids. 48 (2000) 797–826.

[68] C. Miehe, F. Aldakheel, A. Raina, "Phase field modeling of ductile fracture at finite strains: A variational gradient-extended plasticity-damage theory," Int. J. Plast. 84 (2016) 1–32.

[69] P.K. Kristensen, E. Martínez-Pañeda, "Phase field fracture modelling using quasi-Newton methods and a new adaptive step scheme," Theor. Appl. Fract. Mech. 107 (2020) 102446.

[70] M.J. Borden, T.J.R. Hughes, C.M. Landis, I.J. Lee, "A phase-field formulation for fracture in ductile materials: Finite deformation balance law derivation , plastic degradation , and stress triaxiality effects," Comput. Methods Appl. Mech. Engrg. 312 (2016) 130–166.

[71] Z.A. Wilson, C.M. Landis, "Phase-field modeling of hydraulic fracture," J. Mech. Phys. Solids. 96 (2016) 264–290.

[72] Hirshikesh, S. Natarajan, R.K. Annabattula, E. Martínez-Pañeda, "Phase field modelling of crack propagation in functionally graded materials," Compos. Part B Eng. 169 (2019) 239–248.

[73] Hirshikesh, E. Martínez-Pañeda, S. Natarajan, "Adaptive phase field modelling of crack propagation in orthotropic functionally graded materials," Def. Technol. (2020).

[74] W. Mai, S. Soghrati, "A phase field model for simulating the stress corrosion cracking initiated from pits," Corros. Sci. 125 (2017) 87–98.

[75] E. Martínez-Pañeda, A. Golahmar, C.F. Niordson, "A phase field formulation for hydrogen assisted cracking," Comput. Methods Appl. Mech. Eng. 342 (2018) 742–761.

[76] P.K. Kristensen, C.F. Niordson, E. Martínez-Pañeda, "A phase field model for elastic-gradient-plastic solids undergoing hydrogen embrittlement," J. Mech. Phys. Solids. 143 (2020).

[77] E. Martínez-Pañeda, Z.D. Harris, S. Fuentes-Alonso, J.R. Scully, J.T. Burns, "On

the suitability of slow strain rate tensile testing for assessing hydrogen embrittlement susceptibility," Corros. Sci. 163 (2020) 108291.

[78] J. Hicks, Brittle fracture, in: Welded Jt. Des., 1999: pp. 116–122.

[79] W. H. Johnson, "On Some Remarkable Changes Produced in Iron and Steel by the Action of Hydrogen and Acids," Proc. R. Soc. London. 23 (1875) 168–179.

[80] J.P. Hirth, "Effects of hydrogen on the properties of iron and steel," Metall. Trans. A. 11 (1980) 861–890.

[81] S. del Busto, C. Betegón, E. Martínez-Pañeda, "A cohesive zone framework for environmentally assisted fatigue," Eng. Fract. Mech. 185 (2017) 210–226.

[82] R.D. Kane, "Slow strain rate testing for the evaluation of environmentally induced cracking: research and engineering applications," (1993).

[83] G. M. Ugiansky, J.H. Payer, "ASTM STP 665: Stress Corrosion Cracking: The Slow Strain-Rate Technique," (1979).

[84] N. Henry Holroyd, T.L. Burnett, B.C. Palmer, J.J. Lewandowski, "Estimation of environment-induced crack growth rate as a function of stress intensity factors generated during slow strain rate testing of aluminum alloys," Corros. Rev. (2019) 6–13.

[85] N.J.H. Holroyd, T.L. Burnett, M. Seifi, J.J. Lewandowski, "Improved understanding of environment-induced cracking (EIC) of sensitized 5XXX series aluminium alloys," Mater. Sci. Eng. A. 682 (2017) 613–621.

[86] J. Ai, H.M. Ha, R.P. Gangloff, J.R. Scully, "Hydrogen diffusion and trapping in a precipitation-hardened nickel – copper – aluminum alloy Monel K-500 (UNS N05500)," 61 (2013) 3186–3199.

[87] A.M. Brass, A. Chanfreau, "Accelerated diffusion of hydrogen along grain boundaries in nickel," 44 (1996) 3823–3831.

[88] J. Yao, J.R. Cahoon, "Experimental studies of grain boundary diffusion of hydrogen in metals," 39 (1991) 119–126.

[89] D.M. Doyle, G. Palumbo, K.T. Aust, A.M. El-Sherik, U. Erb, "The influence of intercrystalline defects on hydrogen activity and transport in nickel," Acta Metall. Mater. 43 (1995) 3027–3033.

[90] D. Di Stefano, M. Mrovec, C. Elsässer, "First-principles investigation of hydrogen trapping and diffusion at grain boundaries in nickel," ACTA Mater. 98 (2015) 306–312.

[91] X.W. Zhou, R. Dingreville, R.A. Karnesky, "Molecular dynamics studies of irradiation effects on hydrogen isotope diffusion through nickel crystals and grain boundaries," Phys. Chem. Chem. Phys. 20 (2017) 520–534.

[92] B. Osman Hoch, A. Metsue, J. Bouhattate, X. Feaugas, "Effects of grain-boundary networks on the macroscopic diffusivity of hydrogen in polycrystalline materials," Comput. Mater. Sci. 97 (2015) 276–284.

[93] L. Zhu, J. Zhou, H. Yang, Z. Sun, "Energetics and kinetics of hydrogen at the grain boundary of the Ni alloys   : A first-principles study," J. Alloys Compd. 795 (2019) 343–350.

[94] A. Kimura, H.K. Birnbaum, "On the kinetics of intergranular embrittlement of nickel by hydrogen transport from the external surface," Scr. Metall. 21 (1987) 219–222.

[95] M. Henthorne, "The Slow Strain Rate Stress Corrosion Cracking Test - a 50 Year Retrospective," Corrosion. 72 (2016) 1488–1518.

[96] E. Martínez-Pañeda, S. Fuentes-Alonso, C. Betegón, "Gradient-enhanced statistical analysis of cleavage fracture," Eur. J. Mech. A/Solids. 77 (2019) 103785.

[97] A. Pineau, A.A. Benzerga, T. Pardoen, "Failure of metals I: Brittle and ductile fracture," Acta Mater. 107 (2016) 424–483.

[98] X. Qian, S. Zhang, S. Swaddiwudhipong, "Calibration of Weibull parameters using the conventional mechanism-based strain gradient plasticity," Eng. Fract. Mech. 78 (2011) 1928–1944.

[99] G. Papazafeiropoulos, M. Muñiz-Calvente, E. Martínez-Pañeda, "Abaqus2Matlab: A suitable tool for finite element post-processing," Adv. Eng. Softw. 105 (2017) 9–16.

[100] E. Martínez-Pañeda, S. Natarajan, S. Bordas, "Gradient plasticity crack tip characterization by means of the extended finite element method," Comput. Mech. 59 (2017) 831–842.

[101] J. Heerens, D. Hellmann, "Development of the Euro fracture toughness dataset,"

Eng. Fract. Mech. 69 (2002) 421–449.

[102] S. Fuentes-Alonso, E. Martínez-Pañeda, "Fracture in distortion gradient plasticity," (Submitted). (2020) 1–60.

[103] L. Bardella, A. Giacomini, "Influence of material parameters and crystallography on the size effects describable by means of strain gradient plasticity," J. Mech. Phys. Solids. 56 (2008) 2906–2934.

[104] L. Bardella, "A comparison between crystal and isotropic strain gradient plasticity theories with accent on the role of the plastic spin," Eur. J. Mech. A/Solids. 28 (2009) 638–646.

[105] L. Bardella, "Size effects in phenomenological strain gradient plasticity constitutively involving the plastic spin," Int. J. Eng. Sci. 48 (2010) 550–568.

[106] E. Bittencourt, A. Needleman, M.E. Gurtin, E. Van der Giessen, "A comparison of nonlocal continuum and discrete dislocation plasticity predictions," J. Mech. Phys. Solids. 51 (2003) 281–310.

[107] E. Martínez-Pañeda, C.F. Niordson, "On fracture in finite strain gradient plasticity," Int. J. Plast. 80 (2016) 154–167.

[108] S. Qu, Y. Huang, H. Jiang, C. Liu, P.D. Wu, K.C. Hwang, "Fracture analysis in the conventional theory of mechanism-based strain gradient (CMSG) plasticity," Int. J. Fract. 129 (2004) 199–220.

- ARTÍCULO 1-

ON THE SUITABILITY OF SLOW STRAIN RATE
TENSILE TESTING FOR ASSESSING HYDROGEN
EMBRITTLEMENT SUSCEPTIBILITY

Autores: E. Martínez-Pañeda, Z. Harris, S. Fuentes-Alonso, J.R. Scully, J.T. Burns

On the suitability of slow strain rate tensile testing for assessing hydrogen embrittlement susceptibility

Emilio Martínez-Pañeda[a],*, Zachary D. Harris[b], Sandra Fuentes-Alonso[c], John R. Scully[b], James T. Burns[b]

[a] *Department of Civil and Environmental Engineering, Imperial College London, London SW7 2AZ, UK*
[b] *Department of Materials Science and Engineering, University of Virginia, Charlottesville, VA 22904, USA*
[c] *Department of Construction and Manufacturing Engineering, University of Oviedo, Gijón 33203, Spain*

ABSTRACT

The onset of sub-critical crack growth during slow strain rate tensile testing (SSRT) is assessed through a combined experimental and modeling approach. A systematic comparison of the extent of intergranular fracture and expected hydrogen ingress suggests that hydrogen diffusion alone is insufficient to explain the intergranular fracture depths observed after SSRT experiments in a Ni–Cu superalloy. Simulations of these experiments using a new phase field formulation indicate that crack initiation occurs as low as 40% of the time to failure. The implications of such sub-critical crack growth on the validity and interpretation of SSRT metrics are then explored.

1. Introduction

Hydrogen (H)-induced, premature failure of structural metals undermines decades of metallurgical optimization, compromises structural integrity frameworks, and negatively affects industries spanning the aerospace, marine, transportation, and energy sectors [1–4]. While the microscale mechanism(s) governing the H-embrittlement (HE) phenomenon continue to be debated [3–7], it is universally recognized that HE must be explicitly accounted for when designing components that will be exposed to H-containing/producing environments and processes [8]. Historically, the susceptibility of structural metals to environment-assisted cracking (EAC; such as HE) has been assessed *via* a diverse array of experimental protocols[1] (e.g. NACE MR0175 [10], NACE TM0198 [11], ASTM G30 [12], ASTM G39 [13], ASTM G129 [14], ASTM E1681 [15], ASTM F1624 [16], and ISO 7539-7 [17]), which are then utilized to inform a "go/no-go" decision regarding material selection. Specifically, if the evaluated material is found to exhibit susceptibility below an empirically defined 'threshold' parameter level for a given environment/loading combination [18], then the material is generally considered immune to EAC for the lifetime of the component.

The most commonly employed experiment for the assessment of EAC susceptibility is the slow strain rate test (SSRT), as demonstrated by two ASTM STP collections being dedicated to the method [19,20] and its documented use in > 40% of EAC-related publications [21]. The SSRT experimental protocol is codified in the ASTM G129 [14], NACE TM0198 [11], and ISO 7359-7 [17] standards, and can be broadly described as a tensile experiment conducted using a slow, but constant extension rate (which typically yields an initial strain rate $< 10^{-5}\,\text{s}^{-1}$) while the specimen is exposed to the environment of interest [18,21,22]. Numerous changes to this basic framework have been employed in the literature [14,21]. For example, specimens may be (1) exposed to the environment prior to testing (*i.e.* pre-exposed or pre-charged) and/or during the experiment (*in situ*), (2) smooth or notched, (3) cyclically loaded prior to monotonic testing to generate a 'fatigue pre-crack', and (4) modified to include specific features of interest (coatings [23], different microstructural zones induced by welding [24,25], tubular cross-sections [26], etc.). Metrics of interest depend on the specimen geometry [21], with reduction in area (*i.e.* ductility; also assessed *via* strain-to-failure), fracture stress, and time-to-failure quantified for smooth specimens, while notch tensile strength and time-to-failure are typically evaluated for notched specimens.

The primary advantages of the SSRT approach are the simplicity and modularity of the experimental setup, the reduced cost relative to fracture mechanics-based approaches, and the reasonable test duration relative to static testing approaches [21,27]. Specifically, by virtue of

---

* Corresponding author.
  E-mail address: mail@empaneda.com (E. Martínez-Pañeda).
[1] For a complete listing of pertinent standards, see Ref. [9].

the specimen being strained to failure, the SSRT approach avoids specifying a time for test completion, which is often a source of criticism for constant displacement and constant load-based testing strategies [27]. However, there are several complications that affect the efficacy of the SSRT method [18,22,27,28]. First, the results of SSRT experiments have been reported to inadequately compare with in-service performance, with separate reports indicating that SSRT results are either overly conservative or not sufficiently conservative [18,27]. This limitation is explicitly incorporated into ASTM G129 [14], which states that SSRT "results are not intended to necessarily represent service performance" and that the test method is only meant to act as a screening process to identify susceptible materials. These challenges in assessing susceptibility relative to in-service conditions are further complicated by the significant scatter in obtained SSRT metrics [28,29]. Second, depending on the environment of interest, SSRT metrics have been shown to be strongly dependent on testing variables and specimen geometry. In particular, SSRT results have been found to be affected by the applied displacement rate [30–32], the specimen surface finish [26,28,33], and the specimen diameter [30]. For example, McIntyre noted that a slight change in strain rate from 4.0×10^{-6} to $3.5 \times 10^{-6}\,\mathrm{s^{-1}}$ resulted in a 14% decrease in time to failure for testing in a simulated sour gas environment (alloy not specified) [30]. Lastly, and perhaps most critically, if sub-critical crack growth (*i.e.* growth of one or multiple cracks that does not immediately lead to failure) occurs during the SSRT experiment, then the applied remote stress (or nominal net-section stress if the sample is notched) is no longer representative of the operative mechanical driving force (which would instead be described by a *stress intensity* [34,35]). Clear experimental evidence of such crack growth has been documented by Holroyd and coworkers in 5xxx-series Al alloys [35–37]. This sub-critical crack growth will also obfuscate the physical meaning of other traditional SSRT metrics, such as time to failure and elongation. For example, the time to failure under such a scenario would be comprised of both the time for crack initiation and crack propagation [26]. However, despite significant evidence of sub-critical cracking in the SSRT literature [26,35–41], studies that systematically assess (1) the onset of sub-critical cracking during SSRT experiments and (2) the implications of such cracking on the interpretation of SSRT metrics are limited.

The objective of this study is to provide evidence that sub-critical crack growth can occur during typical SSRT experiments and then inform the possible implications of this crack growth on the interpretation of SSRT results. Recent efforts examining the H environment-assisted cracking (HEAC) behavior of a peak-aged Ni–Cu superalloy, Monel K-500, using both SSRT and linear elastic fracture mechanics (LEFM)-based approaches offers a well-characterized platform to assess such effects [42,43]. The potential onset of sub-critical crack growth prior to failure during SSRT testing is evaluated based on systematic comparisons between expected H diffusion distances and the extent of intergranular cracking on the fracture surface of SSRT specimens. Based on this evidence, the time for crack initiation is estimated using an experimentally-calibrated phase field model for H-induced cracking. The results of these calculations are then utilized to discuss how the interpretation of SSRT metrics could be compromised by this sub-critical cracking phenomenon and to inform possible testing strategies to avoid this experimental complication.

2. Experimental methods

2.1. Materials

Monel K-500 is a precipitation-hardened, Ni-base alloy nominally comprised of a face-centered cubic (fcc) Ni–Cu solid solution (γ) matrix and a homogeneous distribution of highly coherent (< 0.1 pct misfit strain), intermetallic γ′ (Ni$_3$(Al,Ti)) precipitates [44–47]. The γ′ precipitates have an ordered Ll$_2$ structure composed of Ni atoms at the faces and Al (or Ti) atoms on the corners of the unit cell [44,47]. Due to the low misfit and interfacial energy anisotropy between the γ and γ′ phases, the precipitates form as spherical particles [44]. Two types of carbides have been observed in Monel K-500: a heterogeneous distribution of MC-type carbides (typically TiC) in the γ matrix and isolated M$_{23}$C$_6$-type carbides (where M: Cr, Mn, Fe, or Ni) on grain boundaries [44]. Regarding the former, literature indicates that the TiC distribution does not appreciably change under typical aging conditions for Monel K-500 [48] and that their contribution to the strength of Monel K-500 is minimal [44].

Four Monel K-500 material heats were evaluated in this study. One heat (termed Allvac) was supplied by Allegheny Technologies Incorporated and underwent the following aging protocol: direct aging at 593 °C (866 K) for 16 h, followed by a furnace cool at 14 °C/h to 482 °C (755 K) and then air cooling. A second heat (termed TR2) was harvested from an engineering component after exposure to a marine environment for 10-15 years; the exact heat treatment and exposure time/conditions are not known for this material heat. However, in order to enter service, the material heat was required to pass the QQ-N-286G federal procurement specification [49], which mandates heat-treating to the near-peak aged condition. The final heats, supplied by the U.S. Naval Research Laboratory, were heat-treated [50] to obtain the lower and upper bound strengths possible under the QQ-N-286G federal specification [49]; denoted as NRL LS (low strength) and NRL HS (high strength), respectively. NRL LS and NRL HS were received in the form of 10.16-cm and 11.29-cm diameter barstock and then thermomechanically processed as follows [50]. NRL LS was hot rolled, continuously annealed at 982 °C (1255 K) followed by water quench, rotatory straightened, rough turned (6.35 mm removed from diameter), 3-point straightened, and then aged at 593 °C (866 K) for 2 h, followed by a furnace cool to 482 °C (755 K) at 55 °C/h and then air cool. The NRL HS was direct-aged at 593 °C (866 K) for 16 h, furnace cooled at 14 °C/h up to 538 °C (811 K), held for 1 h then furnace cooled at 14 °C/h to 482 °C (755 K), held for 1 h, and then air cooled. The bulk and trace composition for each material heat are given in Table 1.

Uniaxial tension tests are conducted to characterize the elastic-plastic response of each material heat. The experimental results are then fitted to a Ramberg–Osgood power law hardening relationship [34], as

$$\varepsilon = \frac{\sigma}{E} + \alpha \frac{\sigma}{E} \left(\frac{\sigma}{\sigma_Y} \right)^n \tag{1}$$

where E is Young's modulus, σ_Y is the yield stress, n is the strain hardening exponent and α is the Ramberg–Osgood hardening parameter. The values measured are reported in Table 2, along with the average grain size for each material heat.

Table 1
Composition of evaluated Monel K-500 material heats.

Heat	Ni	Cu	Al	Fe	Mn	Si	Ti	C	S	P	Sn	Pb	Mg	Zr
	Weight percent (wt.%)								Weight parts per million (wppm)					
Allvac	66.12	28.57	2.89	0.80	0.81	0.08	0.45	0.17	1.6	92	2.4	2.1	39	370
TR2	64.66	30.15	2.73	0.69	0.73	0.09	0.45	0.20	11.0	71	6.9	2.5	130	330
NRL LS	63.06	30.67	3.46	1.27	0.78	0.08	0.47	0.14	0.92	56	1.4	4.8	210	230
NRL HS	63.44	30.74	3.20	0.91	0.85	0.10	0.57	0.14	17.0	40	2.2	3.5	40	650

Table 2
Material properties.

Heat	E (GPa)	ν	σ_Y (MPa)	n	α	Avg. grain size (μm)
Allvac	180	0.3	794.3	20	0.39	13.8
TR2	202	0.3	795	22	0.385	35.3
NRL LS	198	0.3	715.7	21	0.5	22.5
NRL HS	191	0.3	910.1	18	0.405	11.2

Table 3
Diffusible hydrogen concentration $C_{H,Diff}$ (in wppm) for each Monel K-500 heat versus applied potential E_A.

Heat	$E_A = -850\,\text{mV}$	$E_A = -950\,\text{mV}$	$E_A = -1100\,\text{mV}$
Allvac	1.9	4.1	7.5
TR2	3.7	18.6	26.2
NRL LS	1.3	4.7	18.3
NRL HS	4.7	11.9	23.4

The diffusible H concentration, $C_{H,Diff}$, for each tested material heat was previously assessed using electrochemical extraction [42,51]. Briefly, these electrochemical extraction measurements were completed on samples that were pre-charged for 10 days at potentials ranging from -0.7 to $-1.2\,V_{SCE}$ in 0.6 M NaCl with pH adjusted to 8.0 using NaOH. Extraction measurements were taken immediately after H charging *via* H oxidation at -0.85 V versus mercury–mercury sulfate electrode (MMSE) in deaerated borate buffer at pH 10 under ambient temperature conditions [51]. For additional details of the experimental procedure for obtaining $C_{H,Diff}$, see Refs. [42,51]. The values of $C_{H,Diff}$ measured for each material heat are given as a function of the applied potential E_A in Table 3.

2.2. Slow strain-rate testing and characterization

The SSRT experiments modeled in this study were completed using a Cortest, Inc. servo-electric mechanical frame operated at an average cross-head speed of 6×10^{-6} mm/s. Some subtle variations in the cross-head speed were noted across the test matrix (range was $4–8 \times 10^{-6}$ mm/s), but the cross-head speed within a given test was observed to be nominally constant. The cylindrical SSRT specimens were machined with a circumferential notch with dimensions shown in Fig. 1. SSRT testing was completed with the specimen fully immersed in deaerated 0.6 M NaCl (pH of 5.5–6.0) at 25 °C using a cylindrical Plexiglass cell. For each SSRT experiment, the specimen was baked at 450 °C for 48 h to remove any residual H and then placed within the testing cell. Then, prior to the onset of straining, each specimen was pre-charged with H at the testing potential for 48 h using a three-electrode setup, with a Pt mesh as the counter electrode, the specimen as the working electrode, and a saturated calomel electrode (SCE) as the reference electrode. It should be noted that this charging time was not sufficient to achieve H saturation across the specimen thickness, regardless of the applied potential. Each material heat was tested at three applied potentials (-0.95, -1.0, and $-1.1\,V_{SCE}$) and the potential for a given experiment was also applied throughout the duration of the SSRT. It should be understood that the use of a constant applied
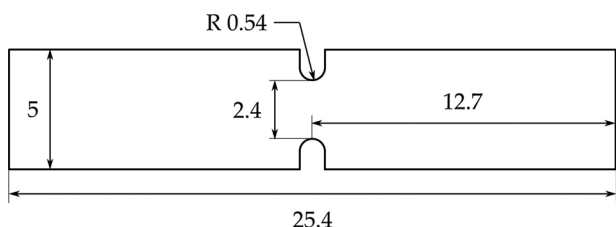

Fig. 1. Dimensions (in mm) of the specimens tested.

potential results in a fixed H surface coverage, which is in equilibrium with the lattice H concentration. This lattice H concentration in turn determines the diffusible H concentration that participates in the H-induced fracture process [52]. Comparison SSRT experiments were completed in laboratory air; these samples were also baked prior to straining for 48 h at 450 °C to ensure the removal of any residual H, but were not pre-charged with H. Additional details of the SSRT experiments are presented elsewhere [42].

Overview fractography was captured for each specimen using a FEI Quanta 650 FEG scanning electron microscope (SEM) after test completion to quantify the extent of intergranular cracking on the fracture surface. From these images, the 2D area of the fracture surface containing evidence of ductile failure was measured using the ImageJ software package and then utilized to calculate an effective ductile area radius. As the ductile region occurred in the center of the SSRT specimen, the intergranular crack penetration distance can then be approximated by subtracting this effective radius from the total radius of the specimen.

3. Numerical model

Hydrogen transport towards the notch tip and subsequent cracking are investigated by means of a coupled deformation–diffusion-phase field fracture finite element framework. The implementation follows the recent work by Martínez-Pañeda *et al.* [53], and extends it to account for the role of plasticity by means of J_2 flow theory. For simplicity, we choose to neglect the stress elevation associated with plastic strain gradients, which is notably less prominent in notches than in cracks [54,55]. However, gradient effects become relevant with crack advance and play an important role in understanding crack growth from existing sub-micron flaws [56]; the implications of adopting conventional plasticity theory will be subsequently discussed in the context of the results.

3.1. Phase field fracture of embrittled elastic–plastic solids

Consider an elastic–plastic solid occupying the domain Ω with a discontinuous surface Γ. The fracture resistance of the solid is characterized by a critical fracture energy G_0, which is a macroscopic variable, akin to the fracture toughness, and can be employed to phenomenologically capture any damage mechanism. In the limiting case of an ideally brittle solid, G_0 corresponds to the Griffith critical energy release rate. As Monel K-500 exhibits predominantly intergranular fracture in the presence of H [42,43,52,57–61], it is assumed that G_0 is dependent on the H coverage at the grain boundary θ, which can be related to the bulk H concentration C through the Langmuir–McLean isotherm:

$$\theta = \frac{C}{C + \exp(-\Delta g_b^0 / RT)} \tag{2}$$

Here, C is given in units of impurity mol fraction, R is the universal gas constant, T is the temperature, and Δg_b^0 is the binding energy for the impurity at the site of interest. We follow Serebrinsky *et al.* [62] and assume $\Delta g_b^0 = 30$ kJ/mol for H trapped at a grain boundary. While it is anticipated that variations in grain boundary character will give rise to a distribution of trap binding energies, the use of 30 kJ/mol in the current study as an average value for H trapped at grain boundaries is justified based on experimental and computational studies [63–65]. Assuming that H linearly degrades the fracture energy, the variation in G_0 with grain boundary H coverage can be defined as:

$$G_0(\theta) = (1 - \chi\theta)G_0(0) \tag{3}$$

where χ is the H damage coefficient, which describes the potency of a unit coverage of H in degrading the fracture resistance of a material. This parameter may be calibrated with experimental data or connected with variables characterizing the underlying physical mechanism(s).

For example, in the case of H-enhanced grain boundary decohesion, it can be inferred from atomistic calculations. The assumption of a linear degradation is supported by recent density function theory (DFT) analyses of H-induced decohesion in nickel, which observed a linear decrease in the surface energy with increasing H coverage [66].

Under the phase field formulation, the discrete crack is approximated *via* the phase field ϕ, which is an auxiliary parameter that resembles the concept of a scalar damage variable in continuum damage mechanics. The phase field order parameter varies from 0 to 1, with $\phi = 0$ describing an intact material and $\phi = 1$ indicating a completely damaged material. The size of the regularized crack surface is governed by the choice of a phase field model-inherent length scale, defined by ℓ. As shown by Γ-convergence, a regularized crack density functional $\Gamma_\ell(\ell, \phi)$ can then be defined, which converges to the functional of the discrete crack as $\ell \rightarrow 0$ [67]. As such, the fracture energy due to the creation of a crack can be approximated as a volume integral

$$\int_\Gamma G_0(C)\,\mathrm{d}\Gamma \approx \int_\Omega G_0(C)\Gamma_\ell(\ell, \phi)\,\mathrm{d}\Omega = \int_\Omega G_0(C)\left(\frac{1}{2\ell}\phi^2 + \frac{\ell}{2}|\nabla\phi|^2\right)\mathrm{d}V \tag{4}$$

This regularized description of the crack topology makes the problem suitable for numerical analysis and enables the capturing of complex crack topologies and trajectories, as well as fracture phenomena such as crack nucleation, branching, and coalescence [68].

The total potential energy of a cracked body can be obtained from the sum of the surface energy associated with the formation of a crack $\Psi^s(\phi, C)$ and the bulk energy $\Psi^b(\boldsymbol{u}, \phi)$, where $\boldsymbol{u}$ is the displacement field:

$$\Psi = \Psi^b(\boldsymbol{u}, \phi) + \Psi^s(\phi, C) = \int_\Omega [(1 - \phi)^2 \psi(\boldsymbol{u}) + G_0(C)\Gamma_\ell(\ell, \phi)]\mathrm{d}V \tag{5}$$

Here, the bulk energy is given by the strain energy density $\psi(\boldsymbol{u})$ of the elastic–plastic solid and a term accounting for the degradation of the stored energy with evolving damage. The strain energy density is additively decomposed into its elastic ψ^e and plastic ψ^p parts, such that $\psi = \psi^e + \psi^p$. In previous studies, see Ref. [53] and the works by Duda and co-workers [69,70], fracture was assumed to be driven purely by the elastic strain energy density. However, here we follow Miehe *et al.* [71] and consider, for the first time in the context of hydrogen embrittlement, the contributions from both the elastic and plastic strain energy densities. In addition, we choose not to define an explicit relation between the plastic yield condition and the damage variable. No plastic-damage coupling is typically defined in similar fracture models, such as cohesive zone approaches (see, for example, Refs. [72,73]).

The strain tensor $\boldsymbol{\varepsilon}$ is computed from the displacement field in the usual manner $\boldsymbol{\varepsilon} = \mathrm{sym}\,\nabla\boldsymbol{u}$ and additively decomposes into an elastic part $\boldsymbol{\varepsilon}^e$ and a plastic part $\boldsymbol{\varepsilon}^p$. The Cauchy stress tensor is defined as $\boldsymbol{\sigma} = \partial_\varepsilon\psi$. Taking the first variation of the total potential energy of the solid (Eq. (5)) with respect to $\boldsymbol{\varepsilon}$ and ϕ renders the weak form of the deformation-phase field fracture problem. Thus, in the absence of body forces and external tractions,

$$\int_\Omega \left\{(1 - \phi)^2\boldsymbol{\sigma}\colon \delta\boldsymbol{\varepsilon} - 2(1 - \phi)\delta\phi\,\psi + G_0(C)\left(\frac{\phi}{\ell}\delta\phi + \ell\nabla\phi\cdot\nabla\delta\phi\right)\right\}\mathrm{d}V = 0 \tag{6}$$

Upon making use of Gauss' divergence theorem, the following coupled field equations are obtained for any arbitrary value of the kinematic variables $\delta\boldsymbol{u}$ and $\delta\phi$,

$$(1 - \phi)^2\nabla\cdot\boldsymbol{\sigma} = \boldsymbol{0} \text{ in } \Omega$$

$$G_c(C)\left(\frac{\phi}{\ell} - \ell\Delta\phi\right) - 2(1 - \phi)\psi = 0 \text{ in } \Omega \tag{7}$$

It is important to note that the phase field length scale ℓ is the material parameter that governs the critical stress at which damage initiates, which can be shown as follows. Consider the homogeneous solution to a one dimensional linear elastic solid with Young's modulus

E subjected to a strain ε. The strain energy reads $\psi = E\varepsilon^2/2$ and the homogeneous phase field can be readily obtained from Eq. (7)b as

$$\phi = \frac{E\varepsilon^2\ell}{G_0(C) + E\varepsilon^2\ell} \tag{8}$$

Thus, the effective stress $\bar{\sigma} = (1 - \phi)^2\sigma$ reaches a maximum at

$$\bar{\sigma}_c = \left(\frac{27EG_0(C)}{256\ell}\right)^{1/2} \tag{9}$$

As such, for a finite ℓ, the phase field model resembles cohesive zone approaches, with the phase field length scale governing the size of the fracture process zone and the critical stress.

3.2. Hydrogen transport

Mass conservation requirements relate the rate of change of the H concentration C with the H flux $\boldsymbol{J}$ through the external surface as follows

$$\int_\Omega \frac{dC}{dt}\,\mathrm{d}V + \int_{\partial\Omega} \boldsymbol{J}\cdot\boldsymbol{n}\,\mathrm{d}S = 0 \tag{10}$$

The strong form of the balance equation can be readily obtained by making use of the divergence theorem and noting that the expression must hold for any arbitrary volume,

$$\frac{dC}{dt} + \nabla\cdot\boldsymbol{J} = 0 \tag{11}$$

For an arbitrary, suitably continuous, scalar field, δC, the variational statement Eq. (11) can be written as:

$$\int_\Omega \delta C\left(\frac{dC}{dt} + \nabla\cdot\boldsymbol{J}\right)\mathrm{d}V = 0 \tag{12}$$

Rearranging Eq. (12), and making use of the divergence theorem, the weak form of the balance equation can be obtained:

$$\int_\Omega \left[\delta C\left(\frac{dC}{dt}\right) - \boldsymbol{J}\cdot\nabla\delta C\right]\mathrm{d}V + \int_{\partial\Omega_q} \delta C q\,\mathrm{d}S = 0 \tag{13}$$

where $q = \boldsymbol{J}\cdot\boldsymbol{n}$ is the concentration flux exiting the body across $\partial\Omega_q$. The diffusion is driven by the gradient of the chemical potential $\nabla\mu$. Accordingly, the mass flux follows a linear Onsager relationship,

$$\boldsymbol{J} = -\frac{DC}{RT}\nabla\mu \tag{14}$$

where D is the diffusion coefficient (under typical H-charging conditions, this would be the trap-modified effective H diffusivity D_{eff}). The chemical potential of H in lattice sites is given by:

$$\mu = \mu^0 + RT\,\ln\frac{\theta_L}{1 - \theta_L} - \bar{V}_H\sigma_H \tag{15}$$

where μ^0 is the chemical potential in the standard case, θ_L is the occupancy of lattice sites, $\bar{V}_H$ is the partial molar volume of H in solid solution, and σ_H is the hydrostatic stress. By substituting Eq. (15) into Eq. (14), and considering the relation between θ_L and the site density N, $\theta_L = C/N$, the flux can be described as follows:

$$\boldsymbol{J} = -\frac{DC}{(1 - \theta_L)}\left(\frac{\nabla C}{C} - \frac{\nabla N}{N}\right) + \frac{D}{RT}C\bar{V}_H\nabla\sigma_H \tag{16}$$

Now, substituting Eq. (16) into Eq. (13), and assuming low occupancy ($\theta_L \ll 1$) and a constant interstitial site concentration ($\nabla N = 0$), the governing H transport equation becomes:

$$\int_\Omega \left[\delta C\left(\frac{1}{D}\frac{dC}{dt}\right) + \nabla\delta C\nabla C - \nabla\delta C\left(\frac{\bar{V}_H C}{RT}\nabla\sigma_H\right)\right]\mathrm{d}V = -\frac{1}{D}\int_{\partial\Omega_q} \delta C q\,\mathrm{d}S \tag{17}$$

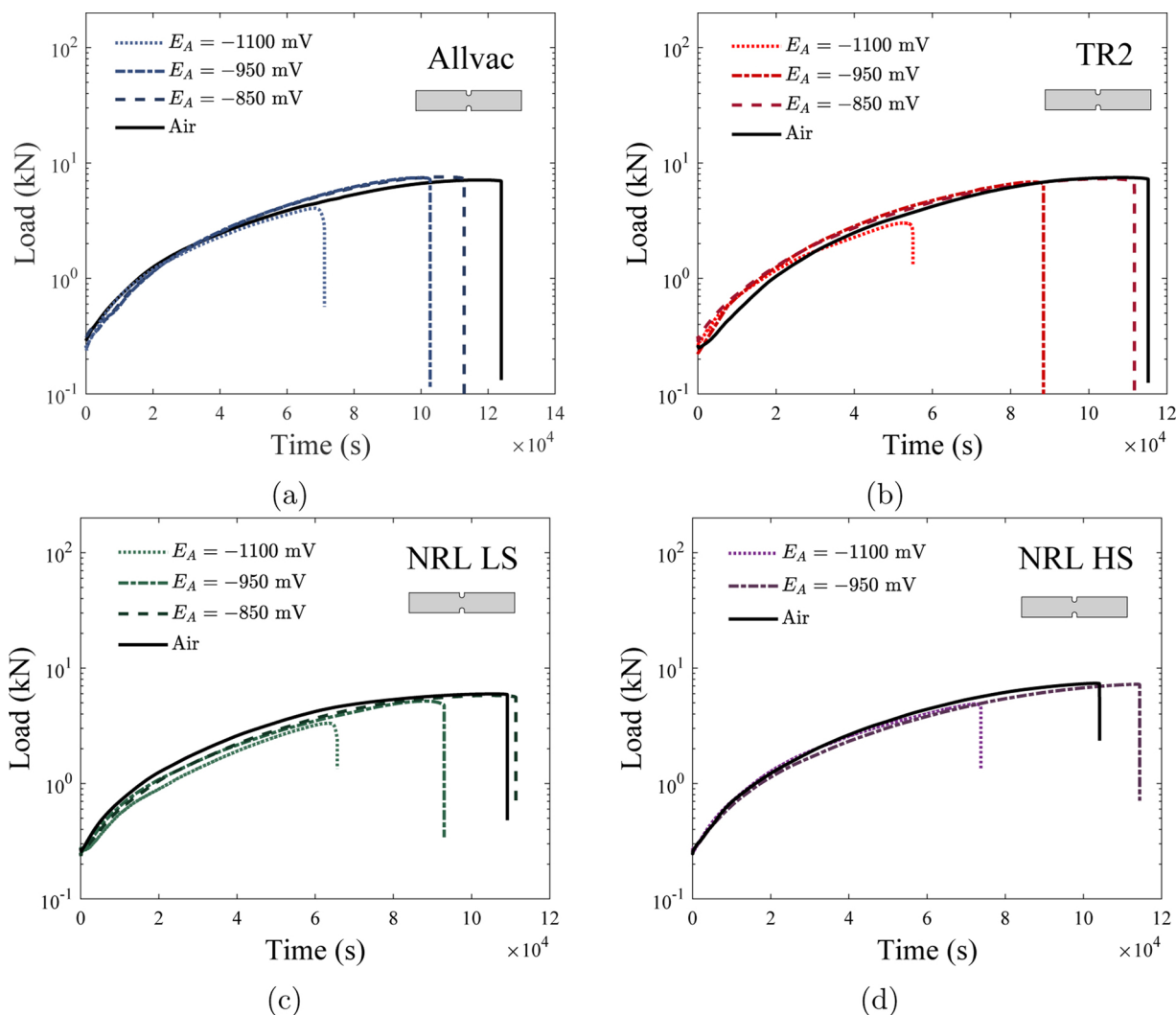Details of the coupling and the finite element implementation of the

Fig. 2. Experimental load versus time results as a function of applied potential for the four evaluated material heats of Monel K-500: (a) Allvac, (b) TR2, (c) NRL LS, and (d) NRL HS.

deformation–diffusion-fracture problem are given in Appendix A. Additionally, it is critical to accurately define the environmental conditions in the presence of a propagating crack. In the current study, a penalty approach is employed to capture how the electrochemical solution promptly occupies the space created with crack advance; details regarding implementation are provided in Appendix B.

4. Results

4.1. SSRT results and assessment of intergranular cracking depth as a function of applied potential and material heat

The force–time data obtained from each SSRT experiment as a function of applied potential for the four tested Monel K-500 material heats are shown in Fig. 2. Consistent with prior fracture mechanics-based testing of HEAC susceptibility in Monel K-500 [7,43,52,58], the time to failure was generally found to decrease across all tested material heats with increasingly negative applied potential; a similar trend was also noted for the applied load. As reported in prior work [42], all specimens exhibited intergranular fracture during testing at $-1100\,\mathrm{mV}_{SCE}$, though the center of the specimens failed *via* ductile microvoid coalescense. For potentials more positive than $-1100\,\mathrm{mV}_{SCE}$, the fracture morphology became increasingly different amongst the tested material heats. Specifically, neither Allvac or NRL HS contained

any evidence of intergranular fracture at -950 or $-850\,\mathrm{mV}_{SCE}$, TR2 had intergranular fracture at $-950\,\mathrm{mV}_{SCE}$, but not $-850\,\mathrm{mV}_{SCE}$, and NRL LS exhibited intergranular fracture at both -950 and $-850\,\mathrm{mV}_{SCE}$. Such heat-to-heat variations in apparent HEAC susceptibility as a function of applied potential are consistent with prior fracture mechanics-based evaluations of Monel K-500 [43].

To assess the extent of intergranular fracture penetration as a function of applied potential and material heat, overview fractographs were collected for each tested specimen. These images were then utilized to determine the effective radius of the central region where ductile fracture was observed, which was then subtracted from the specimen radius to identify the effective depth of intergranular fracture. An example fractograph, from NRL LS tested at $-1100\,\mathrm{mV}_{SCE}$, illustrating this procedure (with the ductile core region delineated by the red line) is shown in Fig. 3a, while the calculated depth of intergranular cracking as a function of material heat and applied potential are shown in Fig. 3b. The depth of intergranular fracture was found to increase with increasingly negative applied potentials, consistent with the increased HEAC susceptibility previously measured in fracture mechanics-based experiments under such conditions [43,52,58]. Interestingly, this depth of integranular penetration was found to appreciably vary across the tested material heats, with NRL LS and TR2 consistently exhibiting increased integranular fracture depths relative to NRL HS and Allvac. A representative, high magnification micrograph of the
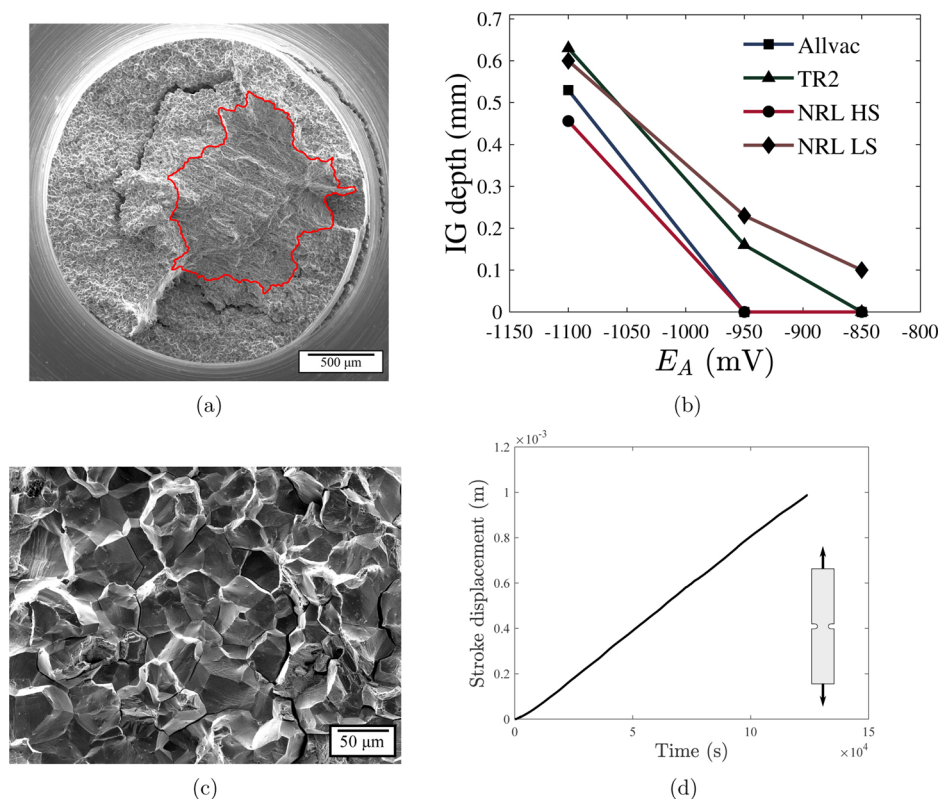
(a)

(b)

(c)

(d)

Fig. 3. (a) Overview micrograph of the fracture surface obtained for NRL LS tested at $-1100\,\text{mV}_{SCE}$ with the region exhibiting ductile fracture outlined by the red dashed line. From these images, the effective depth of intergranular cracking (b) was determined for each of the material heats as a function of applied potential. A representative, higher magnification micrograph from TR2 tested at $-1100\,\text{mV}_{SCE}$ of the observed intergranular fracture morphology in all tested Monel K-500 heats is shown in (c), while a representative stroke displacement versus time trace (d) taken from Allvac tested in air demonstrates the constancy of the cross-head speed during SSRT testing.

observed intergranular fracture morphology, taken from the TR2 specimen tested at $-1100\,\text{mV}_{SCE}$, is shown in Fig. 3c. Lastly, given the sensitivity of SSRT metrics to the applied strain rate [22], it is important to establish that the cross-head speed does not appreciably vary during SSRT experiments. As demonstrated by the observed stroke displacement as function of testing time for the Allvac specimen tested in laboratory air, shown in Fig. 3d, the cross-head speed throughout a given experiment was found to be nominally constant.

4.2. Comparison between integranular cracking depth and hydrogen diffusion distance

Examination of Fig. 3b shows that an intergranular fracture morphology was observed at depths ranging from approximately 0.45 to 0.65 mm for the four Monel K-500 material heats tested in 0.6 M NaCl at an applied potential of $-1100\,\text{mV}_{SCE}$. Such differences in the depth of intergranular fracture across the four material heats are consistent with the heat-to-heat variations in HEAC susceptibility observed in fracture mechanics-based testing of Monel K-500 [43]. These prior efforts also established that all evaluated heats of Monel K-500 failed *via* microvoid coalescence during inert environment testing, suggesting that H must be present for intergranular fracture to occur [43,52,58]. However, as addressed in detail below, non-negligible differences are found between the measured extent of intergranular cracking and the expected H diffusion distance.

The expected extent of H penetration into the specimen is assessed *via* several avenues. First, assuming one-dimensional diffusion, the extent of H diffusion into the SSRT specimen can be estimated from the material diffusion coefficient by the following equation:

$$d = 2\sqrt{D\,t_f} \tag{18}$$

where d is the diffusion distance[2] and t_f is the time over which H was allowed to diffuse. Based on the work of Scully and co-workers [42,51], the H diffusivity for the NRL HS material heat was measured as $D = 1.3 \times 10^{-10}\,\text{cm}^2/\text{s}$. Using this diffusivity and $t_f = 245,960\,\text{s}$ (based on a 48-h pre-charge and 20.3-h test duration), the expected diffusion distance of H is 0.113 mm, which is $\sim 4\times$ smaller than the experimentally observed intergranular crack depth for NRL HS tested at $-1100\,\text{mV}_{SCE}$ (0.45 mm).

The simple analytical approach captured by Eq. (18) neglects critical aspects of the experimental reality that will impact the diffusion behavior (e.g. 3D geometry and hydrostatic stress during loading [75]). As such, more rigorous finite element-based numerical analyses were performed to determine if higher levels of correspondence could be achieved by accounting for such complexities. The H concentration profiles predicted for each material heat are shown in Fig. 4. The results are obtained using the numerical framework described in Section 3 but in the absence of damage, $\phi = 0\ \forall\, \boldsymbol{x}$ throughout the numerical experiment. Circular points denote the predictions of a purely diffusion analysis (ignoring the notch-induced stress field) while a solid line represents the results obtained with the coupled mechanical-diffusion analysis. A nearly identical concentration profile is observed if the local notch-enhanced stress profile is accounted for in the numerical simulation. The limited effect of the hydrostatic stress was not unexpected given the reduced triaxiality associated with a blunt notch, as compared to a sharp crack tip where strong effects of stress are observed on the diffusion behavior [55,76]. In all material heats, the model results show

---

[2] It should be noted that the diffusion distance predicted by Eq. (18) does not calculate the full extent of H diffusion, but instead represents the distance from the surface where the concentration ratio $C/C_b = 1 - \text{erf}(1) \approx 0.157$ will be located after t_f [74]. However, the quantity of $2\sqrt{Dt_f}$ is commonly considered a characteristic quantity for diffusion distance and is therefore utilized as a first-order approximation herein.
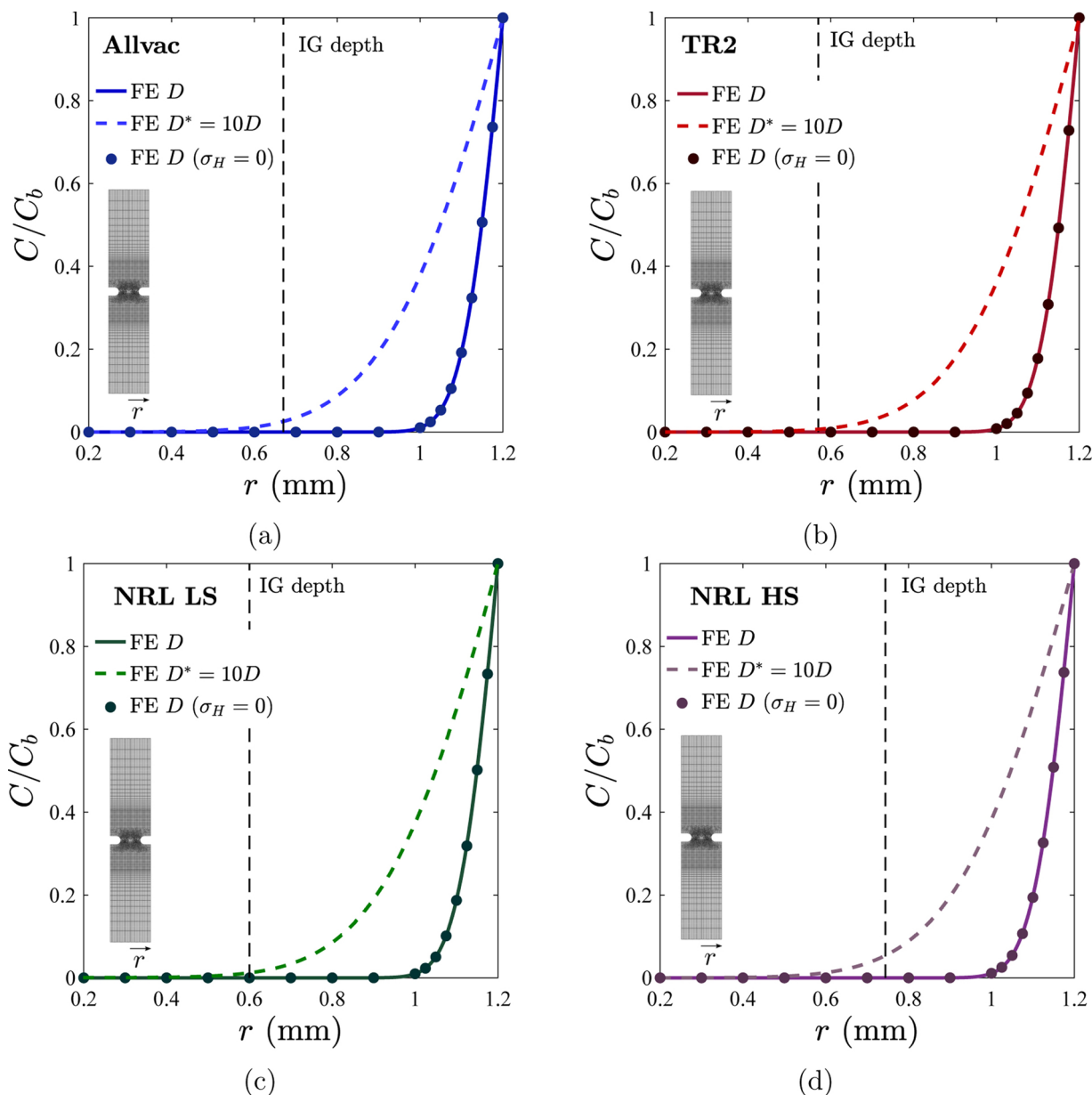
Fig. 4. Normalized hydrogen concentration profiles for (a) Allvac, (b) TR2, (c) NRL LS, and (d) NRL HS in the absence of hydrostatic stress (circular points) and with hydrostatic stress accounted for (solid line). The dashed vertical line indicates the depth of intergranular fracture observed during testing at $-1100\,\text{mV}$ in $0.6\,\text{M}$ NaCl. The dashed colored curve represents the concentration profile if the hydrogen diffusivity is elevated one order of magnitude.

that the H ingress is below 50% of the intergranular fracture depth (indicated by a vertical dashed line); $\sim 30\%$ for NRL LS at $-1100\,\text{mV}_{SCE}$.

The highly localized calculated concentration profile relative to the observed depth of intergranular cracking could potentially be caused by the use of a H diffusivity ($D = 1.3 \times 10^{-10}\,\text{cm}^2/\text{s}$) that is lower than reality. As summarized by Ai *et al.* [51], H diffusivities ranging from $D \sim 8 \times 10^{-11}$ to $D \sim 4 \times 10^{-10}\,\text{cm}^2/\text{s}$ have been measured in Monel K-500, depending on heat treatment and analysis methodology. In addition to such experimentally-induced variations, 'fast' diffusion pathways (e.g. grain boundaries) could also facilitate deeper H penetration over expectations based on the lattice H diffusivity. Such enhanced H diffusion along grain boundaries is supported by both experimental [77–86] and computational results [87–90], which collectively indicate that this diffusivity can be 1000-fold faster than the lattice H diffusivity in Ni. However, the potency of this accelerated local diffusion on the 'effective' diffusivity is strongly sensitive to grain boundary character [88,90,91], grain boundary connectivity [87], grain size [79,86,92],

the presence of other solutes at the grain boundary [89], and the H concentration [81,85,89]. While significant scatter exists in the literature [80,82,92,93], experimental studies conducted on pure Ni with grain sizes similar to the materials used herein (10–30 μm) generally observed a 2- to 8-fold increase in the effective diffusivity [77,79,83,86]. An 8-fold increase in the effective diffusivity is also nominally consistent with the maximum enhancement predicted for grains larger than 1 μm by the computational results of Osman Hoch *et al.* [87].

To assess whether such possible variations in H diffusivity could explain the discrepancy between the intergranular fracture depths and the H penetration distances, the concentration profile for each material was calculated using a H diffusivity ($D = 1.3 \times 10^{-9}\,\text{cm}^2/\text{s}$) that is an order of magnitude faster than that used in the original calculation ($D = 1.3 \times 10^{-10}\,\text{cm}^2/\text{s}$). The modeling results with this enhanced diffusivity (dashed line in Fig. 4) do result in a non-zero H concentration at the intergranular fracture distance. However, the H concentrations achieved at the intergranular fracture depth are likely below the

Table 4

Fracture energy G_0 obtained for each material lot by calibrating with the experiments in air.

	Allvac	TR2	NRL LS	NRL HS
G_0 (MPa mm)	18.5	18.1	15.4	16.9

level necessary for the onset of H-induced cracking. Specifically, it is reasonable to assume (based on the results of Fig. 3b) that the diffusible H concentrations reported for each material heat (Table 3) at the most positive applied potential before intergranular fracture was observed (e.g. $-850\,\mathrm{mV}_{SCE}$ for TR2) are the minimum concentrations required for intergranular cracking. As such, H-induced intergranular fracture is not expected at $-1100\,\mathrm{mV}_{SCE}$ in the tested material heats until C/C_b of at least > 0.5 (Allvac and NRL HS), > 0.1 (TR2), and > 0.05 (NRL LS) are achieved. As shown by the dashed line in Fig. 4, even with a 10-fold enhancement in the H diffusivity, none of the tested material heats reach the H concentrations necessary for intergranular fracture at the experimentally observed intergranular fracture depth. In fact, in order for C/C_b to reach a value of 0.5 at the intergranular fracture depth in the NRL HS and Allvac alloys tested at $-1100\,\mathrm{mV}_{SCE}$, simulations indicate that H diffusivities of $D = 5.4 \times 10^{-9}$ and $D = 7.1 \times 10^{-9}\,\mathrm{cm}^2/$ s would be required, respectively. These values are approximately 40- and 55-fold larger than experimentally measured H diffusivity for these

material heats [42], suggesting that neither experimental variability nor 'fast' diffusion along grain boundaries are sufficient to induce the observed depth of intergranular fracture. This limited influence of grain boundary diffusion in the current study was not unexpected given the grain boundary characteristics of the tested material heats. Specifically, prior work on NRL HS demonstrates that the grain size and the fraction of low-angle and coincident site lattice (CSLs; predominantly Σ3) boundaries were 11.2 μm and ~62%, respectively [43]. Based on the simulations of Osman Hoch *et al.*, these grain boundary characteristics would therefore result in the effective H diffusivity being ~70% of the true lattice diffusivity [87], implying that a grain boundary effect should not be expected in the current testing.

The above results suggest that H diffusion from the broad surface is insufficient to induce the observed depth of intergranular fracture in any of the material heats, even when aided by applied stresses or the expected contribution of 'fast' diffusion pathways. As such, these findings support the occurrence of sub-critical crack growth during the SSRT experiment. During such growth, the electrochemical conditions responsible for H generation move along with the propagating crack, which functionally acts as a moving line source in the context of the diffusion problem [52,94]. This set of boundary conditions has previously been shown to enable embrittlement to depths well beyond what would be possible from diffusion from the specimen surface [94]. To validate this finding and enable commentary on its implications to the SSRT testing method, an experimentally-calibrated phase field
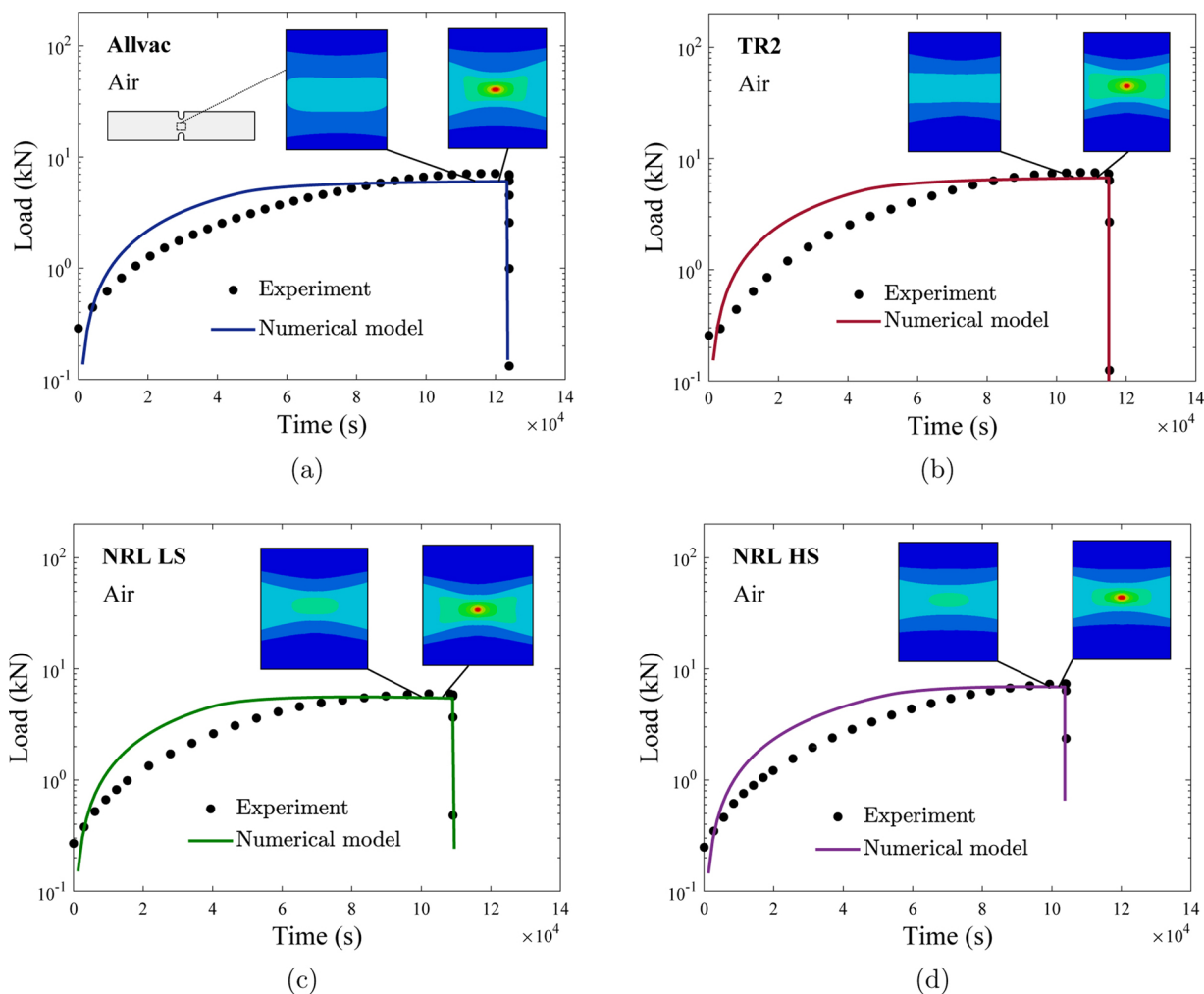
Fig. 5. Comparison of the simulated and experimental load versus time response in the absence of hydrogen for (a) Allvac, (b) TR2, (c) NRL LS, and (d) NRL HS. The inset images indicate the spatial distribution of the phase field damage parameter over a domain of a width of ~0.8 mm centered at the mid-plane of the specimen. Blue and red colors correspond to the completely intact and the fully broken state of the material, respectively.

Table 5
Sensitivity of the hydrogen damage coefficient χ to the material heat for
$E_A = -1100$ mV.

Material lot	Allvac	TR2	NRL LS	NRL HS
Hydrogen damage coefficient χ	0.85	0.86	0.82	0.79

model is utilized in the following sections to predict the onset and subsequent propagation of fracture in the absence and presence of H.

4.3. Phase field modeling of SSRT experiments in laboratory air

Under the phase field modeling paradigm, the fracture response in the absence of H is characterized by the fracture energy G_0 and phase field length scale ℓ. For the current simulations, ℓ is assumed to be 0.015 mm and the value of G_0 was calibrated for each material heat to match the onset of failure in the experimental force versus time data collected during testing in laboratory air (Fig. 2). The magnitude of ℓ governs the size of the fracture process zone, which is on the order of tens of microns for high strength metals in aggressive environments. One should note that the ratio ℓ/G_0 is what governs the critical stress, see Eq. (9). Thus, the magnitude of ℓ is typically chosen based on mesh size considerations, approximately 7 elements are needed to resolve ℓ [53], and the experimental result can then be fitted by calibrating G_0. Here, a total of approximately 24,000 axisymmetric quadratic quadrilateral elements are employed, with the characteristic element size being $h < \ell/10$. The values of G_0 for each material heat that provide the best fit for these laboratory air SSRT experiments are shown in Table 4 and a comparison between the experimental results and numerical simulations using these values of G_0 and ℓ are shown in Fig. 5. The inset maps depicting the spatial distribution of the phase field parameter ϕ in the specimen cross-section show that the model predicts that damage will initiate in the center, high-constraint region of the specimen (indicated by the red color contour). The onset of damage is very close to maximum force, as it is triggered by the necking-induced stability. Such results are consistent with expectations for a ductile fracture event in a notched specimen [95].

While Fig. 5 shows reasonable correspondence between the experimental results and the model, the finite element results (with and without phase field damage) over-predict the hardening behavior in each material heat. Specifically, the numerical results have an increased force for a given time relative to the experimental data. This discrepancy is not unexpected given the inherent differences between the modeling configuration and experimental set-up. The model only accounts for the specimen response utilizing the uniaxial stress-strain data (Table 2) to predict the hardening behavior, with G_0 only informing the conditions required for the onset of fracture. Conversely, the experimental data inherently includes displacement responses associated with both the sample and the load train of the frame operated under stroke control; due to the notched geometry of the specimens (Fig. 1), an extensometer was not employed during testing. Therefore, the displacement observed during the experiment (which is proportional to time since all testing was operated at a fixed stroke displacement rate) is described by:

$$\delta_T(F) = \delta_M(F) + \delta_S(F) \tag{19}$$

where δ_T is the total displacement, δ_M is the machine displacement, and δ_S is the specimen displacement, all of which are functionally dependent on the applied force (F). A common testing artifact induced by this coupled displacement is an apparent reduction in the elastic modulus due to the dominant role of δ_M during the initial stages of deformation [96]. This coupled displacement is likely the source of the discrepancy between the experimental data and model prediction. The implication of this artifact is that the actual displacement of the test specimen (δ_S) will be less than that predicted by the model, suggesting that the G_0

calibrated from the experimental data is an over-prediction. However, given that damage does not initiate until the G_0 criteria is locally satisfied, it is expected that the use of an inflated G_0 will yield conservative results, since an increased amount of deformation relative to reality is inherently required to induce the onset of fracture. The impact of this artifact on the interpretation of modeling results for H-charged specimens will be explored in subsequent sections.

4.4. Phase field modeling of SSRT experiments in 0.6 M NaCl exposed to cathodic polarization

Using the experimentally-calibrated values of G_0 from the testing conducted in laboratory air (Table 4), the H damage coefficient χ for each material heat was calibrated using the experimental results obtained under the most aggressive environmental conditions (0.6 M NaCl at -1100 mV$_{SCE}$; Fig. 2). χ establishes the extent to which G_0 is degraded as a function of H concentration Eq. (3) and is fit such that the final fracture of the model is consistent with that observed during the experiments. Variation of the values of χ (shown in Table 5) indicate a change in the H potency for the different heats of Monel K-500; this is consistent with the results of prior fracture mechanics-based testing [43]. Coupling (1) variations in χ and (2) lot-to-lot differences in the H-uptake and solubility, can be used as the basis to understand the factors governing lot specific HEAC susceptibility. For example, despite consistently exhibiting increased resistance to H-assisted cracking [42,43], the Allvac heat was found to have a χ value (0.85) similar to the more susceptible TR2 (0.86) and NRL LS (0.82) heats. The higher levels of HEAC resistance despite a similar χ likely arises from the low concentration of H available to participate in the fracture process relative to the other heats (Table 3).

It is important to note that the value of χ will likely be affected by other modeling assumptions, such as accounting for the increase in apparent solubility due to hydrostatic stresses [97–99] or the use of strain gradient plasticity to resolve micro-scale deformation [6,100]. Moreover, physical interpretation of the values of χ is hindered by the phenomenological, macroscopic approach adopted, where both the elastic and plastic parts of the strain energy density contribute to fracture and where the damage micromechanisms are not explicitly resolved. While the phase field modeling framework can be extended to provide a direct connection with potential HE mechanisms (AIDE [101], HELP [102], HEDE [103,104], etc.), our objective is to provide a hydrogen-assisted fracture mechanics assessment of cracking in SSRT. Thus, χ does not have the same physical meaning as the hydrogen damage coefficients that can be determined from the atomistic simulations of Jiang and Carter [105] or Alvaro *et al.* [66]. In these prior studies, a brittle fracture paradigm was invoked, where χ would generally be interpreted as the potency of hydrogen in reducing the ideal work of fracture. However, a *total* energy framework is here employed [106], given that Monel K-500 exhibits tangible plastic deformation prior to failing *via* intergranular fracture, even when charged with hydrogen contents reaching > 200 weight part per million [107].

The experimental and simulated force versus time curves for each material heat at -1100 mV$_{SCE}$ in 0.6 M NaCl are shown in Fig. 6. A difference in the hardening behavior between the model prediction and experimental data is noted for the testing in 0.6 M NaCl at -1100 mV$_{SCE}$. However, as was argued for the similar discrepancy in the lab air results, this difference is reasonably attributed to the inclusion of both the specimen and actuator displacement in the experimental data (19). The results demonstrate reasonable agreement between the predicted and experimentally-observed rapid decrease in load associated with specimen failure. Furthermore, the inset maps of the spatial distribution of the phase field parameter ϕ in the specimen cross-section (Fig. 6) reveal the initiation of cracks at the root of the notch in all material heats. This location is notably different from the initiation of damage at the center of the SSRT specimen in the laboratory air testing (Fig. 5). Interestingly, the model predicts crack
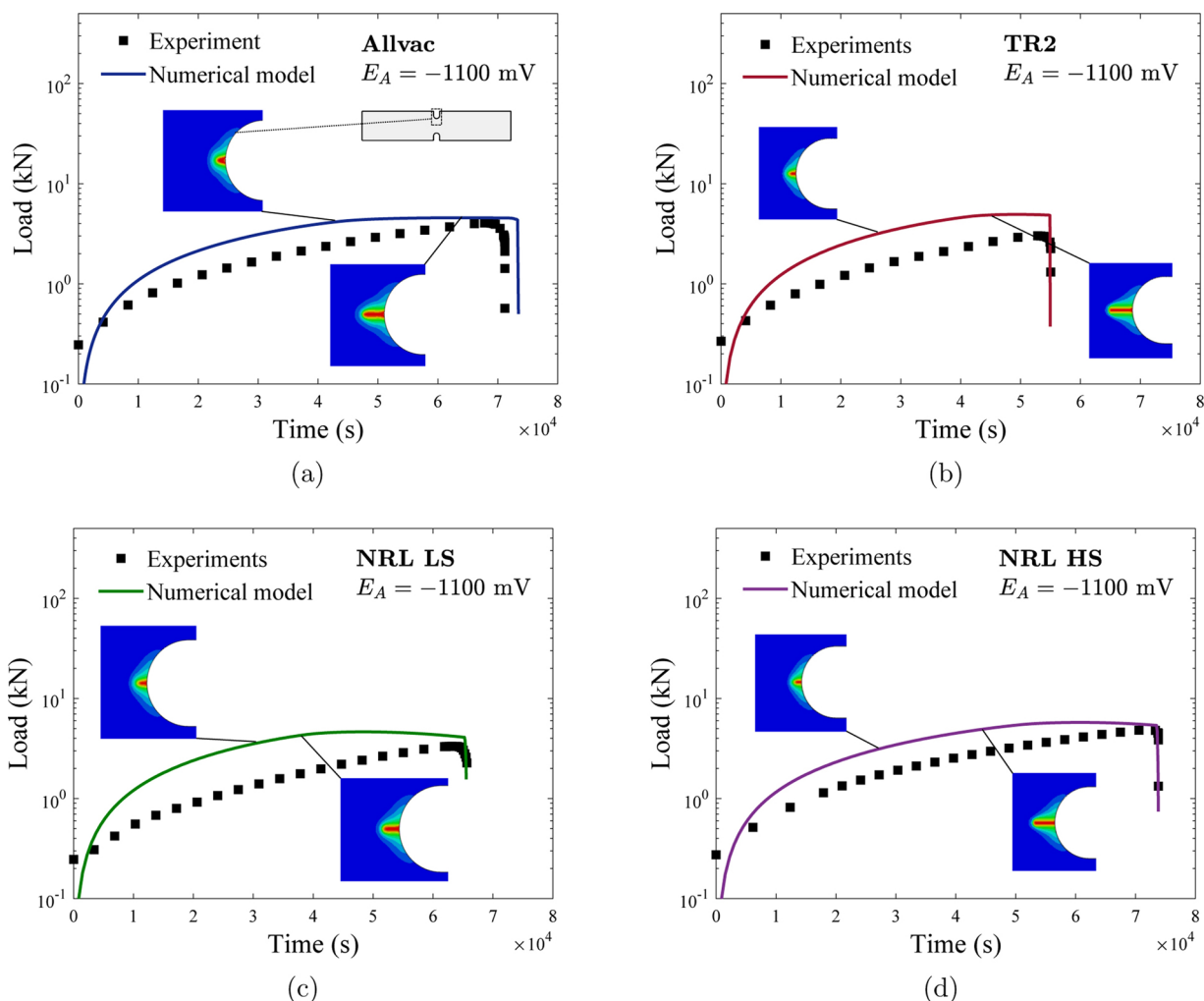
Fig. 6. Comparison of the simulated and experimental load versus time response at $-1100\,\mathrm{mV_{SCE}}$ in 0.6 M NaCl for (a) Allvac, (b) TR2, (c) NRL LS, and (d) NRL HS. The inset images indicate the spatial distribution of the phase field damage parameter over a domain of a width of ~1.2 mm. Blue and red colors correspond to the completely intact and the fully broken state of the material, respectively.
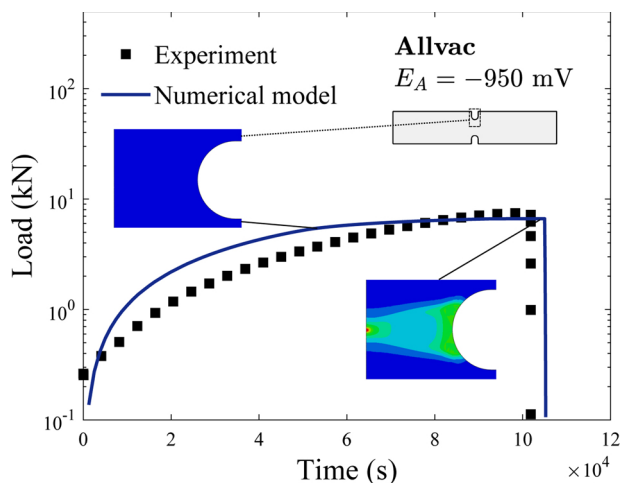

Fig. 7. Comparison of the simulated and experimental load versus time response at $-950\,\mathrm{mV_{SCE}}$ in 0.6 M NaCl for the material heat. The inset images for each material heat indicate the spatial distribution of the phase field damage parameter in the cross-section of the SSRT specimen, with the blue representing $\phi = 0$ and red representing $\phi = 1$.

initiation at between 40% and 60% of the total time to failure for the SSRT experiments at $-1100\,\mathrm{mV_{SCE}}$. Critically, these results imply that sub-critical crack growth will occur for 40–60% of the test duration. As such, the modeling results provide firm support for the preceding diffusion-based arguments that suggest sub-critical crack growth is required to obtained the experimentally-measured intergranular fracture depths (Fig. 3).

It is possible that this artifact could influence the calibrated value of χ, thereby complicating the interpretation of the modeling results. The validity of the modeling parameters is tested by using the calibrated values of χ and G_0 for each material heat to model SSRT experiments conducted at intermediate applied potentials (e.g. -950 or $-850\,\mathrm{mV_{SCE}}$). If χ is independent of (or insensitive to) the coupled displacements artifact, then it should reasonably reproduce the rapid decrease in applied load at the onset of final failure for the intermediate applied potentials. The modeling results for Allvac at $-950\,\mathrm{mV_{SCE}}$ (Fig. 7) show a similar level of agreement with the experimental data as was observed for Allvac at $-1100\,\mathrm{mV_{SCE}}$. Such results were also observed for the other material heats at intermediate applied potentials.[3]

---

[3] Note that the tests conducted on NRL HS and NRL LS at $-850\,\mathrm{mV_{SCE}}$ were not modeled due to their increased time to failure relative to laboratory air testing, which is speculatively attributed to test-to-test scatter in mechanical properties.

These results provide confidence in the general trends predicted by the model (*i.e.* the initiation of sub-critical cracking well before final fracture at $-1100\,\mathrm{mV_{SCE}}$). Interestingly, the model also correctly predicts that at $-950\,\mathrm{mV_{SCE}}$ the final fracture will initiate at the center of the specimen, as demonstrated by the inset maps of ϕ in the specimen cross-section. However, damage proximate to the notch root (indicated by the green field in the inset map of Fig. 7) is also observed. Speculatively, this H-induced surface damage results in the decreased time to failure for $-950\,\mathrm{mV_{SCE}}$ by degrading the resistance of the cross-section to deformation, leading to an earlier plastic instability and concomitant initiation of fracture at the center of the specimen.

5. Discussion

5.1. Evidence for the onset of sub-critical cracking during SSRT experiments

A holistic evaluation of the presented experimental observations and modeling results provides strong evidence for the onset of sub-critical crack growth during notched SSRT experiments. First, a systematic comparison of the expected H diffusion ingress and the observed intergranular fracture depth was conducted for four different material heats of Monel K-500 tested in 0.6 M NaCl at various applied

potentials. The results of this evaluation demonstrate that H diffusion from the specimen surface cannot reasonably explain the observed depth of intergranular fracture. Specifically, even when the effect of applied stress and/or an order of magnitude faster diffusivity are invoked (to simulate an effect of grain boundary diffusion), H ingress from the specimen surface is insufficient to induce the measured extent of intergranular fracture (Fig. 4). These results strongly support the occurrence of sub-critical crack growth during the SSRT experiments, where a moving line source phenomenon would enable the extended intergranular fracture depths [94]. To test this hypothesis, a new phase field formulation that coupled H diffusion and elastic–plastic deformation was employed. Using the experimental results from laboratory air testing and 0.6 M NaCl at $-1100\,\mathrm{mV_{SCE}}$, the critical total fracture energy G_0 and H damage coefficient χ were calibrated for the four material heats (Figs. 5 and 6). These parameters were subsequently validated *via* modeling of tests conducted at intermediate applied potentials (-950 and $-850\,\mathrm{mV_{SCE}}$ in 0.6 M NaCl), which showed reasonable agreement for the onset of failure between the model predictions and experimental results without any modification of the calibrated G_0 and χ values (Fig. 7). Critically, through an evaluation of the phase field parameter ϕ, the fracture initiation location for each material heat/environment combination can be ascertained. For the
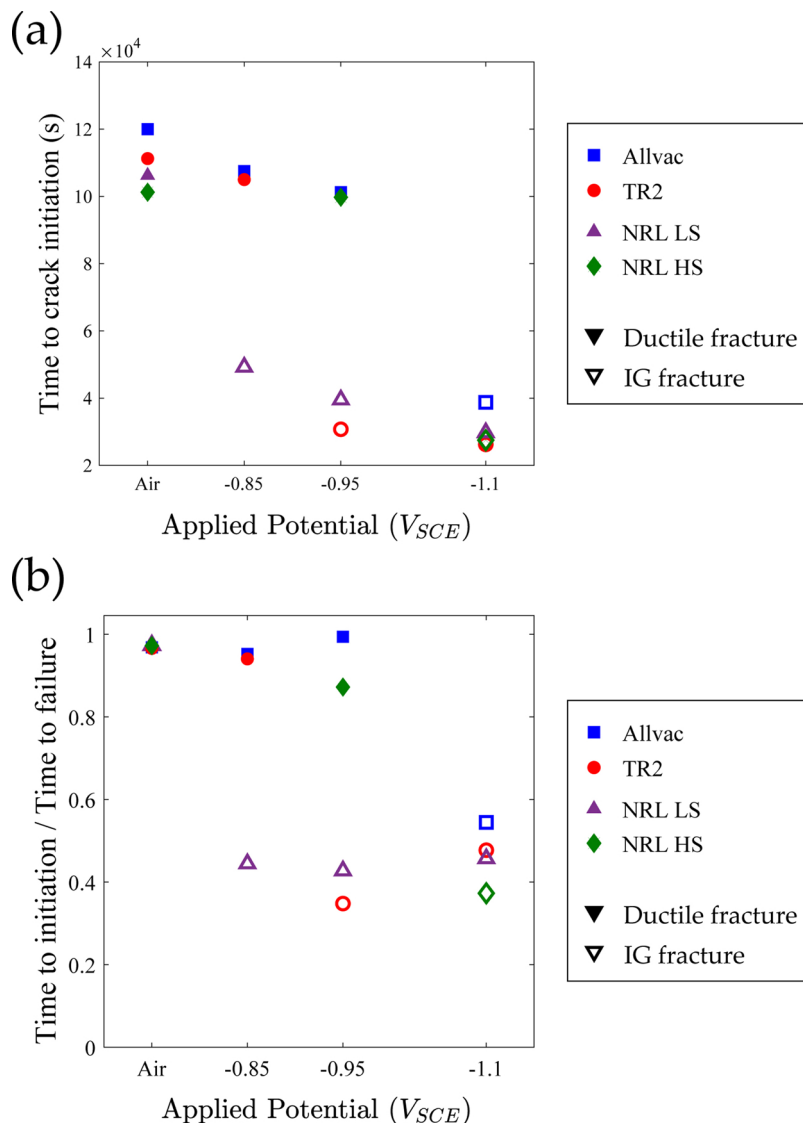

Fig. 8. (a) Time for crack initiation and (b) ratio of the time for crack initiation and time for specimen failure as a function of applied potential for the four tested material heats of Monel K-500. Open and closed symbols indicate specimens that exhibited intergranular (IG) and ductile fracture, respectively.

laboratory air testing that exhibited ductile microvoid coalescence as the dominant fracture morphology, fracture was found to initiate in the center of the specimen (Fig. 5), consistent with expectations for notched tensile bars [95]. Conversely, modeling of the experiments at $-1100 \, mV_{SCE}$ that exhibited intergranular fracture revealed the initiation and subsequent propagation to failure of a crack at the notch root. Critically, and in direct agreement with the inferences drawn from the diffusion-based analysis, the cracks were found to initiate well before final fracture (*i.e.* sub-critical cracking), at times corresponding to 40–60% of the time to failure. Taken together, these two results strongly suggest that sub-critical cracking can occur during SSRT experiments.

This conclusion is consistent with a broad literature survey of prior SSRT experimental results. For example, Holroyd and coworkers have documented the existence of sub-critical cracks during SSRT experiments on 5xxx-series Al alloys [35–37]. In fact, through systematic X-ray computed tomography (XCT), these authors have gone so far as to estimate stress intensity solutions for the observed crack morphologies as well as attempt to characterize crack growth rates during SSRT testing [35]. Similar findings were also reported by Sampath *et al.*, who utilized an imaging technique to assess the topography of matching fracture surfaces in H-exposed Ni-based alloys to determine that cracks could initiate at stresses as low as 33% of the fracture stress [41]. Máthis *et al.* leveraged acoustic emission to assess the efficacy of SSRT experiments on stainless steel tubulars, which identified acoustic events associated with crack initiation and propagation well before final fracture, with subsequent scanning electron microscopy confirming the presence of stress corrosion cracks in the test specimen [40]. SSRT experiments by Haruna and Shibata on cylindrical 316L stainless steel exposed to aqueous NaCl solutions in which the tests were interrupted and then cross-sectioned for evaluation revealed crack initiation and propagation prior to failure [38]. Lee *et al.* speculated that the fracture of AA2024-T351 SSRT specimens exposed to aqueous chloride solutions resulted from the formation of pits, which enabled the initiation and propagation of cracks, leading to final failure [31]. Lastly, modeling of SSRT experiments by Garud explicitly includes the formation and propagation of 'microcracks' as the means by which the net-section load-carrying capacity is diminished [39]. The current diffusion and phase field modeling results support these literature reports that demonstrate sub-critical crack growth can occur during SSRT experiments. As discussed by Ahluwalia [26], the onset of such cracking can alter the assessment of SSRT results by complicating the interpretation of typical metrics like time-to-failure, breaking stress, and ductility. The computation tools developed herein enable an efficient interrogation of the effect that various environment, loading, and material combinations may have on the accuracy and validity of measured SSRT metrics. In the following section, the implications of such complications on the evaluation of the time-to-failure metric is explored leveraging the results of the phase field modeling shown in Fig. 6.

5.2. Implications for the interpretation of SSRT experiments

As demonstrated in Fig. 6, the phase field model enables the assessment of the time for crack initiation, which provides an opportunity to qualitatively establish the implications of sub-critical crack growth on the interpretation of SSRT metrics. As shown in Fig. 8a, the model-predicted time to crack initiation is found to decrease with increasingly more negative applied potentials for all material heats; prior work in Monel K-500 demonstrated that such behavior is due to increasing H generation with increasingly negative applied potential [42,43,52,58]. However, as the most aggressive potential is reached, there is a significant and important difference between the time for crack initiation and the time for failure data. Specifically, the ranking of the HEAC susceptibility of the materials heats based on their time to failure (a common SSRT metric [21]) is not consistent with the ranking obtained when using the time to crack initiation (which is more relevant to the

true HEAC susceptibility). For example, despite being considered one of the more HEAC-resistant heats of Monel K-500 [42,43] based on the traditional SSRT metrics, NRL HS is found to exhibit a similar time to crack initiation as the EAC-susceptible NRL LS and TR2 material heats. Such differences further underscore the reality that the SSRT experiment is a composite of the times required for crack incubation, initiation, Stage I propagation, Stage II propagation, and final fracture. The interpretation of the SSRT test becomes even more convoluted if one considers the ratio of the time to initiation and time to failure, shown in Fig. 8b. Under this paradigm, NRL HS would be considered the worst-performing material, as cracking is found to initiate at times of less than 40% of the time to failure.

As discussed by Ahulwalia [26], this ambiguity in interpreting the results of the SSRT experiments (e.g. three different conclusions are drawn if the data are evaluated in three different ways) highlights the complications introduced upon the onset of sub-critical cracking. Such difficulties also extend to the use of stress-based metrics (e.g. breaking stress), where it would be necessary to determine whether (1) the remote stress at crack initiation, (2) the remote stress at fracture, or (3) a calculated stress intensity is the most rigorous metric. Coupling this challenge in interpretation with the explicit caveat in ASTM Standard G129 that SSRT "results are not intended to necessarily represent service performance" [14], raise questions regarding the efficacy of the SSRT methodology to reliably assess/rank H embrittlement susceptibility (and EAC susceptibility in general). The SSRT experimental approach has several attractive elements relative to other testing methodologies (e.g. low-cost, efficient, modular, simple to perform, etc. [18,21,22,108]). Moreover, it is likely that there are environment/material/loading combinations for which the SSRT remains a useful screening approach. For example, if H diffusion is sufficiently fast to enable the attainment of an uniform H concentration across the SSRT specimen diameter and the alloy toughness is low (e.g. high-strength steels [109]), then it is possible that final fracture could occur immediately upon crack initiation. However, such bounding conditions have not been firmly established to-date, underscoring the need for additional studies to assess the conditions under which the SSRT methodology represents a reasonable pathway for assessing/screening for EAC susceptibility.

Based on the current work, several initial suggestions can be made. First, the use of notched tensile specimens for SSRT should be carefully considered prior to use, as these specimens appear to be particularly susceptible to the onset of sub-critical cracking due to the stress concentration present at the notch root. While the use of such notches enables closer approximation to a typical bolt geometry, ensures fracture occurs at a specific location, and induces failure at reduced loads, these benefits may be out-weighed by the complications associated with sub-critical cracking. Second, the current study establishes the utility of a diffusion-based analysis framework to ascertain whether or not sub-critical cracking occurred during SSRT experiments in H-containing/producing environments. Given the simple geometries generally employed for the majority of SSRT experiments [21], the diffusion problem can be readily solved either analytically [74] or with the aid of finite element software packages. Comparison of these calculations with the depth of EAC-induced brittle fracture provides a rigorous pathway for assessing the validity of SSRT experiments. Simply put, if H cannot reasonably diffuse to the observed extent of brittle fracture, then it is possible that sub-critical cracking occurred and additional efforts should be made before interpreting obtained SSRT metrics. Lastly, if secondary cracks are observed along the gage length of the SSRT specimen after the conclusion of testing, it is possible that sub-critical cracking may have occurred. To assess this possibility, the interrupted testing and cross-sectioning methodology of Haruna and Shibata [38] could be used to confirm that such cracks do not form until final fracture.

The employed modeling framework offers a unique tool to assess the efficacy of the SSRT methodology to evaluate susceptibility to H

embrittlement. Confidence in the modeling is obtained by consistency with prior literature conclusions and diffusion-based arguments as well as the ability to reasonably capture the experimental data from intermediate applied potentials (Fig. 7). However, it should be noted that the model-predicted metrics (*i.e.* time to crack initiation) have yet to be explicitly validated against experimental data. Towards this end, it would be useful to perform a series of systematically interrupted SSRT experiments, which would then be sectioned to experimentally evaluate when crack initiation occurs [7,38]. Alternatively, the XCT approach previously utilized by Holroyd *et al.* [36] or the imaging analysis employed by Sampath *et al.* [41] could be leveraged to determine the onset of subcritical crack growth.

6. Conclusions

The potential for the onset of sub-critical crack growth during slow strain rate tensile testing of Monel K-500 immersed in 0.6 M NaCl and exposed to applied potentials ranging from -850 to $-1100\,\mathrm{mV}_{SCE}$ was systematically evaluated using both H diffusion-based analyses and a new phase field formulation for H-assisted fracture. These efforts, coupled with an examination of prior literature results, reveals several important insights regarding the onset of sub-critical crack growth during SSRT experiments to assess H embrittlement susceptibility:

(1) A systematic comparison of the observed depth of intergranular fracture and the calculated H ingress distance revealed that H cannot reasonably reach the depth of intergranular fracture. These results strongly suggest that sub-critical crack growth occurred during the SSRT experiments.
(2) A phase field formulation that couples elastic–plastic deformation with H diffusion was developed to describe H-assisted fracture. Model parameters were calibrated using the experimental data obtained during SSRT experiments conducted in laboratory air (G_0) and in 0.6 M NaCl at $-1100\,\mathrm{mV}_{SCE}$ (χ), and then validated *via* a systematic comparison with results from SSRT experiments conducted at lower overpotentials.
(3) The phase field model reliably predicted the expected initiation location for fracture for all experiments: at the center of the

specimen for non-embrittling environments and at the notch tip for specimens exhibiting intergranular fracture.
(4) The calibrated model predicted the initiation of cracks at the notch tip at 40–60% of the time to failure, depending on material heat. Critically, the model captured the observed degradation in time-to-failure for experiments (e.g. Allvac at $-950\,\mathrm{mV}_{SCE}$) conducted at applied potentials that did not exhibit intergranular fracture without any modification of calibrated parameters.
(5) The potential impact of sub-critical cracking on the validity of reported metrics from SSRT experiments was explored *via* a comparison the experimentally-obtained time to failure and the model-predicted time to crack initiation. This gedankan experiment revealed a modification in the relative ordering of H embrittlement susceptibility in four material heats of Monel K-500, underscoring the important impact that sub-critical cracking can have on the interpretation of SSRT metrics.

Data availability statement

The data generated during this study will be made available upon reasonable request.

Conflict of interest

The authors declare no conflict of interest.

Appendix A. Finite element implementation

The finite element (FE) method is used to solve the coupled mechanical-diffusion-phase field problem. Using Voigt notation, the nodal values of the displacements, phase field and H concentration are interpolated as follows,

$$\boldsymbol{u} = \sum_{i=1}^{m} \boldsymbol{N}_i \boldsymbol{u}_i, \quad \phi = \sum_{i=1}^{m} N_i \phi_i, \quad C = \sum_{i=1}^{m} N_i C_i \tag{A.1}$$

where m is the number of nodes and $\boldsymbol{N}_i$ are the interpolation matrices – diagonal matrices with the nodal shape functions N_i as components. Accordingly, the corresponding gradient quantities can be discretized by,

$$\boldsymbol{\varepsilon} = \sum_{i=1}^{m} \boldsymbol{B}_i^u \boldsymbol{u}_i, \quad \nabla \phi = \sum_{i=1}^{m} \boldsymbol{B}_i \phi_i, \quad \nabla C = \sum_{i=1}^{m} \boldsymbol{B}_i C_i \tag{A.2}$$

Here, $\boldsymbol{B}_i$ are vectors with the spatial derivatives of the shape functions and $\boldsymbol{B}_i^u$ denotes the standard strain–displacement matrices.

A.1 FE discretization of the deformation-phase field problem

The implementation of the coupling between elastic–plastic deformation and phase field fracture builds upon the work by Miehe *et al.* [110]. Thus, nodal values of displacement and phase field order parameter are obtained by means of a staggered approach, and a history variable H is introduced to ensure irreversibility of the crack phase field evolution

$$H = \begin{cases} \psi & \text{if } \psi > H_t \\ H_t & \text{otherwise} \end{cases} \tag{A.3}$$

Here, H_t is the previously calculated energy at time increment t. Thus, the history field satisfies the Kuhn–Tucker conditions.

Making use of the finite element discretization outlined above and considering that Eq. (6) must hold for arbitrary values of $\delta\boldsymbol{u}$, the discrete equation corresponding to the equilibrium condition can be expressed as the following residual with respect to the displacement field,

$$r_i^u = \int_\Omega \left\{ [(1 - \phi)^2 + k](\boldsymbol{B}_i^{\boldsymbol{u}})^T \boldsymbol{\sigma} \right\} \mathrm{d}V \tag{A.4}$$

with k being a sufficiently small numerical parameter introduce to keep the system of equations well-conditioned; a value of $k = 1 \times 10^{-7}$ is used throughout this work. Similarly, the out-of-balance force residual with respect to the evolution of the crack phase field is obtained by discretizing Eq. (6) and considering Eq. (A.3),

$$r_i^\phi = \int_\Omega \left[-2(1 - \phi)N_i H + G_0(C)\left(\frac{\phi}{\ell}N_i + \ell \boldsymbol{B}_i^T \nabla \phi \right) \right] \mathrm{d}V \tag{A.5}$$

The components of the consistent stiffness matrices can be obtained by differentiating the residuals with respect to the incremental nodal variables:

$$\boldsymbol{K}_{ij}^{\boldsymbol{u}} = \frac{\partial \boldsymbol{r}_i^{\boldsymbol{u}}}{\partial \boldsymbol{u}_j} = \int_\Omega [(1 - \phi)^2 + k](\boldsymbol{B}_i^{\boldsymbol{u}})^T \boldsymbol{C}_{\mathrm{ep}} \boldsymbol{B}_j^{\boldsymbol{u}} \, \mathrm{d}V \tag{A.6}$$

$$\boldsymbol{K}_{ij}^\phi = \frac{\partial r_i^\phi}{\partial \phi_j} = \int_\Omega \left[\left(2H + \frac{G_0(C)}{\ell} \right) N_i N_j + G_0(C)\ell \boldsymbol{B}_i^T \boldsymbol{B}_j \right] \mathrm{d}V \tag{A.7}$$

where $\boldsymbol{C}_{ep}$ is the elastic–plastic consistent material Jacobian.

A.2 FE discretization of mass transport

We assume no external flux in the surface $\partial\Omega_q$ and obtain a residual vector for the mass diffusion problem by discretizing Eq. (17) for any arbitrary virtual variation of the H concentration δC. Accordingly, the residual right hand side vector r_i^C reads

$$r_i^C = \int_\Omega \left[N_i^T \left(\frac{1}{D}\frac{dC}{dt} \right) + \boldsymbol{B}_i^T \nabla C - \boldsymbol{B}_i^T \left(\frac{\bar{V}_H C}{RT}\nabla \sigma_H \right) \right] \mathrm{d}V \tag{A.8}$$

From which a diffusivity matrix can be readily defined,

$$\boldsymbol{K}_{ij}^C = \int_\Omega \left(\boldsymbol{B}_i^T \boldsymbol{B}_j - \boldsymbol{B}_i^T \frac{\bar{V}_H}{RT}\nabla \sigma_H N_j \right) \mathrm{d}V \tag{A.9}$$

where the discretization given in Eq. (A.1) has also been employed to interpolate the time derivatives of the nodal concentrations. The diffusivity matrix is affected by the gradient of the hydrostatic stress, σ_H, which is computed at the integration points from the nodal displacements, extrapolated to the nodes by means of the shape functions, and subsequently multiplied by $\boldsymbol{B}_i$ to compute $\nabla \sigma_H$. Second order elements are employed in the computational implementation.

At the same time, one can readily identify a concentration capacity matrix,

$$\boldsymbol{M}_{ij} = \int_\Omega N_i^T \frac{1}{D} N_j \, \mathrm{d}V \tag{A.10}$$

and the discretized H transport equation reads,

$$\boldsymbol{K}^C \boldsymbol{C} + \boldsymbol{M}\dot{\boldsymbol{C}} = \boldsymbol{0} \tag{A.11}$$

A.3 Coupled scheme

The mechanical deformation, mass diffusion and phase field fracture problems are weakly coupled. First, elastic–plastic deformation impacts diffusion through the stress field, governing the pressure dependence of the bulk chemical potential. Second, mass transport affects the fracture resistance *via* H buildup in the fracture process zone, reducing the critical energy release rate. And third, the H-sensitive phase field degrades the strain energy density of the solid.

We solve the linearized finite element system,

$$\begin{bmatrix} \boldsymbol{K}^u & 0 & 0 \\ 0 & \boldsymbol{K}^\phi & 0 \\ 0 & 0 & \boldsymbol{K}^C \end{bmatrix}\begin{bmatrix} \boldsymbol{u} \\ \boldsymbol{\phi} \\ \boldsymbol{C} \end{bmatrix} + \begin{bmatrix} 0 & 0 & 0 \\ 0 & 0 & 0 \\ 0 & 0 & \boldsymbol{M} \end{bmatrix}\begin{bmatrix} \dot{\boldsymbol{u}} \\ \dot{\boldsymbol{\phi}} \\ \dot{\boldsymbol{C}} \end{bmatrix} = \begin{bmatrix} \boldsymbol{r}^u \\ \boldsymbol{r}^\phi \\ \boldsymbol{r}^C \end{bmatrix} \tag{A.12}$$

by means of a time parametrization and an incremental-iterative scheme in conjunction with the Newton–Raphson method. A time increment sensitivity analysis is conducted in all computations. The modeling framework is implemented in the commercial finite element package ABAQUS *via* a user element (UEL) subroutine. Post-processing of the results is carried out by means of Abaqus2Matlab [111].

Appendix B. Propagating hydrogen boundary conditions

In the presence of a propagating crack, the appropriate chemical boundary conditions on the newly exposed surface require careful consideration. As discussed in Section 4, capturing how H transport is driven through a propagating crack could be key in understanding H embrittlement under *in situ* charging. A suitable approach is to assume that the environment will promptly occupy the space created with crack advance. Accordingly, the value of the H concentration corresponding to the choice of electrochemical solution and applied potential, C_{env}, should be prescribed on the new boundary emerging due to crack propagation. Such scheme could be extended to account for chemical reaction and mass transport limitations [112].

In this work, we choose to effectively prescribe the H concentration in the damaged regions by means of a penalty approach [113]. An alternative procedure is to define a moving boundary *via* general multipoint constraints (MPCs), see Ref. [114]. We choose to enforce $C = C_{env}$ in the cracked

domain ($\phi = 1$), ramping linearly the H concentration from the $\phi > 0.5$ regions by choosing a sufficiently large value of the penalty factor k_p. Thus, we add an extra term to the chemical residual Eq. (A.8), which now reads

$$r_i^C = \int_\Omega \left\{ N_i^T \left[\frac{1}{D}\frac{dC}{dt} + (C - C_{\text{env}})\langle 2\phi - 1 \rangle k_p \right] + \boldsymbol{B}_i^T \nabla CV - \boldsymbol{B}_i^T \left(\frac{\bar{V}_H C}{RT} \nabla \sigma_H \right) \right\} dV \tag{B.1}$$

where $\langle \rangle$ denote the Macaulay brackets, and C and C_{env} are integration point quantities. Accordingly, the diffusivity matrix Eq. (A.9) becomes

$$\boldsymbol{K}_{ij}^C = \int_\Omega \left(N_i^T N_j \langle 2\phi - 1 \rangle k_p + \boldsymbol{B}_i^T \boldsymbol{B}_j - \boldsymbol{B}_i^T \frac{\bar{V}_H}{RT} \nabla \sigma_H N_j \right) dV \tag{B.2}$$

Values of k_p as high as 1×10^6 effectively ensure $C = C_{env}$ in the damaged regions without hindering convergence. Representative contours are shown in Fig. B.9 for the Allvac lot under an applied potential of $E_A = -1100$ mV ($C_{env} = 7.54$ wppm, see Table 3).
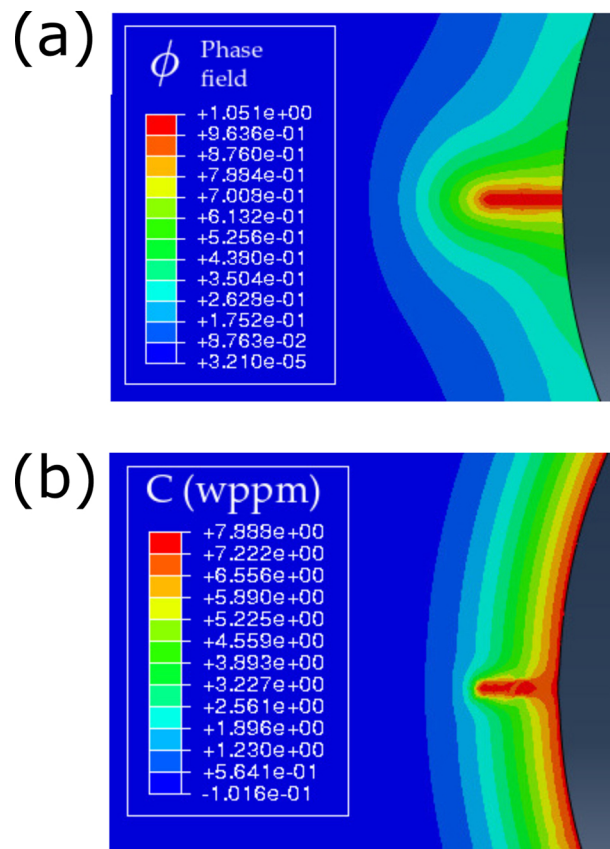

Fig. B.9. Penalty boundary conditions for hydrogen diffusion at the newly created surfaces. Representative results of hydrogen propagation with crack advance, (a) phase field fracture parameter, and (b) hydrogen concentration.

References

[1] R.P. Gangloff, Hydrogen-assisted cracking, in: I. Milne, R. Ritchie, B. Karihaloo (Eds.), Comprehensive Structural Integrity, vol. 6, Elsevier Science, New York, NY, 2003, pp. 31–101.

[2] R.P. Gangloff, Critical issues in hydrogen assisted cracking of structural alloys, in: S.A. Shipilov, R.H. Jones, J.-M. Olive, R. Rebak (Eds.), Environment-Induced Cracking of Materials, vol. 1, Elsevier Science, New York, 2008, pp. 141–165.

[3] I.M. Robertson, P. Sofronis, A. Nagao, M.L. Martin, S. Wang, D.W. Gross, K.E. Nygren, Hydrogen embrittlement understood, Metall. Mater. Trans. B 46 (3) (2015) 1085–1103.

[4] S. Lynch, Discussion of some recent literature on hydrogen-embrittlement mechanisms: addressing common misunderstandings, Corros. Rev. 37 (5) (2019) 377–395.

[5] W.W. Gerberich, Modeling hydrogen induced damage mechanisms in metals, in: R.P. Gangloff, B.P. Somerday (Eds.), Gaseous Hydrogen Embrittlement of Materials in Energy Technologies, vol. II, Woodhead Publishing, 2012, pp. 209–246.

[6] E. Martínez-Pañeda, C.F. Niordson, R.P. Gangloff, Strain gradient plasticity-based modeling of hydrogen environment assisted cracking, Acta Mater. 117 (2016) 321–332.

[7] Z.D. Harris, S.K. Lawrence, D.L. Medlin, G. Guetard, J.T. Burns, B.P. Somerday, Elucidating the contribution of mobile hydrogen-deformation interactions to hydrogen-induced intergranular cracking in polycrystalline nickel, Acta Mater. 158 (2018) 180–192.

[8] R.P. Gangloff, Probabilistic fracture mechanics simulation of stress corrosion cracking using accelerated laboratory testing and multi-scale modeling, Corrosion 72 (7) (2016) 862–880.

[9] V.S. Raja, T. Shoji, Stress Corrosion Cracking: Theory and Practice, Woodhead Publishing Limited, Cambridge, 2011.

[10] NACE Standard MR01795-98, Sulfide Stress Cracking Resistant Metallic Materials for Oilfield Equipment, NACE International, Houston, TX.

[11] NACE TM0198, Slow Strain Rate Test Method for Screening Corrosion-Resistant Alloys (CRAs) for Stress Corrosion Cracking in Sour Oilfield Service, NACE International, Houston, TX.

[12] ASTM G30, Standard Practice for Making and Using U-Bend Stress-Corrosion Test Specimens, ASTM International, West Conshohocken, PA.

[13] ASTM G39, Standard Practice for Preparation and Use of Bent-Beam Stress-Corrosion Test Specimens, ASTM International, West Conshohocken, PA.

[14] ASTMG129-00, Standard Practice for Slow Strain Rate Testing to Evaluate the Susceptibility of Metallic Materials to Environmentally Assisted Cracking, ASTM International, West Conshohocken, PA.

[15] ASTM E1681-03, Standard Test Method for Determining Threshold Stress Intensity Factor for Environment-Assisted Cracking of Metallic Materials, ASTM International, West Conshohocken, PA.

[16] ASTM F1624-12, Standard Test Method for Measurement of Hydrogen Embrittlement Threshold in Steel by the Incremental Step Loading Technique, ASTM International, West Conshohocken, PA.

[17] ISO 7539-7, Corrosion of Metals and Alloys – Stress Corrosion Testing – Part 7: Method for Slow Strain Rate Testing, International Organization for Standardization.

[18] C. Kim, B. Wilde, A review of the constant strain-rate stress corrosion cracking test, in: G. Ugiansky, J. Payer (Eds.), Stress Corrosion Cracking – The Slow Strain-Rate Technique, ASTM International, West Conshohocken, PA, 1979, pp. 97–112.

[19] G.M. Ugiansky, J.H. Payer, ASTM STP 665: Stress Corrosion Cracking: The Slow Strain-Rate Technique, ASTM International, West Conshohocken, PA, 1979.

[20] R.D. Kane, Slow Strain Rate Testing for the Evaluation of Environmentally Induced Cracking: Research and Engineering Applications, ASTM International, West Conshohocken, PA, 1993.

[21] M. Henthorne, The slow strain rate stress corrosion cracking test – a 50 year retrospective, Corrosion 72 (12) (2016) 1488–1518.

[22] D.R. McIntyre, R.D. Kane, S.M. Wilhelm, Slow strain rate testing for materials evaluation in high-pressure H2S environments, Corrosion 44 (12) (1988) 920–926.

[23] D.A. Wright, N. Gage, P.G. Bushell, Verification of the development of low hydrogen embrittling zinc–nickel electroplate by slow strain rate testing, Metal Finish. 93 (4) (1995) 40–45.

[24] G. Theus, J. Cels, Slow strain-rate technique: application to caustic stress corrosion cracking studies, in: G. Ugiansky, J. Payer (Eds.), Stress Corrosion Cracking – The Slow Strain-Rate Technique, ASTM International, West Conshohocken, PA, 1979, pp. 81–96.

[25] P. Klein, R. Hays, P. Moran, J. Scully, Hydrogen cracking initiation of a high-strength steel weldment, in: R.D. Kane (Ed.), Slow Strain Rate Testing for the Evaluation of Environmentally Induced Cracking: Research and Engineering Applications, ASTM STP 1210, American Society for Testing and Materials, Philadelphia, 1993, pp. 202–222.

[26] H. Ahluwalia, Problems associated with slow strain rate quality assurance testing of nickel-base corrosion resistant alloy tubulars in hydrogen sulfide environments, Slow Strain Rate Testing for the Evaluation of Environmentally Induced Cracking: Research and Engineering Applications, ASTM International, West Conshohocken, PA, 1993, pp. 225–239.

[27] J.A. Beavers, G.H. Koch, Limitations of the slow strain rate test for stress corrosion cracking testing, Corrosion 48 (3) (1992) 256–266.

[28] E. Hibner, Improved SSR test for lot acceptance criterion, Slow Strain Rate Testing for the Evaluation of Environmentally Induced Cracking: Research and Engineering Applications, ASTM International, West Conshohocken, PA, 1993, pp. 290–294.

[29] W.J. Pollock, Statistical treatment of slow strain rate data for assessment of hydrogen embrittlement in high strength 4340 steel, Corros. Sci. 33 (7) (1992) 1105–1119.

[30] D. McIntyre, Ranking materials for extreme sour gas service using the slow strain rate method, Hydrogen Embrittlement: Prevention and Control, ASTM International, West Conshohocken, PA, 1988, pp. 178–189.

[31] H. Lee, Y. Kim, Y. Jeong, S. Kim, Effects of testing variables on stress corrosion cracking susceptibility of Al 2024-T351, Corros. Sci. 55 (2012) 10–19.

[32] H. Margot-Marette, G. Bardou, J.C. Charbonnier, The application of the slow strain rate test method for the development of linepipe steels resistant to sulphide stress cracking, Corros. Sci. 27 (10–11) (1987) 1009–1026.

[33] S.L. Hong, Influence of surface condition on primary water stress corrosion cracking initiation of alloy 600, Corrosion 57 (4) (2001) 323–333.

[34] T.L. Anderson, Fracture Mechanics. Fundamentals and Applications, 3rd ed., CRC Press, Taylor & Francis, Boca Raton, 2005.

[35] N. Henry Holroyd, T.L. Burnett, B.C. Palmer, J.J. Lewandowski, Estimation of environment-induced crack growth rate as a function of stress intensity factors generated during slow strain rate testing of aluminum alloys, Corros. Rev. (2019), https://doi.org/10.1515/corrrev-2019-0031 (in press).

[36] N.J.H. Holroyd, T.L. Burnett, M. Seifi, J.J. Lewandowski, Improved understanding of environment-induced cracking (EIC) of sensitized 5XXX series aluminium alloys, Mater. Sci. Eng. A 682 (2017) 613–621.

[37] M. Seifi, N.J. Henry Holroyd, J.J. Lewandowski, Deformation rate and sensitization effects on environmentally assisted cracking of Al–Mg naval alloys, Corrosion 72 (2016) 264–283.

[38] T. Haruna, T. Shibata, Initiation and growth of stress corrosion cracks in type 316L stainless steel during slow strain rate testing, Corrosion 50 (10) (1994) 785–792.

[39] Y.S. Garud, Incremental damage formulation for stress corrosion cracking and its application to crack growth interpretation based on CERT data, Corrosion 46 (12) (1990) 968–974.

[40] K. Máthis, D. Prchal, R. Novotný, P. H“ahner, Acoustic emission monitoring of slow strain rate tensile tests of 304L stainless steel in supercritical water environment, Corros. Sci. 53 (1) (2011) 59–63.

[41] D. Sampath, R. Akid, R. Morana, Estimation of crack initiation stress and local fracture toughness of Ni-alloys 945X (UNS N09946) and 718 (UNS N07718) under hydrogen environment via fracture surface topography analysis, Eng. Fract. Mech. 191 (2018) 324–343.

[42] B.C. Rincon Troconis, Z.D. Harris, H. Ha, J.T. Burns, J.R. Scully, The effect of heat-to-heat variations in metallurgy and hydrogen-metal interactions on the hydrogen embrittlement of Monel K-500, Mater. Sci. Eng. A 703 (2017) 533–550.

[43] Z.D. Harris, J.D. Dolph, G.L. Pioszak, B.C. Rincon Troconis, J.R. Scully, J.T. Burns, The effect of microstructural variation on the hydrogen environment-assisted cracking of Monel K-500, Metall. Mater. Trans. A: Phys. Metall. Mater. Sci. 47 (7) (2016) 3488–3510.

[44] G.K. Dey, P. Mukhopadhyay, Precipitation in the Ni–Cu-base alloy Monel K-500, Mater. Sci. Eng. 84 (1986) 177–189.

[45] L.E. Shoemaker, G.D. Smith, A century of Monel metal: 1906–2006, JOM 58 (2006) 22–26.

[46] G.K. Dey, R. Tewari, P. Rao, S.L. Wadekar, P. Mukhopadhyay, Precipitation hardening in nickel–copper base alloy Monel K 500, Metall. Trans. A 24 (12) (1993) 2709–2719.

[47] J.R. Davis, Nickel, Cobalt, and Their Alloys, ASM International, Materials Park, OH, 2000.

[48] Å. Gustafson, Coarsening of TiC in austenitic stainless steel – experiments and simulations in comparison, Mater. Sci. Eng. A 287 (1) (2000) 52–58.

[49] QQ-N-286G: Nickel–Copper–Aluminum Alloy, Wrought (UNS N05500), (2000).

[50] R.D. Bayles, T. Lemieux, F. Martin, D. Lysogorski, T. Newbauer, W. Hyland, B.A. Green, E. Hogan, T. Longazel, P. Stencel, Monel K-500 hydrogen embrittlement, Naval Surface Treatment Center MR2010 Proceedings (2010).

[51] J.H. Ai, H.M. Ha, R.P. Gangloff, J.R. Scully, Hydrogen diffusion and trapping in a precipitation-hardened nickel–copper–aluminum alloy Monel K-500 (UNS N05500), Acta Mater. 61 (9) (2013) 3186–3199.

[52] R.P. Gangloff, H.M. Ha, J.T. Burns, J.R. Scully, Measurement and modeling of hydrogen environment-assisted cracking in Monel K-500, Metall. Mater. Trans. A: Phys. Metall. Mater. Sci. 45 (9) (2014) 3814–3834.

[53] E. Martínez-Pañeda, A. Golahmar, C.F. Niordson, A phase field formulation for hydrogen assisted cracking, Comput. Methods Appl. Mech. Eng. 342 (2018) 742–761.

[54] E. Martínez-Pañeda, C.F. Niordson, On fracture in finite strain gradient plasticity, Int. J. Plast. 80 (2016) 154–167.

[55] E. Martínez-Pañeda, S. del Busto, C. Betegón, Non-local plasticity effects on notch fracture mechanics, Theor. Appl. Fract. Mech. 92 (2017) 276–287.

[56] E. Martínez-Pañeda, V.S. Deshpande, C.F. Niordson, N.A. Fleck, The role of plastic strain gradients in the crack growth resistance of metals, J. Mech. Phys. Solids 126 (2019) 136–150.

[57] J.A. Harris, R.C. Scarberry, C.D. Stephens, Effects of Hydrogen on the Engineering Properties of MONEL Nickel–Copper Alloy K-500, (2013).

[58] J.T. Burns, Z.D. Harris, J.D. Dolph, R.P. Gangloff, Measurement and modeling of hydrogen environment-assisted cracking in a Ni–Cu–Al–Ti superalloy, Metall. Mater. Trans. A: Phys. Metall. Mater. Sci. 47 (3) (2016) 990–997, https://doi.org/10.1007/s11661-015-3315-4.

[59] K. Efird, Failure of Monel Ni–Cu–Al Alloy K-500 Bolts in Seawater, (1985).

[60] L.H. Wolfe, M.W. Joosten, Failures of nickel/copper bolts in subsea application, SPE Prod. Eng. 3 (3) (1988) 382–386.

[61] L.H. Wolfe, C.C. Burnette, M.W. Joosten, Hydrogen embrittlement of cathodically protected subsea bolting alloys, Mater. Perform. 32 (1993) 14–21.

[62] S. Serebrinsky, E.A. Carter, M. Ortiz, A quantum-mechanically informed continuum model of hydrogen embrittlement, J. Mech. Phys. Solids 52 (10) (2004) 2403–2430.

[63] H.K.D.H. Bhadeshia, Prevention of hydrogen embrittlement in steels, ISIJ Int. 56 (1) (2016) 24–36.

[64] G.M. Pressouyre, I.M. Bernstein, Example of the effect of hydrogen trapping on hydrogen embrittlement, Metall. Trans. A: Phys. Metall. Mater. Sci. 12A (5) (1981) 835–844.

[65] S. Huang, D. Chen, J. Song, D.L. McDowell, T. Zhu, Hydrogen embrittlement of grain boundaries in nickel: an atomistic study, NPJ Comput. Mater. 3 (1) (2017) 1–7.

[66] A. Alvaro, I. Thue Jensen, N. Kheradmand, O.M. Løvvik, V. Olden, Hydrogen embrittlement in nickel, visited by first principles modeling, cohesive zone simulation and nanomechanical testing, Int. J. Hydrogen Energy 40 (47) (2015) 16892–16900.

[67] B. Bourdin, G.A. Francfort, J.J. Marigo, The Variational Approach to Fracture, Springer Netherlands, 2008.

[68] J.-Y. Wu, V.P. Nguyen, C.T. Nguyen, D. Sutula, S. Sinaie, S. Bordas, Phase-field modelling of fracture, Adv. Appl. Mech. 53 (2020).

[69] F.P. Duda, A. Ciarbonetti, P.J. Sánchez, A.E. Huespe, A phase-field/gradient damage model for brittle fracture in elastic–plastic solids, Int. J. Plast. 65 (2015) 269–296.

[70] F.P. Duda, A. Ciarbonetti, S. Toro, A.E. Huespe, A phase-field model for solute-assisted brittle fracture in elastic–plastic solids, Int. J. Plast. 102 (2018) 16–40.

[71] C. Miehe, F. Aldakheel, A. Raina, Phase field modeling of ductile fracture at finite strains: a variational gradient-extended plasticity-damage theory, Int. J. Plast. 84 (2016) 1–32.

[72] H. Yu, J.S. Olsen, A. Alvaro, V. Olden, J. He, Z. Zhang, A uniform hydrogen degradation law for high strength steels, Eng. Fract. Mech. 157 (2016) 56–71.

[73] E. Martínez-Pañeda, N.A. Fleck, Crack growth resistance in metallic alloys: the role of isotropic versus kinematic hardening, J. Appl. Mech. 85 (2018) 11002 (6 p.).

[74] P. Shewmon, Diffusion in Solids, 2nd ed., Springer International Publishing, 2016.

[75] W.C. Johnson, J.Y. Huh, Thermodynamics of stress-induced interstitial redistribution in body-centered cubic metals, Metall. Mater. Trans. A: Phys. Metall. Mater. Sci. 34 (12) (2003) 2819–2825.

[76] E. Martínez-Pañeda, S. del Busto, C.F. Niordson, C. Betegón, Strain gradient plasticity modeling of hydrogen diffusion to the crack tip, Int. J. Hydrogen Energy 41 (24) (2016) 10265–10274.

[77] A. Kimura, H.K. Birnbaum, On the kinetics of intergranular embrittlement of nickel by hydrogen transport from the external surface, Scr. Metall. 21 (2) (1987) 219–222.

[78] A. Oudriss, J. Creus, J. Bouhattate, E. Conforto, C. Berziou, C. Savall, X. Feaugas, Grain size and grain-boundary effects on diffusion and trapping of hydrogen in pure nickel, Acta Mater. 60 (19) (2012) 6814–6828.

[79] A.M. Brass, A. Chanfreau, Accelerated diffusion of hydrogen along grain boundaries in nickel, Acta Mater. 44 (9) (1996) 3823–3831.

[80] T. Tsuru, R.M. Latanision, Grain boundary transport of hydrogen in nickel, Scr. Metall. 16 (1982) 575–578.

[81] T. Mutschele, R. Kirchheim, Segregation and diffusion of hydrogen in grain boundaries of palladium, Scr. Metall. 21 (1987) 135–140.

[82] T.M. Harris, R.M. Latanision, Grain boundary diffusion of hydrogen in nickel, Metall. Trans. A 22 (2) (1991) 351–355.

[83] B. Ladna, H.K. Birnbaum, SIMS study of hydrogen at the surface and grain boundaries of nickel bicrystals, Acta Metall. 35 (10) (1987) 2537–2542.

[84] G. Palumbo, D.M. Doyle, A.M. El-Sherik, U. Erb, K.T. Aust, Intercrystalline hydrogen transport in nanocrystalline nickel, Scr. Metall. Mater. 25 (1991) 679–684.

[85] D.R. Arantes, X.Y. Huang, C. Marte, R. Kirchheim, Hydrogen diffusion and permeation in micro- and nanocrystalline nickel, Acta Metall. Mater. 41 (11) (1993) 3215–3222.

[86] D.M. Doyle, G. Palumbo, K.T. Aust, A.M. El-Sherik, U. Erb, The influence of intercrystalline defects on hydrogen activity and transport in nickel, Acta Metall. Mater. 43 (8) (1995) 3027–3033.

[87] B. Osman Hoch, A. Metsue, J. Bouhattate, X. Feaugas, Effects of grain-boundary networks on the macroscopic diffusivity of hydrogen in polycrystalline materials, Comput. Mater. Sci. 97 (2015) 276–284.

[88] X. Zhou, N. Mousseau, J. Song, Is hydrogen diffusion along grain boundaries fast or slow? Atomistic origin and mechanistic modeling, Phys. Rev. Lett. 122 (21) (2019) 215501.

[89] L. Zhu, J. Zhou, H. Yang, Z. Sun, Energetics and kinetics of hydrogen at the grain boundary of the Ni alloys: a first-principles study, J. Alloys Compds. 795 (2019) 343–350.

[90] D. Di Stefano, M. Mrovec, C. Els”asser, First-principles investigation of hydrogen trapping and diffusion at grain boundaries in nickel, Acta Mater. 98 (2015) 306–312.

[91] X.W. Zhou, R. Dingreville, R.A. Karnesky, Molecular dynamics studies of irradiation effects on hydrogen isotope diffusion through nickel crystals and grain boundaries, Phys. Chem. Chem. Phys. 20 (1) (2017) 520–534.

[92] J. Yao, J.R. Cahoon, Experimental studies of grain boundary diffusion of hydrogen in metals, Acta Metall. Mater. 39 (1) (1991) 119–126.

[93] J. Yao, S.A. Meguid, Hydrogen diffusion and intergranular cracking in nickel, Int. J. Hydrogen Energy 22 (10–11) (1997) 1021–1026.

[94] H.H. Johnson, Hydrogen gas embrittlement, in: I.M. Bernstein, A.W. Thompson (Eds.), Hydrogen in Metals, ASM International, 1974, pp. 35–49.

[95] A. Needleman, V. Tvergaard, An analysis of ductile rupture in notched bars, J. Mech. Phys. Solids 32 (6) (1984) 461–490.

[96] J.R. Davis (Ed.), Tensile Testing, ASM International, 2004.

[97] A. Turnbull, D.H. Ferriss, H. Anzai, Modelling of the hydrogen distribution at a crack tip, Mater. Sci. Eng. A 206 (1) (1996) 1–13.

[98] C.V. Di Leo, L. Anand, Hydrogen in metals: a coupled theory for species diffusion and large elastic–plastic deformations, Int. J. Plast. 43 (2013) 42–69.

[99] A. Díaz, J.M. Alegre, I.I. Cuesta, Coupled hydrogen diffusion simulation using a heat transfer analogy, Int. J. Mech. Sci. 115–116 (2016) 360–369.

[100] E. Martínez-Pañeda, S. Natarajan, S. Bordas, Gradient plasticity crack tip characterization by means of the extended finite element method, Comput. Mech. 59 (5) (2017) 831–842.

[101] S.P. Lynch, Environmentally assisted cracking: overview of evidence for an adsorption-induced localised-slip process, Acta Metall. 36 (10) (1988) 2639–2661.

[102] H.K. Birnbaum, P. Sofronis, Hydrogen-enhanced localized plasticity – a mechanism for hydrogen related fracture, Mater. Sci. Eng. A 176 (1994) 191–202.

[103] R.A. Oriani, A mechanistic theory of hydrogen embrittlement of steels, Berich. Bunsengesellsch. Phys. Chem. 76 (8) (1972) 848–857.

[104] A.R. Troiano, The role of hydrogen and other interstitials in the mechanical behavior of metals: (1959 Edward De Mille Campbell Memorial Lecture), Metallogr. Microstruct. Anal. 5 (6) (2016) 557–569.

[105] D.E. Jiang, E.A. Carter, First principles assessment of ideal fracture energies of materials with mobile impurities: implications for hydrogen embrittlement of metals, Acta Mater. 52 (16) (2004) 4801–4807.

[106] M.L. Jokl, V. Vitek, C.J. McMahon, Microscopic theory of brittle fracture in deformable solids: a relation between ideal work to fracture and plastic work, Acta Metall. 28 (11) (1980) 1479–1488.

[107] Z.D. Harris, J.J. Bhattacharya, J.A. Ronevich, M.A. Ritzo, S.R. Agnew, J.T. Burns, The effect of hydrogen and aging condition on the deformation and fracture behavior of a precipitation-hardened nickel-base superalloy, (2020) (in review).

[108] R.N. Parkins, Development of strain-rate testing and its implications, Stress Corrosion Cracking – The Slow Strain-Rate Technique, ASTM International, West Conshohocken, PA, 1979, pp. 5–25.

[109] Y. Lee, R.P. Gangloff, Measurement and modeling of hydrogen environment-assisted cracking of ultra-high-strength steel, Metall. Mater. Trans. A: Phys. Metall. Mater. Sci. 38A (13) (2007) 2174–2190, https://doi.org/10.1007/s11661-006-9051-z.

[110] C. Miehe, M. Hofacker, F. Welschinger, A phase field model for rate-independent crack propagation: robust algorithmic implementation based on operator splits, Comput. Methods Appl. Mech. Eng. 199 (45–48) (2010) 2765–2778.

[111] G. Papazafeiropoulos, M. Muñiz-Calvente, E. Martínez-Pañeda, Abaqus2Matlab: a suitable tool for finite element post-processing, Adv. Eng. Softw. 105 (2017) 9–16.

[112] A. Turnbull, Perspectives on hydrogen uptake, diffusion and trapping, Int. J. Hydrogen Energy 40 (47) (2015) 16961–16970.

[113] Y. Renard, K. Poulios, Automated FE Modeling of Multiphysics Problems Based on a Generic Weak Form Language, (2019) pp. 1–51 (in review).

[114] S. del Busto, C. Betegón, E. Martínez-Pañeda, A cohesive zone framework for environmentally assisted fatigue, Eng. Fract. Mech. 185 (2017) 210–226.

- ARTÍCULO 2-

GRADIENT-ENHANCED STATISTICAL ANALYSIS

OF CLEAVAGE FRACTURE

Autores: E. Martínez-Pañeda, S. Fuentes-Alonso, C. Betegón

Gradient-enhanced statistical analysis of cleavage fracture

Emilio Martínez-Pañeda[a,*], Sandra Fuentes-Alonso[b], Covadonga Betegón[b]

[a] Department of Engineering, Cambridge University, CB2 1PZ Cambridge, UK
[b] Department of Construction and Manufacturing Engineering, University of Oviedo, Gijón 33203, Spain

ABSTRACT

We present a probabilistic framework for brittle fracture that builds upon Weibull statistics and strain gradient plasticity. The constitutive response is given by the mechanism-based strain gradient plasticity theory, aiming to accurately characterize crack tip stresses by accounting for the role of plastic strain gradients in elevating local strengthening ahead of cracks. It is shown that gradients of plastic strain elevate the Weibull stress and the probability of failure for a given choice of the threshold stress and the Weibull parameters. The statistical framework presented is used to estimate failure probabilities across temperatures in ferritic steels. The framework has the capability to estimate the three statistical parameters present in the Weibull-type model without any prior assumptions. The calibration against experimental data shows important differences in the values obtained for strain gradient plasticity and conventional J2 plasticity. Moreover, local probability maps show that potential damage initiation sites are much closer to the crack tip in the case of gradient-enhanced plasticity. Finally, the fracture response across the ductile-to-brittle regime is investigated by computing the cleavage resistance curves with increasing temperature. Gradient plasticity predictions appear to show a better agreement with the experiments.

1. Introduction

Macroscopic fracturing in metallic materials depends sensitively on properties that pertain to the micro and atomic scales. Not surprisingly, a considerable effort has been made to link scales in fracture mechanics, with the ultimate goal of quantitatively predicting the strength, durability, and reliability of structural components (Suo et al., 1993; Hutchinson, 1997). These endeavours aim at spanning the wide range of scales at stake by enriching continuum theories to properly characterize behaviour at the small scales involved in crack tip deformation.

The deficiencies intrinsic to conventional plasticity theory provide a strong motivation for developing mechanistically-based models. Namely, unrealistically low stresses are predicted ahead of the crack tip, with toughness being unbounded for cohesive strengths of approximately 3 times the yield stress in a perfectly plastic material ($\hat{\sigma}/\sigma_Y \rightarrow 4$ in a mild hardened solid, see Tvergaard and Hutchinson, 1992). Opening stresses on the order of 3–5 times the initial tensile yield stress fail to explain decohesion at the atomic scale. Cleavage fracture in the presence of significant plastic flow has been experimentally observed in numerous material systems (Elssner et al., 1994; Bagchi and Evans, 1996; Korn et al., 2002). Since atomic separation requires traction levels on the order of the theoretical lattice strength

($10\sigma_Y$ or larger), classic continuum theories would appear to rule out a fracture mechanism based on atomic decohesion whenever plasticity develops in the vicinity of the crack. Moreover, conventional plasticity predictions reveal important discrepancies with separation strengths calculated from first principles (Raynolds et al., 1996), and toughness bounds attained by discrete dislocation dynamics (Cleveringa et al., 2000; Irani et al., 2017), highlighting the need to bridge the gap between macroscopic modelling of cracking and the microstructural and atomistic mechanisms of fracture.

Small scale experiments have consistently shown that conventional plasticity theory is unable to characterize the material response of metals at the micro level. Fostered by growing interest in microtechnology, a wide range of mechanical tests on micro-sized specimens have revealed that metallic materials display strong size effects when deformed non-uniformly into the plastic range. Experiments such as indentation (Nix and Gao, 1998), torsion (Fleck et al., 1994), or bending (Stölken and Evans, 1998) predict a 3-fold increase in the effective flow stress by reducing specimen size (*smaller is stronger*). This size effect is attributed to gradients of plastic strain that require a definite density of dislocations to accommodate lattice curvature (Ashby, 1970). These geometrically necessary dislocations (GNDs) are not accounted for in conventional theories of plasticity, neglecting the length

---

* Corresponding author.
  E-mail address: mail@empaneda.com (E. Martínez-Pañeda).

scale dependency intrinsically associated with plastic flow. A large theoretical literature has appeared seeking to extend plasticity theory to small scales by the development of isotropic strain gradient plasticity (SGP) formulations (Aifantis, 1984; Gao et al., 1999; Fleck and Hutchinson, 2001; Anand et al., 2005). Using SGP theories to provide an implicit multi-scale characterization of the mechanical response ahead of a crack appears imperative as, independently of the size of the specimen, the plastic zone adjacent to the crack tip is physically small and contains strong spatial gradients of deformation (Martínez-Pañeda and Betegón, 2015). The investigation of stationary crack tip fields has shown that plastic strain gradients promote local strain hardening and lead to much higher stresses relative to classic plasticity predictions (Jiang et al., 2001; Wei, 2006; Komaragiri et al., 2008; Martínez-Pañeda et al., 2017b). Accurately capturing crack tip stresses has proven to be fundamental in predicting fatigue damage (Gil-Sevillano, 2001; Brinckmann and Siegmund, 2008; Pribe et al., 2019), notch fracture mechanics (Martínez-Pañeda et al., 2017a), microvoid cracking (Tvergaard and Niordson, 2008), and hydrogen assisted failure (Martínez-Pañeda et al., 2016a, b). Since plastic strain gradients can alter crack tip stresses over several tens of μm, it is expected that strain gradient plasticity models will also play an important role in the modelling of cleavage fracture and the ductile-to-brittle transition (Martínez-Pañeda et al., 2019; Qian et al., 2011).

Cleavage fracture models are grounded on the concept of micro-cracks nucleating from defects, such as inclusions or second-phase particles (Pineau et al., 2016). The location of these defects is statistical by nature and, consequently, modelling efforts rely mainly on prob-abilistic analysis. The seminal work by the Beremin group (Beremin, 1983) established the fundamental framework on which most cleavage models stand; Weibull statistics and the weakest link model are em-ployed to estimate the probability of failure P_f, where P_f equals the probability of sampling (at least) one critical fracture-triggering par-ticle. In these models the stress level is the driving force for fracture and, consequently, local strengthening due to plastic strain gradients will influence failure probability predictions.

In this work, we make use of a mechanism-based strain gradient plasticity formulation to accurately characterize crack tip stresses. The constitutive description is coupled with a probabilistic framework capable of obtaining all the statistical parameters of the model without any prior assumptions. The capabilities of the present mechanism-based scheme for probabilistic analysis of brittle fracture are benchmarked against experimental data from the Euro toughness project (Heerens and Hellmann, 2002). Experiments are reproduced over a wide range of temperatures, so as to span the ductile-to-brittle regime. Strain gradient plasticity predictions are compared with results from conventional plasticity and insight is gained into the role of the stress elevation due to strain gradients in assessing cleavage.

2. Numerical model

The implicitly multi-scale statistical framework for brittle fracture presented stands on a Taylor-based strain gradient plasticity formula-tion (Section 2.1), and a three-parametric Weibull type statistical model (Section 2.2). The implementation is carried out by coupling a general purpose finite element program with the statistical tools of Matlab, see Section 2.3. An experimental campaign employing Compact Tension specimens will be reproduced to highlight the capabilities of the model (Section 2.4).

2.1. Mechanism-based strain gradient plasticity

We model strain gradient effects by means of the so-called me-chanism-based strain gradient (MSG) plasticity theory (Gao et al., 1999; Qiu et al., 2003). MSG plasticity is grounded on Taylor's dislocation model. Accordingly, the shear flow stress τ is formulated in terms of the dislocation density ρ as

$$\tau = \alpha \mu b \sqrt{\rho} \tag{1}$$

where μ is the shear modulus, b is the magnitude of the Burgers vector and α is an empirical coefficient that is taken to be equal to 0.5. The dislocation density is additively composed of the density ρ_S for statis-tically stored dislocations (SSDs) and the density ρ_G for geometrically necessary dislocations (GNDs),

$$\rho = \rho_S + \rho_G \tag{2}$$

The GND density ρ_G is related to the effective plastic strain gradient η^p by

$$\rho_G = \bar{r} \frac{\eta^p}{b} \tag{3}$$

where $\bar{r}$ is the Nye-factor which is assumed to be 1.90 for face-centred-cubic (fcc) polycrystals. Gao et al. (1999) used three quadratic in-variants of the plastic strain gradient tensor to represent the effective plastic strain gradient η^p as

$$\eta^p = \sqrt{c_1 \eta_{iik}^p \eta_{ijk}^p + c_2 \eta_{ijk}^p \eta_{ijk}^p + c_3 \eta_{ijk}^p \eta_{kji}^p} \tag{4}$$

The coefficients were determined to be equal to $c_1 = 0$, $c_2 = 1/4$ and $c_3 = 0$ from three dislocation models for bending, torsion and void growth. Accordingly,

$$\eta^p = \sqrt{\frac{1}{4} \eta_{ijk}^p \eta_{ijk}^p} \tag{5}$$

where the components of the strain gradient tensor are obtained from

$$\eta_{ijk}^p = \varepsilon_{ik,j}^p + \varepsilon_{jk,i}^p - \varepsilon_{ij,k}^p \tag{6}$$

The tensile flow stress σ_{flow} is related to the shear flow stress τ by

$$\sigma_{flow} = M\tau \tag{7}$$

with M denoting the Taylor factor, which equals 3.06 for fcc metals. Rearranging (1–3) and substituting into (7) renders

$$\sigma_{flow} = M\alpha \mu b \sqrt{\rho_S + \bar{r} \frac{\eta^p}{b}} \tag{8}$$

The SSD density ρ_S can be readily determined from (8) knowing the relation in uniaxial tension between the flow stress and the material stress-strain curve,

$$\rho_S = [\sigma_{ref} f(\varepsilon^p)/(M\alpha \mu b)]^2 \tag{9}$$

Here, σ_{ref} is a reference stress and f is a non-dimensional function of the plastic strain ε^p, as given by the uniaxial stress-strain curve. Substituting into (8), the flow stress σ_{flow} reads

$$\sigma_{flow} = \sigma_{ref} \sqrt{f^2(\varepsilon^p) + \ell \eta^p} \tag{10}$$

where ℓ is the intrinsic material length parameter that enters the con-stitutive equation for dimensional consistency. The value of ℓ can be obtained by fitting micro-scale experiments and typically ranges be-tween 1 and $10\,\mu m$. The model recovers the conventional plasticity solution when $\ell = 0$.

2.2. Weibull three-parametric

We present a statistical framework that has the capability of pre-dicting brittle and ductile failure and requires no prior assumptions (Muñiz-Calvente et al., 2015; Papazafeiropoulos et al., 2017). First, for a given Weibull stress σ_w and a threshold stress for crack growth σ_{th}, the cumulative probability of failure P_f is given by

$$P_f = 1 - \exp\left[-\left(\frac{\sigma_w - \sigma_{th}}{\sigma_u}\right)^m\right] \tag{11}$$

where σ_u and m respectively denote the scaling parameter and the modulus. Equation (11) is defined in (Beremin, 1983) without σ_{th} but

stresses smaller than the yield stress were considered innocuous, implying the assumption of $\sigma_{th} = \sigma_Y$. A global Weibull stress is defined based on weakest link considerations

$$\sigma_w = \sigma_{th} + \left[\sum_{i=1}^{n_e} (\sigma_1^i - \sigma_{th})^m (V_i/V_0) \right]^{(1/m)} \quad (12)$$

Here V_0 is a reference volume, V_i is the volume of the i*th* material unit in the fracture process zone experiencing a maximum principal stress σ_1^i, and n_e is the number of finite elements/material units in the fracture process zone. The parameter σ_{th} is needed due to the fact that cracks do not propagate below a certain threshold energy value. However, the concurrent estimation of the threshold, modulus and shape parameters remains a complicated task; a common approach lies in assuming a value for σ_{th} and estimating m and σ_u from a set of experiments by means of the maximum likelihood method (Muniz-Calvente et al., 2016a,b). Here, all three parameters (σ_{th}, m and σ_u) will be obtained by means of the following procedure (see Fig. 1):

1) First, the probability of failure is computed for all the experiments conducted at a given temperature. The P_f versus load curve, where the load is expressed in terms of the J-integral, is computed by means of

$$P_f = \frac{j - 0.3}{n_j + 0.4} \quad (13)$$

   where n_j denotes the number of experiments for a given temperature and j is the rank number.

2) A finite element analysis is conducted, and the values of σ_1^i and V_i are computed at each element for the set of critical J_i at which failure has been reported in the experiments. The domain integral method is used to compute the value of J_i in each load increment.

3) The least squares method is employed to fit the Weibull distribution by using cumulative probabilities. Since the threshold parameter σ_{th} is also an unknown, the procedure requires iterating over the following steps:

   3.1) The Weibull stress σ_w is first computed according to (12) from the information provided by the finite element model (Step 2). In (12), m and σ_{th} correspond to the values of the previous iteration (or an initial estimate, in the case of the first iteration).

   3.2) The Weibull stress σ_w is introduced in (11) and the values of σ_u, m and σ_{th} in the current iteration are computed by fitting a univariate distribution using least squares estimates of the cumulative distribution functions. Namely, the cumulative probability of failure (11) is written as,

$$\log(\sigma_u) + \log(-\log(1 - P_f))\frac{1}{m} = \log(\sigma_w - \sigma_{th}) \quad (14)$$

   introducing a linear relationship between $\log(-\log(1 - P_f))$ and $\log(\sigma_w - \sigma_{th})$. From the P_f assigned to each load (Step 1) and the Weibull stress computed for each of those loads (Step 2), we make use of least squares to fit this straight line on the transformed scale. The slope and intercept of the line provide with the values of m and σ_u for a given σ_{th}. The quality of the fit will be given by the choice of σ_{th}; we find the optimum by maximizing the coefficient of determination R^2 over all possible threshold values. The optimum value of σ_{th} is specific to the current iteration and associated values of m and σ_u.

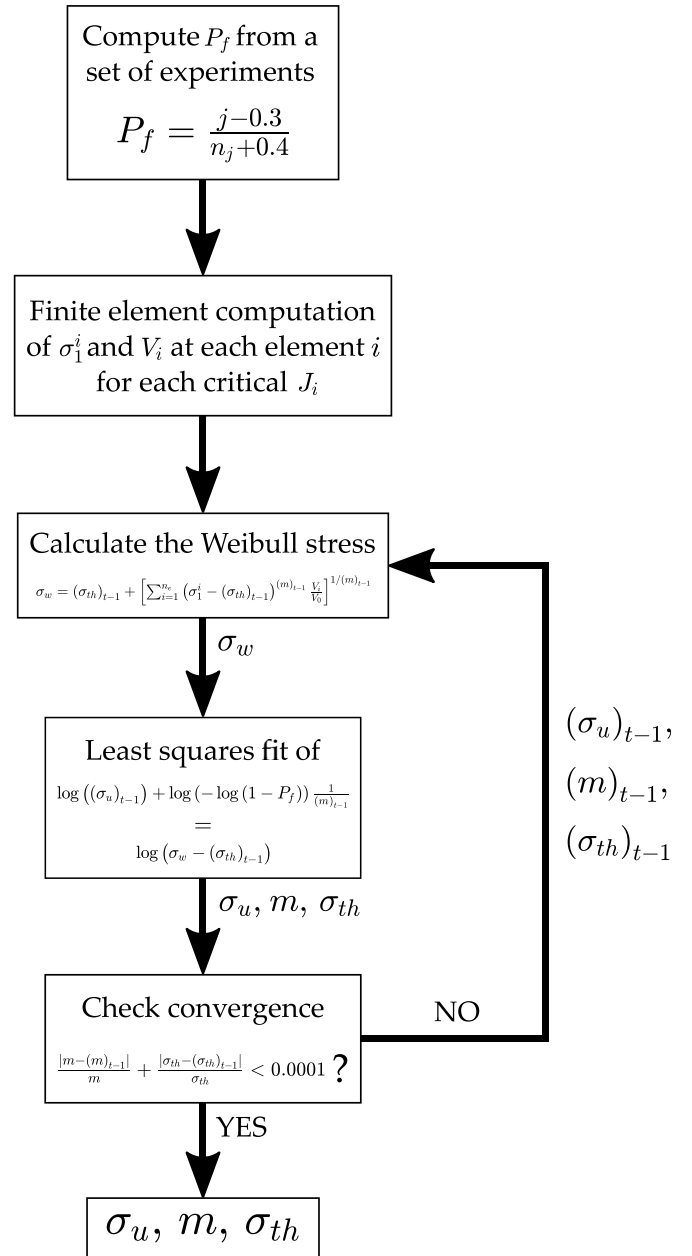   3.3) The procedure is repeated until convergence is achieved. We assume that the solution has converged when the following

Fig. 1. Flowchart describing the combined experimental-computational-statistical procedure for estimating the three Weibull parameters σ_{th}, m, and σ_{th}.

criterion has been met

$$\frac{|(m)_t - (m)_{t-1}|}{(m)_t} + \frac{|(\sigma_{th})_t - (\sigma_{th})_{t-1}|}{(\sigma_{th})_t} < 0.0001 \quad (15)$$

where $(m)_t$ denotes the value of m in the current increment while the subscript $t - 1$ represents its value in the previous increment. Consequently, the outcome of the analysis is the threshold value below which cracking will not occur σ_{th}, along with the two Weibull parameters m and σ_u. A stress level of $\sigma_{th} + \sigma_u$ will denote a 63% failure probability in a given material unit element.

2.3. Numerical implementation

The framework presented in Sections 2.1 and 2.2 is numerically implemented by exploiting Abaqus2Matlab (Papazafeiropoulos et al., 2017). Hence, we run the commercial finite element package Abaqus within the mathematical software Matlab to take advantage of Matlab's in-built capabilities for fitting univariate distributions by means of the least squares method.

We implement MSG plasticity in the commercial finite element package Abaqus by means of a user material subroutine (UMAT). For numerical reasons, we make use of the lower order version of MSG plasticity, commonly referred to as the conventional mechanism based strain gradient (CMSG) plasticity theory (Huang et al., 2004). As shown in (Martínez-Pañeda and Niordson, 2016) and discussed in (Shi et al., 2001), the lower and higher order versions of MSG plasticity predict identical results except for a boundary layer of size roughly 10 nm. This boundary layer falls outside of the domain of physical validity of continuum theories; strain gradient plasticity models a collective behaviour of dislocations and it is therefore applicable at a scale much larger than the dislocation spacing. Fortran modules are used to store the plastic strain components across Gauss integration points, and the plastic strain gradient is computed by numerical differentiation within the element. First, the plastic strain increment is interpolated through its values at the Gauss points in the isoparametric space, and afterwards the increment in the plastic strain gradient is calculated by differentiation of the shape functions. The reader is referred to (Martínez-Pañeda et al., 2017a) for more details.

2.4. Boundary value problem

We employ our framework to assess brittle failure in ferritic steels. Numerical predictions are compared to experimental results from the Euro toughness project on DIN 22NiMoCr37 steel (Heerens and Hellmann, 2002). The Euro toughness project is frequently chosen as paradigmatic benchmark for cleavage models due to the richness of its data set. Experiments are conducted at 7 temperatures, from $-154\,°C$ to $20\,°C$, spanning the entire transition from brittle to ductile fracture.

Mimicking the experimental campaign, we model a compact tension specimen of width $W = 100$ mm, distance between pins $F = 75$ mm and initial notch length $D = 51$ mm, referred to as size 2 T in (Heerens and Hellmann, 2002). The finite element model includes the compact tension specimen and the pins. The load is prescribed by imposing a displacement on the pins, and we model contact between the pins and the specimen by using a surface to surface contact algorithm with finite sliding. The path independent J-integral is computed outside of the plastic zone by means of the domain integral method at each load increment. An initial blunting radius of $2\,\mu m$ is defined at the crack tip. After a mesh sensitivity analysis, the specimen is discretized with 9800 quadrilateral quadratic plane strain elements. As shown in Fig. 2, a very refined mesh is used near the crack tip so as to accurately capture the influence of plastic strain gradients.
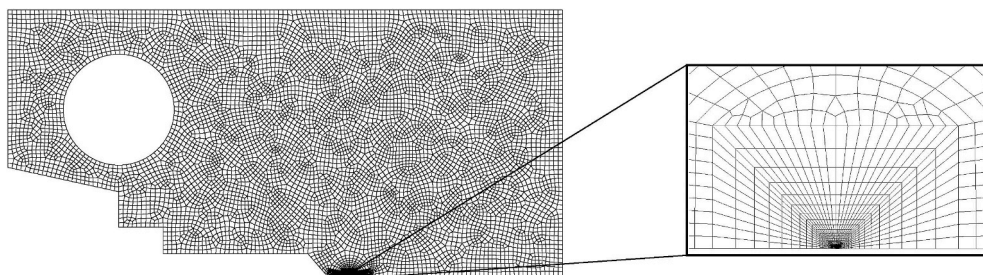
Table 1
Material properties.

Temperature ($^{\circ}C$)	-154	-91	-60	-40	-20	0	20
Yield stress σ_Y (MPa)	570	490	470	450	440	430	425
Strain hardening exponent N	0.14	0.14	0.13	0.13	0.13	0.12	0.12

3. Results

We begin our analysis by investigating the stress elevation of strain gradient plasticity and its influence on the Weibull stress distribution (Section 3.1). Then, we calibrate the Weibull parameters for each temperature and assess the probability of failure due to cleavage with both conventional and MSG plasticity theories (Section 3.2). Section 3.3 explores the response across temperatures aiming to gain insight into the role of plastic strain gradients in the ductile-to-brittle transition.

First, we define our uniaxial stress-strain hardening law as

$$\sigma = \sigma_Y \left(1 + \frac{\varepsilon^p}{\sigma_Y} \right)^N \tag{16}$$

where N is the strain hardening exponent. Thus, in (10), the reference stress equals $\sigma_{ref} = \sigma_Y \left(\frac{E}{\sigma_Y} \right)^N$ and $f(\varepsilon^p) = \left(\varepsilon^p + \frac{\sigma_Y}{E} \right)^N$. Here, Young's modulus takes the value $E = 200$ GPa, and Poisson's ratio equals $\nu = 0.3$. We proceed to calibrate N and σ_Y with the uniaxial stress-strain data available as part of the Euro toughness data set (Heerens and Hellmann, 2002). The values of yield stress σ_Y and strain hardening exponent N obtained at each temperature are listed in Table 1. A representative fit is shown in Fig. 3a for the case of a temperature of $T = -40\,°C$. As shown in Table 1, both σ_Y and N decrease with increasing temperature, in agreement with expectations. One should note that the length scale parameter of MSG plasticity has shown a negligible sensitivity to changes in temperature, as measured by Qian et al. (2014) through nanoindentation. Hence, we consider an intermediate value of $\ell = 5\,\mu m$ for all temperatures (Martínez-Pañeda and Niordson, 2016).
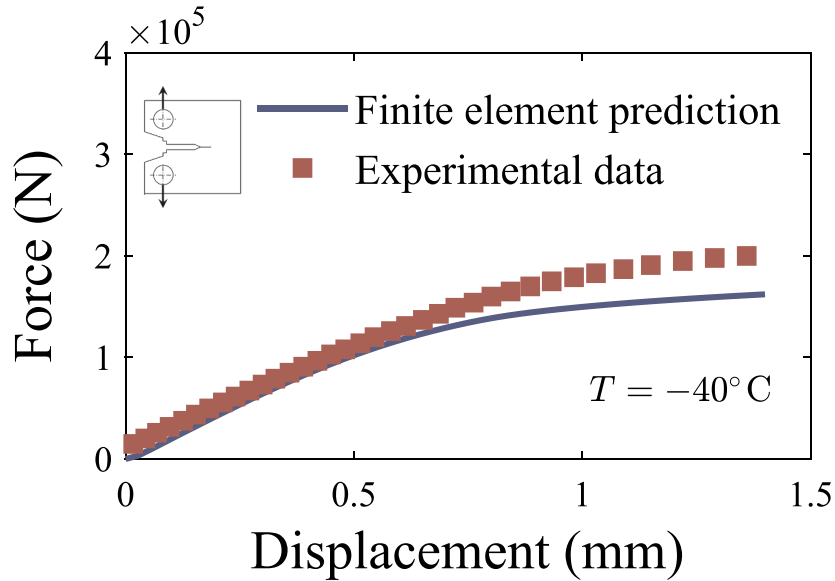
The computation of the force versus displacement curves from the calibrated values of σ_Y and N shows a good agreement with the experimental data. The results obtained for the representative case of $T = -40\,°C$ are shown in Fig. 3b. The influence of the plastic strain gradients is restricted to a small region next to the crack tip and, consequently, the macroscopic force versus displacement curve is almost insensitive to ℓ in the absence of damage. Locally, crack tip stresses are however very sensitive to local strengthening due to gradients of plastic strain.

3.1. Gradient effects on crack tip stresses

We examine first the tensile stress distribution ahead of the crack for a representative case, $T = -40\,°C$, and a specific load level that falls within the range of critical loads reported in the experiments, $J = 290$ N/mm. Results are shown in Fig. 4 for both conventional and MSG

Fig. 2. General and detailed representation of the finite element mesh employed.
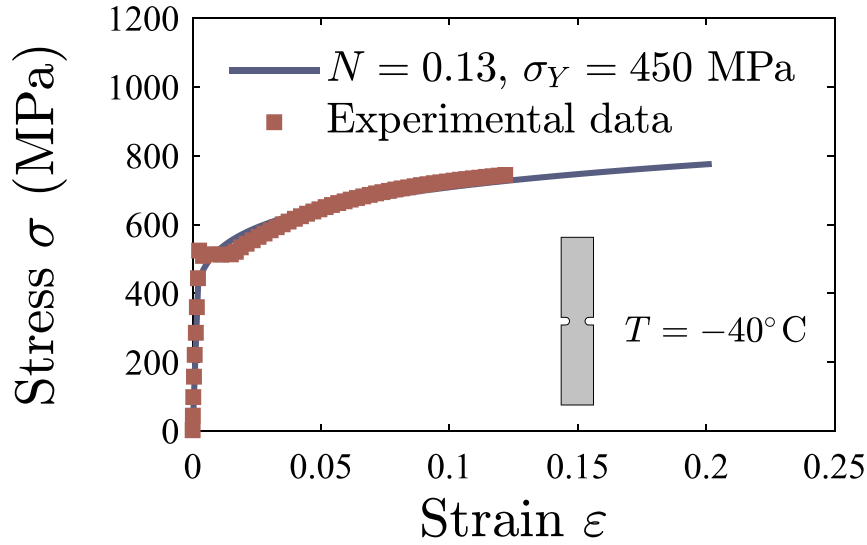
(a)

(b)

Fig. 3. Calibration of material properties: (a) Uniaxial stress-strain response, and (b) force versus displacement curve in a CT specimen. The case of temperature $T = -40\,^\circ$C is chosen as representative.

plasticity with $\ell = 5\,\mu$m. The tensile stress is normalized by the yield strength of the material at $T = -40\,^\circ$C, and the distance ahead of the crack is shown in logarithmic scale to highlight the different responses given by MSG and conventional plasticity theories. As shown in the figure, far away from the crack tip both MSG plasticity and conventional $J2$ plasticity agree but differences start at about 20–$30\,\mu$m ahead of the crack. This distance is sufficiently large to engulf the critical length of various damage mechanisms, including cleavage in ferritic steels. The stress elevation due to plastic strain gradients is associated with large geometrically necessary dislocation (GND) densities that act as obstacles to the motion of statistically stored dislocations and elevate local strength.

The stress elevation associated with large gradients of plastic strain in the vicinity of a crack influences cleavage models by elevating the Weibull stress σ_w. We illustrate this by assuming $m = 3$ and $\sigma_{th} = 2.5\sigma_Y$

and computing the Weibull stress through (12) as a function of the remote load. Results are shown in Fig. 5 for two representative values of the length scale parameter $\ell = 5\,\mu$m and $\ell = 10\,\mu$m, as well as for conventional plasticity. As shown in the figure, the Weibull stress σ_w increases with increasing ℓ and differences increase with the remote load. As we shall show below, differences are sensitive to the values of m and σ_{th}, and the gradient-enhanced σ_w elevation can be substantial. Note that, following (11), strain gradient plasticity elevates the local probability of failure for a fixed value of σ_u, σ_{th} and m.

3.2. Statistical analysis of cleavage

The statistical framework outlined in Section 2 is now employed to estimate the probability of failure as a function of the remote load, as quantified by J. Fig. 6 shows the results obtained for 4 representative
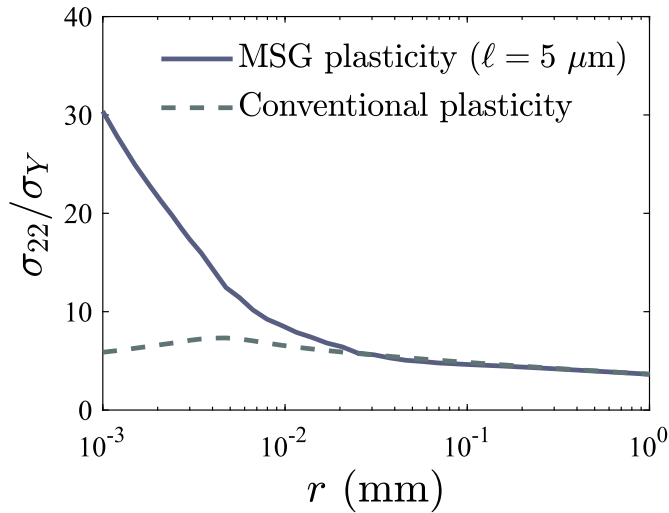
Fig. 4. Tensile stress along the extended crack plane ($x_2 = 0$) for both MSG plasticity and conventional plasticity at $J = 290$ N/mm. The distance ahead of the crack tip is given in logarithmic scale. The case of temperature $T = -40\ °$C is chosen as representative.
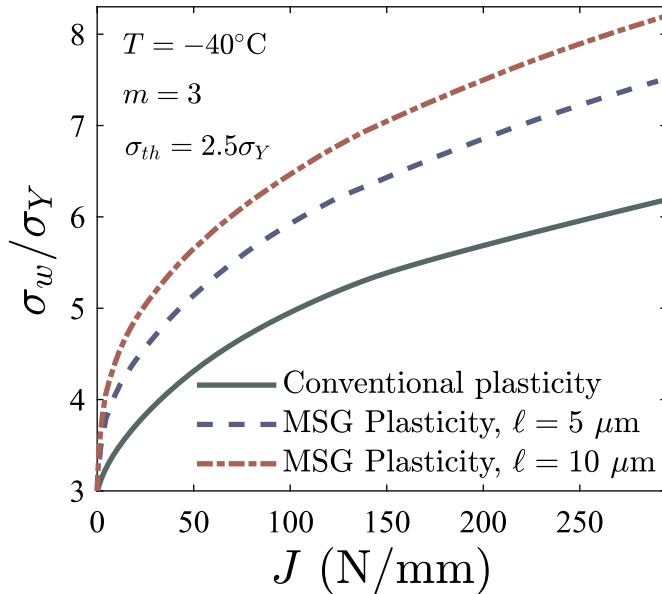

Fig. 5. Weibull stress dependence on the remote load for both MSG plasticity, with $\ell = 5\,\mu$m and $\ell = 10\,\mu$m, and conventional plasticity. The case of temperature $T = -40\ °$C is chosen as representative.

temperatures, $T = -154\ °$C, $T = -91\ °$C, $T = -60\ °$C and $T = -40\ °$C. The figure shows the experimental predictions, as given by (13), along with the results for MSG plasticity with $\ell = 5\ \mu$m and conventional J2 plasticity. Both conventional and MSG plasticity predictions exhibit good agreement with the experiments for the calibrated Weibull parameters.

The calibrated values of the modulus m, the threshold stress for crack growth σ_{th}, and the scaling parameter σ_u are shown in Table 2. Results are shown for 7 temperatures and both strain gradient and conventional plasticity. Considering the effect of plastic strain gradients leads to very significant differences in the values of the calibrated Weibull parameters. Differences between conventional and MSG plasticity are particularly notable in regards to the stress threshold for crack growth σ_{th}; much larger stresses are needed to propagate micro-cracks if the influence of GNDs is accounted for. Furthermore, qualitative differences are observed in the dependence of the threshold stress with

temperature. While the strain gradient plasticity-based prediction exhibits the natural trend of decreasing σ_{th} with decreasing T (the material anticipates a reduced barrier to cleavage), this is not the case for conventional plasticity. A plausible explanation behind the scatter observed lies on the fact that the maximum tensile stress is load-independent in conventional plasticity (McMeeking, 1977); for lower temperatures, a higher stress level is attained for the same J as σ_Y is larger. Contrarily, in strain gradient plasticity, crack tip stresses scale with the remote load (Martínez-Pañeda and Fleck, 2019).

In addition, the conventional plasticity results show noticeably high predictions for m at temperatures $-60\ °$C and $-40\ °$C. For these two temperatures, there is a clear change in the shape of the P_f versus J curve for values of P_f close to 0.75. Reducing the tolerance of the convergence criterion or changing the initial estimations of m and σ_{th} did not have any influence on the outcome of the statistical fitting procedure. Moreover, very similar results were obtained when repeating the procedure with specimens of different geometry; referred to as 0.5 T and 1 T in (Heerens and Hellmann, 2002). The uniqueness of the Weibull parameters (see, e.g., Ruggieri et al., 2000) is addressed by repeating the analysis for four different geometries (0.5, 1 T, 2 T and 4 T) and two temperatures ($-91\ °$C and $-20\ °$C). Computations reveal very similar values of m, σ_{th} and σ_u to those shown in Table 2 for both conventional and strain gradient plasticity. Differences are largest with geometry 4 T but remain below 10% in all cases.

More insight into the influence of plastic strain gradients on local failure probability can be gained by means of a *hazard map*. In a hazard map, the local probability of failure is shown over the entire engineering component, highlighting the areas that are vulnerable to a specific type of failure (Muñiz-Calvente et al., 2016a,b). The local probability of failure is computed as P_f^i in each material unit i from a local σ_w^i. The results obtained are shown in log scale in Fig. 7 for both conventional and strain gradient plasticity. Important differences can be readily observed. While the local P_f only becomes meaningful close to the crack tip in both cases, the potential damage initiation sites are identified to be much more localized for the case of strain gradient plasticity. In other words, only defects within tens of microns, as opposed to several mm, are identified as fracture-triggering particles when plastic strain gradients are accounted for. The critical distance for cleavage fracture in steels is considered to be significantly smaller than 1 mm (Watanabe et al., 1987).

3.3. The ductile to brittle transition

We then proceed to examine the ductile-to-brittle transition by computing the resistance curves for $P_f = 0.1$, 0.5 and 1 across the temperature versus load map. For each value of P_f three curves are shown, the experimental data and the numerically computed results for MSG plasticity and conventional J2 plasticity; see Fig. 8. The results show how the load at which failure is predicted, $P_f = 0.5$, increases with the temperature - ductility is enhanced. As the load and the temperature increase, ductile crack growth is observed, with the largest temperatures showing several cases where crack extension equals $\Delta a = 2$ mm, the limit value for ductile growth tests (Heerens and Hellmann, 2002). In addition, the gradient-enhanced prediction appears to follow more precisely the experimental trend.

3.4. Influence of crack tip constraint conditions

Lastly, we investigate the influence of crack tip constraint conditions by imposing a non-zero elastic T-stress (Betegon and Hancock, 1991). This is achieved by means of the so-called modified boundary layer formulation. Consider a crack plane aligned with the negative x_1 axis of the Cartesian reference frame (x_1, x_2). For a crack tip placed at the origin and a given T value, we choose to prescribe a remote mode I load, K_I, by defining the nodal displacements in the outer periphery of
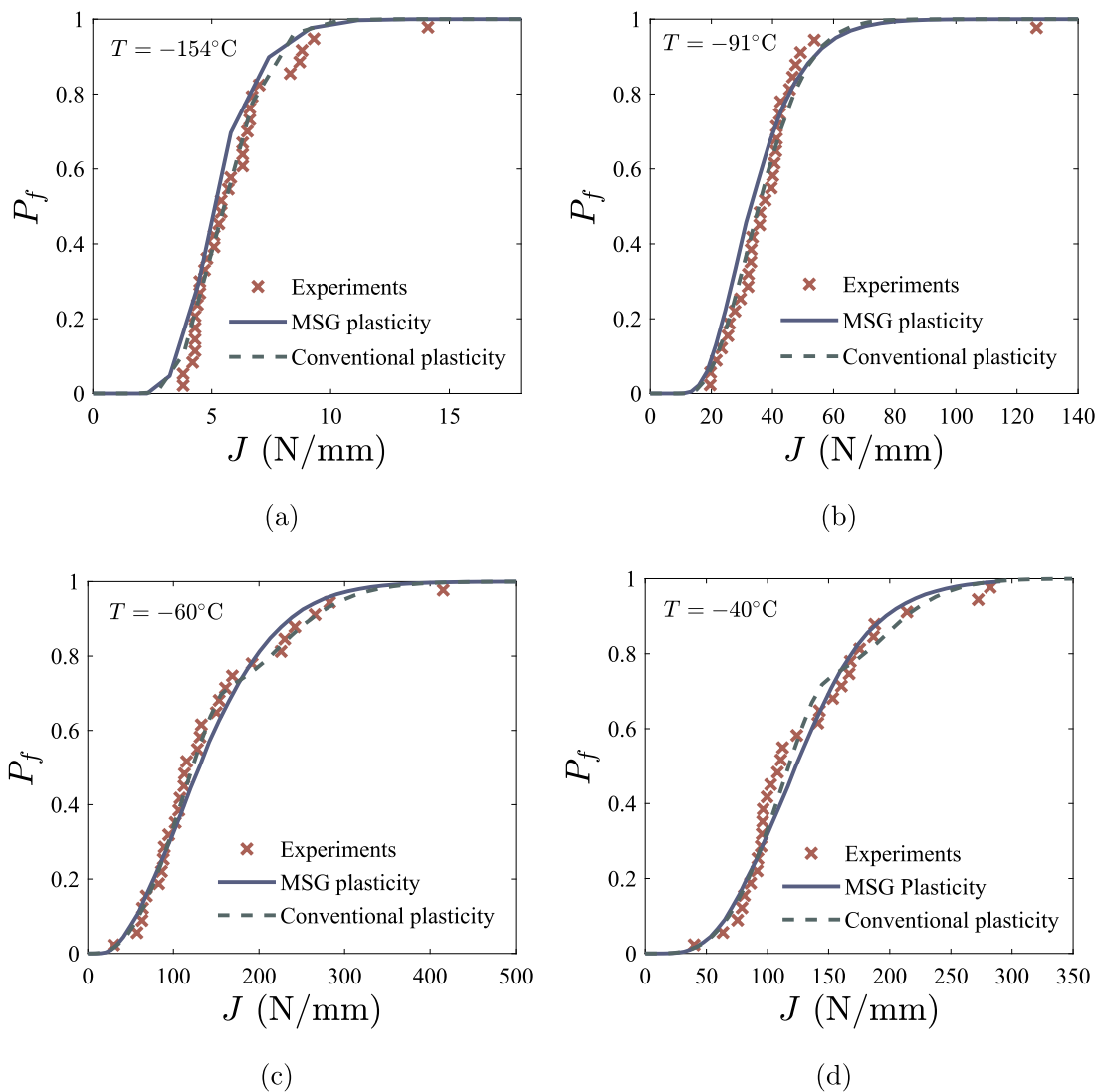
Fig. 6. Failure probability as a function of the external load. The figure includes the experimental data for 22NiMoCr37 steel (Heerens and Hellmann, 2002) and the predictions from the present statistical model for the values of σ_{th}, σ_u and m listed in Table 2. Temperatures (a) $T = -154\,^{\circ}$C, (b) $T = -91\,^{\circ}$C, (c) $T = -60\,^{\circ}$C and (d) $T = -40\,^{\circ}$C are chosen as representative.

Table 2
Calibration of Weibull parameters for MSG plasticity and conventional plasticity as a function of the temperature.

MSG plasticity							
Temperature ($^{\circ}C$)	-154	-91	-60	-40	-20	0	20
σ_u (MPa)	23.6	46.9	632.3	611.7	1060.4	183.0	16948.0
σ_{th} (MPa)	5489.3	7295.1	7670.6	8136.7	8295.9	19888.0	13516.0
m	2.0	1.9	2.9	3.1	3.2	1.7	12.71

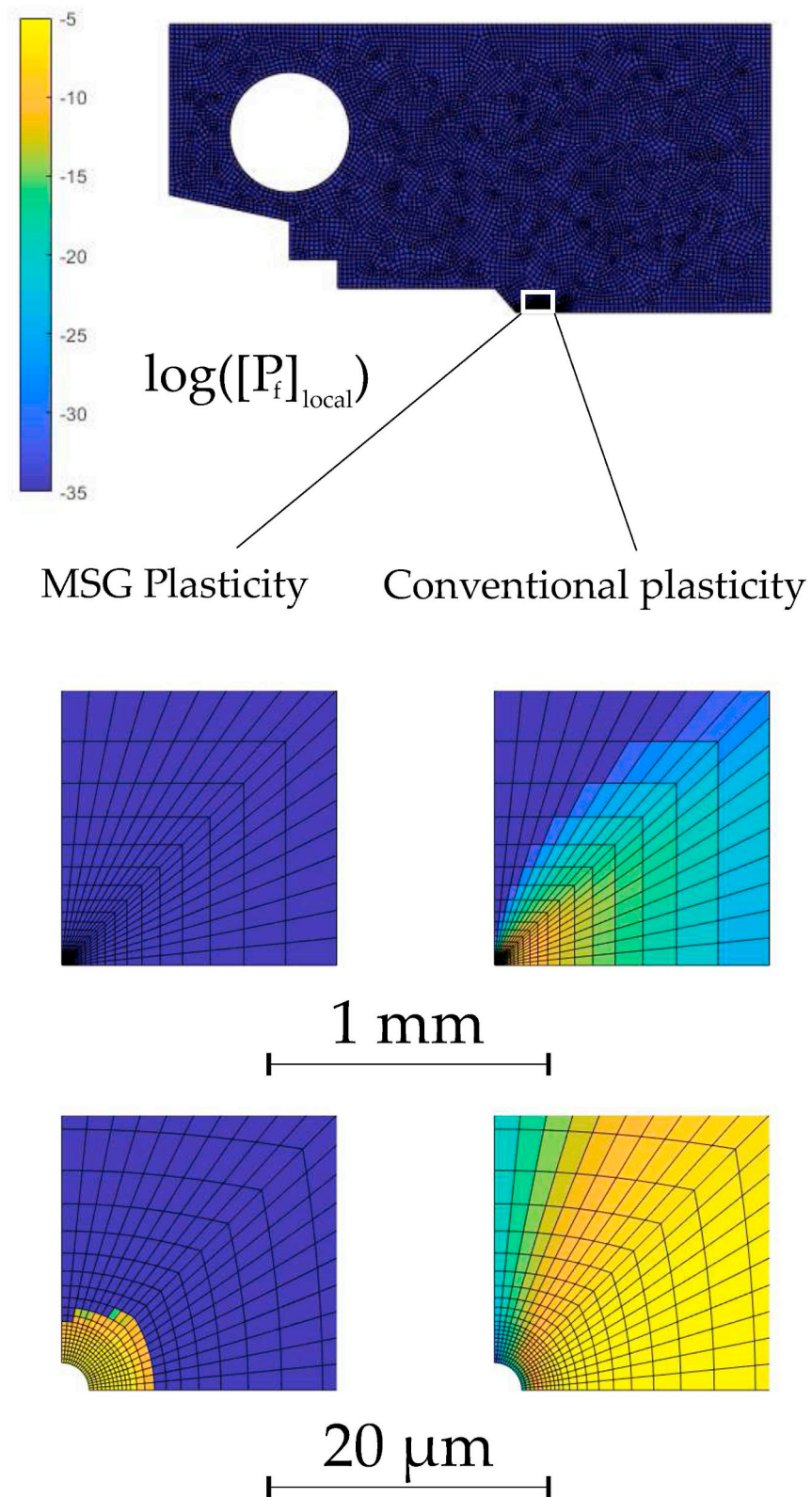| Conventional plasticity							
Temperature ($^{\circ}C$)	-154	-91	-60	-40	-20	0	20
σ_u (MPa)	9.2	14.9	1380.4	911.3	146.0	46.11	1731.7
σ_{th} (MPa)	2251.7	2459.0	1015.7	1477.5	2289.1	2205.0	1474.7
m	1.9	1.8	13.5	12.8	3.2	0.78	19.87

Fig. 7. Hazard map, showing the local probability of failure in log scale at each material unit for the case of $T = -40 \, ^\circ$C and $J = 282.2$ N/mm.
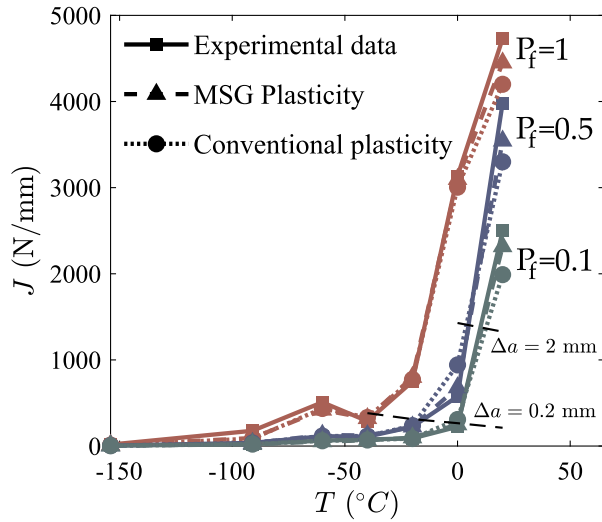
Fig. 8. Cleavage resistance curves ($P_f = 0.5$) and scatter bands ($P_f = 0.1$ and $P_f = 0.9$) for the experimental data, MSG plasticity with $\ell = 5\ \mu m$ and conventional plasticity.

the mesh as

$$u_1(r, \theta) = K_I \frac{1 + \nu}{E} \sqrt{\frac{r}{2\pi}} \cos\left(\frac{\theta}{2}\right)(3 - 4\nu - \cos\theta) + T\left(\frac{1 - \nu^2}{E}\right) r\cos\theta$$

$$(17)$$

$$u_2(r, \theta) = K_I \frac{1 + \nu}{E} \sqrt{\frac{r}{2\pi}} \sin\left(\frac{\theta}{2}\right)(3 - 4\nu - \cos\theta) - T\left(\frac{\nu(1 + \nu)}{E}\right) r\sin\theta$$

$$(18)$$

where r and θ are polar coordinates centred at the crack tip. As shown in Fig. 9, upon exploiting symmetry about the crack plane, only half of the model is analysed. We introduce an initial blunting radius that is 10^5 times smaller than the outer radius. The modified boundary layer model is discretized by means of 6422 quadrilateral quadratic plane strain elements.

The results obtained, in terms of Weibull stress σ_w versus remote load K_I are shown in Fig. 10. As in Fig. 5, we consider a temperature of $T = 40\ °C$ and assume $m = 3$ and $\sigma_{th} = 2.5\sigma_Y$. A range of 3 values of the T-stress is considered: $T/\sigma_Y = -0.5$, $T/\sigma_Y = 0$, and $T/\sigma_Y = 0.5$. The same qualitative trends are obtained for both conventional plasticity and strain gradient plasticity; for a given remote load K_I, the Weibull stress increases with increasing T. However, conventional plasticity predictions of σ_w appear to exhibit a higher sensitivity to crack tip constraint conditions for the values of m and σ_{th} assumed.
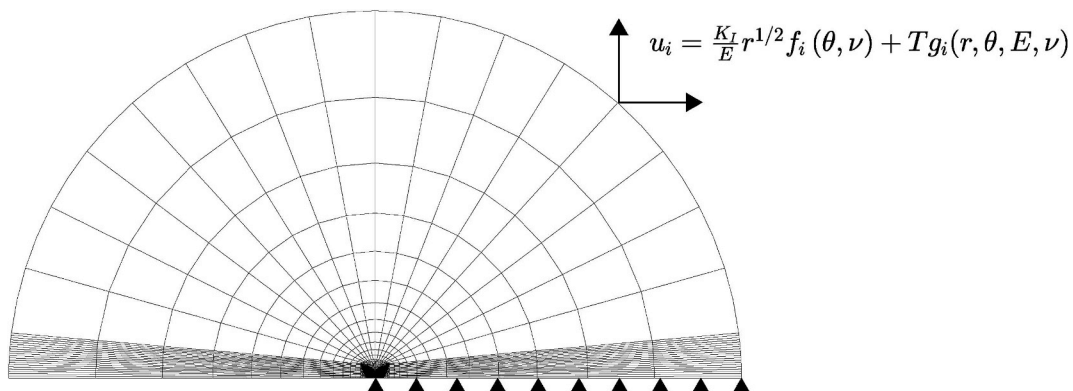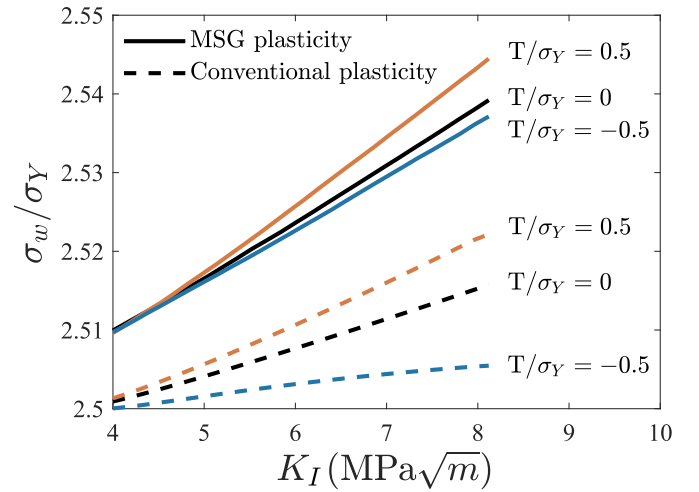

Fig. 10. Weibull stress dependence on the remote load as a function of the elastic T-stress for conventional plasticity and MSG plasticity, with $\ell = 5\ \mu m$.

4. Conclusions

We have presented a 3-parameter statistical framework for cleavage that incorporates the role of large plastic strain gradients in the characterization of crack tip stresses. The model enables to accurately compute Weibull stresses and calibrate - without any prior assumptions - the three statistical parameters: threshold stress σ_{th}, scaling parameter σ_u and modulus m. Finite element analysis is used in combination with Weibull statistics to investigate cleavage in ferritic steels with both conventional J2 plasticity and the mechanism-based strain gradient (MSG) plasticity theory. The main findings are:

i) For given values of σ_{th}, σ_u and m, strain gradient plasticity effects elevate the Weibull stress and the probability of failure.

ii) The calibrated Weibull parameters for MSG plasticity show significant differences with the values obtained with conventional plasticity. The threshold stress required to trigger cracking in the gradient-enhanced case is 2–8 times larger than its conventional plasticity counterpart.

iii) Hazard maps, where the probability of failure is shown in each material unit, show that defects susceptible of initiating cracking are confined in a much smaller region next to the crack tip in the strain gradient plasticity case.

iv) The probability of failure is computed across the ductile-to-brittle transition, with strain gradient plasticity predictions showing a better agreement with experiments.

$$u_i = \frac{K_I}{E} r^{1/2} f_i(\theta, \nu) + T g_i(r, \theta, E, \nu)$$

Fig. 9. Sketch of the modified boundary layer model employed to assess the role of crack tip constraint conditions.

Acknowledgements

References

Aifantis, E.C., 1984. On the microstructural origin of certain inelastic models. J. Eng. Mater. Technol. 106 (4), 326.

Anand, L., Gurtin, M.E., Lele, S.P., Gething, C., 2005. A one-dimensional theory of strain-gradient plasticity: formulation, analysis, numerical results. J. Mech. Phys. Solids 53 (8), 1789–1826.

Ashby, M.F., 1970. The deformation of plastically non-homogeneous materials. Phil. Mag. 21 (170), 399–424.

Bagchi, A., Evans, A.G., 1996. The mechanics and physics of thin-film decohesion and its measurement. Interface Sci. 3, 169–193.

Beremin, F.M., 1983. A local criterion for cleavage fracture of a nuclear pressure vessel steel. Metall. Trans. A 14 (11), 2277–2287.

Betegon, C., Hancock, J.W., 1991. Two-parameter characterization of elastic-plastic crack-tip fields. J. Appl. Mech. 58 (1), 104–110.

Brinckmann, S., Siegmund, T., 2008. Computations of fatigue crack growth with strain gradient plasticity and an irreversible cohesive zone model. Eng. Fract. Mech. 75 (8), 2276–2294.

Cleveringa, H., Van der Giessen, E., Needleman, A., 2000. A discrete dislocation analysis of mode I crack growth. J. Mech. Phys. Solids 48 (67), 1133–1157.

Elssner, G., Korn, D., Rühle, M., 1994. The influence of interface impurities on fracture energy of UHV diffusion bonded metal-ceramic bicrystals. Scr. Metall. Mater. 31 (8), 1037–1042.

Fleck, N.A., Hutchinson, J.W., 2001. A reformulation of strain gradient plasticity. J. Mech. Phys. Solids 49 (10), 2245–2271.

Fleck, N.A., Muller, G.M., Ashby, M.F., Hutchinson, J.W., 1994. Strain gradient plasticity: theory and experiment. Acta Metall. Mater. 42 (2), 475–487.

Gao, H., Hang, Y., Nix, W.D., Hutchinson, J.W., 1999. Mechanism-based strain gradient plasticity - I. Theory. J. Mech. Phys. Solids 47 (6), 1239–1263.

Gil-Sevillano, J., 2001. The effective threshold for fatigue crack propagation: a plastic size effect? Scripta Mater. 44 (11), 2661–2665.

Heerens, J., Hellmann, D., 2002. Development of the Euro fracture toughness dataset. Eng. Fract. Mech. 69 (4), 421–449.

Huang, Y., Qu, S., Hwang, K.C., Li, M., Gao, H., Huang, Y., Qu, S., Hwang, K.C., Li, M., Gao, H., 2004. A conventional theory of mechanism-based strain gradient plasticity. Int. J. Plast. 20 (4–5), 753–782.

Hutchinson, J.W., 1997. Linking scales in fracture mechanics. In: Advances in Fracture Research, Proceedings of ICF10, pp. 1–14.

Irani, N., Remmers, J.J.C., Deshpande, V.S., 2017. A discrete dislocation analysis of hydrogen-assisted mode-I fracture. Mech. Mater. 105, 67–79.

Jiang, H., Huang, Y., Zhuang, Z., Hwang, K.C., 2001. Fracture in mechanism-based strain gradient plasticity. J. Mech. Phys. Solids 49 (5), 979–993.

Komaragiri, U., Agnew, S.R., Gangloff, R.P., Begley, M.R., 2008. The role of macroscopic hardening and individual length-scales on crack tip stress elevation from phenomenological strain gradient plasticity. J. Mech. Phys. Solids 56 (12), 3527–3540.

Korn, D., Elssner, G., Cannon, R.M., Ruhle, M., 2002. Fracture properties of interfacially doped Nb-A12O3 bicrystals: I, fracture characteristics. Acta Mater. 50 (15), 3881–3901.

Martínez-Pañeda, E., Betegón, C., 2015. Modeling damage and fracture within strain-gradient plasticity. Int. J. Solids Struct. 59, 208–215.

Martínez-Pañeda, E., del Busto, S., Betegón, C., 2017a. Non-local plasticity effects on notch fracture mechanics. Theor. Appl. Fract. Mech. 92, 276–287.

Martínez-Pañeda, E., del Busto, S., Niordson, C.F., Betegón, C., 2016a. Strain gradient plasticity modeling of hydrogen diffusion to the crack tip. Int. J. Hydrogen Energy 41 (24), 10265–10274.

Martínez-Pañeda, E., Deshpande, V.S., Niordson, C.F., Fleck, N.A., 2019. The role of plastic strain gradients in the crack growth resistance of metals. J. Mech. Phys. Solids 126, 136–150.

Martínez-Pañeda, E., Fleck, N.A., 2019. Mode I crack tip fields: strain gradient plasticity theory versus J2 flow theory. Eur. J. Mech. A Solid. 75, 381–388.

Martínez-Pañeda, E., Natarajan, S., Bordas, S., 2017b. Gradient plasticity crack tip characterization by means of the extended finite element method. Comput. Mech. 59, 831–842.

Martínez-Pañeda, E., Niordson, C.F., 2016. On fracture in finite strain gradient plasticity. Int. J. Plast. 80, 154–167.

Martínez-Pañeda, E., Niordson, C.F., Gangloff, R.P., 2016b. Strain gradient plasticity-based modeling of hydrogen environment assisted cracking. Acta Mater. 117, 321–332.

McMeeking, R.M., 1977. Finite deformation analysis of crack-tip opening in elastic-plastic materials and implications for fracture. J. Mech. Phys. Solids 25 (5), 357–381.

Muñiz-Calvente, M., Fernández Canteli, A., Shlyannikov, V., Castillo, E., 2015. Probabilistic Weibull methodology for fracture prediction of brittle and ductile materials. Appl. Mech. Mater. 784 (2), 443–451.

Muniz-Calvente, M., Ramos, A., Pelayo, F., Lamela, M.J., Fernández-Canteli, A., 2016a. Statistical joint evaluation of fracture results from distinct experimental programs: an application to annealed glass. Theor. Appl. Fract. Mech. 85, 149–157.

Muñiz-Calvente, M., Ramos, A., Shlyannikov, V., Lamela, M.J., Fernández-Canteli, A., 2016b. Hazard maps and global probability as a way to transfer standard fracture results to reliable design of real components. Eng. Fail. Anal. 69, 135–146.

Nix, W.D., Gao, H.J., 1998. Indentation size effects in crystalline materials: a law for strain gradient plasticity. J. Mech. Phys. Solids 46 (3), 411–425.

Papazafeiropoulos, G., Muñiz-Calvente, M., Martínez-Pañeda, E., 2017. Abaqus2Matlab: a suitable tool for finite element post-processing. Adv. Eng. Software 105, 9–16.

Pineau, A., Benzerga, A.A., Pardoen, T., 2016. Failure of metals I: brittle and ductile fracture. Acta Mater. 107, 424–483.

Pribe, J.D., Siegmund, T., Tomar, V., Kruzic, J.J., 2019. Plastic strain gradients and transient fatigue crack growth: a computational study. Int. J. Fatigue 120, 283–293.

Qian, X., Zhang, S., Swaddiwudhipong, S., 2011. Calibration of Weibull parameters using the conventional mechanism-based strain gradient plasticity. Eng. Fract. Mech. 78 (9), 1928–1944.

Qian, X., Zhang, S., Swaddiwudhipong, S., Shen, L., 2014. Temperature dependence of material length scale for strain gradient plasticity and its effect on near-tip opening displacement. Fatigue Fract. Eng. Mater. Struct. 37 (2), 157–170.

Qiu, X., Huang, Y., Wei, Y., Gao, H., Hwang, K., 2003. The flow theory of mechanism-based strain gradient plasticity. Mech. Mater. 35 (3–6), 245–258.

Raynolds, J.E., Smith, J.R., Zhao, G.L., Srolovitz, D.J., 1996. Adhesion in NiAl-Cr from first principles. Phys. Rev. B 53 (20), 13883–13890.

Ruggieri, C., Gao, X., Dodds, R.H., 2000. Transferability of elastic-plastic fracture toughness using the Weibull stress approach: significance of parameter calibration. Eng. Fract. Mech. 67 (2), 101–117.

Shi, M., Huang, Y., Jiang, H., Hwang, K.C., Li, M., 2001. The boundary-layer effect on the crack tip field in mechanism-based strain gradient plasticity. Int. J. Fract. 112 (1), 23–41.

Stölken, J.S., Evans, A.G., 1998. A microbend test method for measuring the plasticity length scale. Acta Mater. 46 (14), 5109–5115.

Suo, Z., Shih, C.F., Varias, A.G., 1993. A theory for cleavage cracking in the presence of plastic flow. Acta Metall. Mater. 41 (5), 1551–1557.

Tvergaard, V., Hutchinson, J.W., 1992. The relation between crack growth resistance and fracture process parameters in elastic-plastic solids. J. Mech. Phys. Solids 40 (6), 1377–1397.

Tvergaard, V., Niordson, C.F., 2008. Size effects at a crack-tip interacting with a number of voids. Phil. Mag. 88 (30–32), 3827–3840.

Watanabe, J., Iwadate, T., Tanaka, Y., Yokobori, T., Ando, K., 1987. Fracture toughness in the transition region. Eng. Fract. Mech. 28 (5–6), 589–600.

Wei, Y., 2006. A new finite element method for strain gradient theories and applications to fracture analyses. Eur. J. Mech. A Solid. 25 (6), 897–913.

- ARTÍCULO 3-

FRACTURE IN DISTORTION GRADIENT PLASTICITY

Fracture in distortion gradient plasticity

Sandra Fuentes-Alonso[a], Emilio Martínez-Pañeda[b,c,*]

[a] *Department of Construction and Manufacturing Engineering, University of Oviedo, Gijón 33203, Spain*
[b] *Department of Civil and Environmental Engineering, Imperial College London, London SW7 2AZ, UK*
[c] *Department of Engineering, Cambridge University, Cambridge CB2 1PZ, UK*

ABSTRACT

Due to its superior modelling capabilities, there is an increasing interest in *distortion* gradient plasticity theory, where the role of the plastic spin is accounted for in the free energy and the dissipation. In this work, distortion gradient plasticity is used to gain insight into material deformation ahead of a crack tip. This also constitutes the first fracture mechanics analysis of gradient plasticity theories adopting Nye's tensor as primal kinematic variable. First, the asymptotic nature of crack tip fields is analytically investigated. A generalised *J*-integral is defined and employed to determine the power of the singularity. We show that an inner elastic region exists, adjacent to the crack tip, where elastic strains dominate plastic strains and Cauchy stresses follow the linear elastic $r^{-1/2}$ stress singularity. This finding is verified by detailed finite element analyses using a new numerical framework, which builds upon a viscoplastic constitutive law that enables capturing both rate-dependent and rate-independent behaviour in a computationally efficient manner. Numerical analysis is used to gain further insight into the stress elevation predicted by distortion gradient plasticity, relative to conventional J_2 plasticity, and the influence of the plastic spin under both mode I and mixed-mode fracture conditions. It is found that Nye's tensor contributions have a weaker effect in elevating the stresses in the plastic region, while predicting the same asymptotic behaviour as constitutive choices based on the plastic strain gradient tensor. A minor sensitivity to χ, the parameter governing the dissipation due to the plastic spin, is observed. Finally, distortion gradient plasticity and suitable higher order boundary conditions are used to appropriately model the phenomenon of brittle failure along elastic-plastic material interfaces. We reproduce paradigmatic experiments on niobium-sapphire interfaces and show that the combination of strain gradient hardening and dislocation blockage leads to interface crack tip stresses that are larger than the theoretical lattice strength, rationalising cleavage in the presence of plasticity at bi-material interfaces.

© 2020 Elsevier Ltd. All rights reserved.

1. Introduction

In recent years, there has been an increasing interest in characterising the behaviour of metals at the micrometer scale. Examples are found in microelectromechanical systems (MEMS), microelectronic components, and thin film applications. A wide array of micron scale experiments have revealed that metals display pronounced size effects when deformed non-

uniformly into the plastic range; see (Voyiadjis & Song, 2019) for a review. Notable pioneering examples are the wire torsion experiments by Fleck, Muller, Ashby, and Hutchinson (1994), the nanoindentation measurements by Nix and Gao (1998), and the bending of foils by Stölken and Evans (1998). Fleck et al. (1994) tested very thin copper wires (with radius varying from 6 to 85 μm) under both uniaxial tension and torsion. Results revealed only a minor influence of specimen size on tensile behaviour but a systematic increase in torsional strengthening with decreasing wire diameter. Nix and Gao (1998) found a linear relation between the indentation depth and the hardness of single crystal and cold worked polycrystalline copper. This size effect becomes negligible as the indentation depth is increased beyond a characteristic length on the order of micrometers. Stölken and Evans (1998) conducted micro-bending tests on nickel foils of different thicknesses, showing that thinner specimens are stronger and strain harden more than thicker ones. Uniaxial tension tests were also conducted and, as in the work by Fleck et al. (1994), almost no influence of specimen size is observed. Thus, the *smaller is harder* or *smaller is stronger* trends observed in the aforementioned micron scale experiments are intrinsically associated with the presence of strain gradients. In terms of the underpinning dislocation phenomena, work hardening is controlled by the total density of dislocations, part of which is related to the gradients of plastic strain. Thereby, dislocation storage governing material hardening is due to: (i) dislocations that trap each other in a random way and (ii) dislocations required for compatible deformation of various parts of the crystal (Ashby, 1970). The latter are referred to as Geometrically Necessary Dislocations (GNDs) while the former are named Statistically Stored Dislocations (SSDs). GNDs do not contribute to plastic strain but to material work hardening by acting as obstacles to the motion of SSDs. This extra storage of dislocations associated with gradients of plastic strain will manifest its influence when the characteristic length of deformation becomes sufficiently small.

Experimental evidence of strain gradient hardening has been accompanied by a vast literature on the development of enriched isotropic plasticity models, so-called strain gradient plasticity theories (see, e.g. Aifantis, 1992; Berdichevsky & Sedov, 1967; Dillon & Kratochvil, 1970; Fleck & Hutchinson, 1993; Fleck & Hutchinson, 2001; Gudmundson, 2004; Gurtin & Anand, 2005; Idiart, Deshpande, Fleck, & Willis, 2009 and references therein). Consistent with experimental observations, theoretical models are cast in a form where the plastic work depends on both strains and strain gradients; introducing a material length scale ℓ, and reducing to conventional plasticity when the length scales of the imposed deformation gradients are large compared to ℓ. Recent theoretical developments have been aimed at capturing a wide range of experimental observations. Thus, modern strain gradient plasticity formulations consider both dissipative (or unrecoverable) and energetic (or recoverable) gradient contributions, to capture both the strengthening and hardening effects observed (Fleck & Willis, 2009; Gudmundson, 2004; Gurtin & Anand, 2005). In addition, the form of the free energy has received particular interest (Bardella & Panteghini, 2015; Garroni, Leoni, & Ponsiglione, 2010; Lancioni, Yalçinkaya, & Cocks, 2015; Ohno & Okumura, 2007; Panteghini, Bardella, & Niordson, 2019; Wulfinghoff, Forest, & Böhlke, 2015). Gradient effects are accounted for by means of an additional contribution to the Helmholtz free energy, the so-called defect energy. Choices include the use of plastic strains or Nye's tensor as primal higher order kinematic variables, considering one or more invariants of the primal variable, and exploring less-than-quadratic forms of the defect energy. Also, increased attention has been focused on the need to account for the plastic spin in recent years, as originally proposed by Gurtin (2004), to properly describe plastic flow incompatibility and the associated dislocation densities. This class of gradient plasticity models is referred to as *distortion* gradient plasticity, as it builds upon the incompatibility of the plastic part of the displacement gradient and the macroscopic characterisation of the Burgers vector (Burgers, 1939; Fleck & Hutchinson, 1997; Gurtin, 2004; Nye, 1953) to rigorously define Nye's tensor as:

$$\alpha_{ij} = \epsilon_{jkl}\gamma^p_{il,k} \qquad (\boldsymbol{\alpha} = \mathrm{curl}\, \boldsymbol{\gamma}^p) \tag{1}$$

where γ^p_{ij} is the plastic distortion - the plastic part of the displacement gradient. The increasing popularity of distortion gradient plasticity lies on its superior modelling capabilities. As shown by Bardella and co-workers (Bardella and Giacomini, 2008; Bardella, 2009;2010 and Poh and Peerlings (2016), the contribution of the non-symmetric plastic part of the displacement gradient plays a fundamental role in capturing essential features of crystal plasticity. Moreover, Poh and Peerlings (2016) showed that the localization phenomenon that takes place in Bittencourt, Needleman, Gurtin, and Van der Giessen (2003) composite unit cell benchmark problem can only be reproduced by distortion gradient plasticity. Other recent works involve the development of new homogenization formulations (Poh, 2013; Poh & Phan, 2016) and finite element schemes (Martínez-Pañeda, Niordson, & Bardella, 2016c; Panteghini & Bardella, 2016; 2018). However, the implications of distortion gradient plasticity on crack tip mechanics remain to be addressed.

Strain gradient effects are typically characterised *via* micro-scale experiments but are present in any boundary value problem where the strain varies over microns. This is the case of fracture mechanics problems where, independently of the size of the cracked sample, the plastic zone adjacent to the crack tip is typically small and contains large spatial gradients of plastic deformation. The analysis of stationary cracks with strain gradient plasticity reveals that local strain gradient hardening elevates crack tip stresses far beyond conventional plasticity predictions (Komaragiri, Agnew, Gangloff, & Begley, 2008; Martínez-Pañeda & Betegón, 2015; Martínez-Pañeda & Niordson, 2016; Wei & Hutchinson, 1997). The stress elevation predicted by strain gradient plasticity provides a rationale for brittle fracture in the presence of plasticity (Martínez-Pañeda, Deshpande, Niordson, & Fleck, 2019a; Wei & Hutchinson, 1997) and has important implications for a number of structural integrity problems, such as hydrogen embrittlement (Kristensen, Niordson, & Martínez-Pañeda, 2020; Martínez-Pañeda, Niordson, & Gangloff, 2016a), fatigue damage (Brinckmann & Siegmund, 2008; Pribe, Siegmund, Tomar, & Kruzic, 2019), and low-temperature cleavage (Martínez-Pañeda, Fuentes-Alonso, & Betegón, 2019b; Qian, Zhang, & Swaddiwudhipong, 2011).

In some of these applications, quantitative differences are of utmost importance. For example in hydrogen embrittlement, where the crack tip hydrogen content has an exponential dependence on the hydrostatic stress (Martínez-Pañeda, del Busto, Niordson, & Betegón, 2016b). However, fracture studies have focused on a few gradient plasticity models and the impact of recent theoretical developments is yet to be investigated.

In this work, distortion gradient plasticity is used for the first time to model crack tip behaviour. Also, the role of Nye's tensor on fracture mechanics is first elucidated. We combine analytical insight into the asymptotic stress field with detailed finite element analysis of crack tip fields under mode I and mixed mode fracture conditions, revealing some remarkable results. The remaining of the manuscript starts by introducing the flow theory of distortion gradient plasticity (Section 2). This is followed by an analytical investigation of the nature of the asymptotic crack tip solution in Section 3. Our analysis reveals the existence of an *elastic* region close to the crack tip, reminiscent of a dislocation-free zone. This feature is confirmed by numerical computations and extends the recent findings by Martínez-Pañeda & Fleck (2019) to distortion gradient plasticity and strain gradient theories based on Nye's dislocation density tensor. In Section 4, the finite element framework is described, including the development of a new viscoplastic potential. The numerical model is then used in Section 5 to characterize the influence of the plastic spin and material parameters on crack tip fields. It is shown that the use of a defect energy based on Nye's tensor leads to a much weaker stress elevation relative to defect energies employing the plastic strain tensor as primal variable. Finally, insight is shed into the conundrum of atomic decohesion at metal-ceramic interfaces by modelling the classic experiments by Elssner, Korn, and Rühle (1994) and Korn, Elssner, Cannon, and Ruhle (2002). The manuscript ends with concluding remarks in Section 6.

2. The flow theory of distortion plasticity plasticity

The equations of this section refer to the mechanical response of a body occupying a space region Ω with an external surface S of outward normal n_i. More details about the higher order theory of distortion gradient plasticity can be found in Gurtin (2004).

2.1. Variational principles and balance equations

Within a small strain formulation, the displacement gradient $u_{i,j}$ can be decomposed into its elastic and plastic parts:

$$u_{i,j} = \gamma_{ij}^e + \gamma_{ij}^p \tag{2}$$

Where γ_{ij}^p, the plastic distortion, which characterises the evolution of dislocations and other defects through the crystal structure, may in turn be decomposed into its symmetric and skew parts:

$$\gamma_{ij}^p = \varepsilon_{ij}^p + \vartheta_{ij}^p \tag{3}$$

Unlike the plastic strain field ε_{ij}^p, the plastic rotation ϑ_{ij}^p is essentially irrelevant in a conventional theory. However, as pointed out by Gurtin (2004), phenomenological models involving Nye's dislocation density tensor α_{ij} as primal higher order kinematic variable,

$$\alpha_{ij} = \epsilon_{jkl}\gamma_{il,k}^p \quad (\boldsymbol{\alpha} = \text{curl } \boldsymbol{\gamma}^p) \tag{4}$$

must account for the plastic spin since the macroscopic characterisation of the Burgers vector involves both the symmetric and skew parts of the plastic distortion

$$\epsilon_{jkl}\gamma_{il,k}^p = \epsilon_{jkl}\varepsilon_{il,k}^p + \epsilon_{jkl}\vartheta_{il,k}^p \quad \left(\text{curl } \boldsymbol{\gamma}^p = \text{curl } \boldsymbol{\varepsilon}^p + \text{curl } \boldsymbol{\vartheta}^p\right) \tag{5}$$

with ϵ_{jkl} denoting the alternating symbol. The internal virtual work reads:

$$\delta W_i = \int_{\Omega} \left(\sigma_{ij}\delta\varepsilon_{ij}^e + \zeta_{ij}\delta\alpha_{ij} + S_{ij}\delta\gamma_{ij}^p + \tau_{ijk}\delta\varepsilon_{ij,k}^p\right) \text{d}V \tag{6}$$

where the Cauchy stress is denoted by σ_{ij}. In addition to conventional stresses, the principle of virtual work incorporates the so-called micro-stress tensor, S_{ij} (work conjugate to the plastic distortion, γ_{ij}^p), the defect stress ζ_{ij} (work conjugate to Nye's tensor α_{ij}, the curl of the plastic distortion) and the - here, purely dissipative - higher order stress tensor, τ_{ijk} (work conjugate to the plastic strain gradients $\varepsilon_{ij,k}^p$). By taking into account that the micro-stress tensor can be decomposed into its symmetric and skew parts: $S_{ij} = q_{ij} + \omega_{ij}$, the internal virtual work statement can be expressed as:

$$\delta W_i = \int_{\Omega} \left(\sigma_{ij}\delta\varepsilon_{ij} + \zeta_{ij}\delta\alpha_{ij} + \left(q_{ij} - \sigma_{ij}'\right)\delta\varepsilon_{ij}^p + \omega_{ij}\delta\vartheta_{ij}^p + \tau_{ijk}\delta\varepsilon_{ij,k}^p\right) \text{d}V \tag{7}$$

with the prime symbol $'$ denoting deviatoric quantities. Applying Gauss' divergence theorem to (7) renders:

$$\delta W_i = \int_S \left(\sigma_{ij}n_j\delta u_i + \left(\Upsilon_{ij}' + \tau_{ijk}n_k\right)\delta\varepsilon_{ij}^p + \Delta_{ij}\delta\vartheta_{ij}^p\right) \text{d}S - \int_{\Omega} \left(\sigma_{ij,j}\delta u_i - \left(q_{ij} - \sigma_{ij}' - \tau_{ijk,k} + \eta_{ij}'\right)\delta\varepsilon_{ij}^p - \left(\omega_{ij} + \varphi_{ij}\right)\delta\vartheta_{ij}^p\right) \text{d}V \tag{8}$$

where η_{ij} and φ_{ij} are, respectively, the symmetric and skew-symmetric parts of the curl of the defect stress $\xi_{ij} = \epsilon_{jkl}\zeta_{il,k} = \eta_{ij} + \varphi_{ij}$; and equivalently, Υ_{ij} and Δ_{ij} respectively denote the symmetric and skew-symmetric parts of the cross product of the defect stress and the outward normal $\Gamma_{ij} = \epsilon_{jkl}\zeta_{il}n_k = \Upsilon_{ij} + \Delta_{ij}$. Since the volume integral in (8) should vanish for arbitrary variations, three sets of equilibrium equations are readily obtained:

$$\sigma_{ij,j} = 0 \tag{9}$$

$$q_{ij} - \sigma'_{ij} - \tau_{ijk,k} + \eta'_{ij} = 0 \tag{10}$$

$$\omega_{ij} + \varphi_{ij} = 0 \tag{11}$$

Now, identifying the surface in (8) as part of the external work and considering (7), the Principle Virtual Work reads:

$$\int_{\Omega} \left(\sigma_{ij}\delta\varepsilon_{ij} + \zeta_{ij}\delta\alpha_{ij} + \left(q_{ij} - \sigma'_{ij}\right)\delta\varepsilon_{ij}^p + \omega_{ij}\delta\vartheta_{ij}^p + \tau_{ijk}\delta\varepsilon_{ij,k}^p \right) dV = \int_S \left(T_i\delta u_i + t_{ij}^\varepsilon\delta\varepsilon_{ij}^p + t_{ij}^\vartheta\delta\vartheta_{ij}^p \right) dS \tag{12}$$

where T_i are the conventional tractions, work conjugate to the displacements, while t_{ij}^ε and t_{ij}^ϑ denote the higher order tractions work conjugate to plastic strains ε_{ij}^p and plastic rotations ϑ_{ij}^p, respectively. Accordingly, considering (8), the natural boundary conditions read:

$$T_i = \sigma_{ij}n_j \tag{13}$$

$$\Upsilon'_{ij} + \tau_{ijk}n_k = t_{ij}^\varepsilon \tag{14}$$

$$\Delta_{ij} = t_{ij}^\vartheta \tag{15}$$

2.2. Energetic contributions

In order to account for the influence of GNDs, the free energy is chosen to depend on both the elastic strain ε_{ij}^e and Nye's tensor α_{ij}:

$$\Psi = \frac{1}{2}C_{ijkl}\varepsilon_{ij}^e\varepsilon_{kl}^e + \Phi\left(\alpha_{ij}\right) \tag{16}$$

with C_{ijkl} being the elastic stiffness and $\Phi(\alpha_{ij})$ the defect energy that accounts for the recoverable mechanisms associated with the development of GNDs. The widely used quadratic form of the defect energy is adopted

$$\Phi\left(\alpha_{ij}\right) = \frac{1}{2}\mu L_E^2\alpha_{ij}\alpha_{ij} \tag{17}$$

but one should note that exploring other options may lead to further modelling capabilities (Bardella & Panteghini, 2015; Garroni et al., 2010; Lancioni et al., 2015; Ohno & Okumura, 2007; Panteghini et al., 2019; Wulfinghoff et al., 2015). Accordingly, the defect stress equals:

$$\zeta_{ij} = \frac{\partial\Phi\left(\alpha_{ij}\right)}{\partial\alpha_{ij}} = \mu L_E^2\alpha_{ij} \tag{18}$$

with μ being the shear modulus and L_E the energetic material length scale.

2.3. Dissipative contributions

A gradient-enhanced phenomenological effective plastic flow rate is defined,

$$\dot{E}^p = \sqrt{\frac{2}{3}\dot{\varepsilon}_{ij}^p\dot{\varepsilon}_{ij}^p + \chi\dot{\vartheta}_{ij}^p\dot{\vartheta}_{ij}^p + \frac{2}{3}L_D^2\dot{\varepsilon}_{ij,k}^p\dot{\varepsilon}_{ij,k}^p} \tag{19}$$

where L_D is a dissipative length parameter and χ is the parameter governing the dissipation due to the plastic spin. Bardella (2009) has analytically identified the value of χ that captures the mechanical response of a crystal subjected to multi-slip under simple shear:

$$\chi = \left[\frac{3}{2} + \frac{\sigma_Y}{\mu\varepsilon_Y}\left(\frac{L_D}{L_E}\right)^2\right]^{-1} \tag{20}$$

being σ_Y and ε_Y the yield stress and the yield strain, respectively, which implies a value for χ bounded between 0 and 2/3. The flow resistance Σ, work conjugate to $\dot{E}^p$, is given by

$$\Sigma = \sqrt{\frac{3}{2}q_{ij}q_{ij} + \frac{1}{\chi}\omega_{ij}\omega_{ij} + \frac{3}{2L_D^2}\tau_{ijk}\tau_{ijk}} \tag{21}$$

Such that the unrecoverable stresses equal

$$q_{ij} = \frac{2}{3} \frac{\Sigma}{\dot{E}^p} \dot{\varepsilon}_{ij}^p, \qquad \omega_{ij} = \chi \frac{\Sigma}{\dot{E}^p} \dot{\vartheta}_{ij}^p, \qquad \tau_{ijk} = \frac{2}{3} L_D^2 \frac{\Sigma}{\dot{E}^p} \dot{\varepsilon}_{ij,k}^p \tag{22}$$

And consequently the second law of thermodynamics is fulfilled by relating finite stress measures with rates of plastic deformation, in what is referred to as a *non-incremental* form:

$$q_{ij} \dot{\varepsilon}_{ij}^p + \omega_{ij} \dot{\vartheta}_{ij}^p + \tau_{ijk} \dot{\varepsilon}_{ij,k}^p \equiv \Sigma \dot{E}^p > 0 \tag{23}$$

3. Asymptotic analysis of crack tip fields

We begin our study by conducting an asymptotic analysis of the relevant fields at the crack tip under mode I fracture conditions. Consider a crack in a 2D space, with its tip at the origin of a polar coordinate system (r, θ). We will assume that the plastic distortion field γ_{ij}^p is continuous and differentiable, with an asymptotic solution that behaves as follows:

$$\gamma_{ij}^p \sim r^\beta f_{ij}(\theta) \tag{24}$$

for $r \to 0$. By deriving a generalized *J*-integral for distortion gradient plasticity, the order of the singularity (index β) will be determined using energy boundness arguments and its implications for the behaviour of crack tip stresses investigated.

3.1. Deformation theory solid

In a deformation theory context, in the absence of conventional and higher order tractions, the total potential energy assumes the form,

$$U\left(u_i, \varepsilon_{ij}^p, \vartheta_{ij}^p, \varepsilon_{ij,k}^p, \alpha_{ij}\right) = \int_V \left[\Psi\left(u_i, \alpha_{ij}\right) + \varphi\left(\varepsilon_{ij}^p, \vartheta_{ij}^p, \varepsilon_{ij,k}^p\right) \right] \mathrm{d}V \tag{25}$$

with the free energy being given by,

$$\Psi\left(u_i, \alpha_{ij}\right) = \Psi^e(u_i) + \Phi\left(\alpha_{ij}\right) = \frac{1}{2}\left(\varepsilon_{ij} - \varepsilon_{ij}^p\right) C_{ijkl}\left(\varepsilon_{kl} - \varepsilon_{kl}^p\right) + \frac{1}{2} \mu L_E^2 \alpha_{ij} \alpha_{ij} \tag{26}$$

Here, Ψ^e denotes the elastic free energy. Thereby, the Cauchy stresses are derived as,

$$\sigma_{ij} = \frac{\partial \Psi}{\partial \varepsilon_{ij}^e} = C_{ijkl}\left(\varepsilon_{kl} - \varepsilon_{kl}^p\right) \tag{27}$$

and the so-called defect stress ζ_{ij} is given by (18).

On the other hand, the dissipation potential φ is given by,

$$\varphi\left(\varepsilon_{ij}^p, \vartheta_{ij}^p, \varepsilon_{ij,k}^p\right) = \frac{\sigma_Y \varepsilon_Y}{N+1} \left(\frac{E^p\left(\varepsilon_{ij}^p, \vartheta_{ij}^p, \varepsilon_{ij,k}^p\right)}{\varepsilon_Y} \right)^{N+1} \tag{28}$$

where

$$(E^p)^2 = \frac{2}{3} \varepsilon_{ij}^p \varepsilon_{ij}^p + \chi \vartheta_{ij}^p \vartheta_{ij}^p + \frac{2}{3} L_D^2 \varepsilon_{ij,k}^p \varepsilon_{ij,k}^p \tag{29}$$

The choice (28) implies that a homogeneous hardening law relates E^p with its work conjugate, the effective stress Σ,

$$\Sigma = \sigma_Y \left(\frac{E^p}{\varepsilon_Y} \right)^N = \Sigma_0 (E^p)^N \tag{30}$$

where $0 \leq N \leq 1$ is the strain hardening exponent. Hence, the dissipation potential reads,

$$\varphi\left(\varepsilon_{ij}^p, \vartheta_{ij}^p, \varepsilon_{ij,k}^p\right) = \frac{\Sigma E^p}{N+1} \tag{31}$$

Accordingly, the constitutive relations for the deformation theory solid can be readily derived as

$$q_{ij} = \frac{\partial \varphi}{\partial \varepsilon_{ij}^p} = \sigma_Y \left(\frac{E^p}{\varepsilon_Y} \right)^N \frac{2}{3} \frac{\varepsilon_{ij}^p}{E^p} = \frac{2}{3} \frac{\Sigma}{E^p} \varepsilon_{ij}^p \tag{32}$$

$$\omega_{ij} = \frac{\partial \varphi}{\partial \vartheta_{ij}^p} = \sigma_Y \left(\frac{E^p}{\varepsilon_Y} \right)^N \chi \frac{\vartheta_{ij}^p}{E^p} = \chi \frac{\Sigma}{E^p} \vartheta_{ij}^p \tag{33}$$

$$\tau_{ijk} = \frac{\partial \varphi}{\partial \varepsilon_{ij,k}^p} = \sigma_Y \left(\frac{E^p}{\varepsilon_Y} \right)^N L_D^2 \frac{2}{3} \frac{\varepsilon_{ij,k}^p}{E^p} = \frac{2}{3} L_D^2 \frac{\Sigma}{E^p} \varepsilon_{ij,k}^p \tag{34}$$

3.2. A generalized J-integral for distortion gradient plasticity

We proceed to define a generalized J-integral for distortion gradient plasticity. Consider a Cartesian coordinate system (x, y) with the crack tip at the origin and the crack plane along the negative x axis. Defining J as the energy release rate per unit crack extension and w as the strain energy density of the solid, an evaluation of J over a contour Γ that encloses the crack tip gives

$$J = \int_\Gamma \left(w n_x - \sigma_{ij} n_j u_{i,x} - t_{ij}^\vartheta \vartheta_{ij}^p - t_{ij}^\varepsilon \varepsilon_{ij}^p \right) dS \tag{35}$$

The derivation and proof are straightforward and follow the works by Eshelby (1956) and Rice (1968) in the context of conventional deformation solids, and the recent work by Martínez-Pañeda & Fleck (2019) for strain gradient solids. Note that the existence of a J-integral implies that total strain energy density of the solid will asymptotically behave as $w \sim J/r$ so as to give a finite energy release rate J at the crack tip. Following the notation of Section 3.1, this energy boundness constraint can be expressed as:

$$\Psi^e\left(\varepsilon_{ij}^e\right) + \Phi\left(\alpha_{ij}\right) + \varphi\left(\varepsilon_{ij}^p, \vartheta_{ij}^p, \varepsilon_{ij,k}^p\right) \sim \frac{J}{r} \tag{36}$$

for $r \to 0$.

3.3. Asymptotic crack tip fields

We proceed to make use of the constitutive relations and the energy boundness constraint (36) to obtain the singularity power index β in (24). Further, we will make use of the higher order equilibrium Eq. (10) to determine the singularity order of the Cauchy stress σ_{ij}. Note that (10) involves $\tau_{ijk,k}$ and the symmetric part of the curl of the defect stress. Thus, from (24), the analysis requires obtaining the solution for: (i) the curl of Nye's tensor, which is obtained from the curl of the plastic distortion, (ii) the plastic strain gradients, and (iii) the Laplacian of the plastic strain. Consider an incompressible solid where the asymptotic solution for γ_{ij}^p is given by (24); in a polar coordinate system, the individual components of the plastic distortion tensor read,

$$\gamma_{rr}^p = -\gamma_{\theta\theta}^p \sim r^\beta f_1(\theta); \qquad \gamma_{r\theta}^p \sim r^\beta f_2(\theta); \qquad \gamma_{\theta r}^p \sim r^\beta f_3(\theta) \tag{37}$$

Accordingly, the solution for the plastic strain and plastic spin fields is of the following form,

$$\varepsilon_{rr}^p = -\varepsilon_{\theta\theta}^p \sim r^\beta f_1(\theta); \qquad \varepsilon_{r\theta}^p \sim r^\beta f_4(\theta); \qquad \vartheta_{r\theta}^p \sim r^\beta f_5(\theta) \tag{38}$$

And the relevant components of the plastic strain gradient and the Laplacian of the plastic strain readily follow,

$$\varepsilon_{rr,r}^p = \frac{\partial \varepsilon_{rr}^p}{\partial r} = \beta r^{\beta-1} f_1(\theta); \quad \varepsilon_{rr,\theta}^p = \frac{1}{r}\left(\frac{\partial \varepsilon_{rr}^p}{\partial \theta} - 2\varepsilon_{r\theta}^p\right) = r^{\beta-1}\left(f_1'(\theta) - 2f_4(\theta)\right) \tag{39}$$

$$\varepsilon_{r\theta,r}^p = \frac{\partial \varepsilon_{r\theta}^p}{\partial r} = \beta r^{\beta-1} f_4(\theta); \quad \varepsilon_{r\theta,\theta}^p = \frac{1}{r}\left(\frac{\partial \varepsilon_{r\theta}^p}{\partial \theta} + 2\varepsilon_{rr}^p\right) = r^{\beta-1}\left(f_4'(\theta) + 2f_1(\theta)\right) \tag{40}$$

$$\varepsilon_{rr,kk}^p = \frac{\partial^2 \varepsilon_{rr}^p}{\partial r^2} + \frac{1}{r}\frac{\partial \varepsilon_{rr}^p}{\partial r} + \frac{1}{r^2}\frac{\partial^2 \varepsilon_{rr}^p}{\partial \theta^2} - \frac{4}{r^2}\left(\varepsilon_{rr}^p + \frac{\partial \varepsilon_{r\theta}^p}{\partial \theta}\right) = r^{\beta-2}\left[f_1(\theta)\left(\beta^2 - 4\right) + f_1''(\theta) + 4f_4'(\theta)\right] \tag{41}$$

$$\varepsilon_{r\theta,kk}^p = \frac{\partial^2 \varepsilon_{r\theta}^p}{\partial r^2} + \frac{1}{r}\frac{\partial \varepsilon_{r\theta}^p}{\partial r} + \frac{1}{r^2}\frac{\partial^2 \varepsilon_{r\theta}^p}{\partial \theta^2} + \frac{4}{r^2}\left(\frac{\partial \varepsilon_{rr}^p}{\partial \theta} - \varepsilon_{r\theta}^p\right) = r^{\beta-2}\left[f_4(\theta)\left(\beta^2 - 4\right) + f_4''(\theta) + 4f_1'(\theta)\right] \tag{42}$$

Furthermore, the relevant components of Nye's tensor in polar coordinates read

$$\alpha_{rz} = \left(\text{curl}\,\gamma_{ij}^p\right)_{rz} = \frac{\partial \gamma_{r\theta}^p}{\partial r} - \frac{1}{r}\left[\frac{\partial \gamma_{rr}^p}{\partial \theta} - \left(\gamma_{r\theta}^p + \gamma_{\theta r}^p\right)\right] = r^{\beta-1}\left[f_2(\theta)(\beta+1) - f_1'(\theta) + f_3(\theta)\right] \tag{43}$$

$$\alpha_{\theta z} = \left(\text{curl}\,\gamma_{ij}^p\right)_{\theta z} = \frac{\partial \gamma_{\theta\theta}^p}{\partial r} - \frac{1}{r}\left(\frac{\partial \gamma_{r\theta}^p}{\partial \theta} + 2\gamma_{rr}^p\right) = r^{\beta-1}\left[f_1(\theta)(-2-\beta) - f_2'(\theta)\right] \tag{44}$$

Finally, the components related to the curl of the defect stress, $\xi_{ij} = \text{curl}\left(\mu L_E^2\,\text{curl}\,\gamma_{ij}^p\right) = \eta_{ij} + \varphi_{ij}$, are obtained as

$$\xi_{rr} = \frac{1}{r}\left\{\frac{\partial\left[\frac{\partial \gamma_{r\theta}^p}{\partial r} - \frac{1}{r}\left(\frac{\partial \gamma_{rr}^p}{\partial \theta} - \gamma_{r\theta}^p - \gamma_{\theta r}^p\right)\right]}{\partial \theta} - \frac{\partial \gamma_{\theta\theta}^p}{\partial r} + \frac{1}{r}\left(\frac{\partial \gamma_{r\theta}^p}{\partial \theta} + 2\gamma_{rr}^p\right)\right\}$$

$$= r^{\beta-2}\left[f_1(\theta)(2+\beta) + f_2'(\theta)(2+\beta) - f_1''(\theta) + f_3'(\theta)\right] \tag{45}$$

$$\xi_{r\theta} = -\frac{\partial\left[\frac{\partial\gamma_{r\theta}^p}{\partial r} - \frac{1}{r}\left(\frac{\partial\gamma_{rr}^p}{\partial\theta} - \gamma_{r\theta}^p - \gamma_{\theta r}^p\right)\right]}{\partial r} = r^{\beta-2}(1-\beta)\left[f_2(\theta)(1+\beta) - f_1'(\theta) + f_3(\theta)\right] \tag{46}$$

$$\xi_{\theta r} = \frac{1}{r}\left\{\frac{\partial\left[\frac{\partial\gamma_{\theta\theta}^p}{\partial r} - \frac{1}{r}\left(\frac{\partial\gamma_{r\theta}^p}{\partial\theta} + 2\gamma_{rr}^p\right)\right]}{\partial\theta} + \frac{\partial\gamma_{r\theta}^p}{\partial r} - \frac{1}{r}\left(\frac{\partial\gamma_{rr}^p}{\partial\theta} - \gamma_{r\theta}^p - \gamma_{\theta r}^p\right)\right\}$$
$$= r^{\beta-2}\left[f_1'(\theta)(-3-\beta) + f_2(\theta)(\beta+1) - f_2''(\theta) + f_3(\theta)\right] \tag{47}$$

$$\xi_{\theta\theta} = -\frac{\partial\left[\frac{\partial\gamma_{\theta\theta}^p}{\partial r} - \frac{1}{r}\left(\frac{\partial\gamma_{r\theta}^p}{\partial\theta} + 2\gamma_{rr}^p\right)\right]}{\partial r} = r^{\beta-2}(1-\beta)\left[f_1(\theta)(-2-\beta) - f_2'(\theta)\right] \tag{48}$$

We proceed to determine the index of the singularity, β, neglecting the angular functions. Thus, we estimate the singular order of the elastic strain energy density Ψ^e, the defect energy Φ and the dissipation potential φ and take into consideration that the energy released at the crack tip must be finite, see Section 3.2. We consider the general case, $(L_D \neq 0, L_E \neq 0)$, and particularize later.

The gradient term is more singular and dominates the asymptotic behaviour of the generalized plastic strain E^p, see (29); accordingly,

$$E^p \sim L_D \varepsilon_{ijk}^p \sim r^{\beta-1} \tag{49}$$

And its work conjugate stress reads,

$$\Sigma = \Sigma_0(E^p)^N \sim r^{N(\beta-1)} \tag{50}$$

Consequently, the asymptotic behaviour of the dissipative stresses associated with the primal kinematic variable ε_{ij}^p is given by,

$$q_{ij} = \frac{2}{3}\frac{\Sigma}{E^p}\varepsilon_{ij}^p \sim r^{N+\beta} ; \qquad \tau_{ijk} = \frac{2}{3}L_D^2\frac{\Sigma}{E^p}\varepsilon_{ij,k}^p \sim r^{N+\beta-1} \tag{51}$$

Now consider (43)-(44); the asymptotic behaviour of the energetic defect stress reads,

$$\zeta_{ij} = \mu L_E^2\alpha_{ij} = \mu L_E^2\epsilon_{jkl}\gamma_{il,k}^p \sim r^{\beta-1} \tag{52}$$

Finally, the asymptotic behaviour of the Cauchy stress is obtained from the higher order equilibrium, Eq. (10), which involves the Laplacian of the plastic strains *via* the dissipative term $\tau_{ijk,k}$ and the curl of the defect stress *via* the energetic term η_{ij}'. Both terms are more singular than q_{ij} and have in fact the same singularity order: $r^{\beta-2}$ - see (41)-(42) and (45)–(48). Hence,

$$\sigma_{ij}' = q_{ij} - \tau_{ijk,k} + \eta_{ij}' \sim r^{\beta-2} \tag{53}$$

In other words, the singularity exhibited by the crack tip stresses will be the same if only energetic higher order terms are present ($L_E \neq 0, L_D = 0$) and if only dissipative higher order terms are present ($L_D \neq 0, L_E = 0$). The use of Nye's tensor as primal higher order kinematic variable leads to identical asymptotic crack tip behaviour relative to the choice of a defect energy with the plastic strain tensor as primal variable. In all cases a quadratic form of the defect energy is assumed; interestingly, less-than-quadratic defect energies will have important implications in fracture problems: changing the nature of the stress singularity (if $L_D = 0$) or making energetic contributions negligible relative to their dissipative counterparts (if $L_D \neq 0$).

Consider now the relevant energy quantities. The elastic strains will have the same asymptotic behaviour as the Cauchy stresses, and consequently:

$$\Psi^e = \frac{1}{2}C_{ijkl}\varepsilon_{ij}^e\varepsilon_{kl}^e \sim r^{2(\beta-2)} \tag{54}$$

While the defect energy and dissipation potential vary as,

$$\Phi = \frac{1}{2}\mu L_E^2\alpha_{ij}\alpha_{ij} \sim r^{2(\beta-1)} \tag{55}$$

$$\varphi = \frac{\Sigma E^p}{N+1} \sim r^{(N+1)(\beta-1)} \tag{56}$$

Therefore, Ψ^e is the most singular contribution and will dominate the energy released in the vicinity of the crack tip - see (36). Since the total strain energy density must scale as $\sim J/r$ to give a finite energy release rate at the crack tip, we conclude that the singularity index β must be equal to 3/2. The implications of this finding are the following:

- The elastic energy dominates as $r \to 0$ and the plastic field is not sufficiently singular to give any contribution to the energy release rate. If the plastic energy terms, Φ or φ, were to behave asymptotically as J/r, β would be equal to 1 (for $N = 0$) or smaller (if $N > 0$) and the energy release rate at the crack tip would be unbounded ($\Psi^e \sim w \sim r^{-2}$).
- Crack tip stresses follow the linear elastic $r^{-1/2}$ singularity, revealing the existence of an inner elastic K-field that is reminiscent of a dislocation-free zone.
- The plastic strain field ε_{ij}^p tends to zero as the crack is approached. Crack tip asymptotic analyses for distortion gradient plasticity, and similar classes of gradient theories, should not be built on the assumption that plastic strains dominate elastic strains, as done for conventional plasticity (HRR field Hutchinson, 1968; Rice & Rosengren, 1968) and previous studies in strain gradient plasticity (Chen, Wei, Huang, Hutchinson, & Hwang, 1999; Huang, Zhang, Guo, & Hwang, 1997; Xia & Hutchinson, 1996).

We proceed to corroborate these findings with detailed finite element analysis, as well as exploring other interesting features of distortion gradient plasticity predictions in fracture problems.

4. Numerical formulation and solution procedure

The flow theory of distortion gradient plasticity, described in Section 2, is implemented in a robust, backward Euler finite element framework. This is largely facilitated by the definition of a new viscoplastic potential, able to model both rate-dependent and rate-independent behaviour, by extending the work of Panteghini and Bardella (2018).

4.1. Viscoplastic law

Gradient plasticity theories are commonly implemented within a rate-dependent setting, taking advantage of its well-known computational capabilities and circumventing complications associated with identifying active plastic zones in the corresponding time independent model (Nielsen & Niordson, 2013; 2014). In the context of rate-dependent gradient plasticity models, an effective flow resistance Σ is defined,

$$\Sigma\left(\dot{E}^p, E^p\right) = \sigma_F(E^p) V\left(\dot{E}^p\right) \tag{57}$$

which is work conjugated to the gradient-enhanced effective plastic flow rate $\dot{E}^p$. Here, σ_F is the current flow stress, which depends on the initial yield stress σ_Y and the hardening law. Several viscoplastic laws have been proposed in the literature; the most exploited one is arguably the following, (see, e.g., Martínez-Pañeda et al., 2016; Needleman, 1988)

$$\mathscr{V}\left(\dot{E}^p, E^p\right) = \frac{\sigma_F(E^p)\dot{\varepsilon}_0}{m+1}\left(\frac{\dot{E}^p}{\dot{\varepsilon}_0}\right)^{m+1} \tag{58}$$

so that

$$\Sigma\left(\dot{E}^p, E^p\right) = \sigma_F V(\dot{E}^p) = \sigma_F(E^p)\left(\frac{\dot{E}^p}{\dot{\varepsilon}_0}\right)^m \tag{59}$$

with m being the material rate sensitivity exponent, $\dot{\varepsilon}_0$ the reference strain rate and $V(\dot{E}^p)$ the viscoplastic function. However, under this choice the initial tangent is infinite and the derivative $\partial\Sigma/\partial\dot{E}^p$ tends to infinity if $\dot{E}^p \to 0$, making the finite element system ill-conditioned for small values of $\dot{E}^p$. To overcome these numerical issues, Panteghini and Bardella (2016) proposed the following viscoplastic function,

$$V(\dot{E}^p) = \begin{cases} \frac{\dot{E}^p}{2\dot{\varepsilon}_0} & \text{if } \dot{E}^p/\dot{\varepsilon}_0 \leq 1 \\ 1 - \frac{\dot{\varepsilon}_0}{2\dot{E}^p} & \text{if } \dot{E}^p/\dot{\varepsilon}_0 > 1 \end{cases} \tag{60}$$

In this way, the contribution of $\partial\Sigma/\partial\dot{E}^p$ will remain bounded when $\dot{E}^p \to 0$. This viscoplastic function is intended to reproduce the rate-independent limit in a robust manner, which is attained when $\dot{\varepsilon}_0 \to 0$. We extend the work by Panteghini and Bardella (2016) to develop a viscoplastic algorithm that can overcome the aforementioned numerical issues, and enables modelling both rate-dependent and rate-independent behaviour by recovering the well-known viscoplastic function $V\left(\dot{E}^p\right) = \left(\dot{E}^p/\dot{\varepsilon}_0\right)^m$. For this purpose, a threshold effective plastic strain rate is defined $\dot{E}_*^p$ such that the viscoplastic function reads,

$$V(\dot{E}^p) = \begin{cases} \frac{\dot{E}^p}{\varpi\dot{\varepsilon}_0} & \text{if } \dot{E}^p m/\dot{E}_*^p \leq 1 \\ \left(\frac{\dot{E}^p - \frac{1-m}{m}\dot{E}_*^p}{\dot{\varepsilon}_0}\right)^m & \text{if } \dot{E}^p m/\dot{E}_*^p > 1 \end{cases} \tag{61}$$

where ϖ is a small positive constant ($\varpi << 1$). A smooth transition is obtained by computing the critical $\dot{E}_*^p$ from the relation between the derivatives,

$$\dot{E}_*^p = \dot{\varepsilon}_0\left(\frac{1}{\varpi m}\right)^{1/(m-1)} \tag{62}$$
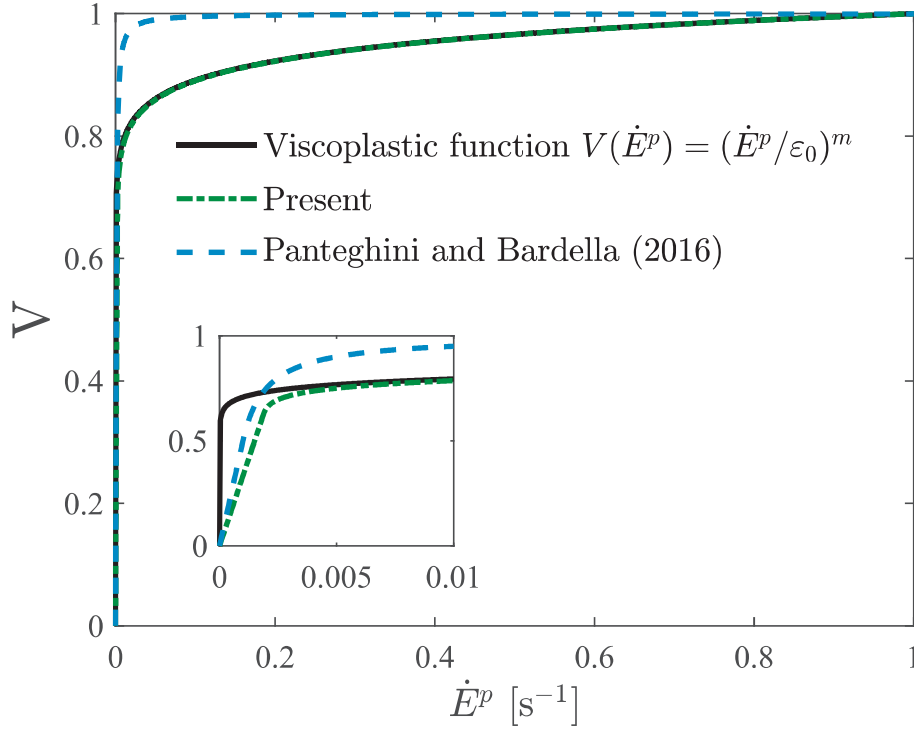
Fig. 1. Comparison between the classic viscoplastic power law, the viscoplastic function presented and the one proposed by Panteghini and Bardella (2016). In the function by Panteghini and Bardella (2016) the reference strain rate $\dot{\varepsilon}_0$ equals 10^3 s^{-1}, while in the other two cases a rate sensitivity exponent of $m = 0.05$ and a reference strain rate $\dot{\varepsilon}_0 = 1$ are adopted; these choices pertain only to the present graph.

and by offsetting the curve a distance $\dot{E}_*^p(1 - m)/m$. This distance corresponds to the intersection between the abscissa axis and the tangent line at the critical point. In this way, we are able to reproduce a mechanical response that accurately follows the classic viscoplastic power law while providing a robust numerical framework. Representative curves for the aforementioned viscoplastic functions are shown in Fig. 1; the regularisation proposed here approximates the classic viscoplastic function very well, enabling it to reproduce the rate sensitivity of metals, while retaining the robustness of the proposal by Panteghini and Bardella (2016).

4.2. Finite element discretisation

The finite element framework takes displacements, plastic strains and plastic spin as the primary kinematic variables. Adopting symbolic and Voigt notation, the nodal variables for the displacement field $\hat{\boldsymbol{u}}$, the plastic strains $\hat{\boldsymbol{\varepsilon}}^p$, and the plastic spin $\hat{\boldsymbol{\vartheta}}^p$ are interpolated as,

$$\boldsymbol{u} = \sum_{n=1}^{k} \boldsymbol{N}_n^{\boldsymbol{u}} \hat{\boldsymbol{u}}_n, \qquad \boldsymbol{\varepsilon}^p = \sum_{n=1}^{k} \boldsymbol{N}_n^{\boldsymbol{\varepsilon}^p} \hat{\boldsymbol{\varepsilon}}_n^p, \qquad \boldsymbol{\vartheta}^p = \sum_{n=1}^{k} \boldsymbol{N}_n^{\boldsymbol{\vartheta}^p} \hat{\boldsymbol{\vartheta}}_n^p \tag{63}$$

Here, N_n denotes the shape function associated with node n, for a total number of nodes k. Similarly, the related gradient and curl-based quantities are discretised as

$$\boldsymbol{\varepsilon} = \sum_{n=1}^{k} \boldsymbol{B}_n^{\boldsymbol{u}} \hat{\boldsymbol{u}}_n, \qquad \nabla \boldsymbol{\varepsilon}^p = \sum_{n=1}^{k} \boldsymbol{B}_n^{\boldsymbol{\varepsilon}^p} \hat{\boldsymbol{\varepsilon}}_n^p, \qquad \boldsymbol{\alpha} = \sum_{n=1}^{k} \left(\boldsymbol{M}_n^{\boldsymbol{\varepsilon}^p} \hat{\boldsymbol{\varepsilon}}_n^p + \boldsymbol{M}_n^{\boldsymbol{\vartheta}^p} \hat{\boldsymbol{\vartheta}}_n^p \right) \tag{64}$$

with the $\boldsymbol{B}$ and $\boldsymbol{M}$ matrices given explicitly in Appendix A. Accordingly, one can discretise the internal virtual work (7) as,

$$\delta W_i = \int_{\Omega} \left\{ \left(\boldsymbol{B}_n^{\boldsymbol{u}} \right)^T \boldsymbol{\sigma} \delta \hat{\boldsymbol{u}}_n + \left[\left(\boldsymbol{N}_n^{\boldsymbol{\vartheta}^p} \right)^T \boldsymbol{\omega} + \left(\boldsymbol{M}_n^{\boldsymbol{\vartheta}^p} \right)^T \boldsymbol{\zeta} \right] \delta \hat{\boldsymbol{\vartheta}}_n^p + \left[\left(\boldsymbol{N}_n^{\boldsymbol{\varepsilon}^p} \right)^T (\boldsymbol{q} - \boldsymbol{\sigma}) + \left(\boldsymbol{B}_n^{\boldsymbol{\varepsilon}^p} \right)^T \boldsymbol{\tau} + \left(\boldsymbol{M}_n^{\boldsymbol{\varepsilon}^p} \right)^T \boldsymbol{\zeta} \right] \delta \hat{\boldsymbol{\varepsilon}}_n^p \right\} \mathrm{d}V \tag{65}$$

Differentiating the internal virtual work with respect to the variation of the nodal variables provides the residuals for each kinematic variable as:

$$\boldsymbol{R}_n^{\boldsymbol{u}} = \int_{\Omega} \left(\boldsymbol{B}_n^{\boldsymbol{u}} \right)^T \boldsymbol{\sigma} \, \mathrm{d}V \tag{66}$$
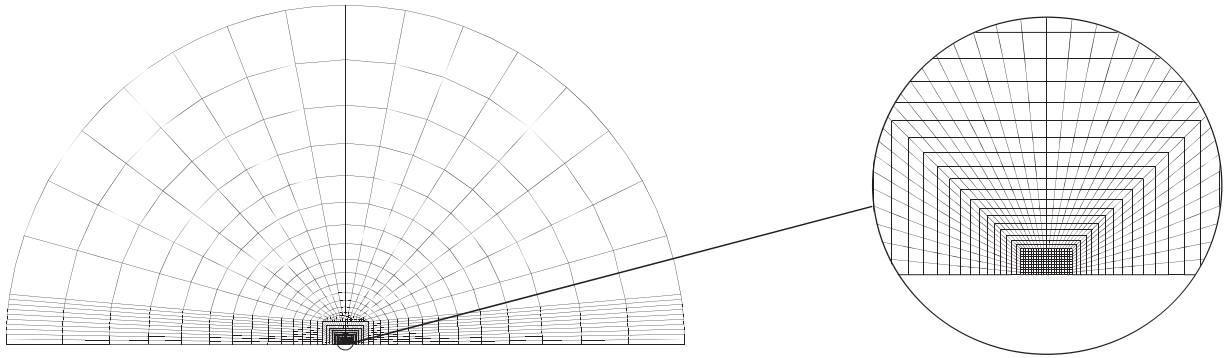
Fig. 2. Boundary layer formulation. Schematic and detailed view of the finite element mesh.

$$R_n^{\varepsilon^p} = \int_\Omega \left[\left(N_n^{\varepsilon^p}\right)^T (q - \sigma) + \left(B_n^{\varepsilon^p}\right)^T \tau + \left(M_n^{\varepsilon^p}\right)^T \zeta \right] dV \tag{67}$$

$$R_n^{\vartheta^p} = \int_\Omega \left[\left(N_n^{\vartheta^p}\right)^T \omega + \left(M_n^{\vartheta^p}\right)^T \zeta \right] dV \tag{68}$$

The components of the consistent tangent stiffness matrices K_{nm} are obtained by considering the constitutive relations and differentiating the residuals with respect to the incremental nodal variables. Details are given in Appendix A. The non-linear system of equations is solved iteratively from time step t to $(t + \Delta t)$ using the Newton-Raphson method,

$$\begin{bmatrix} u \\ \varepsilon^p \\ \vartheta^p \end{bmatrix}_{t+\Delta t} = \begin{bmatrix} u \\ \varepsilon^p \\ \vartheta^p \end{bmatrix}_t - \begin{bmatrix} K^{u,u} & K^{u,\varepsilon^p} & 0 \\ K^{\varepsilon^p,u} & K^{\varepsilon^p,\varepsilon^p} & K^{\varepsilon^p,\vartheta^p} \\ 0 & K^{\vartheta^p,\varepsilon^p} & K^{\vartheta^p,\vartheta^p} \end{bmatrix}_t^{-1} \begin{bmatrix} R^u \\ R^{\varepsilon^p} \\ R^\vartheta \end{bmatrix}_t \tag{69}$$

The present backward Euler time integration scheme follows the work by Panteghini and Bardella (2016); see Ref. Martínez-Pañeda et al. (2016) for a forward Euler based implementation. The finite element framework is implemented into the commercial package ABAQUS by means of a user element (UEL) subroutine.

5. Finite element results

The numerical model described in Section 4 is employed to gain insight into the fracture behaviour of distortion gradient plasticity solids. First, the analysis will be conducted with a boundary layer configuration, under small scale yielding conditions (Section 5.1). Irrotational plastic flow and mode I fracture will be assumed first, to verify the findings of the asymptotic analysis and assess the role of Nye's tensor. Mixed mode conditions are then considered to address the role of the plastic spin. Finally, fracture along a bi-material interface is investigated by reproducing the four-point bending experiments by Korn et al. (2002) with suitable higher order boundary conditions (Section 5.2).

5.1. Small scale yielding

A remote K-field is prescribed by means of the so-called boundary layer formulation, see Fig. 2. Plane strain conditions are assumed. Consider both a polar coordinate system (r, θ) and a Cartesian coordinate system (x, y) centred at the crack tip, with the crack plane along the negative x-axis. The outer K field is imposed by prescribing the nodal displacements in the outer periphery of the mesh as,

$$u_x = \frac{1+\nu}{E} \sqrt{\frac{r}{2\pi}} \left[K_I(3 - 4\nu - \cos\theta)\cos\left(\frac{\theta}{2}\right) + K_{II}(5 - 4\nu + \cos\theta)\sin\left(\frac{\theta}{2}\right) \right] \tag{70}$$

$$u_y = \frac{1+\nu}{E} \sqrt{\frac{r}{2\pi}} \left[K_I(3 - 4\nu - \cos\theta)\sin\left(\frac{\theta}{2}\right) + K_{II}(1 - 4\nu + \cos\theta)\cos\left(\frac{\theta}{2}\right) \right] \tag{71}$$

where E is Young's modulus, ν is Poisson's ratio and K_I and K_{II} respectively denote the mode I and mode II stress intensity factors. Upon exploiting the symmetry about the crack plane, only half of the finite element model is analysed. After a mesh sensitivity study, the domain is discretised with 11,392 quadrilateral quadratic elements with full integration. As shown in Fig. 2, the mesh is progressively refined towards the crack tip to resolve the material strain gradient length ℓ. From the outer
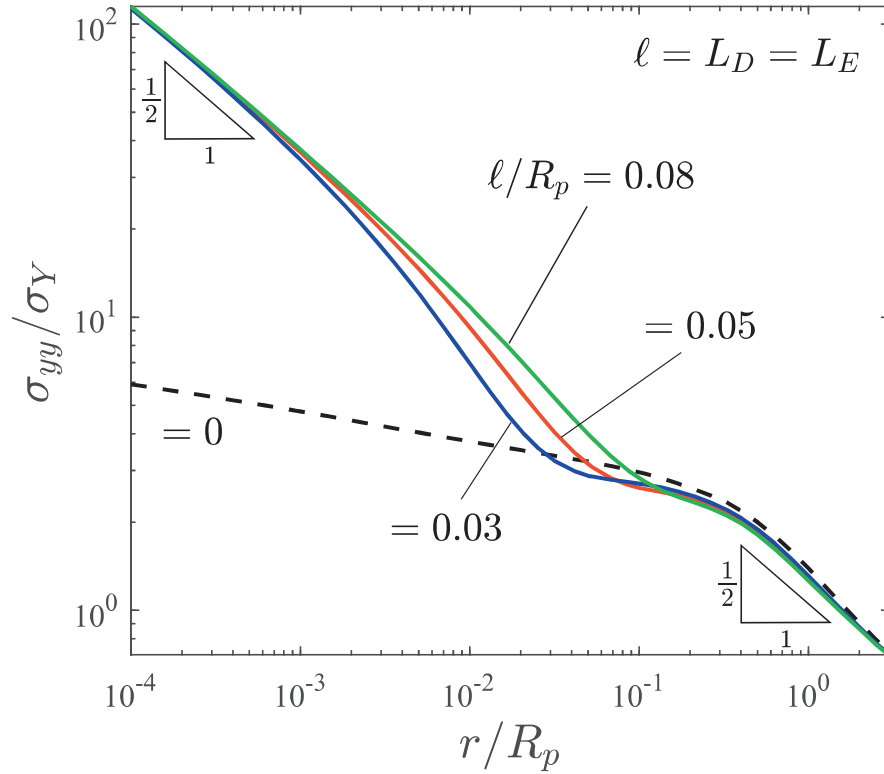
Fig. 3. Tensile stress distribution ahead of the crack tip for selected values of ℓ/R_p. Material properties: $\sigma_Y/E = 0.003$, $\nu = 0.3$, $N = 0.1$, and $\chi \to \infty$.

K-field, a representative length of the plastic zone can be defined as,

$$R_p = \frac{1}{3\pi}\left(\frac{K}{\sigma_Y}\right)^2 \tag{72}$$

We assume that the material obeys the following isotropic power-law hardening rule:

$$\sigma_F = \sigma_Y\left(1 + \frac{EE^p}{\sigma_Y}\right)^N \tag{73}$$

with the current flow stress, σ_F, being related to the gradient-enhanced effective plastic flow rate through the viscoplastic function - see (57). The viscoplastic parameters are chosen to model the rate-independent limit. Specifically, following Ref. Kristensen et al. (2020), we define the following dimensionless constant:

$$c = \frac{\dot{K}\varepsilon_Y}{K\dot{\varepsilon}_0} \tag{74}$$

where $\varepsilon_Y = \sigma_Y/E$ is the yield strain, and make suitable choices for c and m. By comparing with the results obtained with rate-independent J_2 plasticity and the viscoplastic function by Panteghini and Bardella (2016) (with $\dot{\varepsilon}_0 \to 0$), we find that $c = 0.25$ and $m = 0.005$ accurately approximate the rate-independent limit. Throughout Section 5.1, material properties are assumed to be $\sigma_Y/E = 0.003$, $\nu = 0.3$ and $N = 0.1$. We investigate the influence of χ, the parameter that governs dissipation due to the plastic spin, and the ratio ℓ/R_p, where ℓ is a reference length scale $L_E = L_D = \ell$. In addition, insight is gained into the role of the individual energetic L_E and dissipative L_D length scales.

5.1.1. Asymptotic behaviour under Mode I fracture

We proceed to verify the analytical findings of the asymptotic study in Section 3. Assume pure mode I conditions ($K_{II} = 0$) and irrotational plastic flow ($\chi \to \infty$). The tensile stress distribution ahead of the crack tip is shown in log-log scale in Fig. 3 for selected values of ℓ/R_p. The finite element results confirm the analytical findings; for all $\ell/R_p > 0$ values an elastic stress state exists close to the crack tip, where σ_{yy} scales as $r^{-1/2}$.

Several distinct regions are seen in Fig. 3. Far away from the crack tip, the stress field is elastic and exhibits the linear elastic singularity $r^{-1/2}$. As the crack tip is approached a plastic region arises, where the stresses follow the HRR field of conventional J_2 plasticity (Hutchinson, 1968; Rice & Rosengren, 1968), with σ_{yy} scaling as $r^{-N/(N+1)}$. This plastic region is reached at $r \approx 0.5R_p$, as the Irwin approximation for the plastic zone length (72) overestimates its size for strain
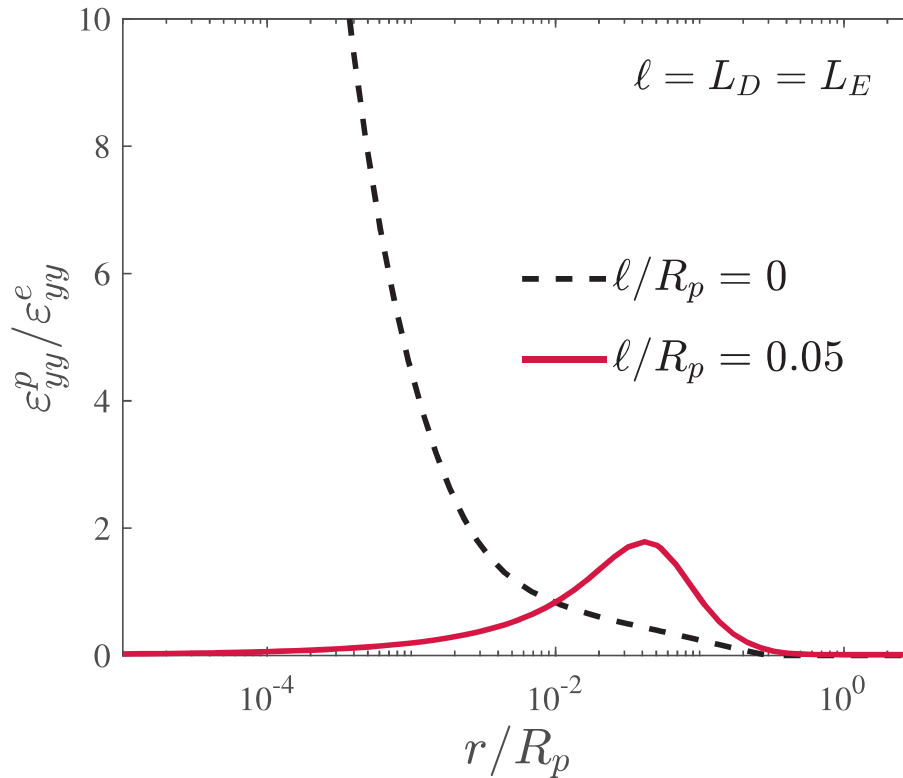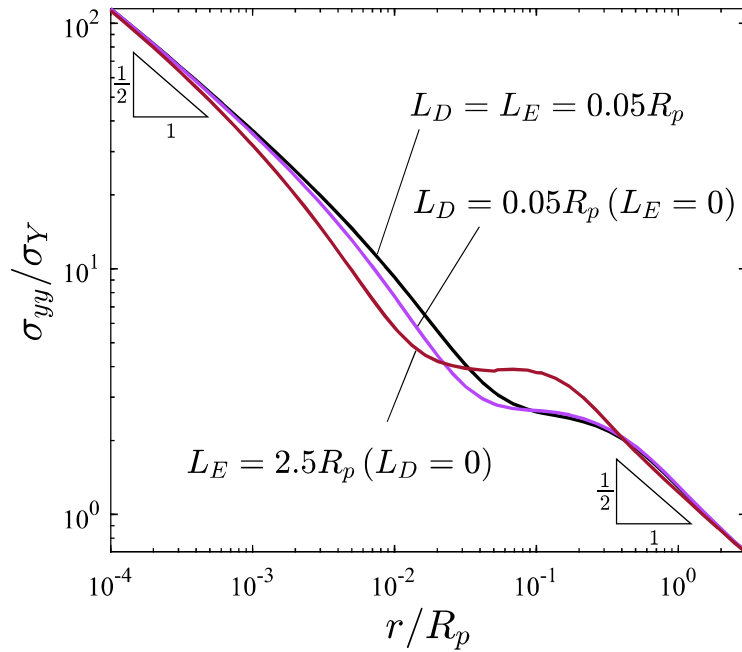
Fig. 4. Distribution ahead of the crack tip of the ratio between the tensile plastic and elastic strains $\varepsilon_{yy}^p/\varepsilon_{yy}^e$ for both conventional plasticity ($\ell/R_p = 0$) and gradient plasticity ($\ell/R_p = 0.05$). Material properties: $\sigma_Y/E = 0.003$, $\nu = 0.3$, $N = 0.1$, and $\chi \rightarrow \infty$.

hardening materials (Anderson, 2005). At approximately $r \leq \ell$, strain gradient hardening starts to play a role and a stress elevation is seen relative to the classic plasticity prediction (black dashed line, $\ell/R_p = 0$). The size of the domain where gradient plasticity and conventional plasticity predictions deviate from each other is governed by ℓ/R_p. Also, in the region $0.001R_p \leq r \leq 0.1R_p$ the degree of stress elevation relative to conventional plasticity increases with ℓ/R_p. However, in the vicinity of the crack tip ($r \approx 0.1\ell$ or smaller), all $\ell/R_p > 0$ cases superimpose, with the stress exhibiting the singular behaviour of linear elasticity $\sigma_{yy} \sim r^{-1/2}$, as predicted in the analytical asymptotic study. Note that path independence of the J-integral (35) implies that the outer and inner elastic K fields must be the same; i.e., the inner K field is identical for all $\ell/R_p > 0$ values and corresponds to the one predicted by linear elasticity. Further insight into this elastic crack tip region is gained by plotting the ratio between the plastic strain and the elastic strain $\varepsilon_{yy}^p/\varepsilon_{yy}^e$; results are shown in Fig. 4 for conventional plasticity ($\ell/R_p = 0$) and gradient plasticity ($\ell/R_p = 0.05$).

As in Fig. 3, three regimes can be identified in Fig. 4. For both $\ell = 0$ and $\ell > 0$, far away from the crack tip the plastic strains are zero but eventually increase as r becomes smaller than R_p. In conventional plasticity the plastic strains are singular and raise sharply as we approach the crack tip. However, when $\ell > 0$ the ratio $\varepsilon_{yy}^p/\varepsilon_{yy}^e$ reaches a peak and then drops, with the elastic strains dominating when $r \rightarrow 0$. An elastic strain (and stress) state exists near the crack tip, where plastic strains are negligible. Thus, the assumption of a dominating plastic strain field as $r \rightarrow 0$ cannot be used to derive the asymptotic fields, as done in the context of conventional plasticity. This crack tip elastic core resembles the concept of a dislocation-free zone (Suo, Shih, & Varias, 1993).

We proceed to assess the role of the individual energetic and dissipative higher order contributions. The crack tip stress distribution and the crack tip opening profile are respectively shown in Fig. 5a and b. Dissipative higher order effects dominate the crack tip response; the magnitude of L_E/R_p has to be increased 50 times relative to L_D/R_p to achieve a similar degree of crack tip stress elevation. Given that we are under nearly proportional loading, differences must be due to the constitutive choices for the energetic defect stress (18) and the dissipative higher order stress tensor (22c). In other words, the use of Nye's tensor as primal kinematic variable considerably reduces the local strengthening predicted ahead of a crack. The effect will likely be more profound if a less-than-quadratic defect energy is employed. Moreover, as it can be deduced from the analysis of Section 3, less-than-quadratic defect energies will change the nature of the singularity - the crack tip stress state will no longer be elastic if $L_D = 0$. For the present formulation, where the defect energy is quadratic, the asymptotic behaviour described by the purely energetic result is the same as in the purely dissipative case; as shown analytically, if $L_E > 0$ or $L_D > 0$ the stress field exhibits the elastic singularity $r^{-1/2}$ as $r \rightarrow 0$. It is important to note that, in both the analytical and numerical analyses, the plastic distortion field is assumed to be continuous. However, for the

(a)
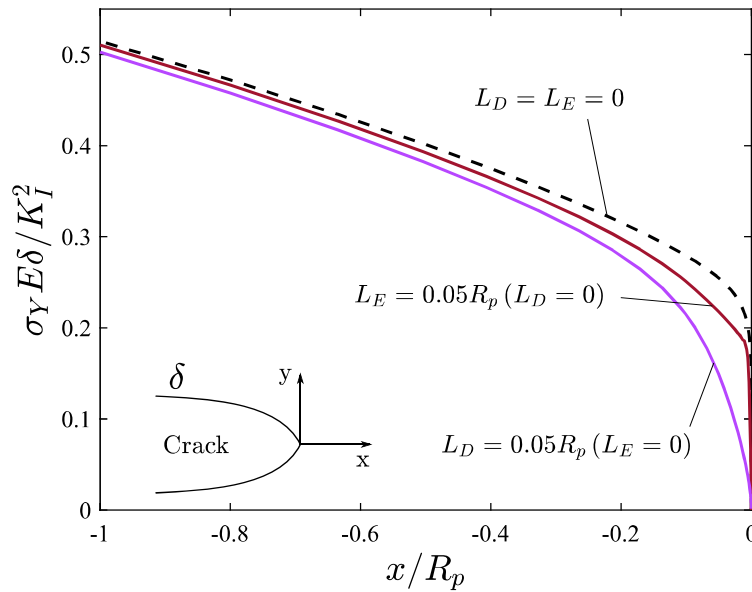
(b)

Fig. 5. Influence of energetic and dissipative length scales: (a) tensile stress distribution ahead of the crack tip, and (b) crack opening profile. Material properties: $\sigma_Y/E = 0.003$, $\nu = 0.3$, $N = 0.1$, and $\chi \to \infty$.

case $L_D = 0$ (where gradient effects are due to Nye's tensor only), the theoretical framework is characterised by kinematic higher order boundary conditions that admit discontinuity in some components of the plastic distortion. Thus, the results reported for the case $L_D = 0$ should be taken with care; an $H(\text{curl})$ finite element framework, such as the one developed by Panteghini and Bardella (2018), is needed to capture the discontinuities that might arise in Nye's tensor components. A very different outcome might be predicted if γ_{ij}^p is allowed to be discontinuous and the solution localises.
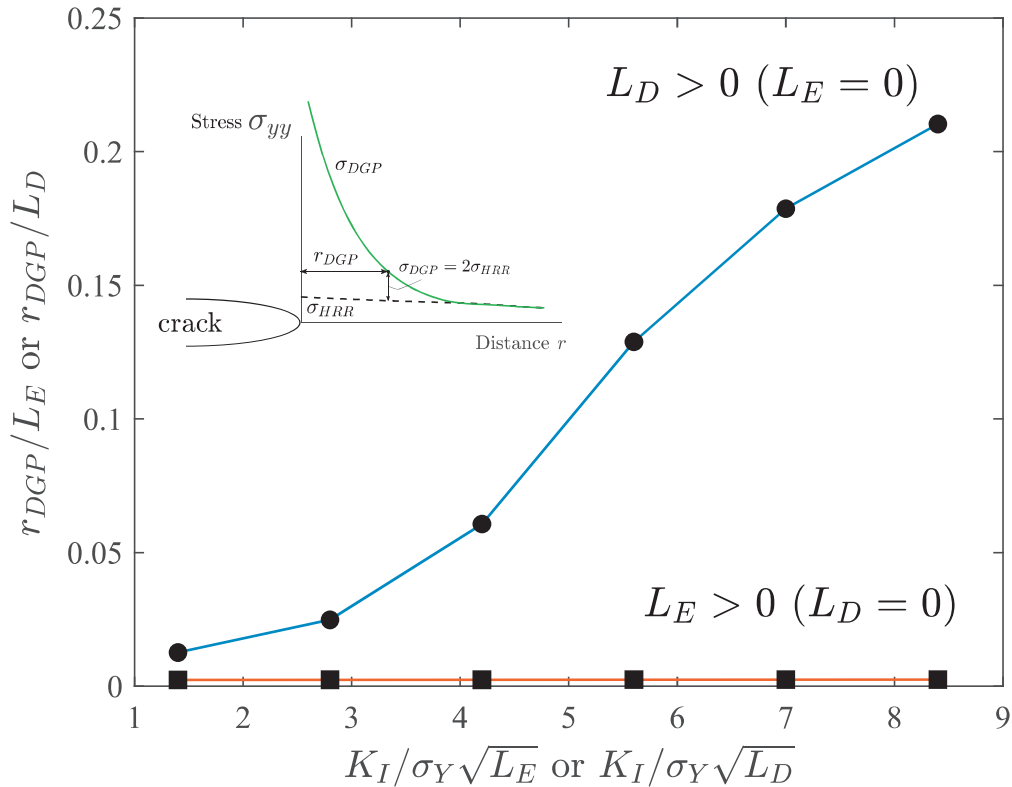
Fig. 6. Distance ahead of the crack tip where gradient effects significantly elevate the stresses relative to conventional plasticity ($\sigma_{DGP} > 2\sigma_{HRR}$). Material properties: $\sigma_Y/E = 0.003$, $\nu = 0.3$, $N = 0.1$, and $\chi \to \infty$.

As shown in Fig. 5b, the assumption of an equal magnitude for L_E and L_D leads to very different crack opening profiles. In the case of $L_D > 0$ blunting is significantly reduced behind the crack tip. The crack profile also sharpens relative to the conventional plasticity prediction when $L_E > 0$ ($L_D = 0$) but to a much lesser extent. Far from the crack tip, the crack profile predictions for energetic gradient plasticity, dissipative gradient plasticity and conventional plasticity agree. Outside of the inner elastic core, the local strengthening predicted by Nye's tensor is much weaker than the one predicted by a gradient contribution based on the plastic strain gradient tensor. This is further explored in Fig. 6, where the gradient dominated zone r_{DGP} is plotted as a function of the remote mode I load K_I. As in Martínez-Pañeda and Niordson (2016), we define r_{DGP} to represent the length of the region ahead of the crack tip where the stress distribution significantly deviates from conventional plasticity: $\sigma_{DGP} > 2\sigma_{HRR}$.

The results shown in Fig. 6 reveal a minor sensitivity of r_{DGP} with the remote load for the case $L_E > 0$ ($L_D = 0$). Tensile stresses are much higher than conventional plasticity in the elastic crack tip region but rapidly decay towards the conventional plasticity result farther away from the crack. Contrarily, in the case of $L_D > 0$ the domain ahead of the crack where gradient effects significantly alter the stress distribution increases with the applied load. At the largest load level, the length of the stress elevation region is more than one order of magnitude larger if dissipative strengthening is accounted for. These differences are undoubtedly rooted in the choice of a free energy based on Nye's tensor. As shown in Martínez-Pañeda et al. (2019) for fracture and in Danas, Deshpande, and Fleck (2012) for bending, the dissipative contribution also outweighs the energetic counterpart when the defect energy is based on the plastic strain gradient tensor albeit differences are significantly smaller.

Insight into the role of Nye's tensor is further gained by plotting the distribution ahead of the crack tip of the relevant component, α_{yz} - see Fig. 7. The peak value of α_{yz} appears to saturate with an increasing remote load, reaching a maximum value on the order of $0.1/L_E$. Given that L_E is typically within the 1–10 μm range (see Table 1), the maximum value of α_{yz} is on the order of 0.01–0.1 μm^{-1}, consistent with experimental observations (Das, Hofmann, & Tarleton, 2018).

The results shown in Figs. 5–7 reveal that, beyond the elastic inner core, a curl-based defect energy requires larger L_E/R_p values to have a similar impact on the stress distribution as gradient-based constitutive choices. This raises the following question: what are the values of L_E that fit the outcome of micro-scale experiments for curl- and gradient-based models? To the best of the authors' knowledge this data does not exist, motivating future work.[1]

---

[1] Bardella and Panteghini (2015) obtained a good fit to the torsion experiments by Fleck et al. (1994) with a curl-based model but employed a logarithmic defect energy.
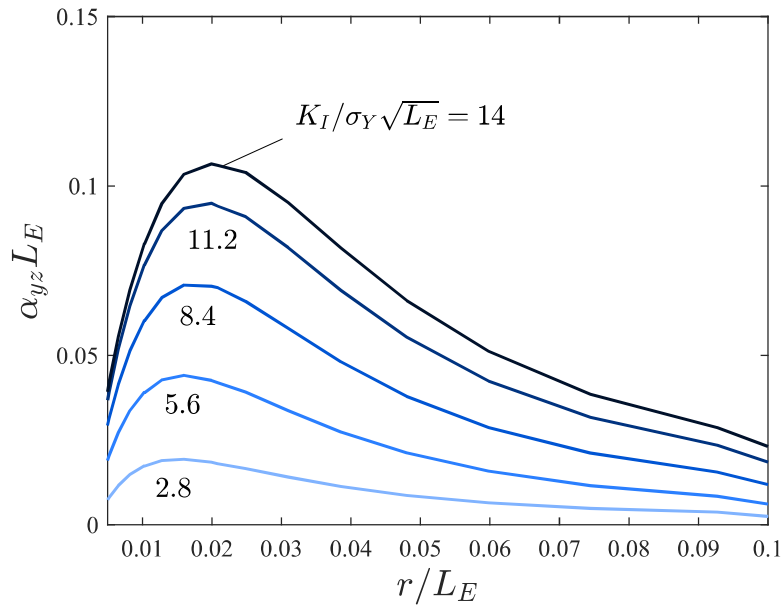
Fig. 7. Nye's tensor component α_{yz} distribution ahead of the crack tip for selected values of the remote load and the case $L_E > 0$ ($L_D = 0$). Material properties: $\sigma_Y/E = 0.003$, $\nu = 0.3$, $N = 0.1$, and $\chi \to \infty$.

5.1.2. Mixed-model fracture - the role of χ

We proceed to assess the role of χ and the plastic spin. For that, mixed-mode fracture conditions are considered, where $K_I > 0$ and $K_{II} > 0$. The degree of mode-mixity can be characterised by the following angle:

$$\psi = \tan^{-1}\left(\frac{K_{II}}{K_I}\right) \tag{75}$$

Note that, in the present model, the dissipation due to the plastic spin gradient is not accounted for. Accordingly, the plastic spin has no influence on the crack tip asymptotic behaviour; i.e., an elastic core exists, independently of the value of χ. The plastic spin can play a role if we assume that the internal work is affected by different plastic rotations of two neighbouring macroscopic material points, as proposed by Bardella (2010). In the context of the original distortion gradient plasticity model (Gurtin, 2004), the influence of the plastic spin is limited to the stress elevation in the plastic region.

Crack tip stress fields are shown in Fig. 8 for $\psi = 45°$ and selected values of the parameter governing the dissipation due to the plastic spin, χ. The choice $\chi = 2/3$ makes the effective plastic flow rate (19) equal to the norm of the plastic distortion in the absence of higher order terms, while $\chi \to \infty$ reproduces the conditions of the theory by Gurtin and Anand (2005) (that is, irrotational plastic flow). The results reveal a small influence of the plastic spin, with the stress level increasing with χ. This agrees with the trends observed by Bardella (2010) in the simple shear problem, where augmenting χ leads to additional material hardening.

The role of the plastic spin in elevating crack tip stresses is further investigated by computing the stress elevation relative to conventional plasticity $\sigma_{DGP}/\sigma_{HRR}$ as a function of the degree of mode mixity, as given by the angle ψ. The results are shown in Fig. 9. It is found that the influence of the plastic spin increases with decreasing ψ, and that the stress elevation increases with increasing ψ.

5.2. Fracture at bi-material interfaces

We proceed to investigate cleavage in the presence of significant plastic flow at bi-material interfaces, a paradigmatic conundrum in metallic fracture. Specifically, we reproduce the classic experiments by Elssner et al. (1994) and Korn et al. (2002) on niobium-sapphire interfaces. Our goal is to properly characterise the interface between elastic and elastic-plastic solids by incorporating, for the first time in fracture, the role of suitable higher order boundary conditions to model dislocation blockage.

In a remarkable series of experiments, Elssner et al. (1994) and Korn et al. (2002) measured both the macroscopic work of fracture and the atomic work of separation of an interface between sapphire and single crystal niobium. The macroscopic toughness turned out to be 1000 times higher than the atomic work of separation, with the difference being attributed to the significant dislocation activity observed in the Nb single crystal. However, fracture occurred by cleavage, with the crack tip remaining atomistically sharp. Since the stress level required to trigger atomic decohesion of a lattice or a strong interface is more than twice the maximum stress around the crack tip predicted by conventional J_2 plasticity, the findings
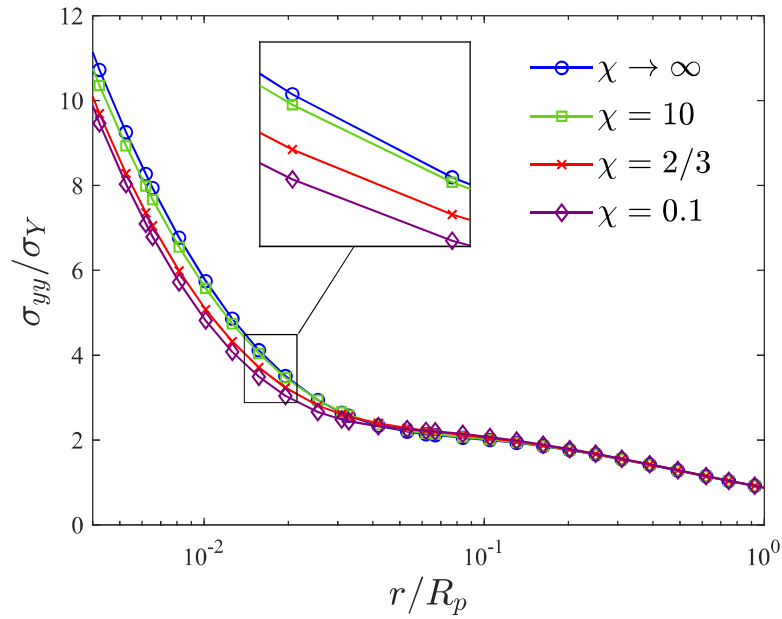
Fig. 8. Tensile stress distribution ahead of the crack tip under mode-mix conditions, $\psi = 45°$, for selected values of χ. Material properties: $\sigma_Y/E = 0.003$, $\nu = 0.3$, $N = 0.1$, and $\ell/R_p = 0.03$.
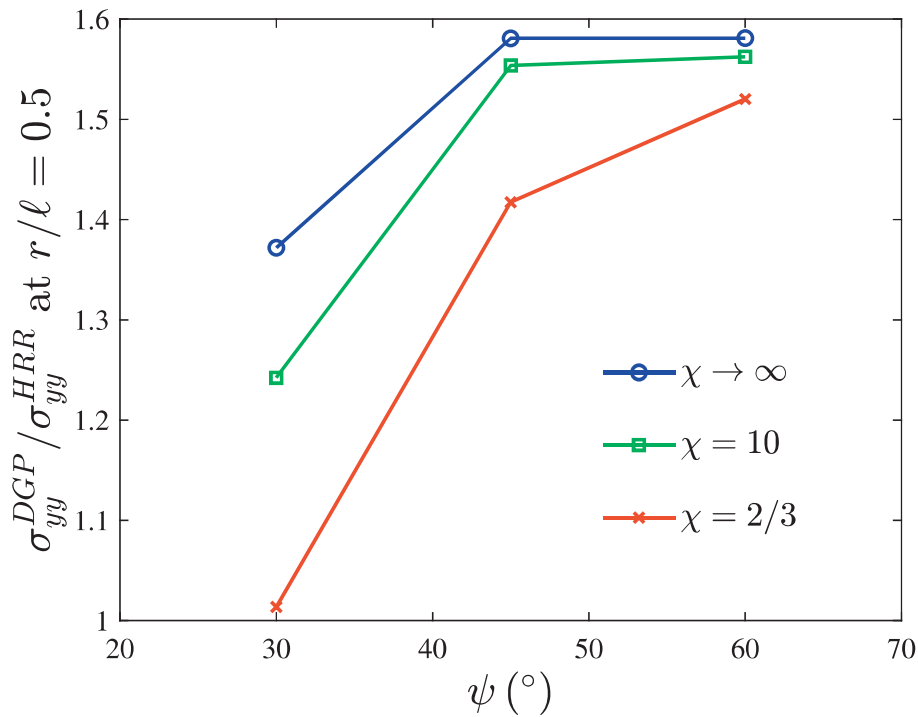

Fig. 9. Stress elevation predicted relative to conventional plasticity for selected values of χ and mode-mix angles. Material properties: $\sigma_Y/E = 0.003$, $\nu = 0.3$, $N = 0.1$, and $\ell/R_p = 0.03$.

by Elssner et al. (1994) and Korn et al. (2002) constitute a paradox in the context of conventional plasticity (Jiang, Huang, Zhuang, & Hwang, 2001; Jiang, Wei, Smith, Hutchinson, & Evans, 2010; Qu et al., 2004). We hypothesize that strain gradient effects, combined with dislocation blockage, will be sufficient to raise crack tip stresses beyond the theoretical strength of the metal, $\approx 10\sigma_Y$, over a sufficiently large distance to trigger fracture. The geometry, configuration and dimensions (in mm) of the four-point bending experiment Korn et al. (2002) are shown in Fig. 10. A sapphire layer is sandwiched between

Table 1
Compilation of experimentally reported length scales with their associated gradient plasticity formulation.

| Work	Material	Experiment	Length scale - Gradient model
Fleck et al. (1994)	Cu	Torsion	3.7 μm - Fleck and Hutchinson (1993)
Nix and Gao (1998)	Cu (cold worked)	Indentation	5.84 μm - Nix and Gao (1998)
	Single crystal Cu	Indentation	12 μm - Nix and Gao (1998)
Stölken and Evans (1998)	Ni	Bending	5.2 μm - Fleck and Hutchinson (1993)
Shrotriya, Allameh, Lou, Buchheit, and Soboyejo (2003)	Ni	Bending	5.6 μm - Fleck and Hutchinson (1993)
Haque and Saif (2003)	Al	Bending	4.5 μm - Gao, Hang, Nix, and Hutchinson (1999)
Ro, Begley, Gangloff, and Agnew (2006)	Al2024	Indentation	0.2 μm - Nix and Gao (1998)
Qian, Zhang, Swaddiwudhipong, and Shen (2014)	Steel S355	Indentation	7 μm - Gao et al. (1999)
	Steel S690	Indentation	7 μm - (1999) Gao et al. (1999)
Guo, He, Lei, Li, and Liu (2017)	Cu	Torsion	3 μm - Fleck and Hutchinson (1993)
Iliev, Chen, Pathan, and Tagarielli (2017)	In	Indentation	85.21 μm - Nix and Gao (1998)
	In	Bending	93.34 μm - Fleck and Hutchinson (1993)
Mu, Hutchinson, and Meng (2014)	Cu	Micro-pillar shear	0.647 μm - Fleck and Hutchinson (1997)
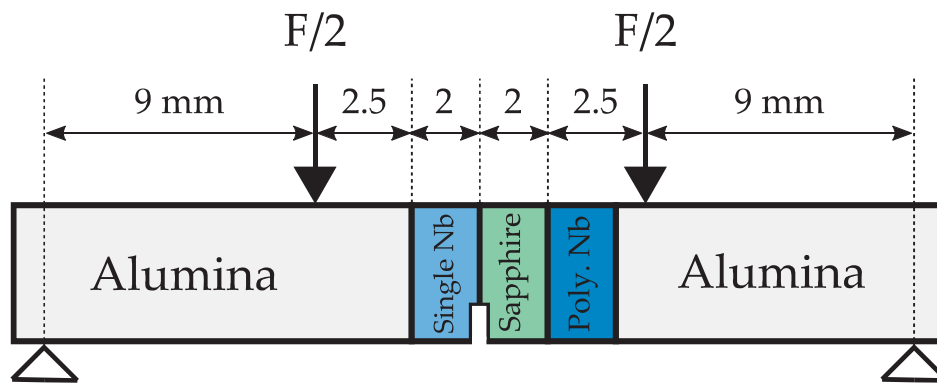
Fig. 10. Geometry and dimensions of the four-point bending experiments by Korn et al. (2002). All dimensions are in mm. The polycrystalline Nb layer has identical dimensions to the single crystal Nb and the sapphire layers. The specimen thickness (in the out-of-plane direction) is 2 mm.

a single crystal and a polycrystalline Nb layers, which are in turn sandwiched by two alumina layers. An initial crack of length $a = 0.4$ mm is placed at the interface between the single crystal Nb and sapphire. A load of $F = 85$ N is applied.

Regarding the material properties, the alumina and the sapphire are linear elastic; alumina has a Young's modulus of $E = 390$ GPa and a Poisson's ratio of $\nu = 0.27$, while sapphire has a Young's modulus of $E = 425$ GPa and a Poisson's ratio of $\nu = 0.16$ (Korn et al., 2002). The polycrystalline niobium has a Young's modulus of $E = 105$ GPa, a Poisson's ratio of $\nu = 0.39$, a yield stress of $\sigma_Y = 105$ MPa and a strain hardening exponent of $N = 0.24$ (Korn et al., 2002; Qu et al., 2004). Furthermore, the single crystal niobium layer is characterised by a Young's modulus of $E = 145$ GPa, a Poisson's ratio of $\nu = 0.36$, and a yield stress of $\sigma_Y = 145$ MPa; as in Ref. Qu et al. (2004), the strain hardening exponent is chosen to be $N = 0.05$ to represent easy glide in single crystal deformation. The magnitude of the material length scales remains to be defined. To the best of the authors' knowledge, no micro-scale experiments have been conducted on single crystal or polycrystalline Nb. A literature review of the experimental works conducted together with a gradient plasticity analysis to obtain the material length scales is provided in Table 1.

As in Section 5.1, we consider a reference length scale $L_E = L_D = \ell$ for simplicity. We follow Qu et al. (2004) and consider the magnitude of ℓ for polycrystalline Nb to be equal to 5.29 μm. This value is close to the average magnitude of the length scale measured for Cu, Ni and Al using torsion, indentation and bending. Regarding single crystal Nb, the work by Nix and Gao (1998) on Cu shows that experiments on single crystal samples are best captured with a length scale that duplicates the magnitude of the length scale employed to fit the tests on polycrystalline samples (see Table 1). Accordingly, we chose to assume a length scale for single crystal Nb of $\ell = 10.58$ μm. For both single crystal and polycrystalline Nb the parameter governing dissipation due to the plastic spin is assumed to be equal to $\chi = 2/3$. The finite element model is constructed using user defined elements, for the elastic-plastic materials, and ABAQUS in-built elements for the elastic materials. A total of 20,336 quadrilateral quadratic elements with full integration are used, with the mesh being very refined close to the crack tip - see Fig. 11. The characteristic length of the elements close to the crack tip is of 10 nm. Plane strain conditions are assumed.

The higher order boundary conditions require special consideration. We assume that the interaction between the dislocations and the various material interfaces in the bending specimen is such that dislocations are not allowed to exit the plastic layers. These *micro-hard* conditions, emulating dislocation blockage, are likely to be a good approximation to the dislocation behaviour at the niobium-sapphire and niobium-alumina interfaces. The degrees of freedom corresponding to the
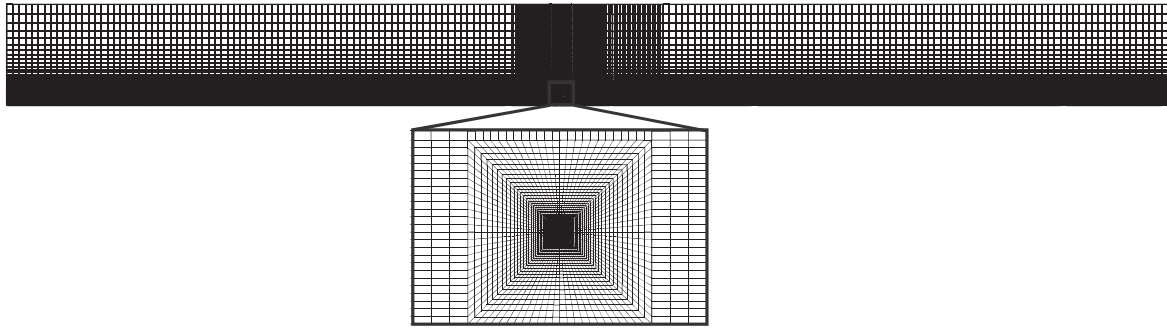
Fig. 11. Schematic and detailed views of the finite element mesh employed to model the four-point bending experiments by Korn et al. (2002).
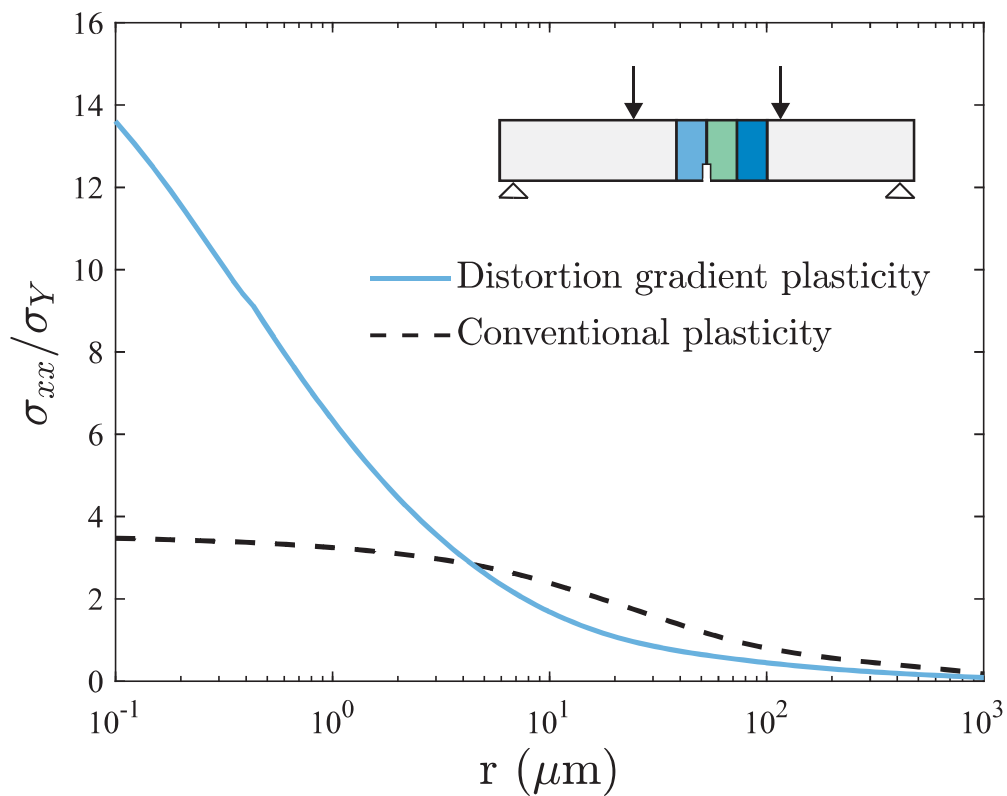

Fig. 12. Tensile stress distribution along the interface between single crystal Nb and sapphire ahead of the crack. The results are shown for distortion gradient plasticity (solid line) and for conventional plasticity (dashed line). The stress distribution is normalised by the yield stress of single crystal Nb.

plastic strain tensor and the plastic spin are therefore constrained $\varepsilon_x^p = \varepsilon_y^p = \varepsilon_{xy}^p = \vartheta_{xy}^p = 0$. Apart from that, the conventional boundary conditions are straightforward, as provided in Fig. 10.

The results obtained from the finite element model are shown in Fig. 12, in terms of tensile stress versus distance along the interface, ahead of the crack tip. The stress distribution is normalised by the yield stress of single crystal niobium and results are shown for both conventional and distortion gradient plasticity. While the maximum stress predicted by conventional plasticity is below $4\sigma_Y$, insufficient to trigger brittle fracture, the stress level predicted with distortion gradient plasticity exceeds the theoretical lattice strength ($10\sigma_Y$) over hundreds of nanometres. Consequently, the combination of local crack tip strengthening and dislocation blockage provides a rational basis for atomic decohesion at bi-material interfaces in the presence of plasticity.

Finally, contours are obtained for the relevant component of Nye's tensor, as shown in Fig. 13. The magnitude of α_{xz} increases in the vicinity of the crack tip, reaching a maximum value that does not exceed 0.01 μm^{-1}. This is in agreement with experimental observations of lattice distortions beneath nano-indents - see Das et al. (2018).
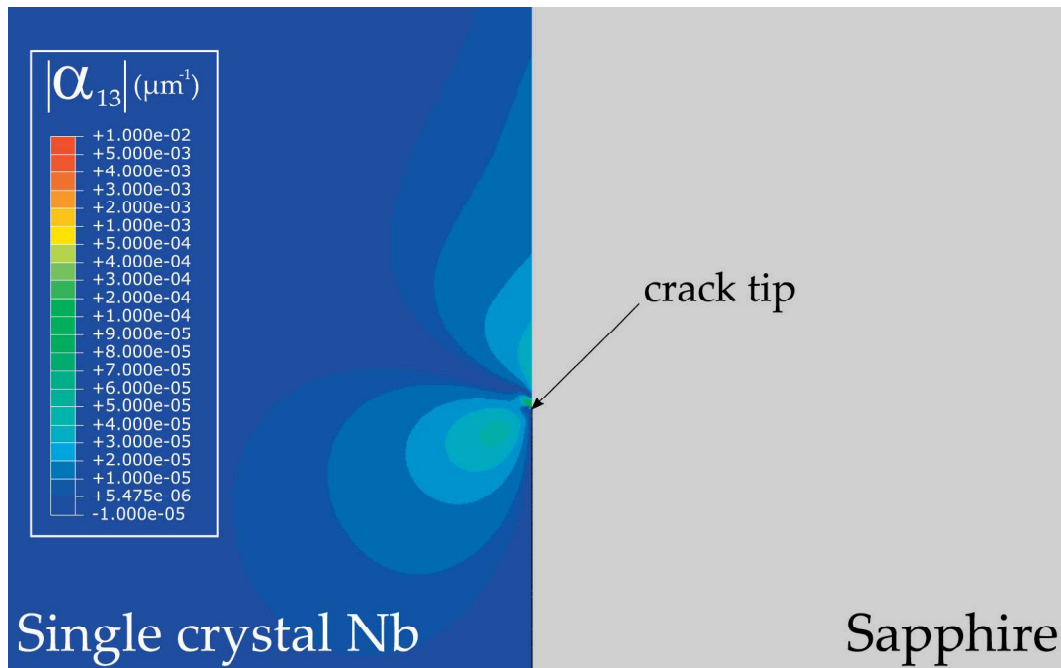
Fig. 13. Contours of the relevant component of Nye's tensor, α_{xz}, in the Nb layer in the vicinity of the crack tip.

6. Conclusions

We investigate, numerically and analytically, the crack tip behaviour of metals by using distortion gradient plasticity. The influence of two notable constitutive features on fracture mechanics predictions is investigated for the first time: (i) the use of Nye's tensor as primal higher order kinematic variable, and (ii) the role of the plastic spin. A generalised J-integral is defined, which is then used to determine the crack tip asymptotic singularity order. On the numerical side, a finite element framework is presented, which builds upon a novel viscoplastic function that enables efficient modelling of both rate-dependent and rate-independent behaviour. The analysis of crack tip fields under mode I and mixed-mode fracture assuming small scale yielding conditions reveals the following main findings:

- An *elastic* region exists close to the crack tip, where the plastic strains are negligible and the Cauchy stress follows the $r^{-1/2}$ singularity of linear elasticity. This elastic core, reminiscent of a dislocation-free zone, is present for both gradient-based and curl-based higher order constitutive choices. However, the nature of the singularity will change for a less-than-quadratic defect energy.
- The stress elevation due to strain gradient hardening predicted in the annular plastic zone embedding the elastic core is very sensitive to the constitutive choice of the defect energy. The use of Nye's tensor leads to a substantially weaker stress elevation, as compared with the plastic strain gradient tensor, for the same value of the material length scale. The values of Nye's tensor predicted in the vicinity of the crack are consistent with experimental observations.
- A small influence of χ, the parameter governing the dissipation due to the plastic spin, is observed. Increasing χ raises crack tip stresses, with the upper bound being given by the irrotational plastic flow scenario.

We emphasise that, for the case where gradients effects are due to Nye's tensor only ($L_D = 0$), our analysis is constrained by the assumption of a continuous plastic distortion field. The framework should be extended to admit discontinuity in some components of the plastic distortion, as in Panteghini and Bardella (2018), and this will be the goal of future work.

Finally, the framework is employed to shed light into the paradox of brittle fracture in the presence of plasticity in bi-material interfaces. By modelling the paradigmatic experiments by Elssner et al. (1994) and Korn et al. (2002) on niobium-sapphire interfaces, we find that:

- The combination of micro-hard higher order boundary conditions, emulating dislocation blockage, and gradient plasticity effects lead to interface crack tip stresses that are larger than the theoretical lattice strength over a distance of hundreds of nm; rationalising quasi-cleavage in bi-material interfaces.

Declaration of Competing Interest

None.

Acknowledgments

Appendix A. Additional details of numerical implementation

Assume 2D plane strain conditions, as in the numerical examples addressed in the paper. Accordingly, for an element with k nodes, the nodal variables read,

$$\hat{\boldsymbol{u}} = \begin{bmatrix} \hat{u}_x^{(1)} & \hat{u}_y^{(1)} & \cdots & \hat{u}_x^{(k)} & \hat{u}_y^{(k)} \end{bmatrix}^T \tag{A.1}$$

$$\hat{\boldsymbol{\varepsilon}}^p = \begin{bmatrix} \hat{\varepsilon}_x^{p\,(1)} & \hat{\varepsilon}_y^{p\,(1)} & \hat{\gamma}_{xy}^{p\,(1)} & \cdots & \hat{\varepsilon}_x^{p\,(k)} & \hat{\varepsilon}_y^{p\,(k)} & \hat{\gamma}_{xy}^{p\,(k)} \end{bmatrix}^T \tag{A.2}$$

$$\hat{\vartheta}_{xy}^p = \begin{bmatrix} \hat{\vartheta}_{xy}^{p\,(1)} & \cdots & \hat{\vartheta}_{xy}^{p\,(k)} \end{bmatrix}^T \tag{A.3}$$

The shape functions matrices for a given node n are then given by,

$$\boldsymbol{N}_n^u = \begin{bmatrix} N_n & 0 \\ 0 & N_n \end{bmatrix}; \qquad \boldsymbol{N}_n^{\varepsilon^p} = \begin{bmatrix} N_n & 0 & 0 \\ 0 & N_n & 0 \\ -N_n & -N_n & 0 \\ 0 & 0 & N_n \end{bmatrix} \tag{A.4}$$

with $\boldsymbol{N}_n^{\vartheta^p}$ being, in plane strain conditions, the scalar N_n for node n. While the interpolation matrices for gradient and curl-based quantities are given by,

$$\boldsymbol{B}_n^u = \begin{bmatrix} \dfrac{\partial N_n}{\partial x} & 0 \\ 0 & \dfrac{\partial N_n}{\partial y} \\ 0 & 0 \\ \dfrac{\partial N_n}{\partial y} & \dfrac{\partial N_n}{\partial x} \end{bmatrix}; \qquad \boldsymbol{B}_n^{\varepsilon^p} = \begin{bmatrix} \dfrac{\partial N_n}{\partial x} & 0 & 0 \\ \dfrac{\partial N_n}{\partial y} & 0 & 0 \\ 0 & \dfrac{\partial N_n}{\partial x} & 0 \\ 0 & \dfrac{\partial N_n}{\partial y} & 0 \\ -\dfrac{\partial N_n}{\partial x} & -\dfrac{\partial N_n}{\partial x} & 0 \\ -\dfrac{\partial N_n}{\partial y} & -\dfrac{\partial N_n}{\partial y} & 0 \\ 0 & 0 & \dfrac{\partial N_n}{\partial x} \\ 0 & 0 & \dfrac{\partial N_n}{\partial y} \end{bmatrix}; \tag{A.5}$$

and,

$$\boldsymbol{M}_n^{\varepsilon^p} = \begin{bmatrix} -\dfrac{\partial N_n}{\partial y} & 0 & \dfrac{1}{2}\dfrac{\partial N_n}{\partial x} \\ 0 & \dfrac{\partial N_n}{\partial x} & -\dfrac{1}{2}\dfrac{\partial N_n}{\partial y} \\ -\dfrac{\partial N_n}{\partial y} & -\dfrac{\partial N_n}{\partial y} & 0 \\ \dfrac{\partial N_n}{\partial x} & \dfrac{\partial N_n}{\partial x} & 0 \end{bmatrix}; \qquad \boldsymbol{M}_n^{\vartheta^p} = \begin{bmatrix} \dfrac{\partial N_n}{\partial x} \\ \dfrac{\partial N_n}{\partial y} \\ 0 \\ 0 \end{bmatrix} \tag{A.6}$$

On the other side, the stiffness matrix components are given by,

$$\boldsymbol{K}_{nm}^{u,u} = \frac{\partial \boldsymbol{R}_n^u}{\partial \boldsymbol{u}_m} = \int_\Omega \left(\boldsymbol{B}_n^u\right)^T \boldsymbol{C} \boldsymbol{B}_m^u \, \mathrm{d}V \tag{A.7}$$

$$\boldsymbol{K}_{nm}^{u,\varepsilon^p} = \frac{\partial \boldsymbol{R}_n^u}{\partial \boldsymbol{\varepsilon}_m^p} = -\int_\Omega \left(\boldsymbol{B}_n^u\right)^T \boldsymbol{C} \boldsymbol{N}_m^{\varepsilon^p} \, \mathrm{d}V \tag{A.8}$$

$$\boldsymbol{K}_{nm}^{\varepsilon^p,u} = \frac{\partial \boldsymbol{R}_n^{\varepsilon^p}}{\partial \boldsymbol{u}_m} = -\int_\Omega \left(\boldsymbol{N}_n^{\varepsilon^p}\right)^T \boldsymbol{C} \boldsymbol{B}_m^u \, \mathrm{d}V \tag{A.9}$$

$$\mathbf{K}_{nm}^{\boldsymbol{\varepsilon}^p, \boldsymbol{\varepsilon}^p} = \frac{\partial \mathbf{R}_n^{\boldsymbol{\varepsilon}^p}}{\partial \boldsymbol{\varepsilon}_m^p} = \int_\Omega \left\{ \left(\mathbf{N}_n^{\boldsymbol{\varepsilon}^p} \right)^T \left[\left(\frac{\partial \mathbf{q}}{\partial \boldsymbol{\varepsilon}_m^p} + \mathbf{C} \right) \mathbf{N}_m^{\boldsymbol{\varepsilon}^p} + \frac{\partial \mathbf{q}}{\partial \nabla \boldsymbol{\varepsilon}_m^p} \mathbf{B}_m^{\boldsymbol{\varepsilon}^p} \right] + \left(\mathbf{B}_n^{\boldsymbol{\varepsilon}^p} \right)^T \left(\frac{\partial \boldsymbol{\tau}}{\partial \boldsymbol{\varepsilon}_m^p} \mathbf{N}_m^{\boldsymbol{\varepsilon}^p} + \frac{\partial \boldsymbol{\tau}}{\partial \nabla \boldsymbol{\varepsilon}_m^p} \mathbf{B}_m^{\boldsymbol{\varepsilon}^p} \right) + \left(\mathbf{M}_n^{\boldsymbol{\varepsilon}^p} \right)^T \frac{\partial \boldsymbol{\zeta}}{\partial \boldsymbol{\alpha}_m} \mathbf{M}_m^{\boldsymbol{\varepsilon}^p} \right\} dV$$

(A.10)

$$\mathbf{K}_{nm}^{\boldsymbol{\varepsilon}^p, \vartheta^p} = \frac{\partial \mathbf{R}_n^{\boldsymbol{\varepsilon}^p}}{\partial \boldsymbol{\vartheta}_m^p} = \int_\Omega \left[\left(\mathbf{N}_n^{\boldsymbol{\varepsilon}^p} \right)^T \frac{\partial \mathbf{q}}{\partial \vartheta_m^p} \mathbf{N}_m^{\vartheta^p} + \left(\mathbf{B}_n^{\boldsymbol{\varepsilon}^p} \right)^T \frac{\partial \boldsymbol{\tau}}{\partial \vartheta_m^p} \mathbf{N}_m^{\vartheta^p} + \left(\mathbf{M}_n^{\boldsymbol{\varepsilon}^p} \right)^T \frac{\partial \boldsymbol{\zeta}}{\partial \boldsymbol{\alpha}_m} \mathbf{M}_m^{\vartheta^p} \right] dV$$

(A.11)

$$\mathbf{K}_{nm}^{\vartheta^p, \boldsymbol{\varepsilon}^p} = \frac{\partial \mathbf{R}_n^{\vartheta^p}}{\partial \boldsymbol{\varepsilon}_m^p} = \int_\Omega \left[\left(\mathbf{N}_n^{\vartheta^p} \right)^T \left(\frac{\partial \boldsymbol{\omega}}{\partial \boldsymbol{\varepsilon}_m^p} \mathbf{N}_m^{\boldsymbol{\varepsilon}^p} + \frac{\partial \boldsymbol{\omega}}{\partial \nabla \boldsymbol{\varepsilon}_m^p} \mathbf{B}_m^{\boldsymbol{\varepsilon}^p} \right) + \left(\mathbf{M}_n^{\vartheta^p} \right)^T \frac{\partial \boldsymbol{\zeta}}{\partial \boldsymbol{\alpha}_m} \mathbf{M}_m^{\boldsymbol{\varepsilon}^p} \right] dV$$

(A.12)

$$\mathbf{K}_{nm}^{\vartheta^p, \vartheta^p} = \frac{\partial \mathbf{R}_n^{\vartheta^p}}{\partial \boldsymbol{\vartheta}_m^p} = \int_\Omega \left[\left(\mathbf{N}_n^{\vartheta^p} \right)^T \frac{\partial \boldsymbol{\omega}}{\partial \vartheta_m^p} \mathbf{N}_m^{\vartheta^p} + \left(\mathbf{M}_n^{\vartheta^p} \right)^T \frac{\partial \boldsymbol{\zeta}}{\partial \boldsymbol{\alpha}_m} \mathbf{M}_m^{\vartheta^p} \right] dV$$

(A.13)

References

Aifantis, E. C. (1992). On the role of gradients in the localization of deformation and fracture. *International Journal of Engineering Science, 30*(10), 1279–1299.

Anderson, T. L. (2005). *Fracture mechanics. fundamentals and applications* (3rd ed.). Boca Raton: CRC Press, Taylor & Francis.

Ashby, M. F. (1970). The deformation of plastically non-homogeneous materials. *Philosophical Magazine, 21*(170), 399–424.

Bardella, L. (2009). A comparison between crystal and isotropic strain gradient plasticity theories with accent on the role of the plastic spin. *European Journal of Mechanics, A/Solids, 28*(3), 638–646.

Bardella, L. (2010). Size effects in phenomenological strain gradient plasticity constitutively involving the plastic spin. *International Journal of Engineering Science, 48*(5), 550–568.

Bardella, L., & Giacomini, A. (2008). Influence of material parameters and crystallography on the size effects describable by means of strain gradient plasticity. *Journal of the Mechanics and Physics of Solids, 56*(9), 2906–2934.

Bardella, L., & Panteghini, A. (2015). Modelling the torsion of thin metal wires by distortion gradient plasticity. *Journal of the Mechanics and Physics of Solids, 78*, 467–492.

Berdichevsky, V. L., & Sedov, L. (1967). Dynamic theory of continuously distributed dislocations. Its relation to plasticity theory. *Journal of Applied Mathematics and Mechanics, 31*(6), 989–1006.

Bittencourt, E., Needleman, A., Gurtin, M. E., & Van der Giessen, E. (2003). A comparison of nonlocal continuum and discrete dislocation plasticity predictions. *Journal of the Mechanics and Physics of Solids, 51*(2), 281–310.

Brinckmann, S., & Siegmund, T. (2008). Computations of fatigue crack growth with strain gradient plasticity and an irreversible cohesive zone model. *Engineering Fracture Mechanics, 75*(8), 2276–2294.

Burgers, J. M. (1939). Some considerations on the fields of stresses connected with dislocations in a regular crystal lattice. *Koninklijke Nederlandse Akademie van Wetenschappen, 42*(1931), 293–325.

Chen, J. Y., Wei, Y., Huang, Y., Hutchinson, J. W., & Hwang, K. C. (1999). The crack tip fields in strain gradient plasticity: the asymptotic and numerical analyses. *Engineering Fracture Mechanics, 64*(5), 625–648.

Danas, K., Deshpande, V. S., & Fleck, N. A. (2012). Size effects in the conical indentation of an elasto-plastic solid. *Journal of the Mechanics and Physics of Solids, 60*(9), 1605–1625.

Das, S., Hofmann, F., & Tarleton, E. (2018). Consistent determination of geometrically necessary dislocation density from simulations and experiments. *International Journal of Plasticity, 109*, 18–42.

Dillon, O. W., & Kratochvil, J. (1970). A strain gradient theory of plasticity. *International Journal of Solids and Structures, 6*(12), 1513–1533.

Elssner, G., Korn, D., & Rühle, M. (1994). The influence of interface impurities on fracture energy of UHV diffusion bonded metal-ceramic bicrystals. *Scripta Metallurgica et Materiala, 31*(8), 1037–1042.

Eshelby, J. D. (1956). The continuum theory of lattice defects. *Solid State Physics, 3*(C), 79–144.

Fleck, N. A., & Hutchinson, J. W. (1993). A phenomenological theory for strain gradient effects in plasticity. *Journal of the Mechanics and Physics of Solids, 41*(12), 1825–1857.

Fleck, N. A., & Hutchinson, J. W. (1997). Strain gradient plasticity. *Advances in Applied Mechanics, 33*, 295–361.

Fleck, N. A., & Hutchinson, J. W. (2001). A reformulation of strain gradient plasticity. *Journal of the Mechanics and Physics of Solids, 49*(10), 2245–2271.

Fleck, N. A., Muller, G. M., Ashby, M. F., & Hutchinson, J. W. (1994). Strain gradient plasticity: Theory and experiment. *Acta Metallurgica et Materialia, 42*(2), 475–487.

Fleck, N. A., & Willis, J. R. (2009). A mathematical basis for strain-gradient plasticity theory. Part II: Tensorial plastic multiplier. *Journal of the Mechanics and Physics of Solids, 57*(7), 1045–1057.

Gao, H., Hang, Y., Nix, W. D., & Hutchinson, J. W. (1999). Mechanism-based strain gradient plasticity - I. Theory. *Journal of the Mechanics and Physics of Solids, 47*(6), 1239–1263.

Garroni, A., Leoni, G., & Ponsiglione, M. (2010). Gradient theory for plasticity via homogenization of discrete dislocations. *Journal of the European Mathematical Society, 12*(5), 1231–1266.

Gudmundson, P. (2004). A unified treatment of strain gradient plasticity. *Journal of the Mechanics and Physics of Solids, 52*(6), 1379–1406.

Guo, S., He, Y., Lei, J., Li, Z., & Liu, D. (2017). Individual strain gradient effect on torsional strength of electropolished microscale copper wires. *Scripta Materialia, 130*, 124–127.

Gurtin, M. E. (2004). A gradient theory of small-deformation isotropic plasticity that accounts for the Burgers vector and for dissipation due to plastic spin. *Journal of the Mechanics and Physics of Solids, 52*(11), 2545–2568.

Gurtin, M. E., & Anand, L. (2005). A theory of strain-gradient plasticity for isotropic, plastically irrotational materials. Part I: Small deformations. *Journal of the Mechanics and Physics of Solids, 53*, 1624–1649.

Haque, M. A., & Saif, M. T. A. (2003). Strain gradient effect in nanoscale thin films. *Acta Materialia, 51*(11), 3053–3061.

Huang, Y., Zhang, L., Guo, T. F., & Hwang, K. C. (1997). Mixed mode near-tip fields for cracks in materials with strain-gradient effects. *Journal of the Mechanics and Physics of Solids, 45*(3), 439–465.

Hutchinson, J. W. (1968). Singular behaviour at the end of a tensile crack in a hardening material. *Journal of the Mechanics and Physics of Solids, 16*(1), 13–31.

Idiart, M. I., Deshpande, V. S., Fleck, N. A., & Willis, J. R. (2009). Size effects in the bending of thin foils. *International Journal of Engineering Science, 47*(11–12), 1251–1264.

Iliev, S. P., Chen, X., Pathan, M. V., & Tagarielli, V. L. (2017). Measurements of the mechanical response of Indium and of its size dependence in bending and indentation. *Materials Science and Engineering A, 683*, 244–251.

Jiang, H., Huang, Y., Zhuang, Z., & Hwang, K. C. (2001). Fracture in mechanism-based strain gradient plasticity. *Journal of the Mechanics and Physics of Solids, 49*(5), 979–993.

Jiang, Y., Wei, Y., Smith, J. R., Hutchinson, J. W., & Evans, A. G. (2010). First principles based predictions of the toughness of a metal/oxide interface. *International Journal of Materials Research, 101*, 1–8.

Komaragiri, U., Agnew, S. R., Gangloff, R. P., & Begley, M. R. (2008). The role of macroscopic hardening and individual length-scales on crack tip stress elevation from phenomenological strain gradient plasticity. *Journal of the Mechanics and Physics of Solids, 56*(12), 3527–3540.

Korn, D., Elssner, G., Cannon, R. M., & Ruhle, M. (2002). Fracture properties of interfacially doped Nb-A12O3 bicrystals: I, fracture characteristics. *Acta Materialia, 50*(15), 3881–3901.

Kristensen, P. K., Niordson, C. F., & Martínez-Pañeda, E. (2020). A phase field model for elastic-gradient-plastic solids undergoing hydrogen embrittlement. *Journal of the Mechanics and Physics of Solids, 143*, 104093.

Lancioni, G., Yalçinkaya, T., & Cocks, A. (2015). Energy-based non-local plasticity models for deformation patterning, localization and fracture. *Proceedings of the Royal Society A: Mathematical, Physical and Engineering Sciences, 471*(2180).

Martínez-Pañeda, E., & Betegón, C. (2015). Modeling damage and fracture within strain-gradient plasticity. *International Journal of Solids and Structures, 59*, 208–215.

Martínez-Pañeda, E., del Busto, S., Niordson, C. F., & Betegón, C. (2016b). Strain gradient plasticity modeling of hydrogen diffusion to the crack tip. *International Journal of Hydrogen Energy, 41*(24), 10265–10274.

Martínez-Pañeda, E., Deshpande, V. S., Niordson, C. F., & Fleck, N. A. (2019a). The role of plastic strain gradients in the crack growth resistance of metals. *Journal of the Mechanics and Physics of Solids, 126*, 136–150.

Martínez-Pañeda, E., & Fleck, N. A. (2019). Mode I crack tip fields: Strain gradient plasticity theory versus J2 flow theory. *European Journal of Mechanics - A/Solids, 75*, 381–388.

Martínez-Pañeda, E., Fuentes-Alonso, S., & Betegón, C. (2019b). Gradient-enhanced statistical analysis of cleavage fracture. *European Journal of Mechanics - A/Solids, 77*, 103785.

Martínez-Pañeda, E., & Niordson, C. F. (2016). On fracture in finite strain gradient plasticity. *International Journal of Plasticity, 80*, 154–167.

Martínez-Pañeda, E., Niordson, C. F., & Bardella, L. (2016c). A finite element framework for distortion gradient plasticity with applications to bending of thin foils. *International Journal of Solids and Structures, 96*, 288–299.

Martínez-Pañeda, E., Niordson, C. F., & Gangloff, R. P. (2016a). Strain gradient plasticity-based modeling of hydrogen environment assisted cracking. *Acta Materialia, 117*, 321–332.

Mu, Y., Hutchinson, J. W., & Meng, W. J. (2014). Micro-pillar measurements of plasticity in confined Cu thin films. *Extreme Mechanics Letters, 1*, 62–69.

Needleman, A. (1988). Material rate dependence and mesh sensitivity in localization problems. *Computer Methods in Applied Mechanics and Engineering, 67*(1), 69–85.

Nielsen, K. L., & Niordson, C. F. (2013). A 2D finite element implementation of the Fleck-Willis strain-gradient flow theory. *European Journal of Mechanics, A/Solids, 41*, 134–142.

Nielsen, K. L., & Niordson, C. F. (2014). A numerical basis for strain-gradient plasticity theory: Rate-independent and rate-dependent formulations. *Journal of the Mechanics and Physics of Solids, 63*(1), 113–127.

Nix, W. D., & Gao, H. J. (1998). Indentation size effects in crystalline materials: A law for strain gradient plasticity. *Journal of the Mechanics and Physics of Solids, 46*(3), 411–425.

Nye, J. F. (1953). Some geometrical relations in dislocated crystals. *Acta Metallurgica, 1*(2), 153–162.

Ohno, N., & Okumura, D. (2007). Higher-order stress and grain size effects due to self-energy of geometrically necessary dislocations. *Journal of the Mechanics and Physics of Solids, 55*(9), 1879–1898.

Panteghini, A., & Bardella, L. (2016). On the finite element implementation of higher-order gradient plasticity, with focus on theories based on plastic distortion incompatibility. *Computer Methods in Applied Mechanics and Engineering, 310*, 840–865.

Panteghini, A., & Bardella, L. (2018). On the role of higher-order conditions in distortion gradient plasticity. *Journal of the Mechanics and Physics of Solids, 118*, 293–321.

Panteghini, A., Bardella, L., & Niordson, C. F. (2019). A potential for higher-order phenomenological strain gradient plasticity to predict reliable response under non-proportional loading. *Proceedings of the Royal Society A: Mathematical, Physical and Engineering Sciences, 475*, 20190258.

Poh, L. H. (2013). Scale transition of a higher order plasticity model - a consistent homogenization theory from meso to macro. *Journal of the Mechanics and Physics of Solids, 61*(12), 2692–2710.

Poh, L. H., & Peerlings, R. H. (2016). The plastic rotation effect in an isotropic gradient plasticity model for applications at the meso scale. *International Journal of Solids and Structures, 78–79*, 57–69.

Poh, L. H., & Phan, V. T. (2016). Numerical implementation and validation of a consistently homogenized higher order plasticity model. *International Journal for Numerical Methods in Engineering, 106*, 454–483.

Pribe, J. D., Siegmund, T., Tomar, V., & Kruzic, J. J. (2019). Plastic strain gradients and transient fatigue crack growth: A computational study. *International Journal of Fatigue, 120*, 283–293.

Qian, X., Zhang, S., & Swaddiwudhipong, S. (2011). Calibration of Weibull parameters using the conventional mechanism-based strain gradient plasticity. *Engineering Fracture Mechanics, 78*(9), 1928–1944.

Qian, X., Zhang, S., Swaddiwudhipong, S., & Shen, L. (2014). Temperature dependence of material length scale for strain gradient plasticity and its effect on near-tip opening displacement. *Fatigue and Fracture of Engineering Materials and Structures, 37*(2), 157–170.

Qu, S., Huang, Y., Jiang, H., Liu, C., Wu, P. D., & Hwang, K. C. (2004). Fracture analysis in the conventional theory of mechanism-based strain gradient (CMSG) plasticity. *International Journal of Fracture, 129*(3), 199–220.

Rice, J. (1968). A path independent integral and the approximate analysis of strain concentration by notches and cracks. *Journal of Applied Mechanics, 35*(2), 379–386.

Rice, J. R., & Rosengren, G. F. (1968). Plane strain deformation near a crack tip in a power-law hardening material. *Journal of the Mechanics and Physics of Solids, 16*(1), 1–12.

Ro, Y. J., Begley, M. R., Gangloff, R. P., & Agnew, S. R. (2006). Effect of aging on scale-dependent plasticity in aluminum alloy 2024. *Materials Science and Engineering A, 435–436*, 333–342.

Shrotriya, P., Allameh, S. M., Lou, J., Buchheit, T., & Soboyejo, W. O. (2003). On the measurement of the plasticity length scale parameter in LIGA nickel foils. *Mechanics of Materials, 35*(3–6), 233–243.

Stölken, J. S., & Evans, A. G. (1998). A microbend test method for measuring the plasticity length scale. *Acta Materialia, 46*(14), 5109–5115.

Suo, Z., Shih, C. F., & Varias, A. G. (1993). A theory for cleavage cracking in the presence of plastic flow. *Acta Metallurgica Et Materialia, 41*(5), 1551–1557.

Voyiadjis, G. Z., & Song, Y. (2019). Strain gradient continuum plasticity theories: Theoretical, numerical and experimental investigations. *International Journal of Plasticity, 121*, 21–75.

Wei, Y., & Hutchinson, J. W. (1997). Steady-state crack growth and work of fracture for solids characterized by strain gradient plasticity. *Journal of the Mechanics and Physics of Solids, 45*(8), 1253–1273.

Wulfinghoff, S., Forest, S., & Böhlke, T. (2015). Strain gradient plasticity modeling of the cyclic behavior of laminate microstructures. *Journal of the Mechanics and Physics of Solids, 79*, 1–20.

Xia, Z. C., & Hutchinson, J. W. (1996). Crack tip fields in strain gradient plasticity. *Journal of the Mechanics and Physics of Solids, 44*(10), 1621–1648.

INFORME SOBRE EL FACTOR DE IMPACTO DE LAS PUBLICACIONES

La siguiente tabla ha sido elaborada considerando la valoración indicada en el "Journal Citation Report 2020" realizado por Clarivate Analytics.

ARTÍCULO A – *"On the suitability of slow strain rate tensile testing for assessing hydrogen embrittlement susceptibility"*

Revista: CORROSION SCIENCE

ISSN: 0010-938X

Factor de Impacto: 6.479

Categoría: Q1

Puesto en la categoría: 695

ARTÍCULO B – *"Gradient-enhanced statistical analysis of cleavage fracture"*,

Revista: EUROPEAN JOURNAL OF MECHANICS A / SOLIDS

ISSN: 09977538

Factor de Impacto: 3.786

Categoría: Q1

Puesto en la categoría: 1917

ARTÍCULO C – *"Fracture in distortion gradient plasticity"*

Revista: INTERNATIONAL JOURNAL OF ENGINEERING SCIENCE

ISSN: 0020-7225

Factor de Impacto: 9.219

Categoría: Q1

Puesto en la categoría: 358